DEVELOPMENT OF A STREAMLINE CURVATURE THROUGHFLOW DESIGN METHOD FOR FAN MODULE OF TURBOFAN ENGINES

A Thesis Submitted to
The Graduate School of Engineering and Sciences of
İzmir Institute of Technology
in Partial Fulfillment of the Requirements for the Degree of

DOCTOR OF PHILOSOPHY

in Mechanical Engineering

by
Sercan ACARER

July 2015
İZMİR

We approve the thesis of **Sercan ACARER**

Examining committee members:

Assist. Prof. Dr. Ünver ÖZKOL
Department of Mechanical Engineering, İzmir Institute of Technology

Assist. Prof. Dr. Murat BARIŞIK
Department of Mechanical Engineering, İzmir Institute of Technology

Assist. Prof. Dr. Mehmet Akif EZAN
Department of Mechanical Engineering, Dokuz Eylül University

Assist. Prof. Dr. Ziya Haktan KARADENİZ
Department of Mechanical Engineering, İzmir Katip Çelebi University

Prof. Dr. Aytunç EREK
Department of Mechanical Engineering, Dokuz Eylül University

13 July 2015

Assist. Prof. Dr. Ünver ÖZKOL
Supervisor, Department of Mechanical
Engineering, İzmir Institute of
Technology

Prof. Dr. Metin TANOĞLU
Head of the Department of Mechanical
Engineering

Prof. Dr. Bilge KARAÇALI
Dean of the Graduate School of
Engineering and Sciences

ACKNOWLEDGMENTS

Firstly, I would like to thank to my supervisor Assist. Prof. Dr. Ünver Özkol for his unfailing guidance, all of his wisdoms and great contributions to my writing skills. I am deeply grateful to my thesis progress and defense jury members Assoc. Prof. Dr. Moghtada Mobedi, Assoc. Prof. Dr. Şebnem Elçi, Assist. Prof. Dr. Murat Barışık, Assist. Prof. Dr. Mehmet Akif Ezan, Assist. Prof. Dr. Ziya Haktan Karadeniz and Prof. Dr. Aytunç Erek for their guidance and suggestions, which contributed significantly to the thesis. I would like to thank Assist. Prof. Dr. Ebubekir Atan and Assist. Prof. Dr. Erkin Gezgin for accepting to be auxiliary thesis defense jury members.

I also would like to thank greatly to Tusaş Engine Industries (TEI) for administratively supporting the studies that are in scope of this thesis.

My parents; Faruk and Leyla, and my sister Ecem have always encouraged and supported my decisions.

Lastly, I gratefully thank to my wife, Gonca Acarer, for her full support and patience during my graduate career.

ABSTRACT

DEVELOPMENT OF A STREAMLINE CURVATURE THROUGHFLOW DESIGN METHOD FOR FAN MODULE OF TURBOFAN ENGINES

Through-flow modeling of turbomachinery flows is the principle tool for inverse design, off-design analysis and post-processing of test data, due to its capability to simulate the principal aspects of turbomachinery flows, swirling flow with rotors and stators, in the axisymmetric meridian plane with minimum two orders of magnitude smaller computational time compared to three-dimensional analysis methods. Turbomachine energy equation and empirical models for incidence, deviation, pressure loss and blockage are used to define source terms for an axisymmetric compressible flow solution. Even though the subject has been studied in numerous aspects for compressors and turbines, open literature on fully coupled fan and splitter design of turbofan engines is still limited.

The present study addresses this void by developing a new split-flow method for inverse streamline curvature flow solution methodology in the course of this thesis. Hybridized empirical models that are compiled from the literature are implemented as a baseline to be calibrated.

The method is validated both experimentally and numerically on a total of six different test cases within a three-step validation strategy. Firstly, split-flow solutions of the developed method for three representative duct geometries, but without a turbomachinery, are validated. Secondly, two different single-stream transonic fans, NASA 2-stage fan and a custom-designed fan stage are used to experimentally and numerically validate the empirical models, respectively. Thirdly, experimental data of GE-NASA by-pass fan is used to validate the complete models.

It is shown that the accuracy of solutions in the tested cases are within less than 1.6% in pressure ratio, 2.3% in efficiency, 8% in velocity and 1.8 degree in flow angle. With this accuracy level, the proposed method is shown to be valid and can be implemented into existing compressor streamline curvature methodologies with minimal numerical effort.

ÖZET

TURBOFAN MOTORLARIN FAN MODÜLÜ İÇİN AKIM ÇİZGİSİ EĞRİLİĞİ METODU İLE EKSENEL-SİMETRİK TASARIM METODU GELİŞTİRİLMESİ

Turbo makine akışlarının eksenel-simetrik modelleri, tersine tasarım, analiz ve test verisinin işlenmesinde ana araçlardır. Bu metodların gücü, bu akışların esasen çevreselde ortalanmış akışta rotor ve stator kaynaklı akış döngüleri ile temsil edilebilmesinden kaynaklanmaktadır. Bu sayede hesaplama süresi üç boyutlu analiz metodlarının en az yüzde biri mertebesindedir. Bunu gerçekleştirmenin yolu ise turbo makine enerji denklemleri ile birlikte görgül kanatçık basınç kaybı, isabet açısı, sapma açısı ve tıkama modellerinin her kanadın kökünden ucuna kadar akış çözümüne tanımlanmasıdır. Konu kompresör ve türbinler için açık literatürde birçok açıdan çalışılmasına rağmen turbofan motorların fan ve ayırıcı sistemlerinin tersine tasarımı için yapılan çalışmalar çok kısıtlıdır.

Bu çalışmanın amacı, bu eksikliği gidermek için yeni bir ayrık akış metodunun akım çizgisi eğriliği tersten akış çözüm metodu için geliştirilmesidir. Çözücüye eklenecek görgül modeller ise literatürden kalibre edilmek üzere derlenmiştir.

Metod hem deneysel hem de sayısal veri ile toplam altı değişik model üzerinde üç aşamada doğrulanmıştır. İlk olarak, kanatçık içermeyen ve sadece eksenel-simetrik ayrık akışlı kanal çözümünü doğrulamak için tasarlanan üç farklı model kullanılmıştır. Sonraki aşamada bahsi geçen görgül modeller transonik ve ayrık akış içermeyen NASA 2-kademe fanı ve tezin kapsamında tasarlanmış fan kademesi üzerinde sırasıyla deneysel ve sayısal verilerle doğrulanmıştır. Son aşamada ise GE-NASA ayrık akışlı fan sistemi kullanılarak tüm modellerin deneysel doğrulaması yapılmıştır.

İncelenen geometriler için hesaplamalarda gözlemlenen en büyük hatalar basınç oranı için 1.6%, verim için 2.3%, hız için 8% ve akış açısı için 1.8 derecedir. Tüm bu çalışmalar sonucunda geliştirilen metodun doğruluğu gösterilmiştir ve mevcutta bulunan ayrık akış içermeyen kompresör eksenel-simetrik metodlarına asgari çaba ile uygulanabilirdir.

To my wife Gonca, and my family

TABLE OF CONTENTS

APPENDICES

LIST OF FIGURES

LIST OF TABLES

LIST OF SYMBOLS

ϖ_m	Mach corrected minimum loss profile loss coefficient
ϖ	Reference total pressure loss coefficient
$\bar{h}$	Average blade height [m]
$\bar{t}$	Average pitch of a complete 3D blade [m]
$\bar{r}$	Average profile radial position based on the engine axis [m]
$\dot{m}$	Mass flow rate [kg/s]
$\varpi_{off-design}$	Off-design loss coefficient
ϖ_{shock}	Shock loss coefficient for supersonic-inlet profiles
$\varpi_{shock-transonic}$	Shock loss coefficient for transonic-inlet profiles
ϖ_{TOTAL}	Total loss coefficient (profile + shock)
ε	Angle between streamline true normal and quasi-orthogonal [^{o}]
ω	Rotation angular velocity [rad/s]
ϕ	Streamline angle with axial [^{o}]
ρ	Density [kg/m^3]
μ	Dynamic viscosity [Ns/m^2]
φ	Flow coefficient (see Appendix A)
ψ	Modified stagger angle parameter in throat correlation [^{o}]
λ	Quasi-orthogonal angle with radial [^{o}]
σ	Solidity (*c/t*)
γ	Specific heat ratio (flow eqns.) or profile stagger angle (cascades)
θ	Tangential direction (flow eqns.) or profile camber angle (cascades [^{o}])
θ_{mom}	Boundary layer momentum thickness [m]
ψ	Work coefficient (see Appendix A)
$(\delta_0^*)_{10}$	Reference minimum loss deviation for 10% thick NASA 65 profile [^{o}]
Γ^*	Circulation parameter used in equivalent diffusion factor correlation
δ^*	Reference minimum loss deviation [^{o}]
δ_{disp}	Boundary layer displacement thickness [m]

β_1, β_2	Profile inlet and outlet flow angles at relative frame of reference, respectively [^{o}]
α_1, α_2	Profile inlet and outlet flow angles at absolute coordinates, respectively [^{o}]
$\alpha_{obliqueness}$	Local obliqueness angle of the shock surface [^{o}]
δ_{3D}	Additional deviation due to 3D effects [^{o}]
$(i_0^*)_{10}$	Reference minimum loss incidence for 10% thick NASA 65 profile [^{o}]
δ_m	Deviation corresponding to minimum loss incidence and 2D cascades [^{o}]
ρ_p	Average density at the profile throat [kg/m^3]
θ_{SS}	Suction surface camber angle [^{o}]
$\theta_{supersonic}$	Suction surface camber angle between inlet and the shock location [^{o}]
δ_{Vm}	Additional deviation due to rotor or stator meridional velocity ratio [^{o}]
A	Area [m^2]
a	Chord-wise distance of max camber location [m]
A_{a1}	Profile inlet streamtube area for the diffusion factor correlation [m^2]
A_{a2}	Profile inlet streamtube area for the diffusion factor correlation [m^2]
A_p^*	Area factor for equivalent diffusion factor correlation
b	Distance between chord line and point of maximum camber [m] or an exponent in reference deviation correlation
c	Chord length [m]
C_1, C_2	Constants in the loss correlation
C_{l0}	Lift coefficient
c_m	A coefficient in the off-design empirical models
c_p	Constant pressure specific heat [J/kgK]
C_{Re}	Reynolds number correction in the loss model
ct	Constant
$d_{1,2,3}$	A coefficient in the off-design empirical models
D_{eq}	Equivalent diffusion factor
eps	A coefficient in the off-design empirical models
h, H	Static and stagnation (total) enthalpy, respectively [J/kg]
H'	Stagnation (total) enthalpy in relative frame [J/kg]
H_{shape}	Boundary layer shape factor
i	Incidence angle [^{o}]
I	Rothalpy ($= H - \omega r V_\theta$)

i^*	Reference minimum loss incidence angle [^{o}]
i_c	Choke incidence angle [^{o}]
i_m	Mach corrected minimum loss incidence angle [^{o}]
i_s	Stall incidence angle [^{o}]
K_1, K_2	Profile inlet and outlet metal angles, respectively [^{o}]
K_m	Streamline curvature [1/m]
K_{sh}	Shape correction for reference incidence, deviation and loss correlations
K_{SS}	Suction surface inlet metal angle [^{o}]
$K_{t,\delta}$	Thickness correction for reference incidence correlation
$K_{t,i}$	Thickness correction for reference incidence correlation
K_w	Blockage factor due to boundary layers or wakes
M	Mach number
m	Meridional direction (radial + axial) or a slope factor for reference minimum loss deviation correlation
M_{1-rel}	Cascade inlet relative Mach number
$M_{critical}$	Profile relative inlet Mach number at which sonic flow first emerges on a profile
M_{max}	Maximum suction surface relative Mach number
n	Slope factor for reference minimum loss incidence correlation
o	Throat opening [m]
p	An exponent in reference incidence correlation
P	Static pressure [Pa]
P_0	Stagnation (total) pressure [Pa]
P_0'	Stagnation (total) pressure in relative frame [Pa]
PP_1	A coefficient in the off-design empirical models
PP_2	A coefficient in the off-design empirical models
Π	Total-to-total pressure ratio
q	An exponent in reference incidence correlation
r	Radius [m]
R_c	Angular range to choke [^{o}]
R_g	Gas constant [m^2/s^2K]
Re_c	Reynolds number based on profile chord
R_s	Angular range to stall [^{o}]
r_{SS}	Suction surface radius of curvature [1/m]

s	Entropy [J/kgK]
t	Pitch [m]
T	Static temperature [K]
T_0	Stagnation (total) temperature [K]
T_0'	Stagnation (total) temperature in relative frame [K]
th	Max profile thickness [m]
U	Rotational velocity at a given radius ($=\omega r$) [m/s]
V	Velocity at absolute frame of reference [m/s]
W	Velocity at relative frame of reference [m/s]
W_{max}	Maximum suction surface relative velocity [m/s]
W_{throat}	Average profile throat velocity [m/s]
y	Quasi-orthogonal direction (Figure 19)
z	Axial direction

Abbreviations

CFD	Computational fluid dynamics
DCA	Double circular arc
IGV	Outlet guide vane
MCA	Multiple circular arc
OGV	Outlet guide vane
Q3D	Quasi-three-dimensional
QO	Quasi-orthogonal
SLC	Streamline curvature method

Subscripts

θ	Tangential component
$1, 2$	Inlet and outlet stations of an airfoil profile, respectively
01	Total conditions at the inlet of a turbomachine
m	Meridional component
r	Radial component
z	Axial component
std	Sea-level standard conditions

CHAPTER 1

INTRODUCTION

The aerodynamic design of a fan or compressor is a complex multi-aspect process, where vast of coupled aerodynamic parameters must be decided simultaneously as design choices. Considering mechanical integrity and acoustics, the complete design is even a more complex multi-disciplinary process. Those aspects require multi-fidelity and complexity aerodynamic modeling and solvers to be utilized in different stages of design. In this regard, the 2D through-flow modeling of turbomachinery is the principle modeling approach. But prior to discussing it, theory of fans (and similarly compressors) is discussed in this chapter as a guideline for the following chapters.

1.1. Basic Principles and Main Definitions

The axial-flow-dominant (or simply ‘axial’) fans and compressors are commonly utilized in turbofan engines due to their higher mass flow at a given frontal area, and higher efficiency. The axial fans are simply a relatively large, high-flow-rate and low hub (lower casing)/shroud (upper casing) ratio compressors placed in front of turbofan engines. Different than compressors, the single or multiple stage fan component provides pressurized air to both by-pass duct and core engine (Figure 1).

By-passing relatively high amount of air benefits from the fact that the momentum thrust is proportional with the jet mass flow rate and velocity; but the corresponding fuel consumption is proportional with the mass flow rate and square of the velocity (i.e. kinetic energy). Therefore it is much more efficient, for a specified thrust, to heat lower amount of air at the core engine and provide majority of thrust with by-passed (unheated) air at a lower jet velocity but higher mass flow rate, as for the case of high by-pass ratio civil engines. Faster aircrafts require lower by-pass ratios, which ultimately may reduce to zero (no by-pass) for turbojets that have highest jet speeds. In this case, fuel efficiency tends to be much lower [1].

The fans and compressors used in aero-engines refer to the same type of turbomachine except the minor differences referred above. Therefore only compressors will be referred in the following sections for the sake of generality, keeping in mind that the entire topic will also be valid for the fans.

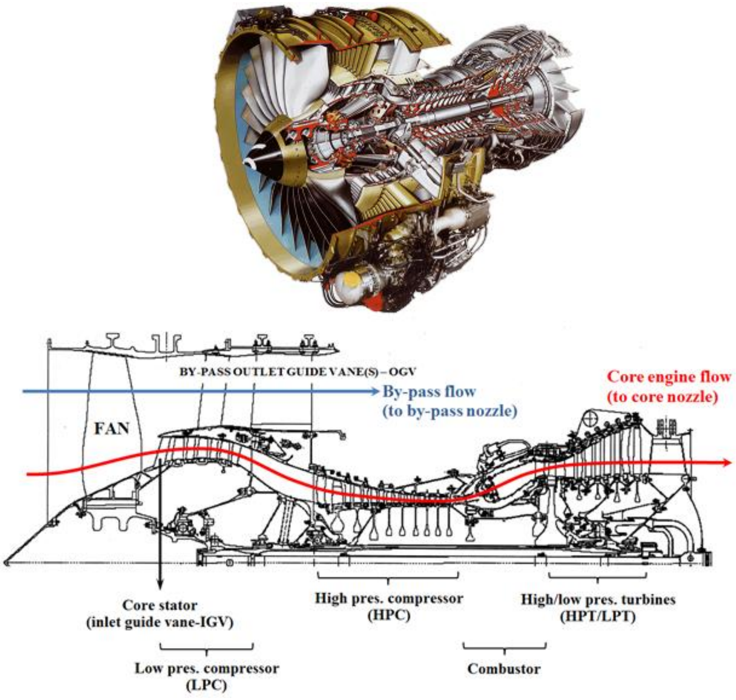

Figure 1. Cut view of a turbofan engine [2]

Following Wu [3], turbomachinery flowfields may be decomposed into two types of stream surfaces, namely S_1 (blade-to-blade) and S_2 (through-flow), as visualized in Figure 2. Consequently, 3D flowfields may be simulated by the coupled solution of the flows in S_1 and S_2 stream surfaces. Such an approach is known as the quasi-three-dimensional (Q3D) modeling. Approaches based on this definition enabled understanding of turbomachinery flows, and powerful design and analysis tools to be created. As iterating between many surfaces that distort in 3D is quite complex, simplifications in practice are usually made such that generally only one S_2 surface is assumed at a constant polar angle (named the ‘meridional plane’, which is also called S_2 surface) and consequently S_1 surfaces becomes surfaces of revolution of the meridional streamlines.

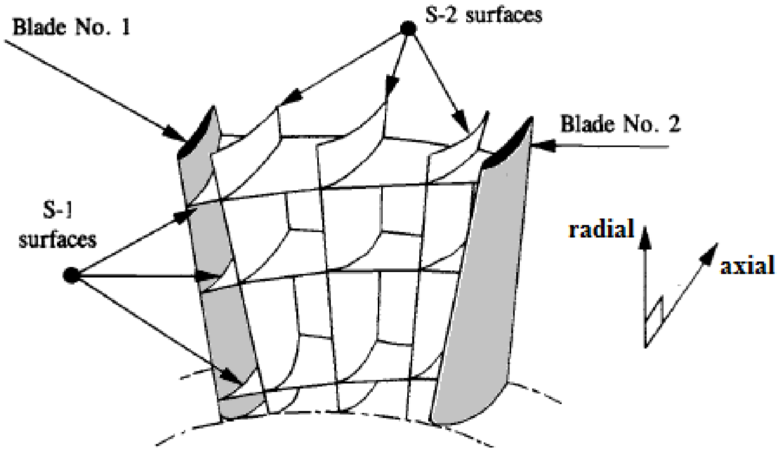

Figure 2. Quasi-three-dimensional approach [3]

The work done by a compressor rotor is due to addition of angular momentum to the flow (Figure 3), as described by Euler's turbomachine equation:

$$Power = \dot{m}\,\omega(r_2 V_{\theta 2} - r_1 V_{\theta 1}) \tag{1.1}$$

This added energy is in the form of tangential kinetic energy (swirl) rise, therefore stators are required to convert this kinetic energy into internal energy (e.g. static pressure) by their divergent type passage or additionally with increase in radius. Such a rotor and stator pair is known as a stage. Static pressure rise also occurs in rotors as their passage is similar to that of stators. The divergent type passage means that the velocity magnitude in the blade relative frame of reference (rotating frame for rotors and stationary frame for stators) decreases as the flow leaves the rotor passage.

Those principles are demonstrated in Figure 4 for an arbitrary streamline that lay on one of the blade-to-blade surfaces. 'V' and 'W' are absolute and relative (relative to blade) velocities, respectively; 'U' is the rotation velocity at the given radius. The outlet area 'A_{out}' is bigger than the inlet area, 'A_{in}' as shown in the right of the Figure 4 [4]. In case, there is no dominant streamline contraction or radius change in the meridional plane, the relative velocity leaving the cascade (blade-to-blade passage) is lower than the relative velocity entering it so that $W_2 < W_1$.

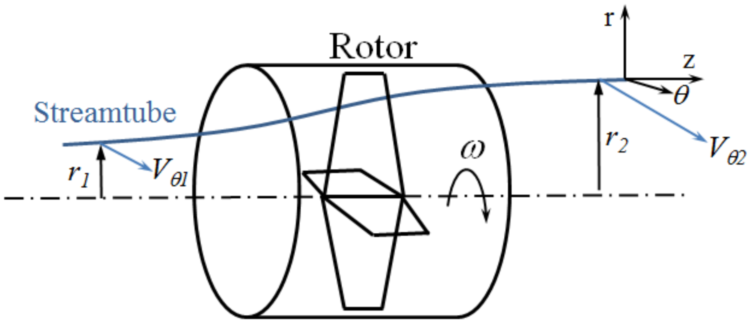

Figure 3. Angular momentum addition to the flow

Problems and challenges arise with the above principle of compressors, the presence of diffusion (i.e. adverse pressure gradient) inside the rotor or stator blades. If the diffusion is high enough, i.e. when the blade aerodynamic loading is beyond the limits, the boundary layer may separate, especially at the suction surface of blades, which leads to stall or surge [5]. The principle way to avoid this is to use multiple rotor-stator pairs (stages) and raising the pressure in many smaller steps, resulting in smaller adverse pressure gradients in each stage. This is the main reason why the number of compressor stages is much higher than corresponding turbine stages.

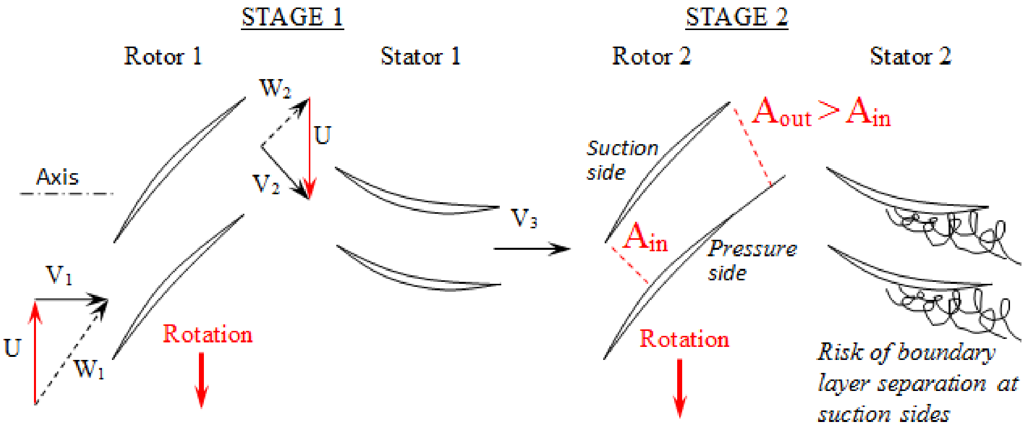

Figure 4. Blade-to-blade view of a two-stage compressor and velocity triangles

Today, first stages of almost all the compressors and fans are transonic for much higher compression ratios per stage (see Eq.1), for compactness and weight considerations. The inlet relative Mach numbers at the blade tip regions are either transonic or supersonic (Mach~0.8-1.7) but high subsonic at the blade hub regions. The rapidly growing shock losses with increasing Mach number may be tolerated (overbalanced) by very high compression ratios in successful designs. In designs prior to 70's, the supersonic tip speeds were avoided not only for mechanical issues (stress, supersonic flutter), but also for the flow's (shock structure's) greatly increasing sensitivity to geometry. This requires more precise design/analysis tools as well as manufacturing processes that handle tighter tolerances. High Mach numbers also significantly reduce the operating range (see the following text for the definition).

In case the relative inlet flow at a blade portion (usually towards tip profiles) is transonic (0.8<Mach<1) but exceeds a critical value unique to each profile, the subsonic flow accelerates at the entrance of the suction side and it exceeds sonic velocity (see Figure 5, left). Further supersonic acceleration due to Prandtl-Meyer expansion occurs if the suction side is of convex shape [6]. Then there forms one or more supersonic regions (pockets) inside the passage followed mostly single normal shock, which creates high losses, thickening the boundary layer and may ultimately cause instability/boundary layer separation due to shock-boundary layer interaction (see lambda shock in Figure 5, left), which may lead to stall.

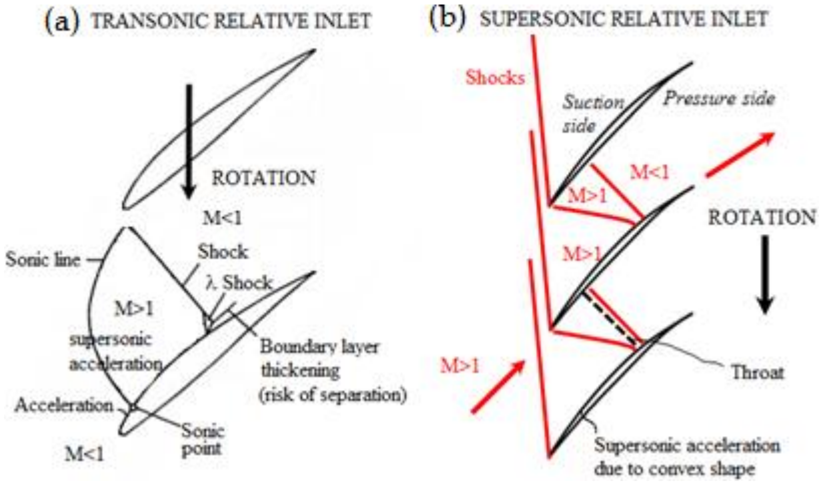

Figure 5. Blade-to-blade of transonic (a) and supersonic (b) flows [7]

When the inlet relative flow is supersonic at a blade profile (see Figure 5, right), then a weak bow shock, that is not strong enough to make flow subsonic, attached to the leading edge is followed by a strong normal shock located at or downstream of the throat (min passage area). As the throat Mach number reaches sonic speed, then the flow gets choked, therefore maximum mass flow capacity is limited for given inlet relative total conditions, independent of the exit conditions. The incidence (angle between flow and metal at the leading edge) is mostly determined by the suction side inlet angle, independent of the backpressure, which is called “unique incidence” [8]. The peak efficiency (design condition) is obtained when the normal shock coincides with the throat (see Figure 5, right). Otherwise (when the normal shock is downstream of the throat), supersonic acceleration after the throat will cause a much stronger normal shock, thus a much higher loss. This condition is obtained when the backpressure is decreased from a peak efficiency condition. In contrary, when the backpressure is increased, the normal shock may ultimately be merged with the bowshock, but this time detached to the leading edge, altering the unique incidence condition (high incidence occurs) and generate instability. This is the stall of supersonic profiles. Those off-design considerations are characterized by compressor/fan performance map and discussed in the following text.

The so far discussed shock losses may be controlled with the use of sweep, by creating an inclination with the flow in the streamwise direction. Then the normal component of the Mach number will be important in generating shocks. Moreover, the sweep has also some other effects other than modifying shock surfaces [8, 9], which is not the topic of this study but given for the sake of completeness. Those make the extensive use of sweep in high speed rotors.

1.1.1. Operational Range

The most important parameter for an aero-engine compressor/fan is, without doubt, the range of operation. This is because the component, especially belonging to military engines, may easily depart from its design point by:

- Sudden actions that alter engine mass flow before the inert wheel (spool) adapts to changes for conditions other than inlet distortion. Those actions include sudden maneuvers (inlet average pressure drop as well as its distortion), firing guns, sudden stepping on the gas, throttling the exhaust, etc.

- Erosion of blades

Those operability conditions and its range are measured in terms of performance maps, a chart with the 'sea-level corrected' mass flow in x-axis and pressure rise and efficiency in y-axes for various 'sea-level corrected' speedlines, as demonstrated in Figure 6 [10]. See Appendix A for details of turbomachinery flow similarity (e.g. sea-level correction).

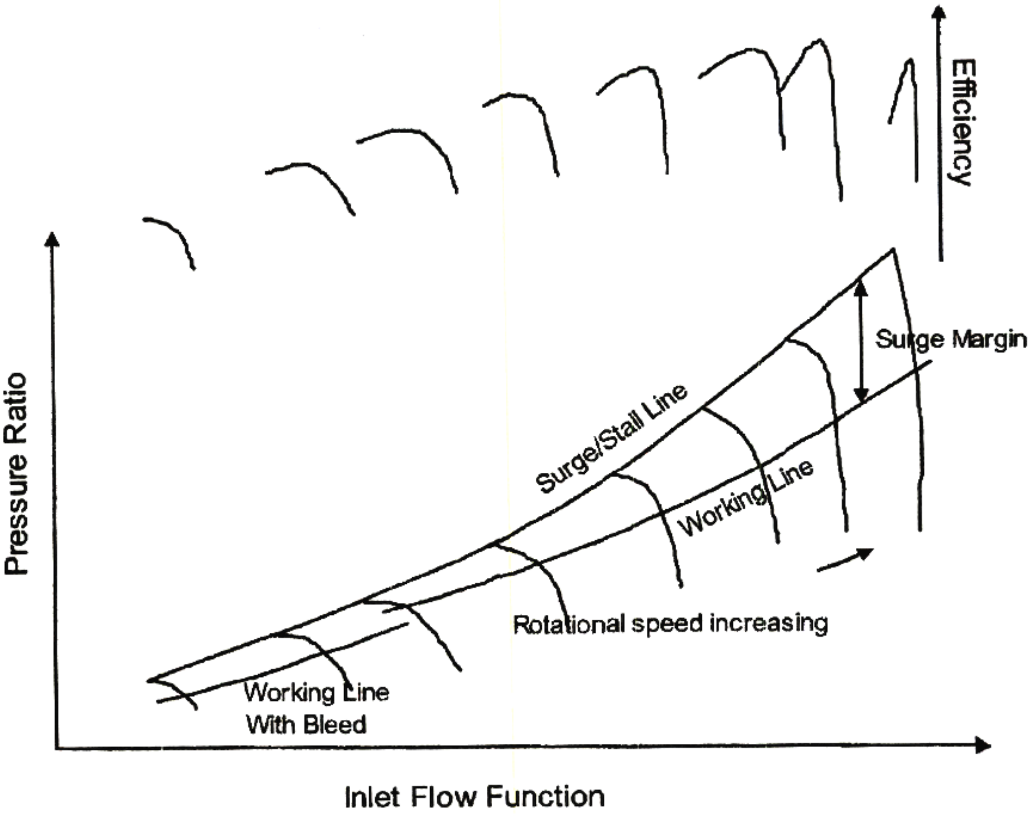

Figure 6. A typical compressor performance map [10]

The working line is the operating line where the flow is '*ideally*' aligned with the blade (optimum or minimum loss incidence). The maximum allowable mass flow is defined by choke limit, which is dependent on the throat area and inlet relative Mach number. Once the throat Mach number is or above sonic, the mass flow becomes independent of the pressure ratio (See straight characteristics in Figure 6) for constant inlet “relative” total conditions. A certain maximum mass flow is required based on application. Therefore careful adjustment of the throat area and blade shape must be ensured. Finally, the minimum allowable mass flow for a constant wheel (spool) speed is limited by boundary layer separation, shock detachment and increasing instabilities; namely stall/surge conditions. Stall is the start of instabilities due to reduction in mass flow (increase in backpressure relative to inlet total pressure). It starts from the rotated stall (only some passages and spanwise positions are stalled and they jump from one passage to another, typically on the order of 50-100Hz) and spreads all over the stage as the mass flow further decreases. It is a condition that must be avoided as it damages and then may destroy the machine. The surge and its reasons are very similar with stall, but it indicates a cycle of subsequent flow reversal-unstall, generally at a frequency of around 3-10Hz. Surge causes combustion chamber flame to go out of compressor in reverse direction and is evidently catastrophic when experienced for a non-instant time periods [8].

To prevent such cases, the machine must have a sufficient margin from the operating point to the stall/surge condition. This is called stall/surge margin (stall and surge are generally used interchangeably), as defined below, should be bigger than around 15-20%, depending on the application.

$$\text{Surge margin} = \left(\frac{\Pi_{stall}}{\Pi_{design}} \times \frac{\dot{m}_{std-design}}{\dot{m}_{std-stall}} \text{-}1 \right) \times 100 \tag{1.2}$$

Where the subscripts “stall” and “design” indicate stall and design conditions for fixed rpm, respectively. The stall margin is dependent on:

- Blade loading levels (in combination with the meridional flowpath)
- Mach & Reynolds numbers (the latter significantly varies between business jet engines and large engines of wide body aircrafts)
- Secondary flows (especially tip vortex due clearance of rotors)

To further increase this margin, for a given vortex and flowpath design, tip flow treatments (active/passive) and apply of sweep are the methods available [8].

1.1.2. Efficiency

Aerodynamic efficiency of a machine is defined as the ratio of the work into the idealized machine to the work into the actual machine without mechanical losses (in that case it is called overall efficiency). Its level, ahead from surface finish and fine details, is first determined by the severity of aerodynamic loading, its distributions over blade rows and then the shape of aerodynamic surfaces, which all together defines boundary layer velocity profiles (e.g. amount of adverse pressure gradients, turbulence), presence of shear layers (such as secondary flows) and compressibility. Typical total-to-total (calculated from total conditions at the inlet and outlet) efficiency map of a compressor is shown in Figure 6. Efficiency affects the engine through fuel consumption (therefore hot gas temperature). 1% increase in efficiency corresponds to specific fuel consumption drop of 0.5-0.8% for core compressors [9] and 0.75% for fans [11].

CHAPTER 2

LITERATURE REVIEW ON THROUGHFLOW METHODS

The aim of this section is to review the literature on through-flow methods, the design and analysis in the meridional plane (defined in the introduction section). The pressure and entropy rise and turning effects of blades and blade-endwall interactions are taken into account by introducing detailed empirical source terms into the axisymmetric flow solution. The solution time of such a modeling approach for a single-stage fan domain is around 30 seconds on a single core. On the other hand, the computational time of the same case with 3D computational fluid dynamics (CFD) is no less than one hour for a modern computer (2015 standards) with four cores. Therefore the through-flow methods are two orders of magnitude faster than 3D CFD methods. Moreover, the through-flow methods do not require exact 3D blade geometry, which makes them excellent tools for parametric studies.

Within the through-flow approach, design refers to obtain required geometry (e.g. blade angle distribution) from given flowfield (swirl or total enthalpy distributions) while the analysis (direct mode) refers to obtaining flowfield from given geometry. Through-flow models are also widely used for post-processing of test data by imposing (generally limited) measured data of total pressure, total temperature and flow angle into the solution [8].

The design mode will be focused in the context of this study, although the analysis mode will be cited for the sake of completeness. In the first subsection, the state-of-the art role of through-flow design in overall aero design will be discussed. Then time-evolution and variants of through-flow methods will be reviewed in the second sub-section.

2.1. The Role of Through-flow in State-of-the-Art Design Systems

The turbomachine design (in this case fans/compressors) is a step-by-step, but highly iterative procedure starting from engine thermodynamic cycle definition (tasks of components) to 1D meanline design (number of stages, work split between stages and basic flowpath) followed by through-flow design. The latter defines the spanwise distribution of velocity triangles at each row (blade twists) and more detailed flowpath that take into account the real effects of blades through correlations or tabular data. The next task is to design efficient airfoil sections on resulting through-flow streamlines that performs the required task. The last two processes are coupled and iteration may be required because the new blade performances may feed the through-flow model. Once the airfoils at each section are designed according to through-flow targets, they are stacked to form 3D blade rows. The 3D steady Navier-Stokes computations are then used to refine the blades in terms of fully 3D effects (mainly sweep and endwall regions). Finally, other than the tests, even a higher-fidelity analysis may be performed, which may additionally model unsteadiness and some features that are neglected previously (such as rotor-stator leakages, some imperfections, etc.). The procedure is summarized in Figure 7. Each of those fidelity levels are usually incorporated in advanced organizations [12].

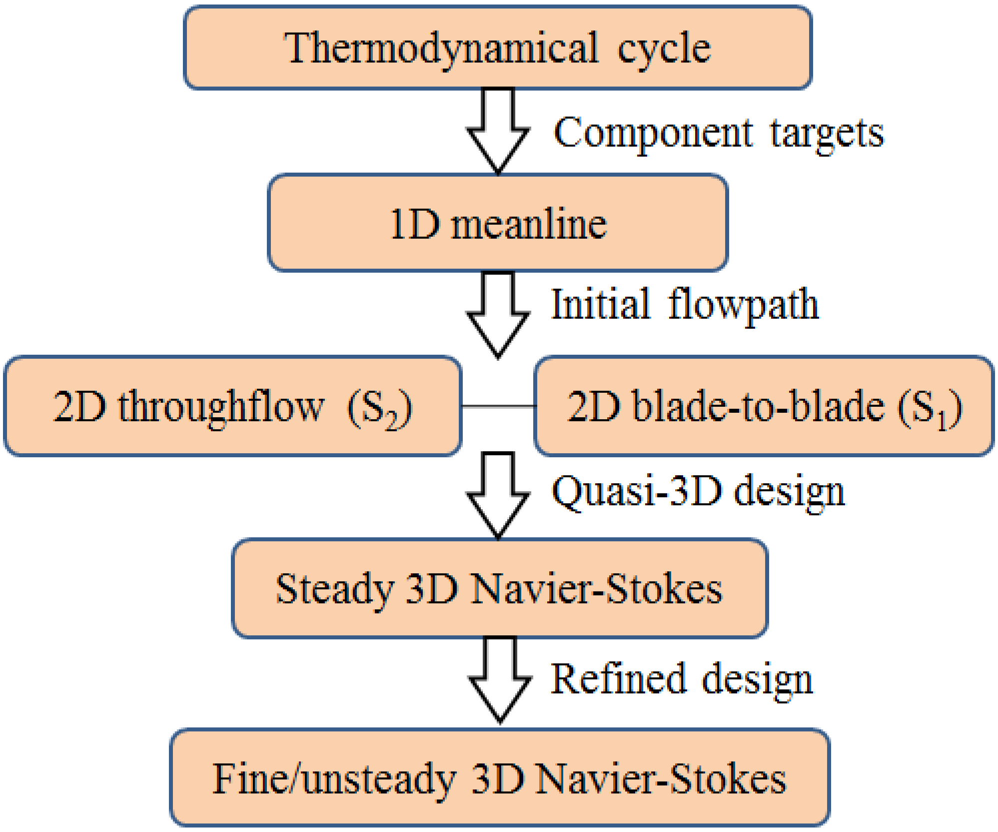

Figure 7. Turbomachine aerodynamic design process

The through-flow methods, coupled with properly calibrated empirical models and subsequent design of Q3D airfoil sections on the through-flow streamlines were the only means of detailed design before the regular use of 3D Navier-Stokes computations. The engines designed till the start of or mid 1990’s were flying with components almost purely designed with these methods, where the newly emerged 3D viscous or inviscid computations were utilized at the rather later stages of design to final-check validity [13-15].

The steady 3D Reynolds-Averaged Navier-Stokes (RANS) solvers with turbulent modeling are routinely used today in design (nevertheless, empiricism of the past has not been eliminated since the effect of turbulent stresses and wall effects on time-averaged flow and some other aspects still incorporate high level of simplifications). The main drawback of such computations is that, contrary to inverse Q3D/2D through-flow or blade-to-blade solvers, they are analysis methods and does not indicate what geometric changes are necessary to obtain the desired performances [16].

To be able to make designs with 3D codes, 3D inverse solvers were developed, relatively late, to obtain the geometry that fulfills specified performances [17, 18]. But defining the ‘desired’ performances requires deep understanding of turbomachinery flows and may not be performed by inexperienced engineers. Alternatively, and probably more commonly, analysis computations are now used in design by systematic trial-and-errors. Optimization algorithms are used to find new trials (geometries) to analyze. It is not topic of this text to review vast number of optimization methods, but some common applications are given for the sake of completeness. For all optimization methods that utilize 3D Navier-Stokes solver, shape definition and modification is accomplished thanks to the parameterization of the geometry (e.g. by Bezier curves. Coordinates of its control points are subject to change to generate a new shape). The deterministic methods (e.g. the ones that use adjoint equation) try to calculate sensitivities based on previous computations to search for better shapes [19]. The stochastic methods, generally genetic algorithms, rely on generating geometry generations within a population, that is initiated from baseline design (Q3D output or subsequent 3D hand-refined blade), to reach the Pareto front (the optimum geometries that minimize different conflicting objective functions with different degrees) [12, 20]. This procedure requires very high number of computations and practically not feasible for 3D Navier-Stokes based optimizations. As a solution, simple models (e.g. surrogate models created by response surface approach that are continuously updated) are employed to reduce number of high-fidelity computations [12].

Nevertheless, a parameterized 3D shape has many control points and increasing the number and limits of parameters results in a dramatic increase in the required number of analyses. Even if the research effort is to improve the simple surrogate models to speed-up the procedure, degree of freedom of those parameters are limited with computational sources. Therefore supply of good performing baseline geometry is crucial. Therefore through-flow methods, with matured empirical loss/deviation database, remain key tools in design systems [21], in which around 80-90% of overall design freedom is fixed [11, 15, 16, 22-26].

2.2. Through-Flow Methods

First axial compressors are emerged in 1930s and 1940s. In those first designs, only the blade-to-blade surface at the mean-line (50% height of the duct) is considered, for low speed (incompressible) machines, and the radial dimension is neglected (untwisted blades). The blade losses/ blockages/ deviations were taken into account by the cascade test data of that time for NACA profiles [27]. Today the more advanced forms of mean-line calculations, taking into account real-life effects from empirical database, are still a key element in design, and used to define 1D channel dimensions (e.g. mean radii and channel height as a function of streamwise position) and number of stages and load distribution (mean streamline flow angles) between the stages in the preliminary phase [28]. Such a modeling domain is illustrated in Figure 8 for a two stage axial compressor.

In real compressors, however, especially of lower hub/tip ratio, the rotational speed varies significantly from hub to shroud, radial (or spanwise for generality) distributions of the velocity vectors and flow properties form the very major aspect of aero-design. Especially first stages of some multi-stage compressors and fans have so low hub-to-tip ratios that different flow regimes occurs between hub-to-tip, e.g. subsonic flow at the hub, transonic flow at the middle radii and supersonic flow at the tip regions; giving rise to completely different airfoils to be designed.

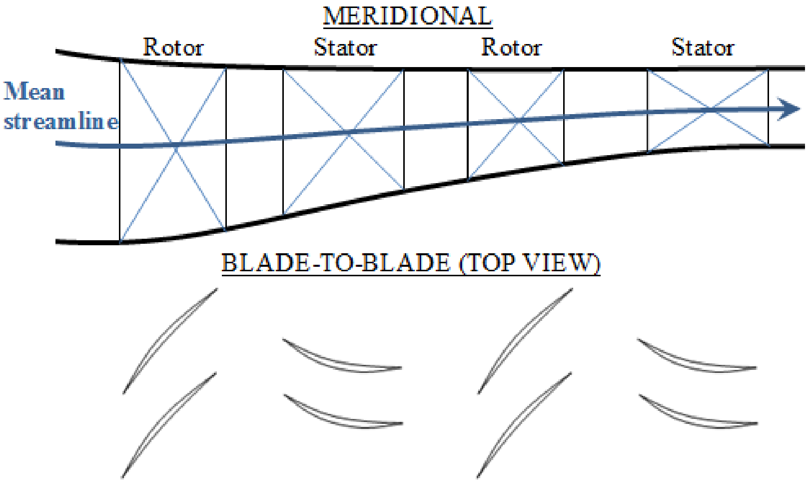

Figure 8. Mean-line model of a two stage axial compressor

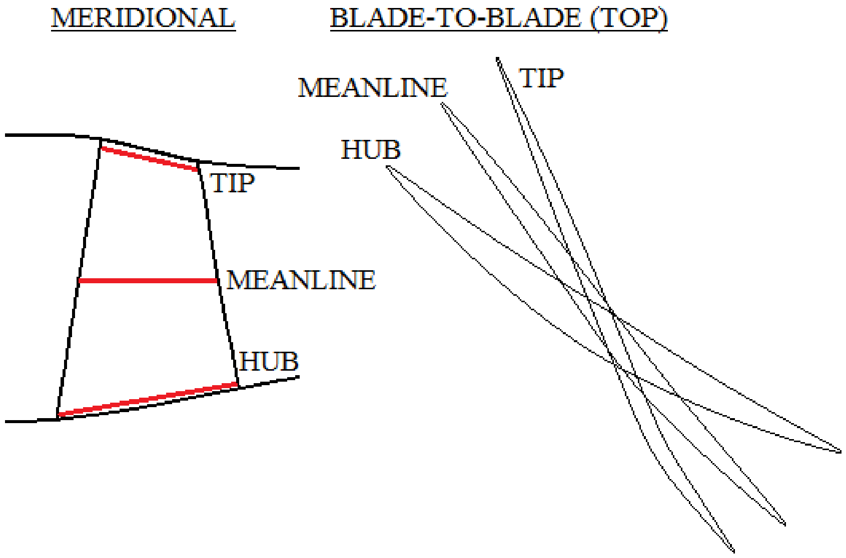

Figure 9. Change of blade cross-sections from hub to tip

First methods incorporating radial dimension is the simple radial equilibrium solution in the meridional plane, which is the balance of pressure with swirl field imposed by the blades. This neglects effects of radial component of velocity and streamline curvature in the meridional plane (conical streamlines are allowed). Empirical loss/blockage/deviation correlations simulating blade effects are required for the solution. It links different airfoil sections in the radial direction and allows blade designs that satisfy radial equilibrium [29]. This method was the most advanced tool in the late 40s and 50s, with free vortex swirl designs [30] and even still can be used for preliminary design studies, where streamline curvature effects are negligible, such as rear stages of compressors. Details of this approach are given in Appendix B.

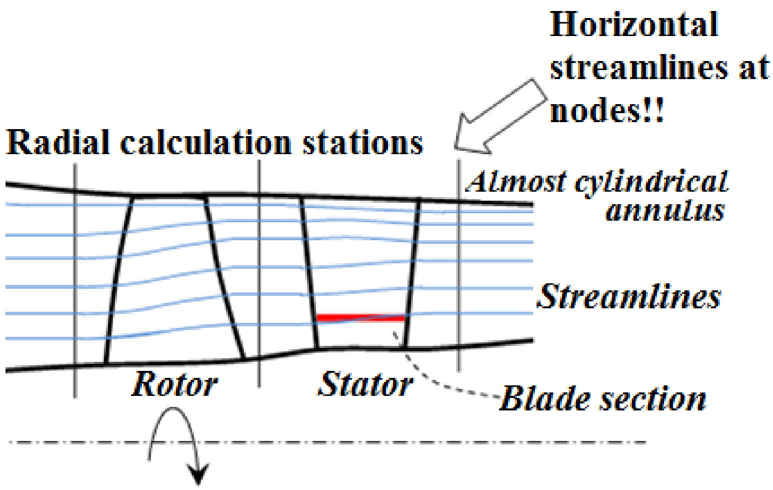

Figure 10. Simple radial equilibrium

More complete approaches take more elements from the original Q3D approach, which was defined in the introduction section (see Figure 2). Smith [31] was probably the first to publish full radial equilibrium derived by circumferentially averaging the 3D inviscid compressible flow equations from suction side to pressure side. Those include circumferential stress terms that take into account non-axisymmetry from existence of blades. The equation is basically the Euler equations derived in local streamline coordinates. The major assumptions are steady, adiabatic, inviscid, compressible flow, where the total enthalpy and entropy are conserved along streamlines (no local streamwise derivatives, but flow-normal derivative exists). But the cumulative effects of those are explicitly added into the solution using separate viscous models (loss/deviation/blockage/mixing). Being in line with the major Q3D modeling assumptions mentioned in the introduction section, the problem reduces to using one meridional surface instead of many S_2 surfaces (as in Figure 11, top). Then, the S_1 (blade-to-blade) surfaces becomes the surface of revolution of the meridional streamlines and they do not distort as they pass through the passage (Figure 11).

The modeling of circumferential stress terms arising from non-axisymmetry is not studied; but its effect, assuming linear variation in the circumferential direction, is compared with axisymmetric assumption with added blade body force and it is shown for the investigated case that axisymmetric assumption is adequate even inside the blades.

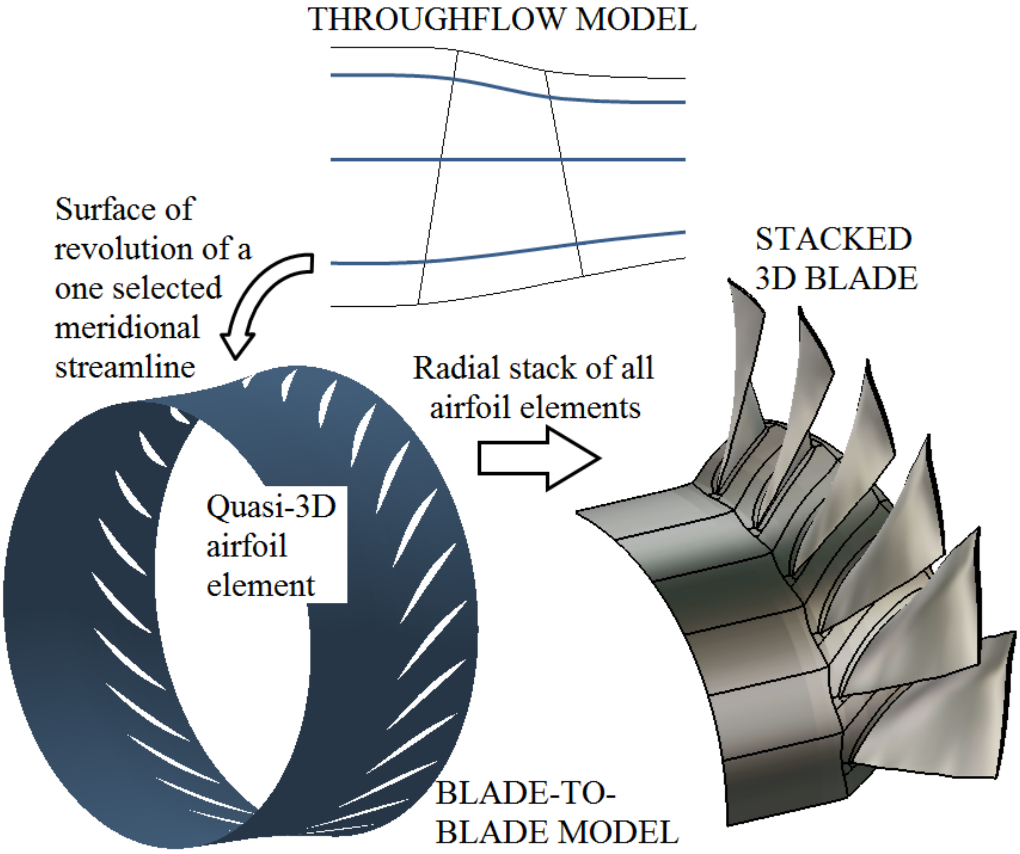

Figure 11. Through-flow modeling with single meridional surface

At the same time with Smith; Novak [32], after deriving radial equilibrium equation for the meridional plane directly from 3D equations without circumferential averaging, presented detailed information about the solution approach with the streamline curvature method (SLC), probably for the first time, although Smith's equations are also governing equations of SLC method. The SLC is given in detail in the next chapter, but a brief introduction will be given here:

- Assume streamlines (local streamline curvature, slope and angle between calculation direction and true streamline normal are guessed)
- Solve full radial (or normal) equilibrium equation for given design inputs, coupled with viscous models (iteration loop 1) and assumed constant of integration (meridional velocity generally at hub or midline)
- Adjust total mass flow rate and re-solve radial equilibrium for updated guess of integration constant until convergence (iteration loop 2)

- Adjust streamlines based on continuity in each stream tube and repeat above procedure until streamlines converge

SLC is the far most commonly used method in through-flow modeling such that it is used synonymous with through-flow, even if it is a method of flow solution. Nevertheless, there are other alternatives available:

The matrix method, first demonstrated by Marsh [33], uses the stream-function equation discretized with finite difference method. Solution is obtained by matrix inversion. The finite element method, presented by Hirsch and Warzee [34], is similar with the matrix method, but uses finite element discretization rather than finite difference method. Spurr [35] presented finite volume through-flow with time marching approach for solution of Euler equations for transonic turbines, in analysis mode, probably for the first time. It has the advantage of shock capturing, direct treatment of choking and handling of reverse flows within the meridional plane. There are various finite volume approaches such as references [36-38] for Euler equations and reference [39] for Navier-Stokes equations (Figure 12). Bladed regions are represented by distributed body forces and blockage as source terms.

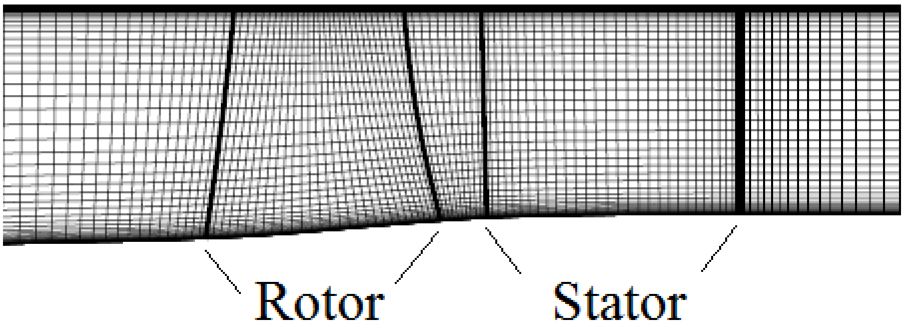

Figure 12. A typical Navier-Stokes through-flow grid [39]

There is almost no clear advantage between SLC, matrix method and finite element methods in subsonic flows, where the last two utilize the stream-function formulation. As the terms in SLC correspond to physical quantities rather than the stream-function and SLC performs much better in supersonic flows, it is the more commonly used one over the two. Time-marching finite volume Euler and Navier-Stokes methods are more recent and have some numerical advantages in shock capturing and handling reverse flows, but computationally more expensive and practically do not yield extra accuracy. Rather, correlations taking into account the effects of 3D blade passages define the success of the solution. Due to those reasons, finite volume methods did not replace SLC, which is still the most robust, fast, feasible and commonly used method [21].

2.2.1. Assessment of Blade Profiles and Real 3D Effects

The through-flow solvers (of all kinds) are coupled with viscous and 3D effects originated from blades and endwalls, to simulate reality. Those effects are originated from:

a. Blade profile losses (friction and shocks),
b. Endwall effects (tip leakage flow, other endwall secondary flows, turbulent mixing, etc.),
c. Blockage of boundary layers & wakes,
d. Choke condition (sonic or supersonic velocity at the blade passage minimum area-the throat)
e. Deviation (difference between metal and flow angle at the blade exit/trailing edge)
f. Design incidence (flow and metal angle difference for minimum loss at the blade inlet/leading edge).

Those are where S1-S2 coupling comes from. Therefore iterative process between the meridional and blade-to-blade surfaces is required. With the inclusion of these data, the throughflow modeling can be a very accurate representation of the reality [23].

In obtaining the blade profile information (“a”, “d”, “e”, “f” and partly “c” in above list), correlations based on cascade tests (tests simulating blade-to-blade flows) mainly served for this purpose for years for standard profiles, which are created before reliable use of numeric flow simulations, contrary to turbines, due to difficulty in blading in adverse pressure gradients.

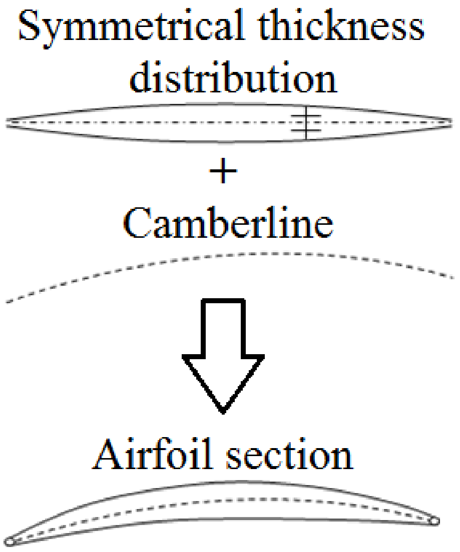

Figure 13. Definition of camberline and thickness distributions

Those standard profiles have scalable thickness distributions such as NACA65 series used in USA and C4 series used in GB in 1950s. Those scalable symmetric thickness distributions are applied to (generally) a circular camberline to obtain a blade profile with turning (camber), as demonstrated in Figure 13.

The NACA65 and C4 are subsonic profiles, appropriate for relative inlet Mach numbers smaller than around 0.7. The double circular arc (DCA) is the standard transonic profile (relative inlet Mach number range around 0.5 to 1.2). Its definition may also optionally be different than the other two as two circles are directly drawn and connected with other two small circles at the leading and trailing edges rather than applying thickness distribution on a camberline. For supersonic inlet sections (Mach greater than around 1.2), thin wedge or concave-suction-sided (s-shape) profiles must be created in order to reduce suction side acceleration, therefore shock losses (see introduction section). Sample NACA-65, C4 and DCA profiles are shown in Figure 14, where DCA is defined as a thickness distribution. The definition of angles and important geometric parameters that are used in correlations, for an arbitrary profile are defined in Figure 15.

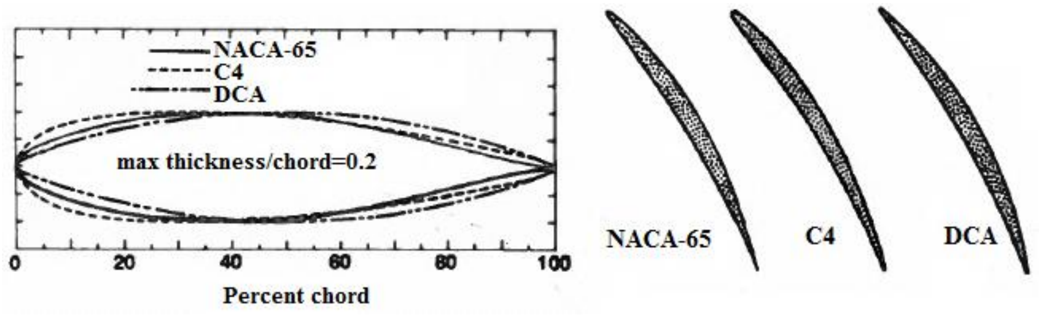

Figure 14. Sample NACA-65, C4 and DCA profiles [8]

NACA in 1950s performed extensive tests to obtain deviation and loss correlations mainly for NACA65 series, but also for DCA and C4 profile families with simple correction factors [40, 41]. They are mainly presented for design point operation, namely the optimum or design incidence condition, which is generally defined as is the incidence for minimum loss, although alternative or theoretically more correct definitions (highest lift/drag ratio, etc.) exist [8]. Based on the design incidence, the deviation is estimated based on main cascade parameters (Figure 15). The correlations are not purely for 2D flow, but also radius and streamtube height variations (Q3D flow), obtained from throughflow output, can be taken into account [42]. Using these correlations, it is possible to estimate the entropy rise through each blade-to-blade surface [43]. This is used in the governing equations to estimate local spanwise entropy gradients and thermodynamic state on each node. Those correlations are generally known as Lieblein correlations, and the baseline correlations are collected in NASA SP36 report [44]. They are continuously being updated and modified versions are still commonly used, together with its major and more complete alternative (loss only) Koch and Smith correlations [45].

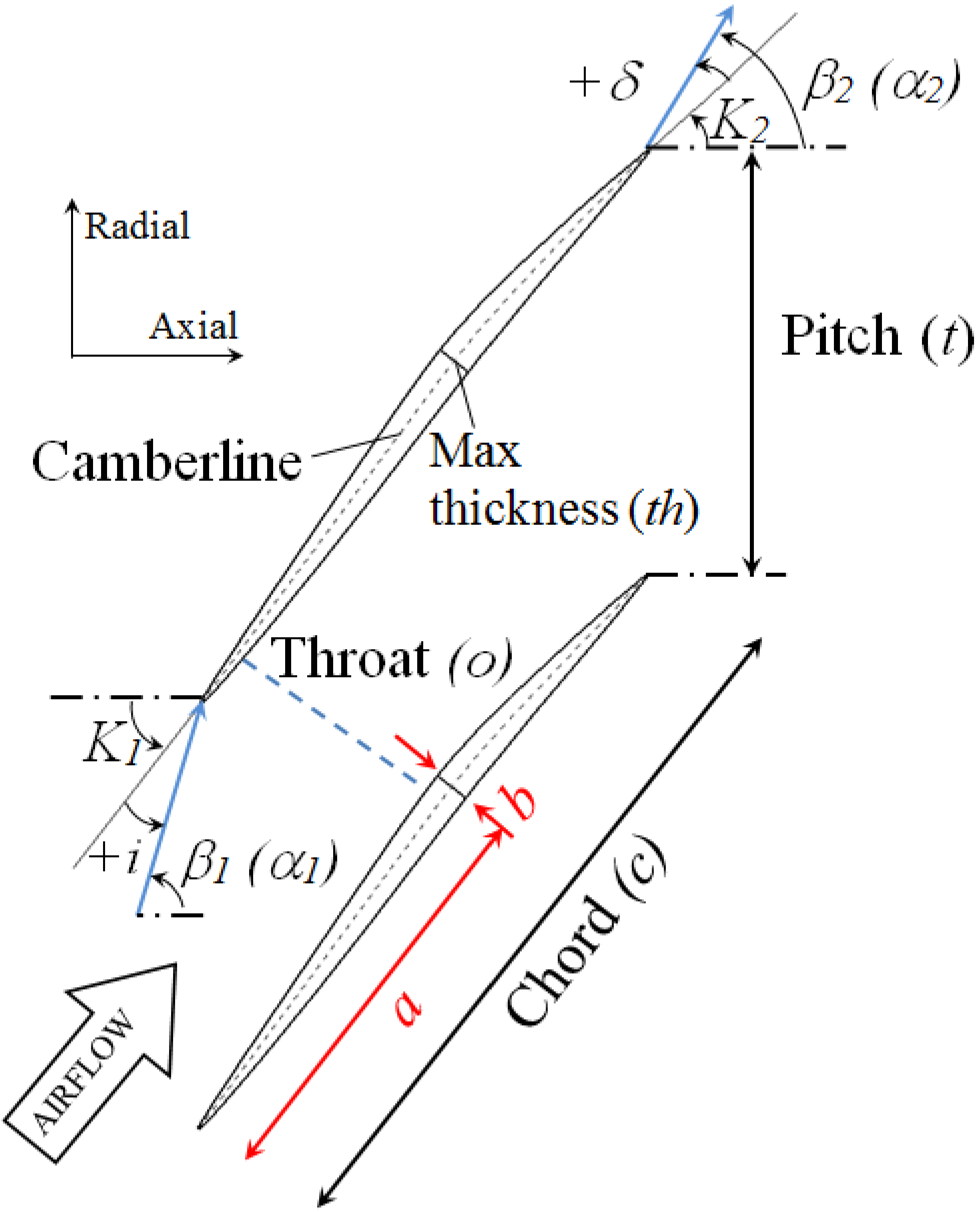

Figure 15. Cascade parameters definition

The standard profiles are reliable and efficient, but better custom-designed controlled diffusion profiles are available for a long time in industry [46-48]. Lichtfuss [49] gives an overview on emerge of custom designed profiles.

For custom profiles, the above correlations for standard profiles are no longer valid. There are two alternatives to overcome this problem:

Alternative 1: Add S_1 (blade-to-blade) design/calculations at each section as a subroutine to S_2 (through-flow), as a fully coupled Q3D solution [50].

Alternative 2: Modify standard blade family correlations (e.g. Lieblein) to simulate custom designed profiles (relies on organization know-how) [15].

Alternative 1 is costly, and not generally preferred. Instead, alternative 2 is selected more commonly [11, 15]. This means:

Step 1: Perform through-flow supported by correlations,

Step 2: Then design custom blade profiles at each section based on through-flow output,

Step 3: Knowing actual airfoil performance data, return to through-flow to check validity of results (thus correlations) if necessary (but in a less tightly coupled manner compared to alternative 1 above),

Step 4: If there is no significant inconsistency, directly go through 3D design.

The effects other than airfoil sections, i.e. the 3D effects (b and partially c in the above list), are either obtained from test database of companies [8] or 3D Navier-Stokes-based correlations, where the latter implies more continuous interaction between through-flow and 3D Navier-Stokes models rather than one-way progress of older designs [15, 51].

2.2.2. Improvements

A rather early, but complete review on both the through-flow methods and loss correlations are reviewed by Hirsch and Denton [52] for design. As an addition to previous study, loss sets for both design and off-design are reviewed by Cetin et.al [53] for transonic machines. Schmitz [54] used artificial neural networks and vast of geometrical parameters to obtain a correlation for airfoil profiles. Boyer [55] developed shock loss model for off-design operation for improved analysis with SLC. Pachidis et.al [56] implemented an approach to calibrate correlations with experimental data. Dunham [57] developed a method to predict end-wall losses. Horlock [58] reviewed end-wall blockage estimation methods and developed an approach, suitable for multi-stage machines.

Probably the most important improvement was the investigation of spanwise mixing due to secondary flows and turbulence. This is especially very critical in the last stages of multistage compressors, where viscous effects become important. A typical effect of mixing model on spanwise total temperature distribution is presented in Figure 16. Adkins and Smith [59], after a series of tests, concluded that the dominant mechanism in mixing is the deterministic (non-turbulent) secondary flows; hence turbulence plays a minor role. They developed a simple theory-guided empirical model for design point through-flow calculations; considering secondary flow theory, endwall boundary layers, tip clearance, blade boundary layer cross-flow. Good improvement was observed in through-flow calculations with the inclusion of the model. Gallimore and Cumpsty [60], on the other hand showed for their research compressor that turbulence mixing is the dominant mechanism over the secondary flows. They developed a simple model considering only turbulence mixing, and again good improvement was observed in through-flow calculations in the second part of their paper [61]. Finally, Wisler et. al [62], in their experimental campaign that utilize particle tracking and hot-wire anemometry techniques, concluded that both the secondary flows and turbulence may be equally important in some specific cases. They suggest Adkins and Smith model to additionally include turbulent mixing or Gallimore and Cumpsty model to additionally include secondary flow effects to improve their accuracies over a broader range of cases. The modeling of the phenomenon received improvements over time such as the work of Dunham [63] and Monig et.al [64]. The former improved mixing modeling by improving blade boundary layer and wake modeling. The latter made improvements by splitting endwall boundary layer into meridional and circumferential components and better predict the effects of 3D boundary layers.

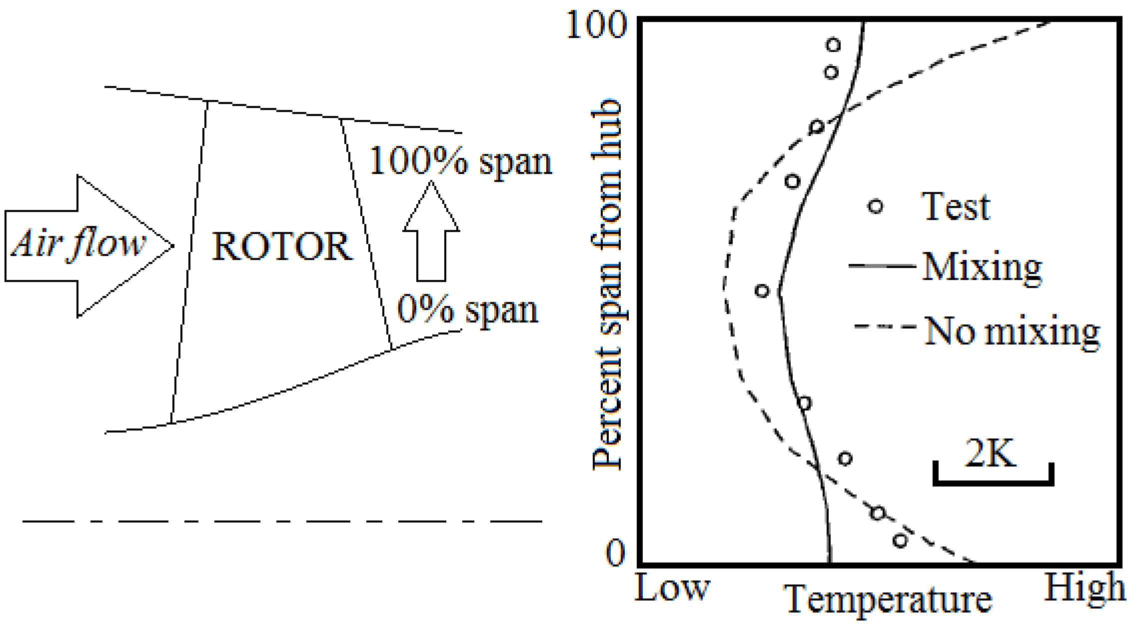

Figure 16. Effect of spanwise mixing on temperature [61]

Apart from the spanwise mixing, which is considered as the most important improvement for any through-flow method for especially viscous regions, the SLC methods have received improvements more recently. Boyer [55], as also cited above in loss improvement considerations, improved an existing SLC code capability to handle shock losses better through a new shock model and calibration of all loss models for a test case, enabling more accurate off-design analyses for transonic or supersonic speeds (Figure 17). Pachidis [56], also as cited above in the same paragraph, improved capability of SLC through improved loss assessment. Dunham [63] and Mönig et al. [64] are significant improvements for SLC methods by improving viscous effects. Casey and Robinson [65] developed a new SLC code, mainly for centrifugal compressors, that implements a new model for spanwise mixing and inter-blade calculation stations to improve accuracy. Pachidis et.al [66] integrated SLC code into thermodynamic cycle studies for whole engine simulation to be carried out more accurately. Tiwari et. al [21] developed a procedure to improve analysis-mode SLC program for transonic applications to overcome dual solution problem in supersonic speeds and handling choke, for both compressors and turbines. It is reported to be a significant improvement for SLC handling high speed machines and (to the author's knowledge) the most up-to-date improvement in this area for a SLC.

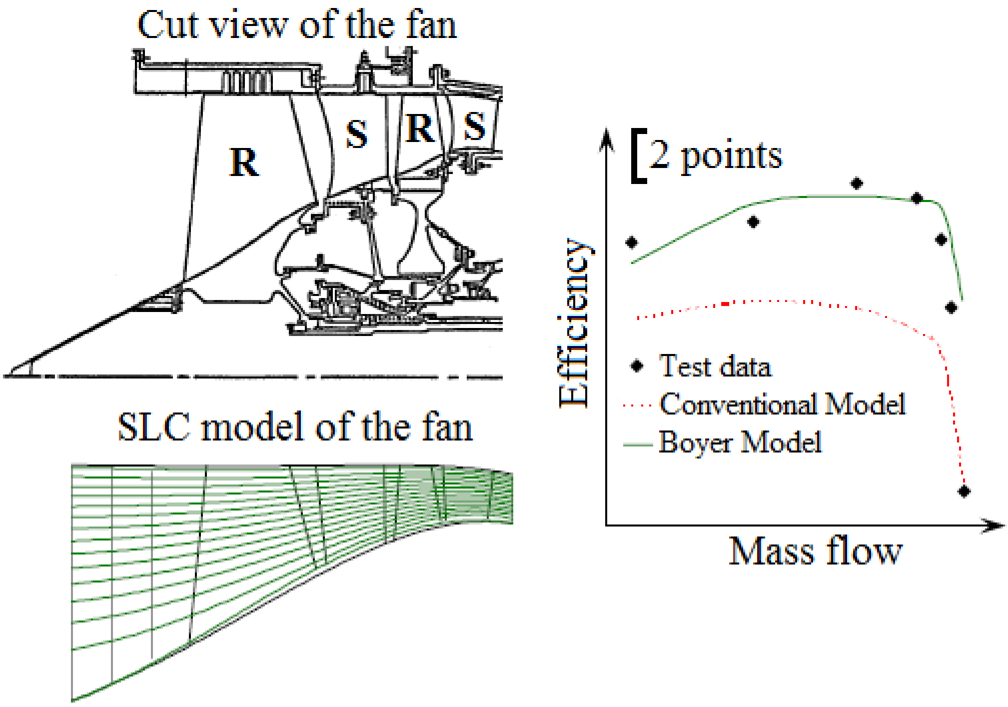

Figure 17. Boyer test case fan and its sample result [55]

2.2.3. Modeling Split-Flow Turbomachinery Systems

All the literature cited are for single stream machines. None of those papers, except Novak [32] and Shan [67], in SLC based modeling, dealt with a method for fan with downstream flow splitter and ducts, used in split-flow fans of turbofan engines (such as Figure 1). There exists SLC-based studies specifically related to fan design, but they either consider geometries without a by-pass duct [15] or (the ones related to by-pass fan systems) probably mostly use Novak's method without much emphasis given on the details of the program utilized, although results of designs are presented, such as references [11, 13, 68-72]. Sturmayr [36] presents a through-flow analysis case for a representative civil engine split-flow fan system, but the computational model was built around a time-marching Euler through-flow solution. The reason for lack of discussion in literature is may be that either the turbofan design may be carried out in a de-coupled manner (first designing the fan and then designing downstream ducts in a spatial marching fashion) or Novak's method is deemed sufficient to handle split-flow fan system coupled design/analysis problems. To the author's best knowledge, confidentiality may be the other important reason. Those statements are only for 2D through-flow modeling, and do not imply that flow splitter effects on fan performance are not investigated by a computer model or theoretically, such as [73, 74]. It will be later discussed that an alternative method to Novak's may be advantageous in design problem.

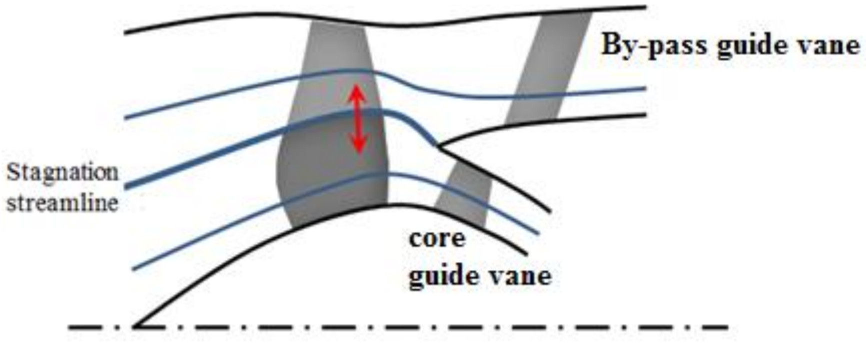

Figure 18. Iterative scheme between two solution domains

Novak's method is based on the definition of a stagnation streamline, which stagnates at the edge of the splitter, as shown in Figure 18. The presence of the stagnation streamline fixes the by-pass ratio (the ratio of by-passed mass flow to the core engine mass flow), because stream-tube mass flow rates must be specified as a boundary condition. Initially assumed stagnation streamline shape is iteratively improved through separate through-flow calculations performed at sub-domains. The problem may be attacked by performing first through-flow solution at the outer ring (covering fan outer portion and by-pass duct, Figure 18) and the second through-flow at the inner ring (covering fan inner portion and core engine compressor, see the same figure). Iteration is done between the two through-flow calculations until the stagnation streamline shape and bounding static pressure fields no longer change beyond specified convergence tolerances.

Shan's method is to alter stream-tube mass flow rates and splitter blockage factors artificially to model low by-pass turbofans as an organic whole, and it is limited to rather thin and horizontal splitters found in low by-pass turbofan engines. Moreover, the by-pass and core guide vanes downstream of the fan are treated as a single unified stator vane divided by a flow splitter (contrary to the separate vanes shown in Figure 18). Therefore it cannot be treated as a general method of solution.

2.3. Motivation and Goal of the Present Study

In reference to the literature survey of the previous section, to the authors’ best knowledge, there is a definite gap related to combined fan and splitter through-flow modeling. The current study addresses this void by presenting a practical streamline curvature through-flow methodology that is suitable for inverse design for such a problem. The developed split-flow method for the streamline solver, alternative to the publicly available and above-cited analysis-oriented method of Novak [32], is implemented and initially compared with 2D axisymmetric CFD on three representative geometries for high, medium and low by-pass ratios. The empirical models for incidence, deviation, loss and end-wall blockage are compiled from the literature and calibrated against two test cases: experimental data of NASA 2-stage fan and 3D CFD of a custom-designed transonic fan stage. Finally, experimental validation against GE-NASA by-pass fan case is accomplished to validate the complete methodology, both the split-flow capable streamline solver and the empirical models. The proposed method is an extension to the available compressor streamline curvature through-flow methodologies and may be applied to those with minimum numerical effort.

In the next section, the baseline streamline curvature method for through-flow solution for single stream machines will be explained in detail since the split-flow method developed in this thesis is based on this theory. Empirical models for incidence, deviation, loss and blockage assessment that are gathered from open literature are also given in this chapter. Finally, details of the proposal are discussed in CHAPTER 4 with its coding structure in 4.1. Validation of the method is finally given in CHAPTER 5.

CHAPTER 3

STREAMLINE CURVATURE METHOD

The far most common numerical method so far for the through-flow solution is the streamline curvature method, as discussed in the literature review section. Details of this method will be discussed in this section. The main governing equation for the streamline curvature method is the (full) normal equilibrium equation, a momentum equation along a direction that is roughly normal to streamlines. This equation for turbomachinery through-flow solution may either be axisymmetric or non-axisymmetric (the case for bladed or wake regions). In the non-axisymmetric case, other than invalidity of axisymmetric-based assumptions, additional circumferential stresses due to averaging of circumferential flow properties arise, which can be obtained either approximately or from blade-to-blade calculations. Nevertheless the algorithm remains unchanged for the both modeling approaches. In this study, only axisymmetric approximation is considered, which is adequate and common for practical applications [15]. The full normal equilibrium equation must be solved together with continuity, thermodynamic state and turbomachinery energy equations; and a body of empirical models for viscous effects, i.e. loss/blockage/incidence/deviation.

The numerical solution of the differential equation is carried-out through curves (those will be called “computing stations”) that are ideally locally-normal to each streamline to obtain the simplest form of the full normal equilibrium equation. However this generally causes unnecessary complexities, because the computing stations must be modified during iterations, where the streamlines are updated. To cope with this, computing stations, generally created as straight lines rather than curves, are placed approximately normal to streamlines, prescribed before the start of calculation. Those lines are called “quasi-normals” or “quasi-orthogonals”, as shown in Figure 19. If radial lines are prescribed as quasi-orthogonals, then the “full normal equilibrium” is called “full radial equilibrium”. Nothing is neglected with the use of quasi-orthogonals rather than true-normals, but an additional term of meridional acceleration of the meridional velocity (V_m) emerges. Nevertheless, evaluation of this term may be inaccurate if the quasi-orthogonal is excessively deviated from true-normal, i.e. when streamline is almost parallel with quasi-orthogonal. The nodal points (intersections of streamlines with quasi-orthogonals) are allowed to float on local y-directions (Figure 19). This is used to iteratively update streamlines based on streamtube continuities, after each normal-equilibrium calculation.

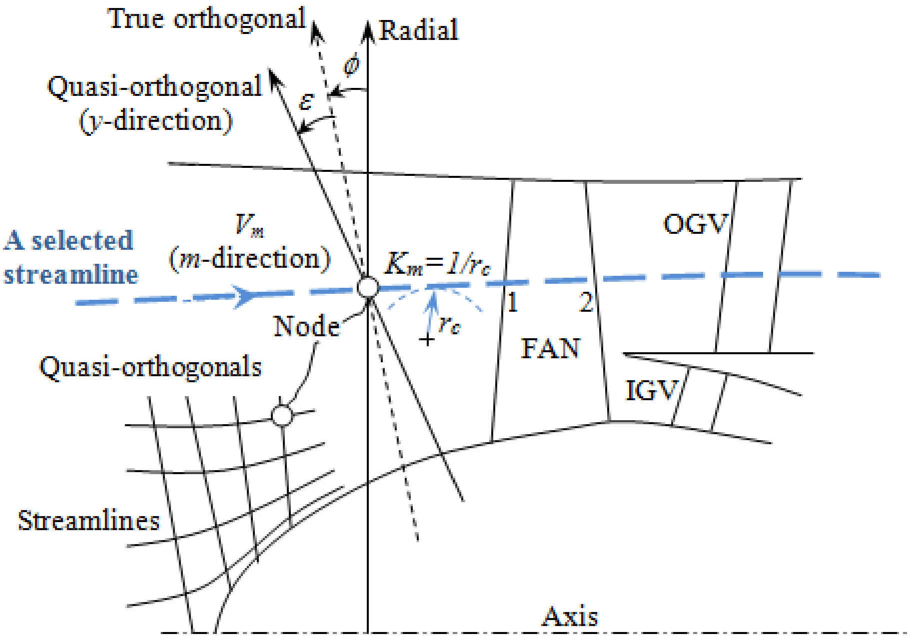

Figure 19. Streamline curvature method

3.1. Solution along a Quasi-Orthogonal

The major assumptions of the governing equations, as discussed in the literature review section, are axisymmetric steady adiabatic inviscid compressible flow, where total enthalpy and total entropy conserves along a streamline locally (no derivative). This simplifies the streamwise momentum equation to the linking equations (discussed in the subsection below related to linking) [42]. Although the solution itself is inviscid, the viscous and 3D effects are considered within entropy, enthalpy and swirl velocity terms by the use of external empirical models (see literature review section). Derivation of the full normal equilibrium equation may be found in various sources, presented in literature review section. It is a non-linear partial differential equation both depending on *y* and *m* (see Figure 19). It is the main equation for turbomachine meridional flow. Wennerstrom [15] highly recommends that any serious designer should memorize this equation "because it will give clear guidance to many decisions that will have to be made in the course of many designs". The equations given in Aungier [42] are used here. Its final form is:

$$V_m \frac{\partial V_m}{\partial y} = \frac{\partial I}{\partial y} - T\frac{\partial s}{\partial y} - \frac{W_\theta}{r}\frac{\partial (rV_\theta)}{\partial y} + V_m \sin\varepsilon \frac{\partial V_m}{\partial m} - K_m V_m{}^2 \cos\varepsilon \qquad (3.1)$$

This is written in rotating frame of reference, rotating with blade speed (ω), for generality. For stationary frame of reference (the preferred one), put V_θ instead of W_θ and *H* instead of *I* (the conversion between relative and absolute frames are: $V_\theta = W_\theta + \omega r$, $V_m = W_m$ and conversion between *I* and *H* is given in Eq.3.2). In any case, the first term on the left-hand side (LHS) represents the (~spanwise) gradient of the meridional velocity. First term on the right-hand-side (RHS) represents the gradient of total enthalpy (work or heat transfer), the second term represents the gradient of pressure loss, the third term represents the centrifugal acceleration effect of swirl velocity on the spanwise pressure gradient, the fourth term represents the effect of meridional acceleration when the quasi-orthogonal is not aligned with the local true normal of a streamline. The fifth (and the last) term finally represents the centrifugal acceleration effect on the spanwise pressure gradient due to the curvature of meridional (axisymmetric) streamlines. Instead of static pressure, this equation is cast in terms of total enthalpy and entropy with the use of Gibbs equation. Therefore the gradients of total enthalpy and entropy (first two terms on the RHS) actually represent the gradient of static pressure.

In the first term of RHS, *I* is the so-called rothalpy and is derived from first law of thermodynamics. Its importance comes from its constancy along streamlines passing from rotors, analogous to constancy of total enthalpy in stators. It is defined by:

$$I = H - \omega r V_\theta \qquad (3.2)$$

Angle between streamline true normal and quasi normal (ε, see Figure 19) is defined by:

$$\varepsilon = \phi - \lambda \tag{3.3}$$

Where λ is the local angle between quasi-orthogonal and radial, defined by:

$$\lambda = \tan^{-1}\left(\frac{\partial z}{\partial r}\right)_{\text{along quasi-orthogonal}} \quad = \quad \tan^{-1}\left(\frac{z_{hub} - z_{shroud}}{r_{shroud} - r_{hub}}\right)_{\text{(for straight quasi-orthogonal)}} \tag{3.4}$$

ϕ is the local slope of streamline with axial:

$$\phi = \arctan\left(\frac{\partial r}{\partial z}\right) \tag{3.5}$$

K_m is the local streamline curvature (inverse of radius of curvature), which gives the name to the method:

$$K_m = -\frac{d^2 r}{dz^2} \Bigg/ \left[1 + \left({}^{dr}\!/_{dz}\right)^2\right]^{3/2} \tag{3.6}$$

This is calculated from the first derivative of the local streamline slope in the course of this study, rather than second order differentiation, as discussed in the following section. This is called '*double-differentiation*'. Positive curvature implies convex-shaped streamline while negative curvature implies concave-shaped streamline.

The derivative with respect to m in Eq.3.1 depends on the solution of downstream quasi-orthogonals, therefore complicates the problem. Nevertheless, this derivative may be calculated analytically for subsonic meridional velocities, using current estimate of the local streamline shape [42]:

$$\frac{\partial V_m}{\partial m} = -V_m \left[\frac{\left(1+M_\theta^2\right)}{\left(1-M_m^2\right)} \frac{\sin\phi}{r} + \frac{1}{\left(1-M_m^2\right)} \frac{1}{\cos\varepsilon} \frac{\partial\phi}{\partial y} + \frac{1}{\left(1-M_m^2\right)} K_m \tan\varepsilon \right] \tag{3.7}$$

Where M_θ is the tangential Mach number in “absolute” frame of reference (based on V_θ). In case meridional velocity is sonic or supersonic, the derivative must be calculated numerically; using the information on upstream and downstream quasi-orthogonals (relative velocity on blades can still be well supersonic).

With the use of the analytical relation Eq.3.7 for obtaining the meridional gradient term, Eq.3.1 becomes an ordinary differential equation as long as following unknowns are assumed as known at all nodes, but continuously updated through iterations:

- Absolute swirl velocities (rV_θ) : Prescribed as a design requirement (in design mode)
- Rothalpy or total enthalpy distribution : Calculated from rV_θ using the turbomachinery energy equation
- Streamlines (local streamline curvatures, K_m and angles with axial, ϕ): Obtained within the solution
- Tangential and meridional Mach number (so V_m and sound velocity) : Obtained within the solution
- Entropy distribution (losses) : Obtained within the solution from empirical correlations
- Thermodynamical properties : Obtained iteratively within the solution

Having prescribed swirl velocity distributions, all remaining unknowns are the outputs of solution.

Eq.3.1 may be written in a more compact form [42]:

$$\frac{\partial V_m}{\partial y} = f_1(y)V_m + f_2(y) \tag{3.8}$$

Where,

$$f_1(y) = -K_m \cos\varepsilon + \frac{\sin\varepsilon}{V_m}\frac{\partial V_m}{\partial m} \tag{3.9}$$

$$f_2(y) = \left[\frac{\partial I}{\partial y} - T\frac{\partial s}{\partial y} - \frac{W_\theta}{r}\frac{\partial(rV_\theta)}{\partial y}\right]\frac{1}{V_m} \tag{3.10}$$

Integrating Eq.3.8 from y=0 (hub) to y, and rearranging for V_m yields:

$$V_m(y) = V_m(0)F(y) + F(y)\int_0^y \frac{f_2(y)}{F(y)}dy \tag{3.11}$$

Where,

$$F(y) = \exp\left[\int_0^y f_1(y)dy\right] \tag{3.12}$$

Equation 3.11 is the final form of the equation, used to obtain V_m distribution along a quasi-orthogonal assuming the above listed items are known, plus the V_m at the hub. All initially guessed unknowns are then updated in three iteration loops (see the overall algorithm in Section 3.4). $V_m(0)$ (meridional velocity at the hub) is obtained from the mass continuity along the complete quasi-orthogonal:

$$\dot{m} = 2\pi K_B \int_0^{SHROUD} K_W r \rho V_m \cos \varepsilon dy \qquad (3.13)$$

Where K_w and K_B are the blockage coefficients due to wakes and endwall boundary layers. They are defined as the ratio of unblocked area to full area.

Once the solution is converged for given streamlines (first two iteration loops), then the streamlines are adjusted (nodes float in y direction, see Figure 19) based on continuity of each streamtube (outer loop iteration).

$$\Delta \dot{m} = \rho V_m \Delta A \qquad (3.14)$$

Where $\Delta A = 2\pi r K_W \cos \varepsilon \Delta y$.

The above equations describe the equilibrium within a single quasi-orthogonal. Linking must be done between successive quasi-orthogonals, which will be investigated in Section 3.3.

3.1.1. Treatment of Inter-Blade Quasi-Orthogonals

The inclusion of inter-blade stations (Figure 20) may improve accuracy but require blockage and blade force terms at each node (also fluctuation stresses for non-axisymmetric case may be included) and streamwise distribution of losses between leading and trailing edges. Those require some approximate information (such as linear variation in simplest case) inside blade-rows. Effects of blade lean can also be taken into account by this way with the inclusion of spanwise blade force term. With developer and user know-how (guesses, quick blade-to-blade analyses, databases), this proved to be reliable [8, 15]. With those additional inputs included, the procedure is the same as the method without inter-blade quasi-orthogonals. In this study, however, quasi-orthogonals are only placed at leading-trailing edges and duct regions for simplicity.

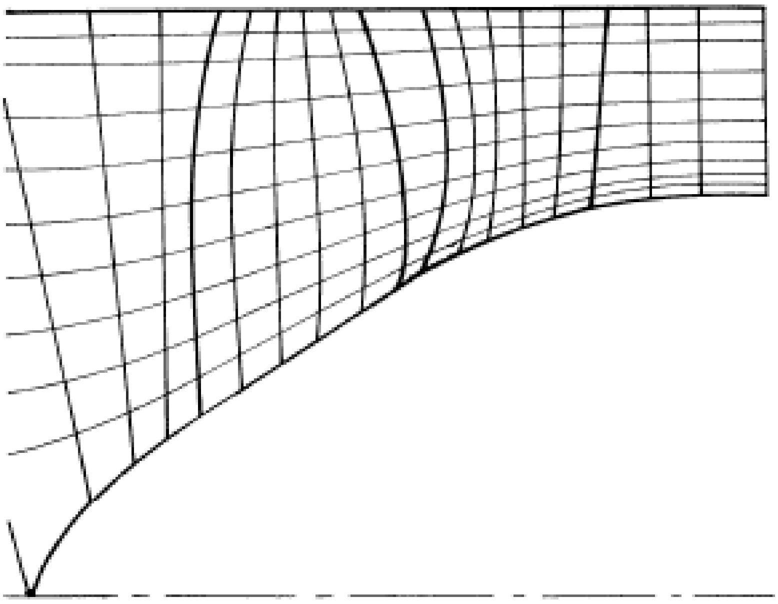

Figure 20. A typical grid with inter-blade stations [15]

3.2. Marching to the Downstream Quasi-Orthogonals

The topic discussed above deals with solution along a quasi-orthogonal. The streamwise momentum, which is simplified by the aforementioned assumptions, serves as linking of a quasi-orthogonal with the upstream quasi-orthogonal.

The equations given here are extracted from [42]. Linking two quasi-orthogonals in the absence of a blade (duct) is the constancy of angular momentum with no change in entropy and enthalpy:

$$\left(rV_\theta\right)_2 = \left(rV_\theta\right)_1 \tag{3.15}$$

$$s_2 = s_1 \tag{3.16}$$

$$I_2 = I_1 \quad \left(= H_2 - \omega(rV_\theta)_2 = H_1 - \omega(rV_\theta)_1\right) \tag{3.17}$$

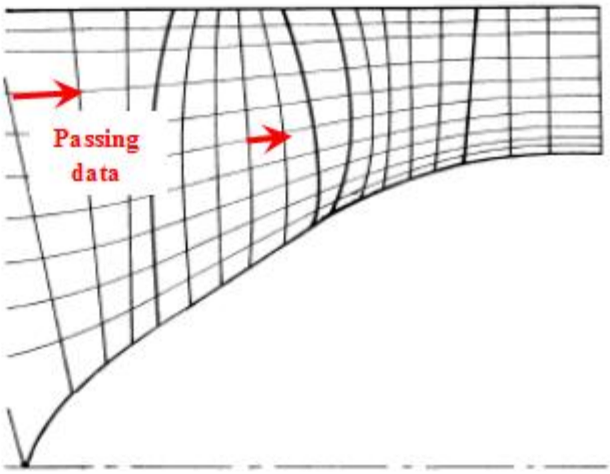

Figure 21. Linking quasi-orthogonals

When linking two quasi-orthogonals in case an airfoil element exists between them, the effect of rotational or stationary airfoil is imposed in terms of flow turning (swirl and total enthalpy) and the associated loss (entropy rise). First of all, the inlet relative conditions must be known:

$$I_1 = H_1 - \omega(rV_\theta)_1 \tag{3.18}$$

$$W_{\theta 1} = V_{\theta 1} - r_1\omega \tag{3.19}$$

$$W_1 = \sqrt{W_{m1}{}^2 + W_{\theta 1}{}^2} \tag{3.20}$$

P_{01}', T_{01}' and T_{02}' can be calculated from the available data. Rothalpy remains constant in streamline that passes through a rotor:

$$I_2 = I_1 \tag{3.21}$$

$$H_2' = I_2 + \frac{1}{2}(r_2\omega)^2 \tag{3.22}$$

The discharge relative total pressure for no-loss (ideal P_{02}') is first calculated from the equation of state, using the known discharge relative total enthalpy and inlet entropy. Then the real discharge relative total pressure is calculated from total pressure loss coefficient, defined by the fractional loss of inlet relative dynamic pressure:

$$P_{02}' = \left(P_{02}'\right)_{ideal} - \varpi\left(P_{01}' - P_1\right) \tag{3.23}$$

Other relative total thermodynamic conditions, entropy and absolute total pressure at the discharge are computed using Gibb's (*T ds*) equation, found in elementary books.

The evaluation of loss coefficient requires inlet-outlet flowfield to be known. Therefore an iterative process is required. Once convergence is reached, the discharge absolute total conditions can be calculated as:

$$V_{\theta 2} = W_{\theta 2} + r_2\omega \tag{3.24}$$

$$H_2 = I_2 + \omega(rV_\theta)_2 \tag{3.25}$$

3.3. Numerical Techniques

Direct use of finite difference method is employed to evaluate most derivatives in the equations, rather than from curve-fitting methods, except streamline slope and curvature. This is to improve stability, considering accuracy is not sacrificed if mesh independency is ensured, which can easily be achieved without increasing computational time excessively (see Wilkinson [75]). The integrations in Equations 3.11 and 3.12 may be carried-out by any numerical integration scheme and details can be found in textbooks on numerical methods.

The streamline terms (Eqs.3.5 and 3.6), especially curvature, on the other hand, is subject to question in terms of accuracy [75, 76], relative to other derivatives and integrations. This is because the streamline curvature term has to be calculated on streamlines, which are defined by rather loosely spaced nodes located on successive quasi-orthogonals (see Figure 22). The minimum quasi-orthogonal spacing is limited due to a practical limitation in maximum grid aspect ratio, otherwise very high damping factors are required [75] to prevent oscillations in streamlines.

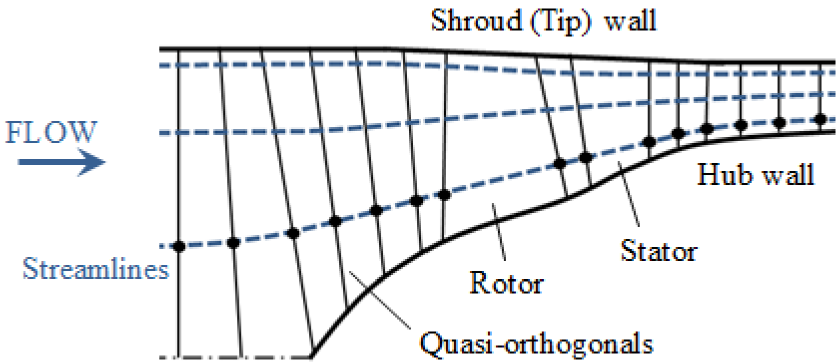

Figure 22. Streamline by curve-fitting of discrete points

Aungier [42] recommends direct use of finite difference method rather than spline-fit for the streamline curvature calculation, through using the first derivative (streamline slope) as data. This is expected to be accurate only for some compressors, where streamline curvature effects are small, or quasi-orthogonals are sufficiently closely spaced. Therefore the method is not preferred for a more general case. The two of the studies dealing with the issue are Wilkinson [75] and Shaalan & Daneshyar [77], who investigated many alternative curvefits on the cosine wave to obtain the best curvefit method, which is the curve with most accurate answer at minimum wavelength (of cosine) to point spacing ratio. When this ratio is bigger than 20, almost all methods give the same answer. The use of simple three-point parabola had preferred over many more complicated methods by many developers, mainly due to the reason that empirical inputs are more important than numeric method used, as reviewed in [76]. Nevertheless, using more complicated methods are assessed as feasible, and although parabola-fit is better than many more complicated methods, it is not the best method available as Wilkinson suggests. Wilkinson empirically recommends the blend of spline-fit (and differentiates twice for curvature) and three-point parabola fit, which is proposed to give accurate answer down to the ratio of almost 2. Being accurate down to the ratio of 5, Shaalan&Daneshyar recommends the use of double spline-fit to obtain the curvature, fitting a second spline using the slope obtained from the first spline-fit as the data, rather than differentiating a single spline-fit twice. This is also assessed as a good method by Wilkinson and implemented to the calculation method presented in this study.

3.4. Solution Algorithm

The overview of the complete procedure implemented in this study is summarized in Figure 24. Initially, flowpath and quasi-orthogonals (including leading and trailing edges) are specified and kept fixed throughout the solution. The required quasi-orthogonal angles with radial (λ) are calculated and stored in the memory. The boundary conditions are inlet total pressure/temperature (enthalpy) and total mass flow rate. Required initial guesses are meridional velocity distribution (such as uniform initial guess) and streamlines (usually equally spaced in annulus), where the latter gives initial values of node positions, streamline curvatures (K_m) and streamline angles (ϕ) (and those then continuously updated by third loop iteration).

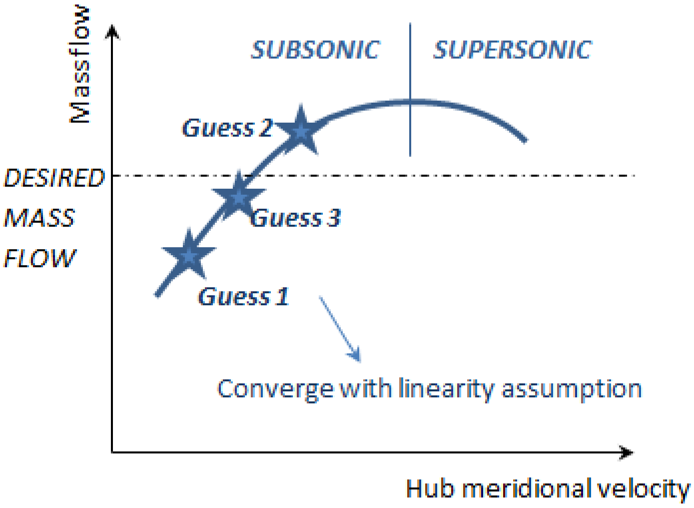

Figure 23. Hub velocity iteration [76]

The latest guess of streamline shape for the present third loop iteration, even though not converged yet, is known. Therefore, the normal momentum equation given in the main chapter is solved in the current quasi-orthogonal to obtain V_m distribution that yield flow thermo-physical properties and empirical models that depend on the flowfield (this is the first loop iteration). Linking with the upstream quasi-orthogonal is carried out in this stage. Those all assumes, V_m at the hub (constant of integration, $V_m(0)$, in Eq.3.11) is known at the current quasi-orthogonal. Once convergence is reached in the first iteration loop, the continuity along the quasi-orthogonal is checked using Eq.3.13 to update the previously guessed V_m at the hub to satisfy overall mass flow rate (Figure 23). Linear variation is assumed here for simplicity. The second loop runs until convergence is reached in the total mass flow rate. Then, streamlines are re-adjusted based on mass continuity in each streamtube (Eq.3.14). This last iteration loop is challenging due to highly unstable nature of the solution. Therefore under-relaxation factors must be carefully applied both to streamline movement and curvature [75].

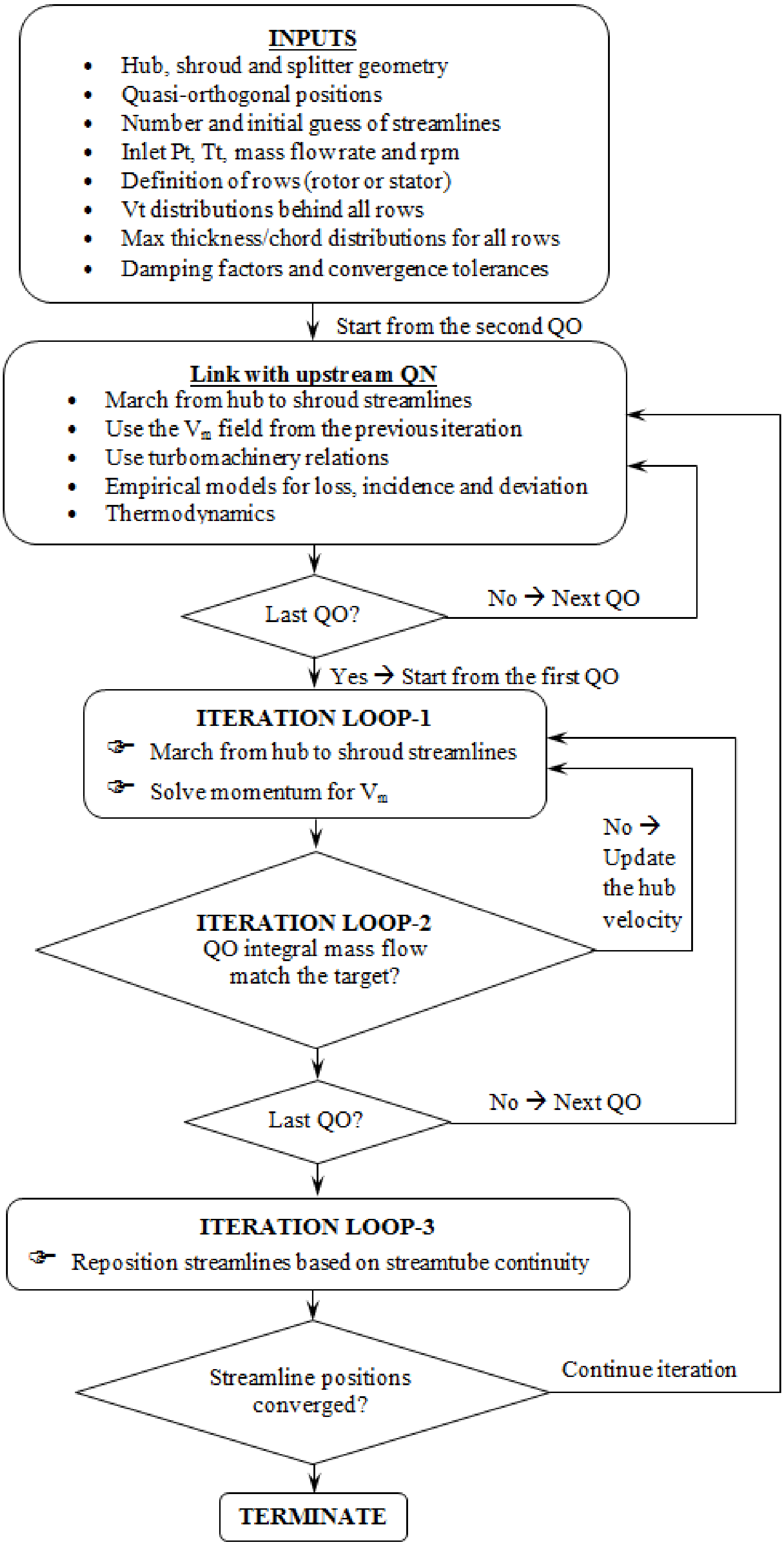

Figure 24. Flow chart of streamline curvature methodology

3.4.1. Convergence Criteria

A separate convergence tolerance is defined for each loop. For the first iteration loop (velocity iteration), the criteria is the maximum damp-independent change of meridional velocity between two successive iterations on each quasi-orthogonal. An arbitrary convergence tolerance of 0.01% is defined for the maximum change. For the second iteration loop (mass flow rate iteration), similarly, the change of mass flow rate between two successive iterations is considered for each quasi-orthogonal. The same convergence tolerance (0.01%) is employed. Finally, for the third iteration loop, where streamlines are adjusted, the maximum normalized spanwise movement of streamlines is considered. Once the maximum movement is less than 0.01%, the calculation is terminated. The convergence of meridional velocity field through the above iteration loops also means the convergence of outputs of the empirical loss models.

3.5. Employed External Empirical Models

This section gives complete set of baseline empirical models utilized in this study; compiled from open literature reviewed in Section 2.2. Calibration or modification of the models is given in section 3.5.6. The models required for through-flow analyses are correlations of reference incidence angle for minimum loss, total pressure loss and deviation at each profile. Nomenclature is given in Figure 15.

3.5.1. Minimum Loss Incidence Model

Minimum loss incidence, as discussed in literature review section, is an important parameter in design because it is used to define inlet angle of blade section relative to the known flow angle (from through-flow) for intended design point operation. On the other hand, designers may intentionally use a different incidence for design point operation (e.g. for wider off-design range at the expense of design efficiency loss). Even in this case, minimum loss incidence angle of a blade section remains an important parameter because it is used as a reference angle that is required in loss and deviation correlations (e.g. the models given throughout this chapter). It mainly depends on parameters such as blade type (thickness distribution), maximum thickness, camber (turning) and turning distribution (camberline shape, Figure 15).

The formulas given by Aungier [42] and Kleppler [78], mostly derived from cascade test data of NASA SP36 [44] and later experiences, are used. Minimum loss incidence for incompressible flow is defined below:

$$i^* = K_{sh} K_{t,i} (i_0^*)_{10} + n\theta \tag{4.1}$$

Where $(i_o^*)_{10}$ is the baseline parameter, defining minimum loss incidence for symmetrical (no camber, $\theta=0$) and staggered NACA 65 thickness distribution (Figure 14) having 10% max thickness to chord ratio (th/c). It is correlated by:

$$(i_0^*)_{10} = \frac{\beta_1^{\,p}}{5 + 46\exp(-2.3\sigma)} - 0.1\sigma^3 \exp\left[(\beta_1 - 70)/4\right] \tag{4.2}$$

With

$$p = 0.914 + \sigma^3/160 \tag{4.3}$$

Where σ is solidity (*c/t*), as given in Figure 15. K_{sh} is shape factor, used to modify this correlation for other blade types or thickness distributions (e.g. 0.7 for double circular arc blades). $K_{t,i}$ is thickness parameter, a correction factor, for *th/c* different than 10%, defined by:

$$K_{t,i} = (10th/c)^q \tag{4.4}$$

$$q = 0.28/[0.1 + (th/c)^{0.3}] \tag{4.5}$$

$n\theta$ takes into account effect of camber. The correction factor n is correlated by:

$$n = 0.025\sigma - 0.06 - \frac{(\beta_1/90)^{(1+1.2\sigma)}}{1.5 + 0.43\sigma} \tag{4.6}$$

Angles in all these correlations are expressed in degrees. Once the incompressible minimum loss incidence is obtained, stall and choke angular ranges must be estimated (e.g. the low-loss operation angular range in Figure 25), even for design condition to establish compressibility corrections. Reference (low-speed or incompressible) range from design incidence to choke incidence (i_c), denoted as R_c, can be estimated from [78]:

$$i_c - i^* = -R_c = -\left(10 - \theta\frac{(K_1 - 40)}{450}\right)\left(0.5 + 5\frac{th}{c}\right) \tag{4.7}$$

The correlation given by Aungier is not used because the profile thickness is taken into account in this alternative correlation, which is assessed as a major parameter. Moreover, Aungier's correlation requires iteration to obtain the ranges. Similarly, reference range from design incidence to stall incidence (i_s) can be estimated by:

$$i_s - i^* = R_s = 1.5\left(10 + \theta\frac{(55 - K_1)}{150}\right)\left(0.5 + 5\frac{th}{c}\right) \tag{4.8}$$

Ranges estimated from above equations are narrowed considerably with increasing inlet relative Mach number, as shown in Figure 25, which is taken from NASA SP 36 [44]. It is evident from the figure that choke (lower incidence) range reduces much faster than stall range. As a result, minimum loss incidence increases with increasing Mach number. Aungier suggest below corrections for compressibility effects:

$$i_{c\ (compressible)} = i^* - R_c / \left[1 + 0.5 M_{1-rel}{}^3\right] \tag{4.9}$$

$$i_{s\ (compressible)} = i^* + R_s / \left[1 + 0.5 \left(K_{sh} M_{1-rel}\right)^3\right] \quad \left(for\ K_{sh} \leq 1\right) \tag{4.10}$$

Although i_c indicates choking side (negative incidence-higher flowrate) high loss limit, it does not necessarily indicate the choking condition. Above formula is valid as long as i_c is bigger than the choke limit. An additional limit is put for i_c such that it must be higher than the real choke incidence at an amount (according to Aungiers practice) causing 2% more mass flow rate than the choke mass flow of the profile investigated. This limit results:

$$i_{c\ (compressible)} = \beta_{1choke} - K_1 + 1^o \tag{4.11}$$

Where β_{1choke} is flow angle at which passage chokes at the throat and 1^o is an empirical adder. β_{1choke} may be estimated from:

$$\rho_1 W_1 t \cos(\beta_{1choke}) = o \rho_{sonic} W_{sonic} \tag{4.12}$$

Where 'o' is the throat opening of investigated profile and subscript '*sonic*' denotes sonic conditions at the throat (conditions for *Mach=1*), which can be obtained using thermodynamic state equation and inlet total pressure and temperature.

Throat opening (geometric throat) must ideally be obtained from the actual airfoil shape (such as Figure 15), but it is unknown during the design phase since it changes rapidly with continuously updated flow angles during the solution. Therefore, empirical formulas given by Aungier are employed in this study to estimate the throat-to-pitch ratio, where pitch of a profile is known as a function of radius and number of blades.

$$o/t = \left[\left(1 - th\sqrt{\sigma}/c\right)\cos\psi\right]^{\sqrt{\sigma}} \tag{4.13}$$

Where ψ is modified stagger parameter defined as:

$$\psi = \gamma(1 - 0.05C_{l0}{}^{1.5}) + 5C_{l0}{}^{1.5} - 2 \tag{4.14}$$

Where C_{l0} is a lift coefficient. For a general loading distribution, the maximum camber location (normalized by chord length) should be given as an input. Therefore a generalized formulation based on the parabolic camber line is used and the circular-arc camberline ($a/c=0.5$) approximation is abandoned:

$$C_{l0} = \frac{\tan(\theta/4)}{0.05515}\left(\frac{a}{c}\right) \tag{4.15}$$

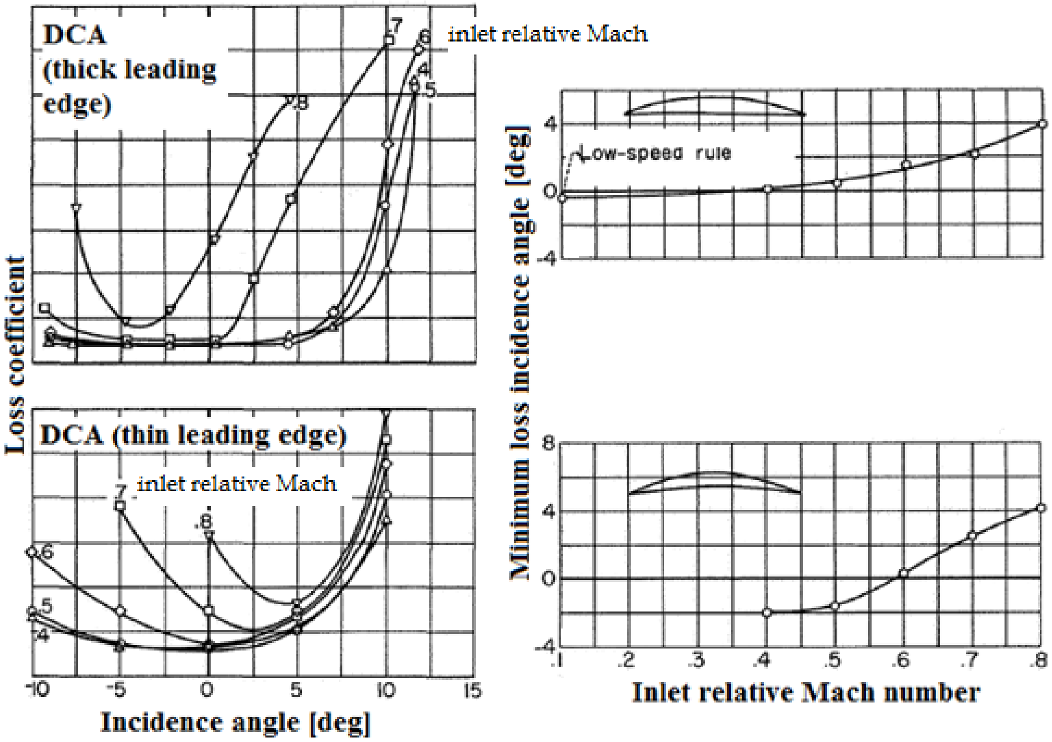

Figure 25. Variation of minimum loss incidence [44]

It is important to define or estimate an ‘optimal’ or ‘feasible’ stagger angle in this phase (to be used in Eq. 4.14 and also during airfoil section design), as a function of max camber location and blade angles. For a circular arc camberline, it is the average of inlet and outlet metal angles. But for a more general loading distribution (other than *a/c*=0.5), this is no longer feasible. For a general case, it is shown [42] for parabolic camberlines that the distance between chord line and point of maximum camber (Figure 15) is:

$$\frac{b}{c}=\left\{\sqrt{1+(4\tan\theta)^{2}\left[\frac{a}{c}-\left(\frac{a}{c}\right)^{2}-\frac{3}{16}\right]}-1\right\}/\tan(\theta) \tag{4.16}$$

Finally, the corresponding stagger angle is obtained from [42]:

$$\gamma = K_1 - \arctan\left[4\frac{b}{c} / \left(4\frac{a}{c} - 1\right)\right] \tag{4.17}$$

Once compressible stall and choke range are estimated, minimum loss incidence may be estimated from:

$$i_m = i_c + (i_s - i_c)R_c / (R_c + R_s) \tag{4.18}$$

3.5.2. Deviation Model

Deviation, as discussed in the literature review section, is angular departure of flow relative to exit angle of the blade section (see Figure 15). It causes misguidance of flow and subsequently results in less work input to flow (for compressors) for a given metal turning. Moreover, additional pressure loss occurs due to thicker boundary layer. Although it is mainly an inviscid phenomenon due to airfoil exit non-uniformity (pressure side fluid moves to the relatively lower pressure suction side at the exit of airfoil), presence of boundary layer or more importantly boundary layer separation plays an important role [43]. A good airfoil profile should be designed to minimize deviation for lowest losses and minimum turning for demanded work. Moreover, any small error in its prediction leads to a higher error in a compressor performance prediction. Therefore, it is one of the most important parameters in design.

A similar approach with the incidence model is followed for estimation of deviation at minimum loss incidence condition. Again, the formulas given by Aungier [42] and Boyer [55], mostly derived from cascade test data of NASA SP36 [44], are used. The general formula is:

$$\delta^* = K_{sh} K_{t,\delta} (\delta_0^*)_{10} + m\theta \tag{4.19}$$

Where $(\delta_o^*)_{10}$, similar to $(i_o^*)_{10}$, is deviation for 10% thick NACA 65 profile. It can be estimated from:

$$(\delta_0^*)_{10} = 0.01\sigma\beta_1 + \left[0.74\sigma^{1.9} + 3\sigma\right]\left(\beta_1 / 90\right)^{(1.67+1.09\sigma)} \tag{4.20}$$

This baseline deviation, likewise incidence correlations, is corrected for different blade shape and thickness and camberline. K_{sh} is the same parameter that used in incidence correlations. In a similar manner, $K_{t,\delta}$ is a correction factor for a *th/c* that is different than 10%, defined by:

$$K_{t,\delta} = 6.25(th/c) + 37.5(th/c)^2 \tag{4.21}$$

The scaling factor m for camber effect is defined for a general camberline (by Boyer [55]) with specified maximum camber location (*a/c*) is:

$$m = \frac{\left[0.249 + 0.074\left(\frac{\beta_1}{100}\right) - 0.132\left(\frac{\beta_1}{100}\right)^2 + 0.316\left(\frac{\beta_1}{100}\right)^3 + 0.5\left(\frac{a}{c} - 0.5\right)\right]}{\sigma^b} \tag{4.22}$$

Where the factor *b* is given as:

$$b = 0.9625 - 0.17(\beta_1/100) - 0.85(\beta_1/100)^3 \tag{4.23}$$

The reference deviation model should also be corrected for meridional acceleration or deceleration (but with limit ±5^o), which can be modeled by [55]:

$$\delta_{V_m} = 10\left(1 - \frac{V_{m2}}{V_{m1}}\right) \tag{4.24}$$

The final deviation (δ_m), corresponding to minimum loss incidence, is sum of baseline design deviation (δ^*), meridional acceleration or deceleration correction (δV_m) and 3D correction (δ_{3D}) (the latter will be included after calibration with test cases):

$$\delta_m = \delta^* + \delta_{V_m} + \delta_{3D} \tag{4.25}$$

3.5.3. Relative Total Pressure Loss Model

Prediction of losses during design phase has great importance because the gradient of entropy along quasi-orthogonal (~spanwise) direction plays a major role in the normal equilibrium equation (see Eq.3.1). Therefore misprediction of losses will result in wrong spanwise distribution velocity triangles; and the subsequently designed machine will not operate at intended operation.

The profile loss (excluding shock and losses due to 3D effects) is mainly a function of diffusion (deceleration) within an airfoil section. It is represented by the so-called equivalent diffusion factor, ratio of profile relative maximum suction surface velocity to exit velocity. This is demonstrated in Figure 26.

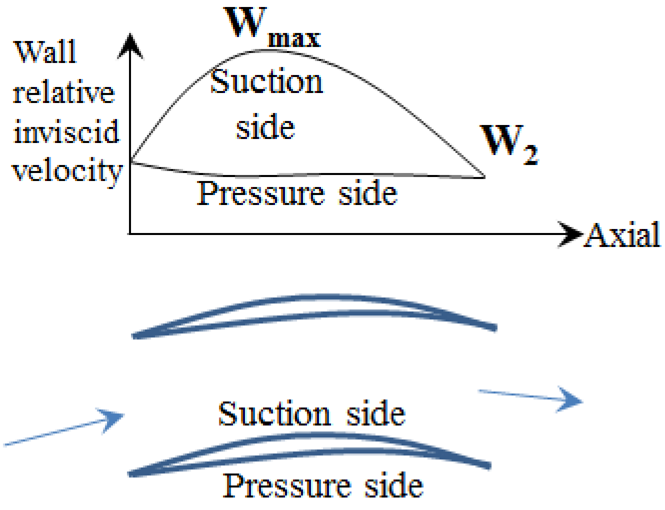

Figure 26. Physical background of diffusion factor

The correlation of Koch and Smith [45] is utilized in this study to estimate equivalent diffusion factor of profiles:

$$D_{eq} = \frac{W_{\max}}{W_2} \tag{4.26}$$

Where this is expressed as products of throat average relative velocity to inlet relative velocity ratio, maximum suction surface relative velocity to throat average relative velocity ratio and inlet to outlet relative velocity ratio:

$$D_{eq} = \frac{W_{throat}}{W_1} \frac{W_{\max}}{W_{throat}} \frac{W_1}{W_2} \tag{4.27}$$

Where below formulas are utilized to obtain the first two terms (the third term comes from the throughflow solution):

$$\frac{W_{throat}}{W_1}=\left\{(\sin\beta_1-0.2445\sigma\Gamma^*)^2+\left[\frac{\cos(\beta_1)}{A_p^*(\rho_p/\rho_1)}\right]^2\right\}^{1/2} \tag{4.28}$$

$$\Gamma^*=(r_1V_{\theta 1}-r_2V_{\theta 2})/(\bar{\mathrm{r}}\sigma W_1) \tag{4.29}$$

$$\bar{\mathrm{r}}=\frac{r_1+r_2}{2} \tag{4.30}$$

$$A_p^*=\left[1-\left(0.4458\sigma\frac{th}{c}\right)/\cos\bar{\beta}\right]\left(1-\frac{A_{a1}-A_{a2}}{3A_{a1}}\right) \tag{4.31}$$

$$\bar{\beta}=\frac{\beta_1+\beta_2}{2} \tag{4.32}$$

$$\frac{\rho_p}{\rho_1}=1-\frac{M_z{}^2}{1-M_z{}^2}\left(1-A_p^*-0.2445\frac{\tan\beta_1}{\cos\beta_1}\sigma\Gamma^*\right) \tag{4.33}$$

$$\frac{W_{\max}}{W_{throat}}=1+0.7688\frac{th}{c}+0.6024\Gamma^* \tag{4.34}$$

Once the equivalent diffusion factor is calculated, reference loss coefficient at minimum loss incidence angle for incompressible flow is defined as below:

$$\varpi^*=C_1\left[C_2+3.1(D_{eq}-1)^2+0.4(D_{eq}-1)^8\right]\frac{2\sigma}{\cos(\beta_2)}\left(\frac{W_2}{W_1}\right)^2 \tag{4.35}$$

Where the terms other than the diffusion factor come from the throughflow solution and K_1 and K_2 are empirical constants and given by Aungier as:

$$C_1=0.0073 \tag{4.36}$$

$$C_2=1+(\bar{t}/\bar{h})\cos\beta_2+0.004C_{\mathrm{Re}}/C_1 \tag{4.37}$$

Where C_{RE} is the Reynolds number correction factor defined as:

$$C_{Re} = \begin{cases} \sqrt{2.5\text{x}10^5 / Re_c} - 1 & (Re_c < 2.5\text{x}10^5) \\ \left[\log(2.5\text{x}10^5) / \log(Re_c) \right]^{2.58} - 1 & (Re_c < 2.5\text{x}10^5) \end{cases} \tag{4.38}$$

Once the loss coefficient is obtained, Mach number correction is applied:

$$\varpi_m = \varpi^* \left[1 + (i_m - i^*)^2 / R_s{}^2 \right] \tag{4.39}$$

This excludes shock losses for transonic profiles, where inlet Mach number is lower than unity, but higher than the critical Mach number, the relative inlet Mach number at which sonic velocity on the suction side first emerges. Consequently local supersonic pockets and shock waves become occur on the suction side as Mach number is further raised from the critical Mach number (see the introduction chapter). The magnitude of critical Mach number can be estimated using the above equivalent diffusion factor correlations of Koch and Smith. For such profiles, the additional shock loss coefficient is:

$$\varpi_{shock-transonic} = K_{sh} \left[(M_{1-rel} / M_{critical} - 1) W_{sonic} / W_1 \right]^2 \tag{4.40}$$

Finally, for these transonic profiles, the total loss coefficient is:

$$\varpi_{TOTAL} = \varpi_m + \varpi_{shock-transonic} \tag{4.41}$$

For profiles with supersonic relative inlet, the classical MLH model [79] is utilized. In this model, the shock is assumed to be normal at the line connecting leading edge and suction side, where the line is normal to the suction side (Figure 27). This is a condition close to peak efficiency condition and all the neglected effects (the oblique shocks, leading edge bluntness, precise location of the shock, etc.) are lumped into this normal shock through a proper model calibration process.

The model assumes that the normal shock loss can be estimated by a representative Mach number, which is average of the inlet relative Mach number and accelerated suction side flow (Figure 27). Different than the original MLH model, where the representative Mach number is the arithmetic average of the two Mach numbers, Aungier suggests [42] geometric averaging should be done, as incorporated in this study. In addition, the present study utilizes the model of Wennerstrom and Puterbaugh [80] to take into account spanwise obliqueness of the shock surface (Figure 28). This is done by multiplying both M_{1-rel} and M_{max} by sine of the leading edge and shock impingement (point of M_{max}) obliqueness angles ($\alpha_{obliqueness}$), respectively. In conclusion, the representative Mach number is:

$$M_{SHOCK} = \sqrt{M_{1-rel} M_{\max} \left|\sin(\alpha_{obliqueness})\right|_{\text{leading edge}} \left|\sin(\alpha_{obliqueness})\right|_{\text{impingement point}}} \tag{4.42}$$

To estimate M_{max}, the suction side acceleration is estimated by a Prandtl-Mayer expansion angle ($\theta_{supersonic}$) (see any elementary text book on compressible flows, e.g. [81] or Section 1.1). But, such an expansion has to be estimated on a circular camberline in a correlation. The estimated expansion is calibrated for a real supersonic camberline in the scope of this thesis (see Section 3.5.6). The equations leading to $\theta_{supersonic}$ for a circular arc camberline are [42]:

$$\tan(\theta_{SS} / 4) = \tan(\theta / 4) + \frac{th}{c} \tag{4.43}$$

$$r_{SS} = \frac{c}{2\sin\left(\theta_{SS}\right)} \tag{4.44}$$

$$K_{SS} = 90 - \frac{\theta_{SS}}{2} - K_1 + \frac{\theta}{2} \tag{4.45}$$

$$\theta_{\text{supersonic}} = \arctan\left(\frac{t\cos(K_{SS})}{t\sin(K_{SS}) + r_{SS}}\right) \tag{4.46}$$

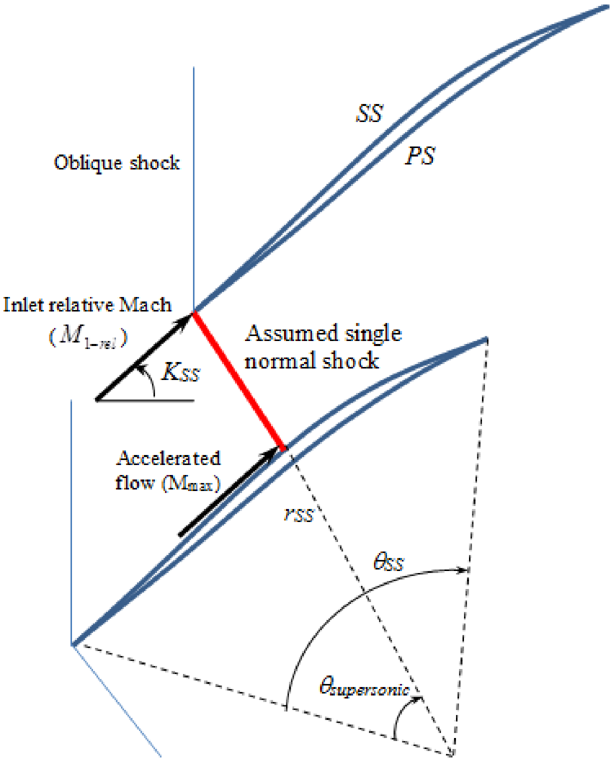

Figure 27. Nomenclature of the shock loss model

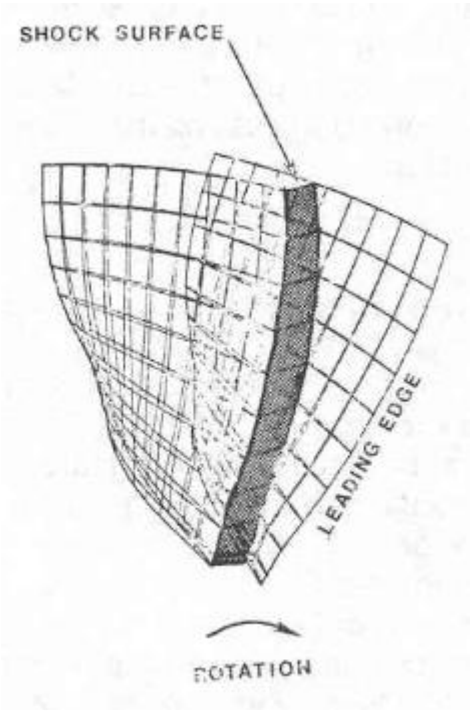

Figure 28. 3D obliqueness of the shock [80]

The obliqueness angle at the leading edge is calculated from:

$$\alpha_{obliqueness\ \text{(Leading edge)}} = \arccos(\cos\beta_1 \cos(lean)\sin(\varepsilon) - \sin\beta_1 \sin(lean)) \qquad (4.47)$$

The calculation at the impingement point is difficult because the blade shape must be known (analysis mode). For design, blade shape changes rapidly with iterative solution and it is not feasible to calculate real value of it at teach iteration. A simple approach is used here. If blade span is defined from 0 (hub) to 1 (tip), assume impingement point obliqueness is equal to the leading edge obliqueness. If it is bigger than 0.5, then the impingement point obliqueness is two times the leading edge obliqueness. This is correlated from typical fan or compressors given in the study of Wennerstrom and Puterbaugh.

Once the maximum suction side Mach number is calculated using $\theta_{supersonic}$ and the representative shock Mach number is estimated, the generic 1D normal shock relation (any book on compressible fluid mechanics or ref. [81]) is used to estimate relative total pressure loss due to the shock. Finally, it must be converted to the total pressure loss coefficient form (ϖ_{shock}). As for the transonic profiles, the total loss coefficient is the sum of profile (including secondary loss) and shock losses:

$$\varpi_{TOTAL} = \varpi_m + \varpi_{shock} \tag{4.48}$$

3.5.4. Off-Design Correlations

The off-design correlations derived by Cetin et. al. [53] and Creveling [82] are used to treat off-design loss and deviation. This is used to take into account the effect of real incidence in the validation cases of sections 5.2 and 5.4 (The 3D CFD-based calibration model of section 5.3 operates at the minimum loss incidence angle and does not need an off-design model). The test incidence is seldom very close to the minimum loss incidence even though peak efficiency test results are used to validate and calibrate the models.

For MCA profiles, below relations are given:

$$c_m = 0.02845 M_{1-rel} - 0.01741 \text{ (for incidence} < i_m) \tag{4.49}$$

$$c_m = 0.00363 M_{1-rel} - 0.00065 \text{ (for incidence} \geq i_m) \tag{4.50}$$

For DCA profiles, below relations are used:

$$c_m = 0.05336 M_{1-rel} - 0.02937 \text{ (for incidence} < i_m) \tag{4.51}$$

$$c_m = 0.00500 M_{1-rel} - 0.00075 \text{ (for incidence} \geq i_m) \tag{4.52}$$

Finally, the off-design loss coefficient is given by the below relation:

$$\varpi_{off-design} = \varpi_m + c_m \left(incidence - i_m \right)^2 + \varpi_{shock} \tag{4.53}$$

For off-design deviation angle, after testing may off-design deviation angle correlations, Cetin et. al. [53] recommends correlation derived by Creveling [82], which are:

$$eps = K_1 - K_2 - \delta_m + i_m \tag{4.54}$$

$$PP_1 = \left(incidence - i_m \right) \ / \ eps \tag{4.55}$$

If PP_1 is positive, then the coefficients are: d_1=-0.2928, d_2=0.5588 and d_3=-0.000809. If PP_1 is negative, then d_1=-0.3452, d_2=0.4800 and d_3=0.0001191. Those coefficients are used in the below equation:

$$PP_2 = d_1 PP_1^2 + d_2 PP_1 + d_3 \tag{4.56}$$

Finally, the off-design deviation is given by:

$$\delta_{off\text{-}design} = \delta_m + eps\ PP_2 \tag{4.57}$$

3.5.5. Endwall Boundary Layer Calculation

End wall boundary layer has a big impact on a compressor performance due to causing blockage and triggering 3D flow features. For compressors with many stages, an error in blockage error is responsible for bad stage matching. More truly, rather than the true prediction of blockage, consistency with the empirical models are more important because errors due to empirical models may compensate errors due to blockage and organizations seek consistent blockage factor estimations rather than its exact distribution [8]. The end wall boundary layer is highly 3D and the utilized simplified analysis techniques are not universal. In a classical SLC approach, boundary layers are taken into account only by a simple annulus blockage factor and the loss caused by end walls are lumped into the loss models. This study adopts a simplified estimation technique [83], which assumes an incompressible boundary layer with the meridional velocity dominating the flow. Although it is a very simplified approach, similar approaches are used in proved methodologies such as the one of Petrovic et. al [84]. Also, there is no guarantee that more complicated methods are more successful in this highly 3D and turbulent flowfields [8, 42, 45]. As the consistency with the loss models is the key aim, the success of the method will be evaluated as a whole in the validation chapter.

Following Pachidis [83], the method assumes that the momentum thickness at any axial location z can be obtained by the below integration:

$$\theta_{mom}(z) = \theta_{mom}(z_{inlet}) + \left(\frac{\int_{z_{inlet}}^{z} V_m^4(z)dz}{V_m^{3.2}(z)} \right)^{0.8} \tag{4.58}$$

Where the inlet momentum thickness, by definition, is the ratio of inlet displacement thickness to inlet boundary layer shape factor:

$$\theta_{mom}(z_{inlet}) = \frac{\delta_{disp}(z_{inlet})}{H_{shape}(z_{inlet})} \tag{4.59}$$

In this equation, the inlet shape factor can be estimated as 1.4, which is typical for a flat plate flow. If the inlet displacement thickness is known, this equation can be used to estimate the inlet momentum thickness. Once the inlet momentum thickness is known and the axial distributions of momentum thicknesses for both hub and shroud walls are obtained using the above equation, the shape factor distributions for the both walls can be obtained by the below equation:

$$H_{shape}(z) = 1.5 + 30\frac{d\theta_{mom}(z)}{dz} \tag{4.60}$$

Finally, displacement thickness axial distributions at the both end walls are obtained by:

$$\delta_{disp}(z) = \theta_{mom}(z)H_{shape}(z) \tag{4.61}$$

The annulus blockage factor at any quasi-orthogonal can easily be obtained by the ratio of the available annular area to the metal annular area:

$$K_w = \frac{\text{Avaliable area}}{\text{Metal area}} \tag{4.62}$$

3.5.6. Further Extensions Based on Test Cases

The empirical incidence, deviation and loss sub-models given in the prior sub sections, after some trial and error processes, are already complied from the literature to better agree the test cases presented in CHAPTER 5. However, some modifications still required. Below items are the extensions made to the original correlations:

- The pitch of any profile is calculated by the inlet radial position (relative to the machine axis) but the solidity is calculated the average radius,

- In case there is overturning, where outlet metal angle sign is different than the inlet metal angle sign (as seen in front stage fan roots), the outlet metal angle is taken as zero in camber terms of Equations 4.1 and 4.15 (not the case for other equations),
- For the transonic shock losses given by Eq.4.40, the exponent ‘2’ is made 1.6 to better match the test cases,
- The Prandtl-Mayer supersonic expansion angle ($\theta_{supersonic}$), calculated by equations 4.43-4.46, is multiplied by 0.95 for inlet relative Mach numbers lower than 1.25 and multiplied by 0.45 for inlet relative Mach numbers bigger than 1.4. Linear variation is assumed in between inlet Mach numbers 1.25 and 1.4. The correction is summarized in Figure 29. This correction is to model more modern blade profiles where the expansion is less than that occurs in an ideal circular arc blade. Especially in high supersonic profiles, the use of wedge or pre-compression suction surfaces is responsible for low (0.45 in this case) expansion angles. The correction also includes design point tip leakage effects of the investigated test cases (CHAPTER 5).

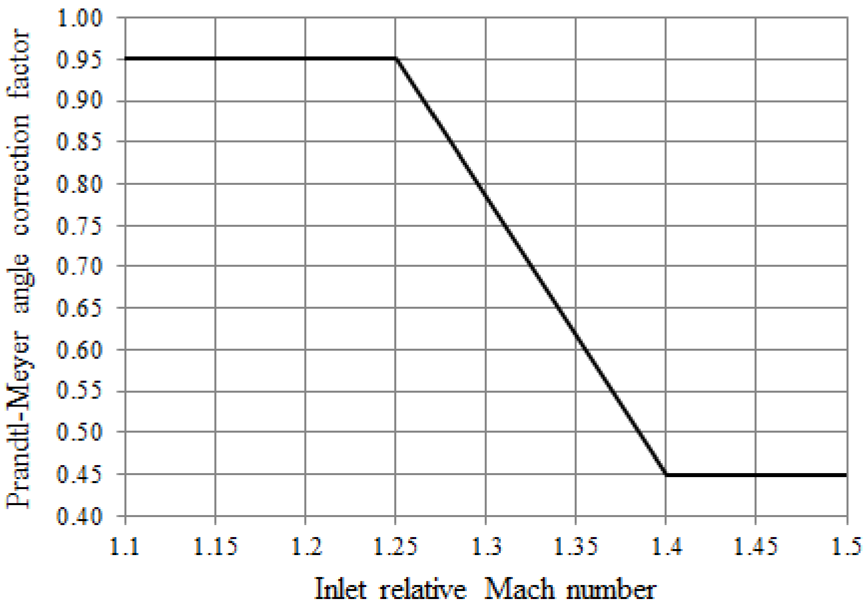

Figure 29. Corrective multiplier for Prandtl-Mayer expansion angle

- The deviation correlation that is presented in this chapter is also calibrated relative to the test cases to include 3D effects (δ_{3D} term in equation 4.25). The NASA SP36 correlation [44] is observed to be unsatisfactory in this manner. Reducing the resultant deviation by 1 degree resulted in good results. Moreover, the tip section deviation is increased by 2 degrees (over the -1 degree correction) and the correction linearly reduces to zero degrees at 90% span from hub. The overall correction is summarized in Figure 30.

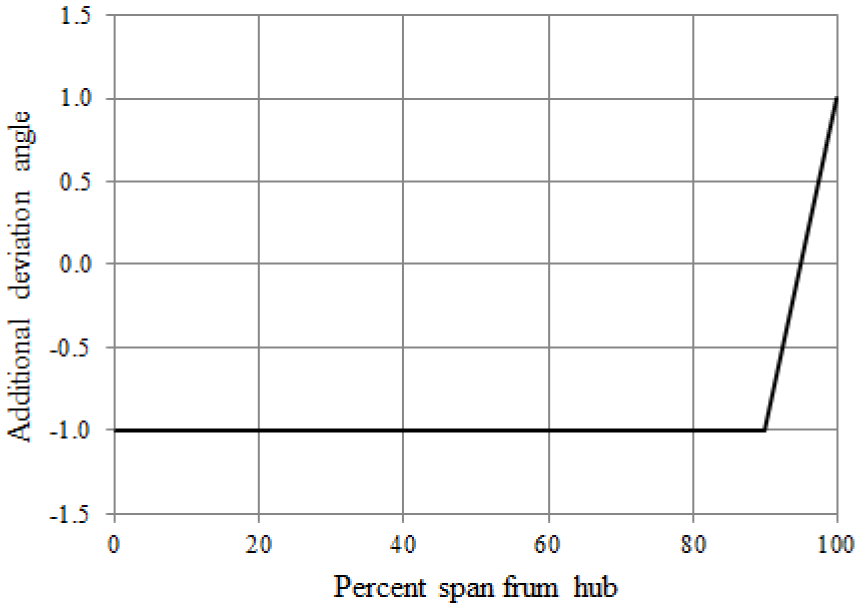

Figure 30. Additional deviation as a function of spanwise position

CHAPTER 4

PROPOSED SPLIT-FLOW MODELLING

The open literature on split-flow fan modeling is reviewed at the end of Chapter 2.2, where it is evident that literature addressing the issue is limited. In the generally applicable SLC-based method reviewed, shortly, the streamline that stagnates at the splitter (leading) edge is defined at the very beginning and its final shape, upstream of the splitter, is obtained by an iterative solution of subdomains (see Figure 32, bottom left). In analysis mode, where the machine geometry required for SLC model is known and its off-design performance with off-design by-pass ratios is sought, this is a viable approach. However, in design mode, there may be difficulties with this approach, because the flowpath and blading is not fixed yet and parametric variation of them affects the flow field significantly. As definition of a stagnation streamline inherently fixes the ratio of mass flows between the two downstream ducts (by-pass ratio), there is high probability during design iterations that streamlines distort near the splitter edge (see Figure 32, bottom left), leading to high (or extreme) velocity gradients due to high streamline curvatures. This is simply a result of high angle of attack of the splitter leading edge and may easily cause solution to diverge. Even if a converged solution is obtained, the result of high angle of attack is an undesirable one for design because of high losses and risk of flow separation. Adjusting splitter angle to overcome this problem is obviously possible, but it may require cumbersome iterations in both manual and automatized designs. Moreover, when the problem is solved by an iterative method at upper-lower domains (domain 1 and domain 2 in Figure 32, bottom left), as summarized in Chapter 2.2, the fan stage is divided by the stagnation streamline, causing stepwise jump of properties along the span during iterative solution. Those are also recently addressed by Shan [67].

In taking into account of the upstream effect of any obstacle in SLC method, in this case effect of splitter and downstream ducts on the fan stages, the only mechanism is the streamline geometry; i.e. streamline curvature (K_m), angular difference between quasi-orthogonal / true-orthogonal (ε) and meridional gradient term of Eq.3.7 $(\partial V_m / \partial m)$ in Eq.3.1. This means, any pressure propagation to upstream is felt by means of centrifugal acceleration of streamlines due to curvature and linear acceleration of velocity along '*quasi-orthogonals*' when they are not exactly normal with streamlines ($\varepsilon \neq 0$). Figure 31 visualizes this concept at stagnation region of an arbitrary blunt body, where the curvature of streamlines are responsible for stagnation pressure increase in SLC method.

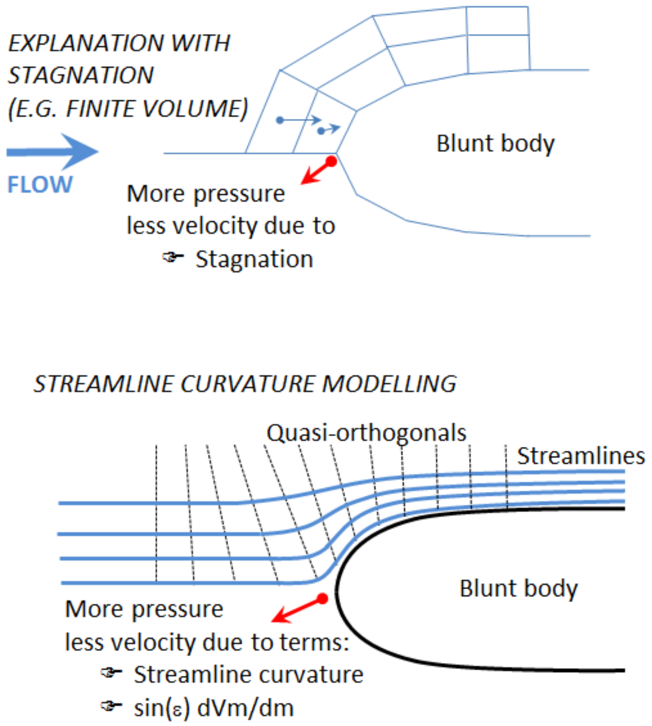

Figure 31. Upstream propagation modeling in SLC

The principle described in above paragraph forms the basis of proposed modeling for turbofan compression system that include any kind of fan module, downstream flow splitter of any thickness/shape and by-pass/core compressor ducts of any shape. When solving fan domain, if streamline terms are calculated from nodes of fan domain only, then obviously the downstream splitter and ducts will not be felt by the flow. On the other hand, if downstream portions of the same streamlines are also taken into account in calculation of the streamline terms (not known yet but will be obtained by iterative means), then all the back-propagation interactions are modeled correctly, as aimed in this study. This requires one of the streamtubes to divide into two by the splitter, always at right angle, without streamline distortion. As no stagnation streamline is defined from the start, the streamtube that stagnates onto the splitter edge and its thickness and position relative to splitter are a result of specific inputs of case investigated; and may change dramatically with altered inputs. The concept is visualized and compared with conventional approach in Figure 32. With this approach, by-pass ratio is the result of computation rather than a prescribed variable as in the conventional method, but it can easily be set to desired value by mainly altering splitter edge or adjacent splitter bottom surface when splitter edge is fixed. This is much easier than the required iteration with the conventional treatment due to lack of undesired flowfield caused by high streamline distortion. Considering the approximate nature of the through-flow design process and future final refinements on basis of detailed 3D CFD and component/engine tests, this is considered to be a viable approach.

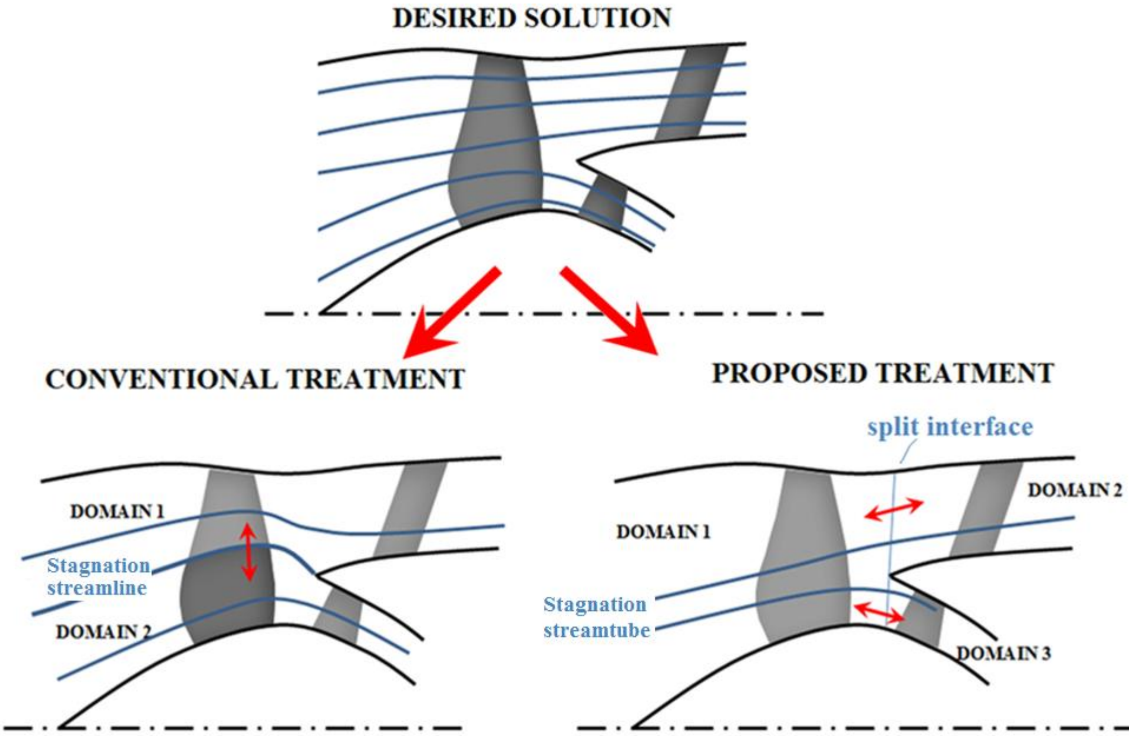

Figure 32. Proposed split-flow treatment

The solution procedure is summarized in Figure 33. The solution starts with the solution of fan domain. The exit boundary of the fan domain (the line drawn in Figure

32, right) is defined as the split interface. It must be coinciding with the splitter edge, and arbitrarily defined as linear in this study, like all other quasi-orthogonals used in this study. Once the fan solution is finished, the streamlines just below and above the flow splitter is detected and the split of mass flows to the both ducts are established. In the dividing stream-tube (flow between two streamlines just below and above of splitter), this implementation assumes linear variation of velocity and density. This is reasonable compared to curve fitting, because the distance is very small between the two streamlines to allow linear variation when mesh dependency is satisfied. The next step is transmitting the required data from fan domain to the two downstream ducts at the splitting interface. The required data, other than mass flows, are streamlines exit positions, total pressure, total temperature/enthalpy and entropy. The splitting interface, being divided by the splitter, is also the first quasi-orthogonals of by-pass and core solutions. Because the flowfield is already obtained there during the fan solution, the subsequent solutions of by-pass and core ducts start from their second quasi-orthogonals. This time the upstream (fan domain) nodes, although kept constant, are also taken into account in streamline terms calculation by means of single curve-fitting (the bottom-most figure in Figure 33).

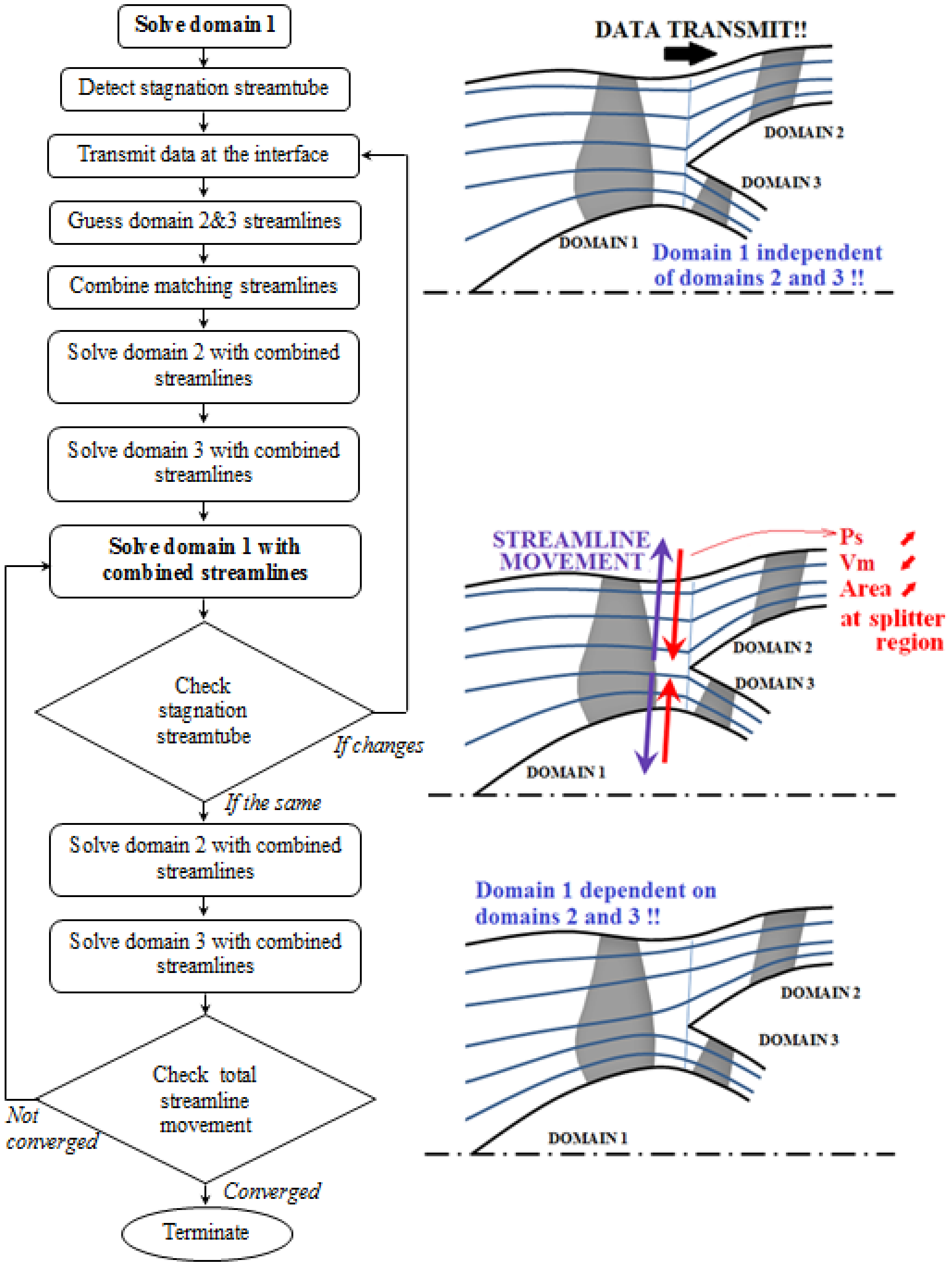

Figure 33. Algorithm for the proposed methodology

Once the first solutions of by-pass and core ducts are completed, the second and all future fan solutions similarly imports and uses nodes of core and by-pass domains in addition to its own nodes. This enables splitter and downstream duct interferences to be simulated. Care must also be taken to the possible change of stagnation streamtube, which is checked after each fan solution. If the streamtube is changed compared to the previous solution, the by-pass and core ducts are reinitialized. The procedure continues until the fan / by-pass / core iteration becomes to modify streamlines and flowfield within specified tolerances.

4.1. Coding the Methodology

This section intends to discuss the structure of the developed code. It aims to implement the algorithms presented in Figure 24 and Figure 33 for single stream SLC solution and the proposed split-flow modeling, respectively. The general structure of the code is given in Figure 34, which presents utilized main code, its subroutines and connection between the subroutines. The following text introduces each subroutine.

In the routine “MAIN_PROGRAM”, the flowpath (fan, bypass and the core), positions of quasi-orthogonals, number of total (the fan domain) streamlines, inlet total pressure, total temperature, total mass flow rate, shaft rotational speed, coefficients of the temperature dependent constant pressure specific heat (c_p), damping factors and convergence tolerances of the iterative loops, positions and numbers of blade rows, number of inter-blade stations for each blade row, polynomials defining swirl and maximum thickness-to-chord ratio distributions and their assignments to the blade rows are all inputted. The main program also pre-allocates variables of the fan domain. By-pass and core domain streamline numbers are not known in this stage, hence they are pre-allocated later in the subroutine “SUB_Split_Interface”, which will be discussed in the following paragraphs. Finally, the main program coordinates the solution of fan, by-pass and core domains by subsequent call of “MAIN_SOLVER” and “SUB_Split_Interface”. Once the solution is finished, “SUB_Post” is called to present main outputs.

In the routine “MAIN_SOLVER”, the SLC solution is performed using the algorithm discussed in Figure 24, for any single-stream domain. It is recalled separately each time a fan domain, by-pass domain or core domain solution is to be done.

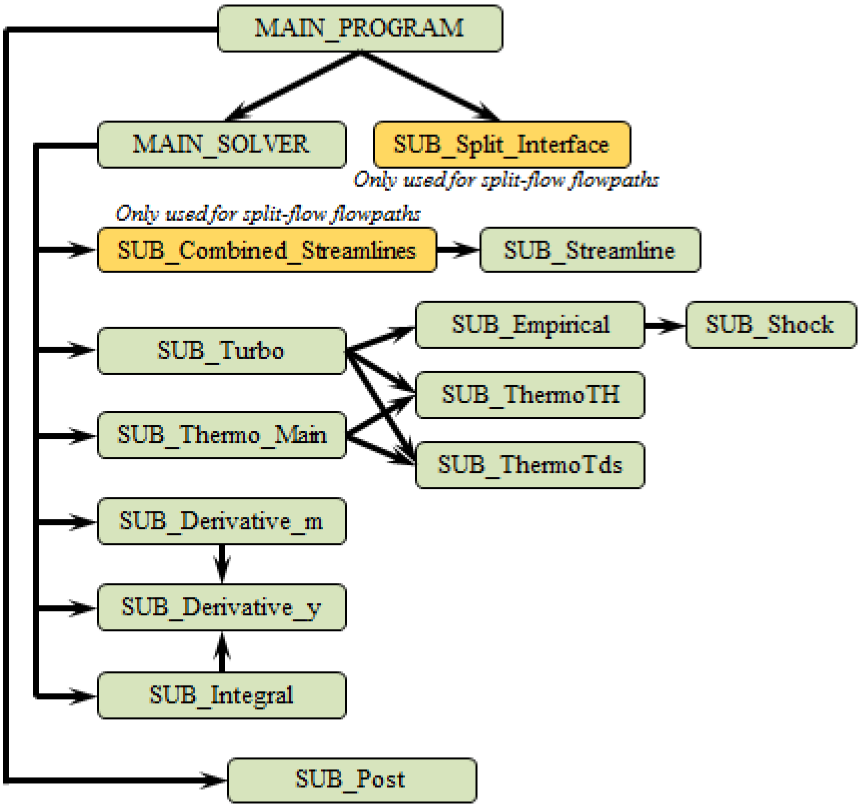

Figure 34. Structure of the code

In the subroutine “SUB_Split_Interface”, once a fan domain solution using the MAIN_SOLVER routine is completed, flow variables at the exit are transmitted to the by-pass and core domains as the inlet conditions, again to be used in the “MAIN_SOLVER”. The duty of “SUB_Split_Interface” is to accomplish this transmission each time a fan domain solution is finished. “SUB_Split_Interface” is disabled if split-flow capability is disabled.

The duty of “SUB_Combined_Streamlines” is to convert the separate streamlines of fan, by-pass and core domains into combined streamlines as upper (fan upper region and by-pass) and lower (fan root and core) streamlines (see Figure 33). Splitter upper and lower surface are also added to those two sets, respectively. Those are then sequentially inputted to “SUB_Streamlines” subroutine, which calculates local streamline slopes and curvatures for a single stream domain (such as fan, by-pass and core; or upper and lower combined streamlines). Once the local slopes and curvatures of the combined upper and lower streamlines are calculated, they are re-distributed to the nodes of fan, by-pass and core domains to be used in fan, by-pass and core solutions (performed in “MAIN_SOLVER”), respectively.

“SUB_Combined_Streamlines” is disabled if the split flow capability is disabled. Then, “SUB_Streamlines” is directly used to calculate local slope and curvatures.

“Sub_Turbo” is the subroutine that imports from the “MAIN_SOLVER” the absolute flow properties at inlet and outlet of each airfoil section belonging to rotors and stators. Those absolute quantities are then converted blade-relative quantities. It then calculates the change of state across the airfoil passage being investigated (see Section 3.2), such as blade discharge absolute total temperature, total enthalpy, entropy, total pressure and outputs of the empirical models (using “SUB_Empirical” and “SUB_Shock”) to the through-flow solver (MAIN_SOLVER).

“SUB_Thermo” subroutine is the main thermodynamic state subroutine. It calculates physical quantities, including static quantities, from total quantities and velocity. “SUB_ThermoTH” is a subroutine of “SUB_Thermo” and calculates unknown temperature from a known temperature and enthalpy change without assuming specific heat is constant. Instead, temperature-dependent specific heat is assumed. “SUB_ThermoTds” is also a subroutine of “SUB_Thermo” and calculates unknown pressure from a known pressure and temperature change via isentropic and ideal compressible flow relations.

The subroutine “SUB_Derivative_y” and “SUB_Derivative_m” are used to obtain derivative of a quantity along y (quasi-orthogonal) or m (streamwise) directions by using finite difference method. “SUB_Integral” is used to obtain integral of a quantity along y (quasi-orthogonal) direction.

CHAPTER 5

VALIDATION OF THE COMPLETE METHODOLOGY

5.1. Validation with 2D CFD on Split-Flow Ducts without Blades

The proposed method of solution for axisymmetric duct with splitter of any geometry, without a turbomachinery, is compared with finite volume method of solutions for the same common geometries for validation purposes. High, medium and low by-pass ratio cases are investigated to cover wide range of by-pass ratios. Only the inviscid approximation is considered for the benchmark finite volume method of solution (SLC is already inviscid). This is because flow is essentially three-dimensional when turbomachinery is present and those 3D viscous effects cannot be modeled by a viscous 2D model. Instead, as discussed in the literature review section, 3D viscosity effects are imposed to the inviscid 2D solution by means of external loss models or data based on engine component rig tests (circumferentially averaged entropy increase and total pressure loss). In this regard, this section aims to validate the inviscid SLC solver itself in representative flowpaths, isolated from any turbomachine effects.

The utilized finite volume solver is one of the most widely-used commercial software: Fluent© CFD package. The theory of finite volume CFD method is not given here as it is highly comprehensive and not in scope of this study. Readers are referred to books on CFD for details, such as [85] or the theory guide of Fluent©. Although no comparison with experimental data is presented for pure duct solution (no blades), the comparison is believed to be meaningful and will serve as a validation for the solver because a finite volume code that is validated against many generic cases [86] and what is more all viscous and turbulence models are disabled is expected to be quite reliable if mesh in-dependency is satisfied and artificial viscosity due to numerical errors are minimized (and its effects are analyzed). Moreover, further experimental and 3D Navier-Stokes based validations of the next chapters, which additionally consider blades and empirical models, will support the results outlined in this chapter.

5.1.1. High By-Pass Ratio Case

The first case investigated is the high by-pass ratio case, which is a geometry that has a design (flow aligned with the flowpath splitter) by-pass ratio of 6.5. To ensure that it is applicable to a real engine flowpath, it is made similar to a typical civil turbofan engine compression system gaspath with almost uniform inlet and outlet flows (excluding intake, combustor diffuser or exhaust nozzle geometries): part of fan flowpath (domain upstream of the splitter), part of by-pass duct (the upper flowpath downstream of the splitter) and part of the core engine duct (the bottom flowpath downstream of the splitter). However, compared to a real engine flowpath, wall curvatures and flowpath ramp angles are intentionally designed aggressive (very high) (channel height over max radius of curvature is roughly 2.4 and ramp angle is roughly ~45deg) to test the real capability of the SLC solver by generating both streamwise and spanwise sharp pressure gradients. In addition to the test-case geometry, the domain must be extended at the inlet and outlets to reduce numerical errors and uncertainty in distributions of boundary conditions. Those are called dummy inlets or outlets, and are generated conservatively (longer) based on the study in APPENDIX C. They do not correspond to intake, combustor diffuser or exhaust; they are just to eliminate numerical errors that may occur at inlets and outlets. The term '*real geometry*' is used in this section to distinguish the test case geometry from dummy extensions. The high by-pass ratio case computational domain, with dummy extensions, is presented in Figure 35. It is constructed by flowpath control points, which define four cubic splines that pass from those points; one for tip, one for hub and one for splitter upper and bottom surfaces. The sharp corner at the stagnation point, denoted in Figure 35 by '*intended geometry*', is smoothed for simplification. SLC or finite volume mesh of any size can be generated on the computational domain, enclosed by those four splines and inlet and outlet.

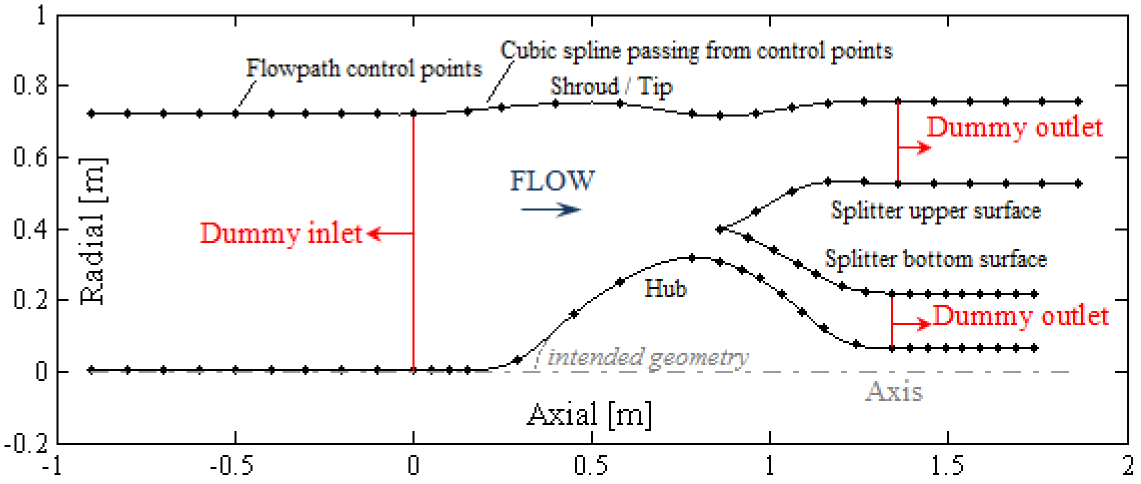

Figure 35. The computational domain of the high by-pass ratio case

Boundary conditions for the case are presented in Table 1. The by-pass and core ducts exit pressure values are outputs of SLC solution as a function of (apart from inlet total pressure and temperature) specified mass flow rate, when the meridional flow is subsonic. Therefore the current values that are shown in the table are obtained from the SLC solution. This is contrary to finite volume solutions, where exit pressure is specified and mass flow rate is obtained as an output. Therefore, in order to perform a comparison, the SLC-obtained exit static pressure values for the both ducts are specified to the finite volume solver to carry out computations. In all these computations, the resultant mass flow rate of finite volume solutions must be the same as the mass flow specified to SLC solutions. The utilized SLC mesh is presented in Figure 36, where 32, 24 and 25 quasi-orthogonals are used for fan, by-pass and core domains, respectively. 60 streamlines are used at the fan domain. Once convergence is reached, 38 of them split to the by-pass duct and the remaining 22 splits to the core duct. These are based on the mesh independency study of APPENDIX D.

Table 1. Boundary conditions for the case

Inlet total pressure [Pa]	Inlet total temperature [K]	Total mass flow rate [kg/s]	By-pass duct exit static pressure [Pa]	Core duct exit static pressure [Pa]
101325	288.15	200	84092	82578

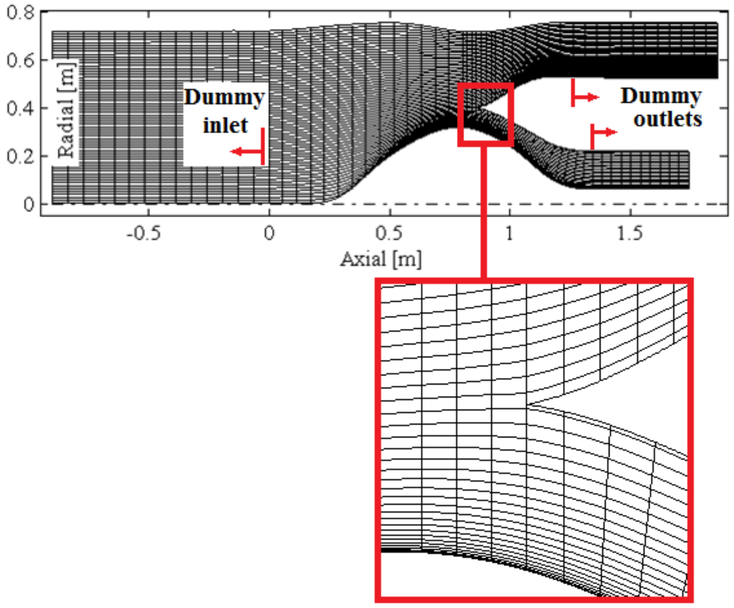

Figure 36. The SLC mesh

The corresponding finite volume mesh consists of approximately 1.1 million structured quadrilateral volumes. Grid edge divisions are shown in Figure 37, together with a representative sectional view of the mesh near the splitter edge. The complete view of the mesh is not shown due to poor visibility for such a highly dense mesh. As shown in the figure, there are 875 divisions in spanwise (~radial) direction in the domain upstream of the splitter. 625 of those separate to by-pass duct and the remaining 250 divisions separate to the core duct. In streamwise (~axial) direction, the domain upstream of the splitter (including dummy inlet) has 800 divisions and the downstream by-pass and core ducts have around 450 and 425 divisions, respectively. The mesh size is selected to satisfy mesh independence that also include minimization of artificial viscosity, which is discussed in APPENDIX E.

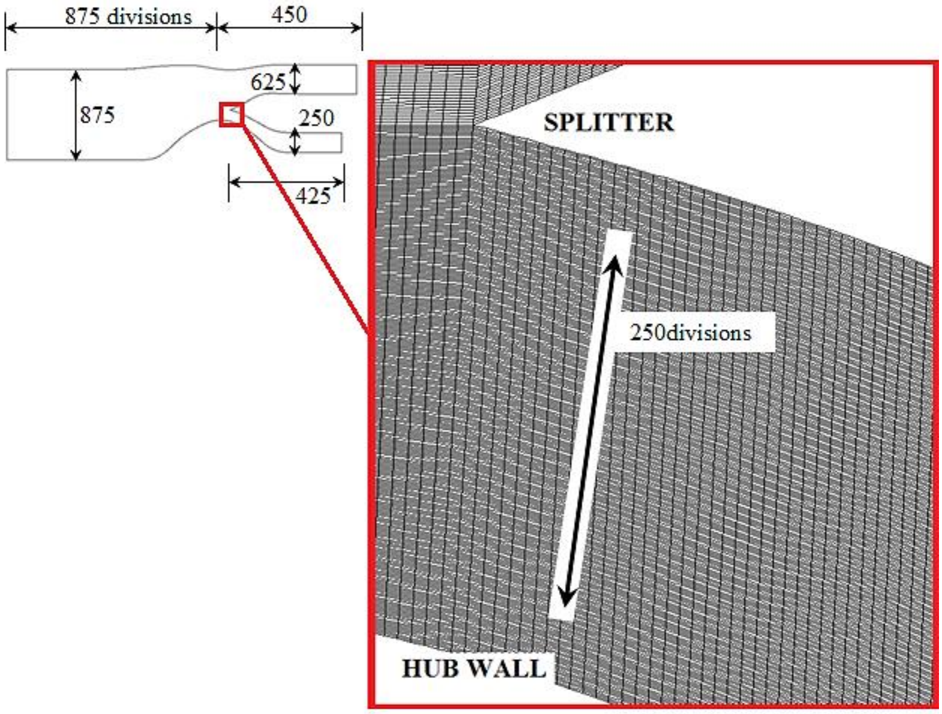

Figure 37. The finite volume grid edge divisions and a representative view

Based on the given boundary conditions, mass flow distribution to by-pass and core ducts is presented in Table 2. Very good agreement is observed in mass flow rates between SLC and finite volume solutions. The small differences are within accepted error band that is set during the mesh dependency study.

Comparison of wall pressures is presented in Figure 38, where both finite volume and SLC produce essentially the same output at all walls: hub, tip and splitter upper and lower surfaces. The local discrepancy observed near the leading edge of splitter (smaller axial positions of splitter upper and lower surfaces) is expected to be due to insufficient local mesh density, but it is assessed as within accepted tolerance band in the SLC mesh-dependency study (equal or less than 1% in velocity in worst region locally and much lower error in bulk domain). The comparison shows that SLC solver captures 2D flow features well.

Table 2. SLC-Fluent comparison of mass flow distributions

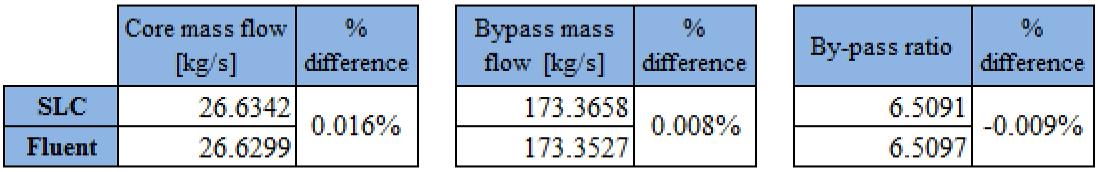

	Core mass flow [kg/s]	% difference
SLC	26.6342	0.016%
Fluent	26.6299	

Bypass mass flow [kg/s]	% difference
173.3658	0.008%
173.3527	

By-pass ratio	% difference
6.5091	-0.009%
6.5097	

Meridional (streamline) velocity radial profile comparisons along various surveys are also presented. There are 9 surveys in total. One is at the interface where flow divides into two. The interface intersects all the three ducts. The remaining 8 surveys are distributed to the ducts as flows: 3 in fan duct (upstream of splitter), 2 in by-pass duct and 3 in core duct. The survey locations are defined in Figure 39 and corresponding radial velocity profiles are presented in Figure 40 for survey 1, Figure 41 for survey 2, Figure 42 for survey 3, Figure 43 for survey 4(split interface), Figure 44 for survey 5, Figure 45 for survey 6, Figure 46 for survey 7, Figure 47 for survey 8 and Figure 48 for survey 9.

Results at the surveys show that both SLC and finite volume almost produce the same outputs. Especially, agreement in surveys 1, 2, 6 and 9 are excellent (much less than 1%). The local slight deviation near the splitter leading edge in surveys 3 (Figure 42) and 4 (Figure 43) can be attributed to combination of two reasons: more dominantly, artificial viscosity error of the finite volume model as discussed in APPENDIX E; and partly due to insufficient number of streamlines near splitter leading edge region. Artificial viscosity error distributions that are presented APPENDIX E for this specific case are roughly consistent with errors presented in the Figures. Therefore it should be the more dominant error source. Streamline density may also have smaller role due to splitter region resolution in Figure 43. The local discrepancies in surveys 5, 7 and 8 can also be attributed to aforementioned two error sources.

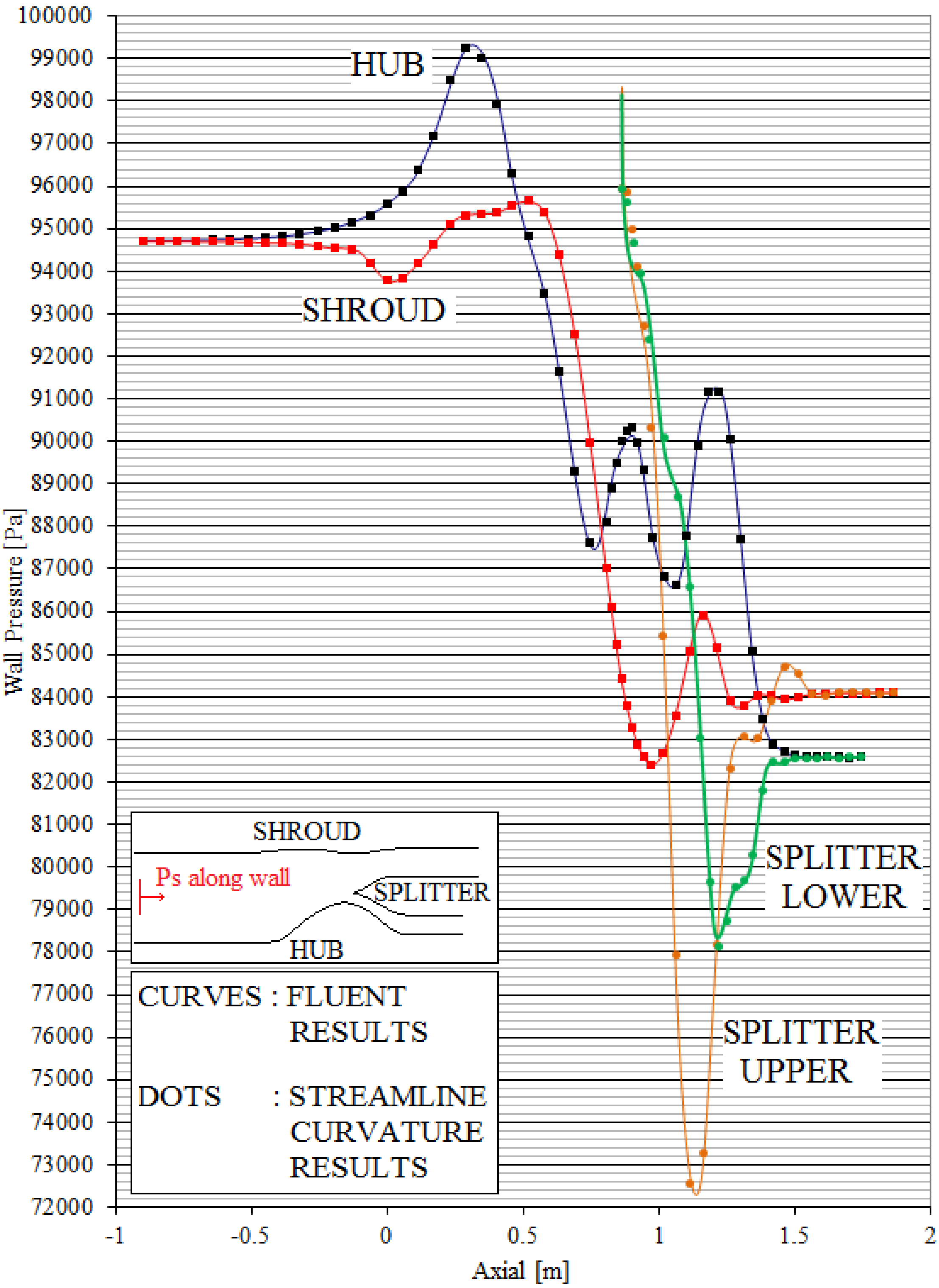

Figure 38. SLC-Fluent comparison of wall pressures

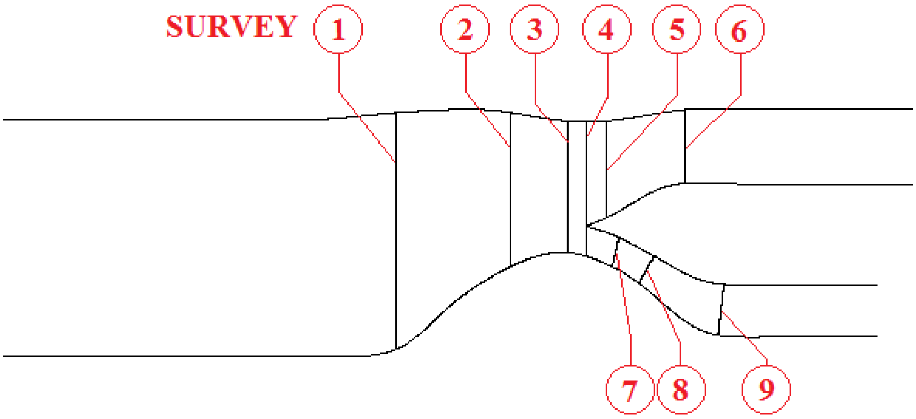

Figure 39. Survey locations for the comparisons

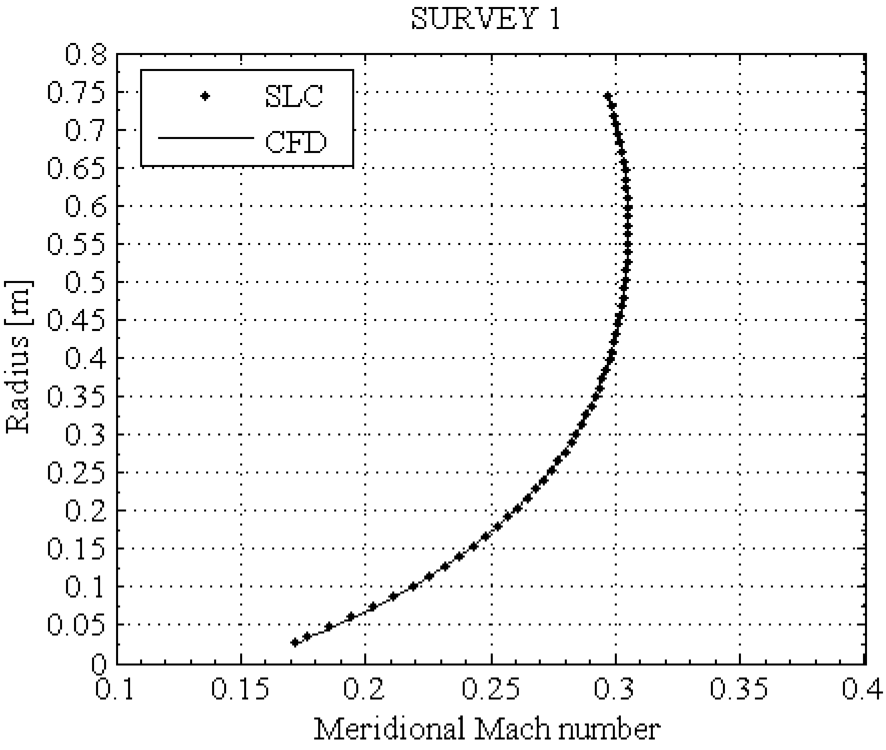

Figure 40. Radial meridional Mach distribution at survey 1

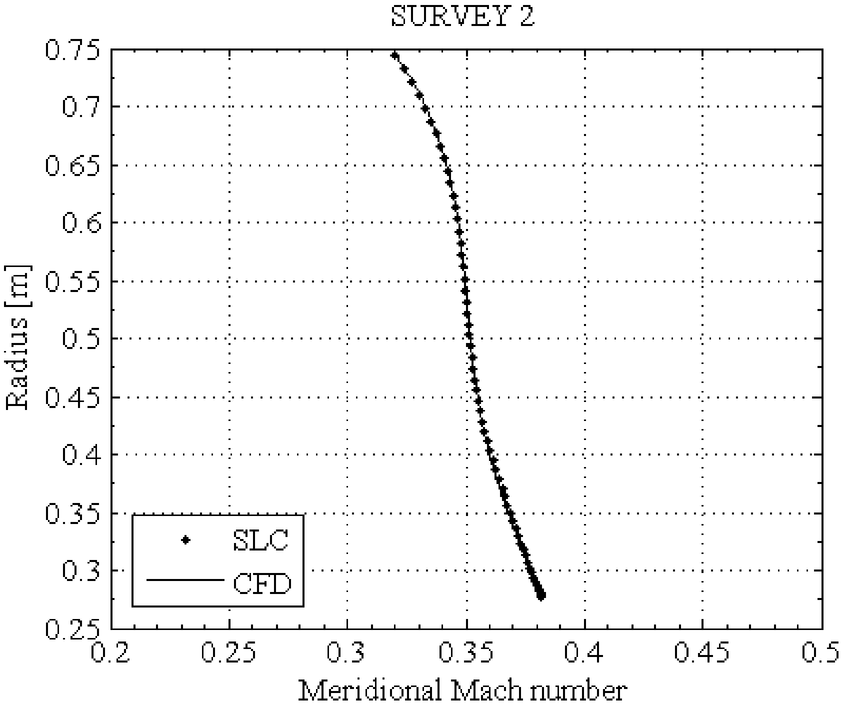

Figure 41. Radial meridional Mach distribution at survey 2

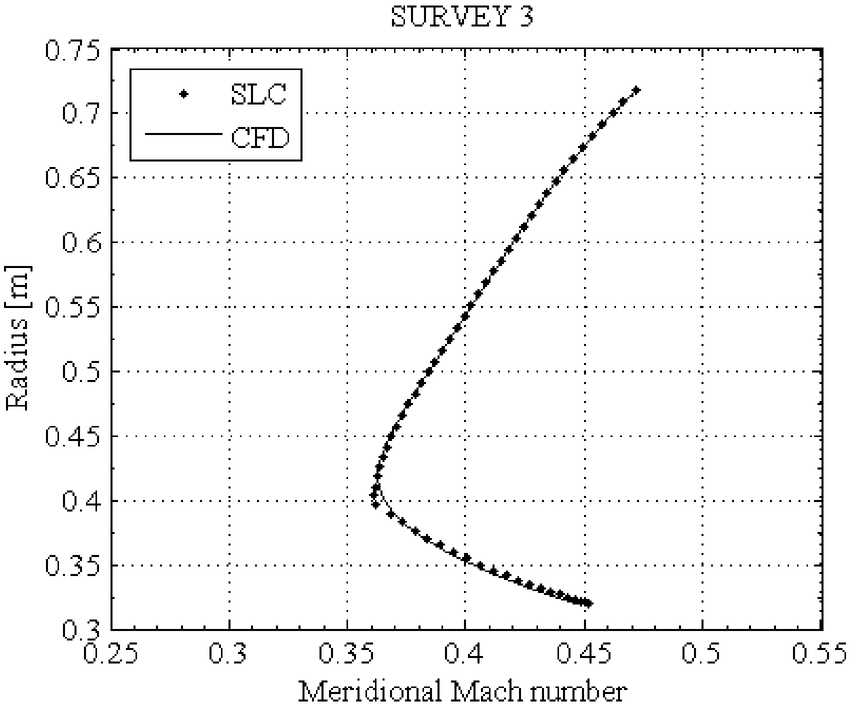

Figure 42. Radial meridional Mach distribution at survey 3

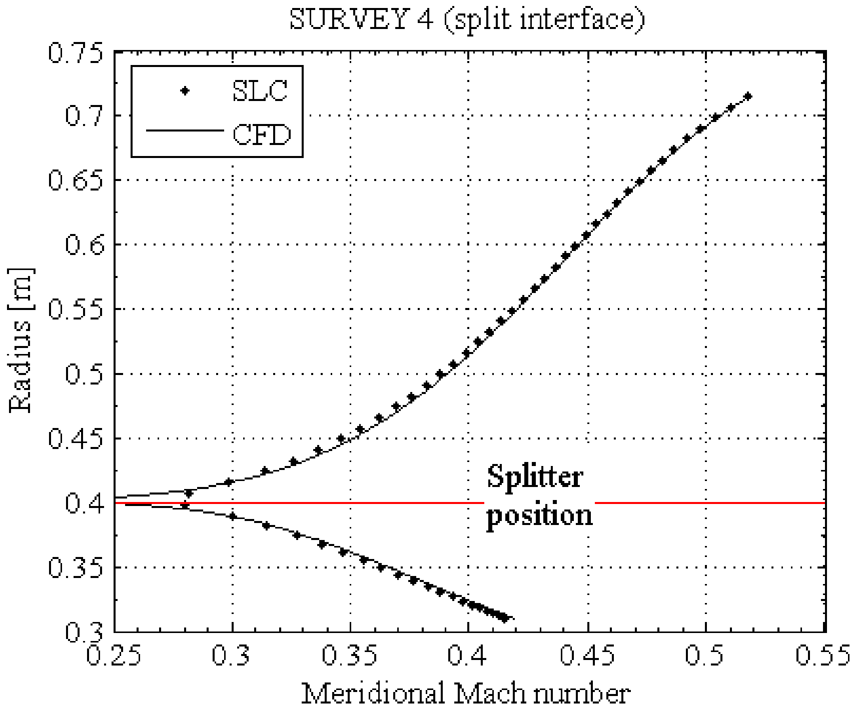

Figure 43. Radial meridional Mach distribution at survey 4

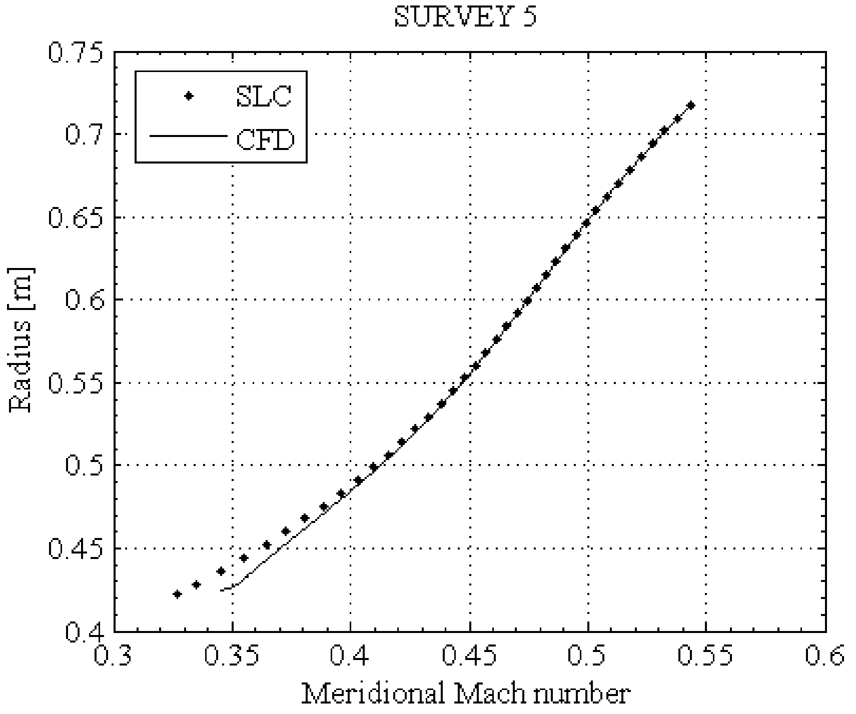

Figure 44. Radial meridional Mach distribution at survey 5

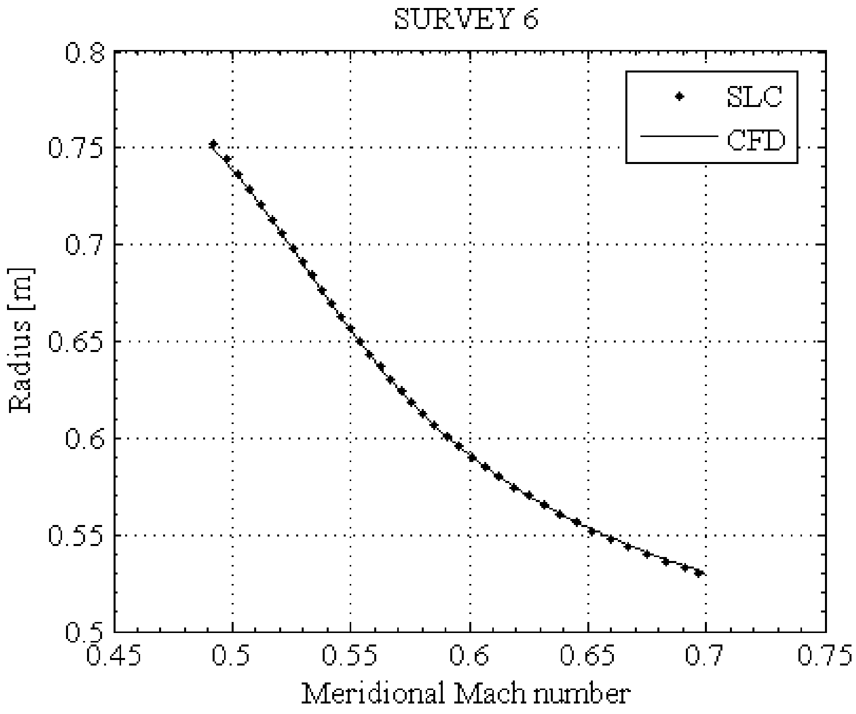

Figure 45. Radial meridional Mach distribution at survey 6

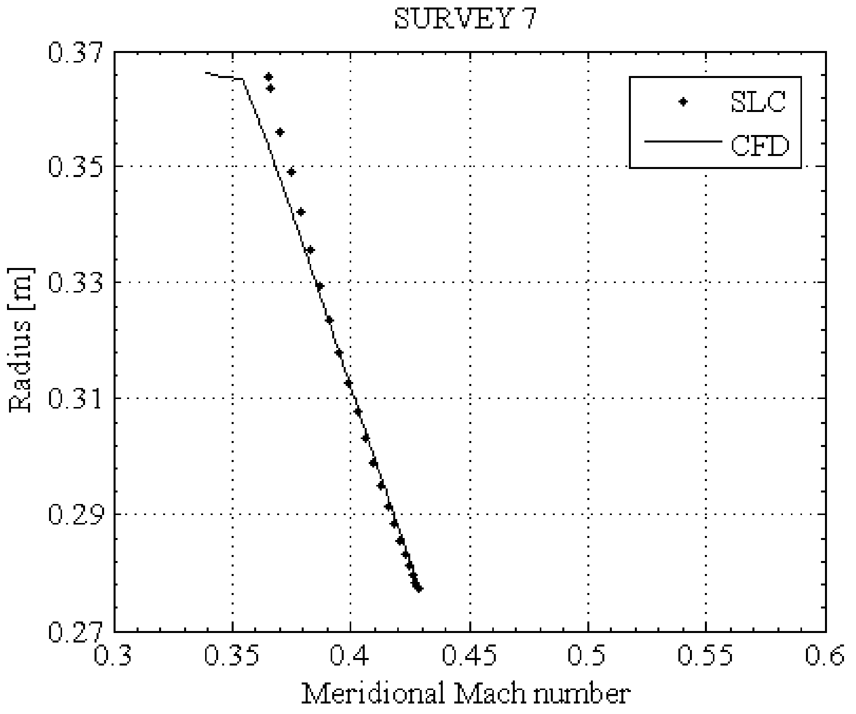

Figure 46. Radial meridional Mach distribution at survey 7

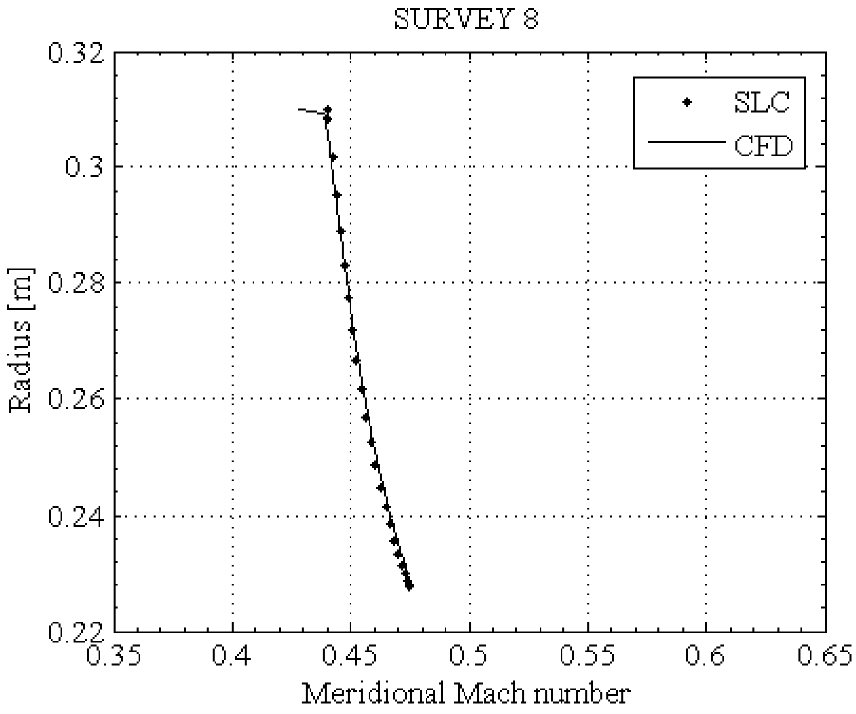

Figure 47. Radial meridional Mach distribution at survey 8

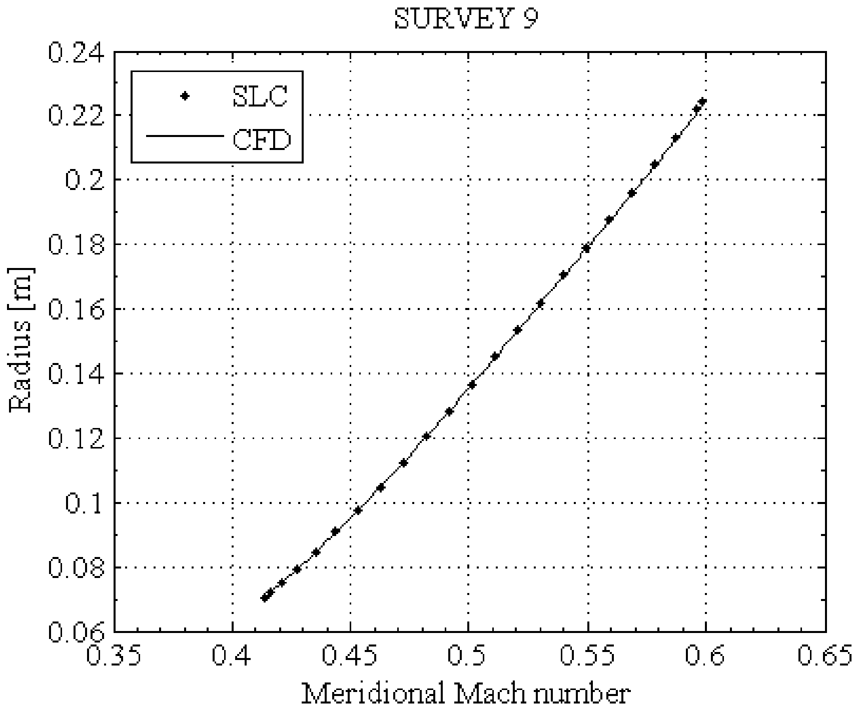

Figure 48. Radial meridional Mach distribution at survey 9

5.1.2. Low and Medium By-Pass Ratio Cases

The low and medium by-pass ratio models, together with mesh-independent SLC meshes, are presented in Figure 49 and Figure 50, respectively. These are essentially the same geometries except that the medium by-pass ratio model is generated by radially shifting the splitter inwards and the splitter bottom surface is slightly modified. Similar to the high by-pass ratio case, the models are arbitrarily generated and no design iterations are made, but similar criteria are observed. The corresponding finite volume grids are generated in a similar manner to that of the high by-pass ratio model. Utilized boundary conditions for the two cases are given in Table 3.

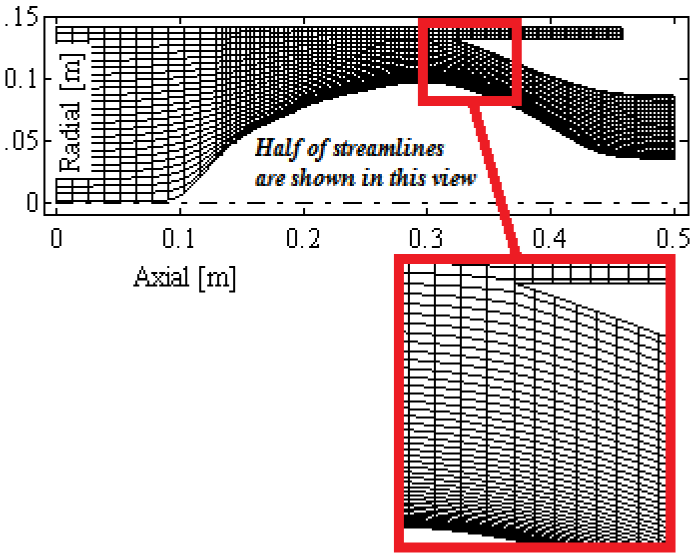

Figure 49. Low by-pass case and the SLC mesh

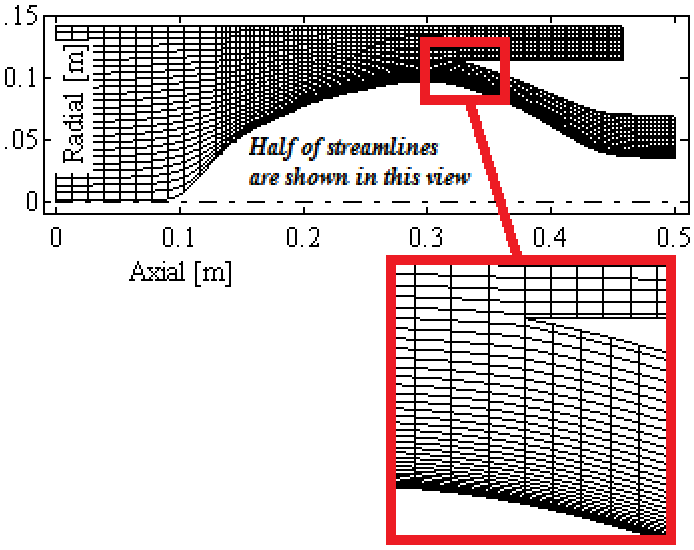

Figure 50. Medium by-pass case and the SLC mesh

Mass flow distributions for the two cases are presented in Table 4. As applied in the previous case, the finite volume models use SLC-predicted exit static pressures (as a function of inlet mass flow rate). Both the SLC and the finite volume models produce the same by-pass and core mass flows, therefore the same by-pass ratio. More detailed results in terms of wall static pressure axial distributions of hub, shroud and splitter surfaces are also given in Figure 52 and Figure 53 for the both cases. Again, very good agreement is observed.

Table 3. The boundary conditions

Low by-pass ratio case				
Inlet total pressure [Pa]	Inlet total temperature [K]	Total mass flow rate [kg/s]	By-pass duct exit static pressure [Pa]	Core duct exit static pressure [Pa]
101325	288.15	5.3	93662	75383
Medium by-pass ratio case				
Inlet total pressure [Pa]	Inlet total temperature [K]	Total mass flow rate [kg/s]	By-pass duct exit static pressure [Pa]	Core duct exit static pressure [Pa]
101325	288.15	5.3	91141	85365

Table 4. The global results

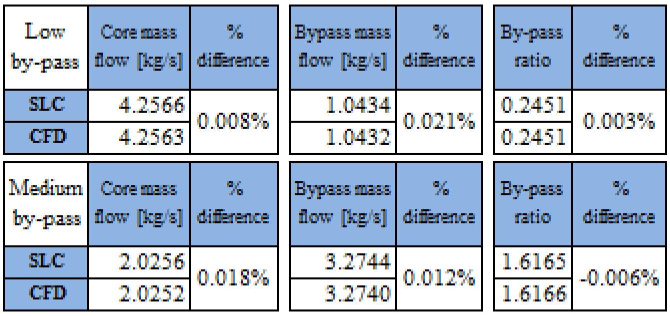

Low by-pass	Core mass flow [kg/s]	% difference	Bypass mass flow [kg/s]	% difference	By-pass ratio	% difference
SLC	4.2566	0.008%	1.0434	0.021%	0.2451	0.003%
CFD	4.2563		1.0432		0.2451	
Medium by-pass	Core mass flow [kg/s]	% difference	Bypass mass flow [kg/s]	% difference	By-pass ratio	% difference
SLC	2.0256	0.018%	3.2744	0.012%	1.6165	-0.006%
CFD	2.0252		3.2740		1.6166	

Finally, radial distributions of meridional Mach number at three surveys, defined by Figure 51, are compared with finite volume method in Figure 54 and Figure 55 for low and medium by-pass ratio cases, respectively. Very good agreement is observed for the both cases. The small artificial viscosity errors that are observed in the high by-pass ratio case are not repeated here, probably due to the flatter splitter geometry.

In conclusion, when isolated from the viscous effects, the methodology is capable of simulating these low and medium by-pass ratio cases.

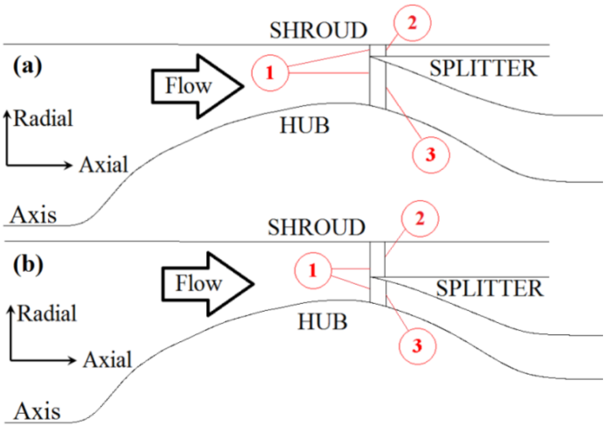

Figure 51. Survey locations for low (a) and medium (b) by-pass cases

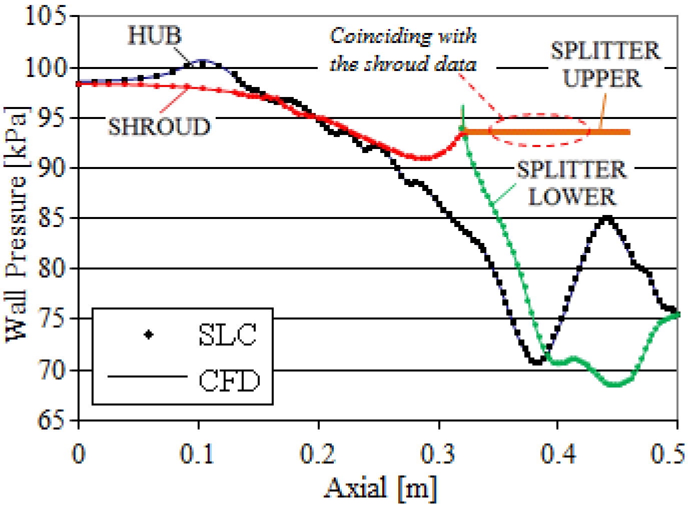

Figure 52. Wall pressure comparisons for the low by-pass ratio case

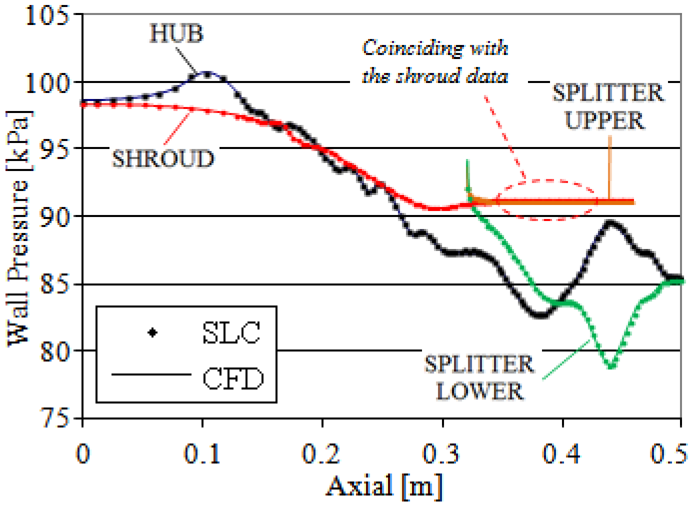

Figure 53. Wall pressure comparisons for the medium by-pass ratio case

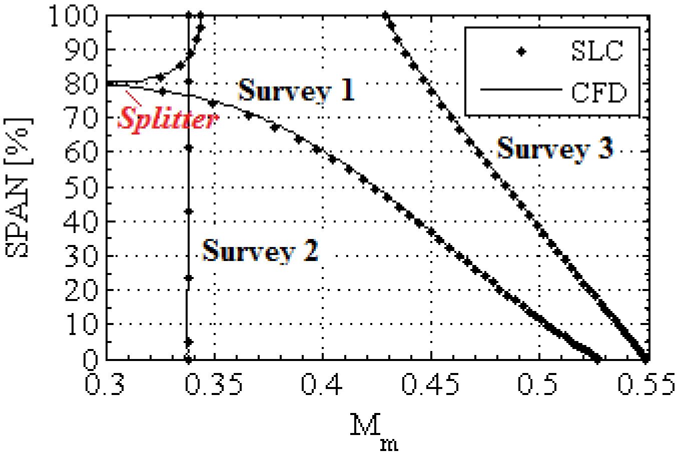

Figure 54. Comparison of M_m profiles for the low by-pass ratio case

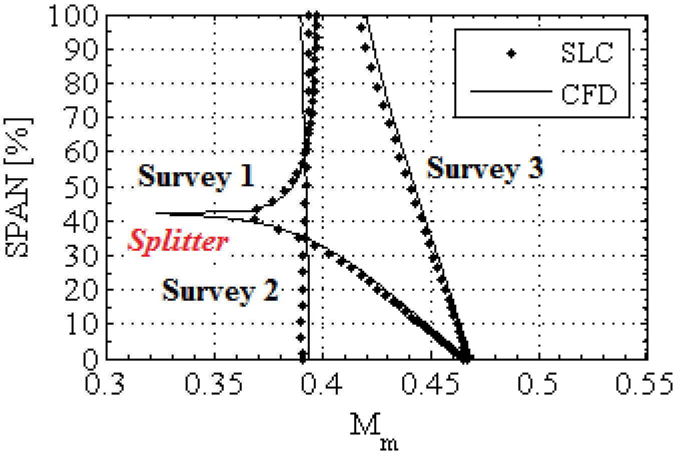

Figure 55. Comparison of M_m profiles for the medium by-pass ratio case

5.2. Experimental 3D Validation with NASA 2-Stage Fan

This section presents validation of the code with NASA 2-stage (single-stream or compressor-like) fan with wide-chord 1st stage rotor, reported in reference [87]. It is the aim of this section to experimentally validate the compressor mode of the code (without the proposed split-flow method). This includes validation and calibration of the compiled empirical models of Section 3.4.1, which will then also be valid for a split-flow fan with similar parameter ranges (i.e. the by-pass fan of Section 5.4). It should be noted that the calibration not only considers the NASA 2-stage fan of this sub-section but also the single-stage fan of Section 5.3. Therefore it is common with both these test cases such that both have satisfactory results. Then, the complete methodology is tested on GE-NASA by-pass fan of Section 5.4, without any modification in the calibration.

Even there is no split-flow, the validation and calibration with NASA 2-stage fan (and also the custom-designed compressor stage test case of the next section) serves as an experimental support for the previous section by showing that the code works properly for a compressor solution.

Only the peak-efficiency data at 100% design speed is considered as it is approximately coinciding with the intended design point. The main parameters are given in Table 5. The meridional view of the fan is presented in Figure 56 and the computational grid with meridional Mach number contour is presented in Figure 57. The 1st stage rotor and tip sections of the 2nd stage rotor are made of multiple-circular-arc (MCA) profiles, where maximum thickness locations are shifted rearwards to reduce supersonic expansion. Lower sections of 2nd stage rotor and stators are made of DCA profiles.

Table 5. Main peak efficiency parameters of the NASA 2-stage fan

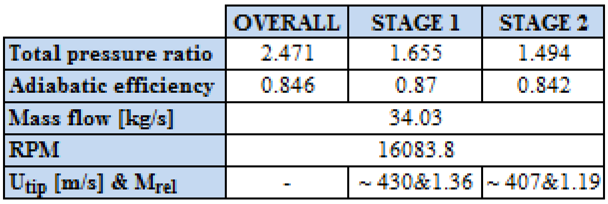

	OVERALL	STAGE 1	STAGE 2
Total pressure ratio	2.471	1.655	1.494
Adiabatic efficiency	0.846	0.87	0.842
Mass flow [kg/s]	34.03		
RPM	16083.8		
U_{tip} [m/s] & M_{rel}	-	~ 430&1.36	~ 407&1.19

Boundary conditions given are mass flow rate and spanwise distributions of total pressure, temperature and swirl (although minor) at the inlet; and absolute swirl velocity spanwise distributions at the exit of each row. Those data is supplied at spanwise locations 5, 10, 20…80, 90, 95%, therefore cubic splines are used for interpolation and extrapolation along the span. Measurement uncertainties are reported to be ±0.3kg/s in mass flow rate, ±30 in rpm, $\pm 1^{o}$ in flow angle, ±0.6K in temperature and ±0.7-1.7kPa in total pressure. The confidence level and uncertainties due to data reduction method (a SLC code) are not reported. Area blockage coefficients, treated as a function of axial distance, are also specified based on a prior design report for the same machine except having high-aspect 1st stage rotor [88].

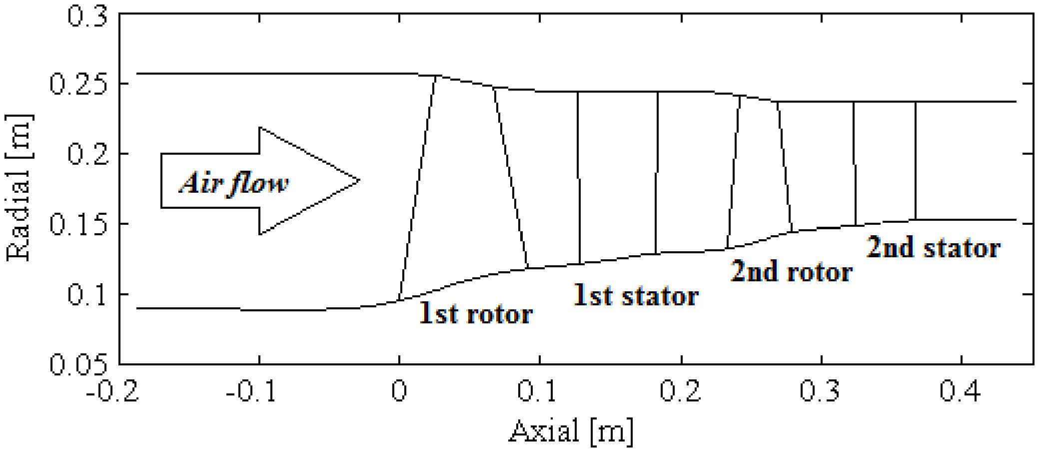

Figure 56. Meridional view of NASA 2-stage fan

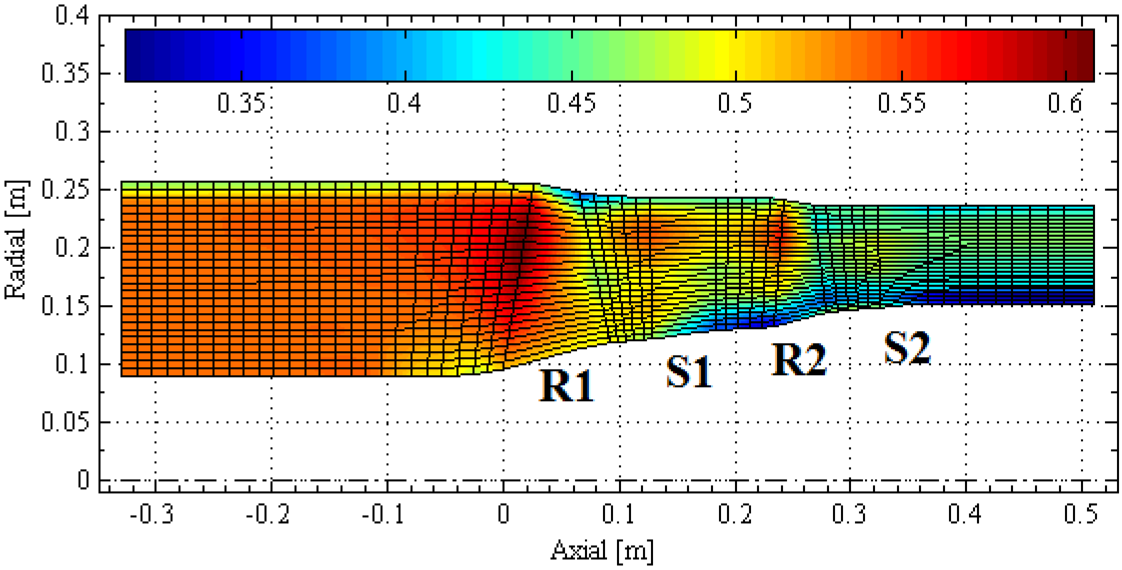

Figure 57. Utilized SLC grid and meridional Mach number contour

Before presenting the results with empirical incidence, loss, deviation and blockage models; the results with specified test-based pressure loss coefficients are presented in the following sub-section to ensure validity of the solver and turbomachinery equations. In the next sub-section, the loss coefficients will no longer be specified and instead they will be calculated from the empirical models.

5.2.1. Results with Test-Specified Pressure Loss Coefficients

Comparisons of SLC outputs with test data are presented in Figure 58 through Figure 67, showing radial distributions of total pressure ratios at all rows and leading/trailing edge meridional velocities of rotors and stators of both stages. The agreement is very good and discrepancies seem to be acceptably small. Those can be attributed to errors mainly due to interpolation/extrapolation, lack of inter-blade QOs and treatment of blockage as 1D (especially the discrepancy in Figure 58). In summary, those results indicate that the developed SLC code is a valid tool to model compressors and it is also suitable for data processing of experimental data.

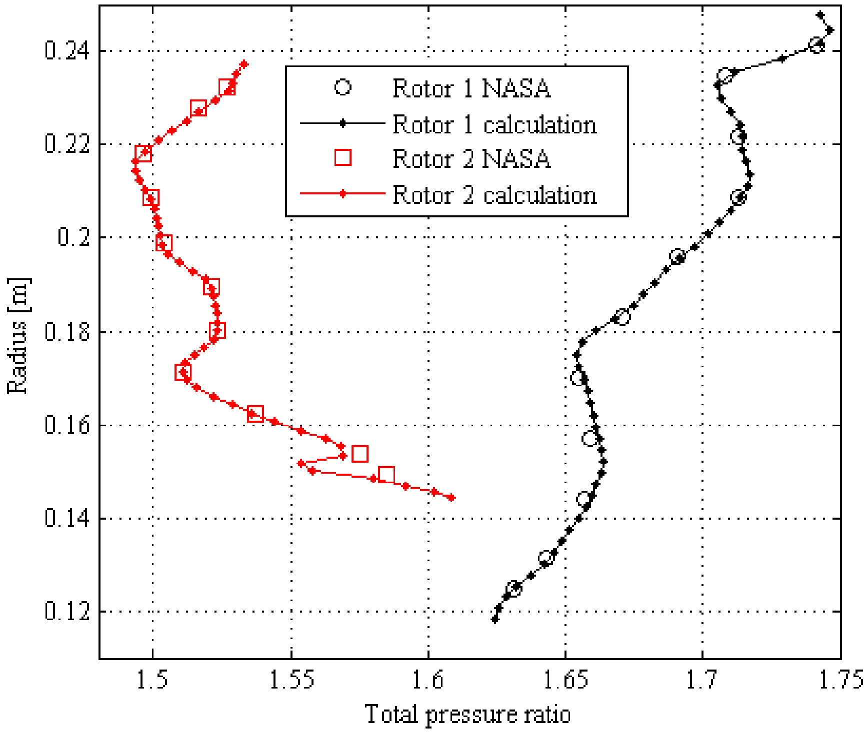

Figure 58. Total pressure ratio profiles of rotor 1 and rotor 2

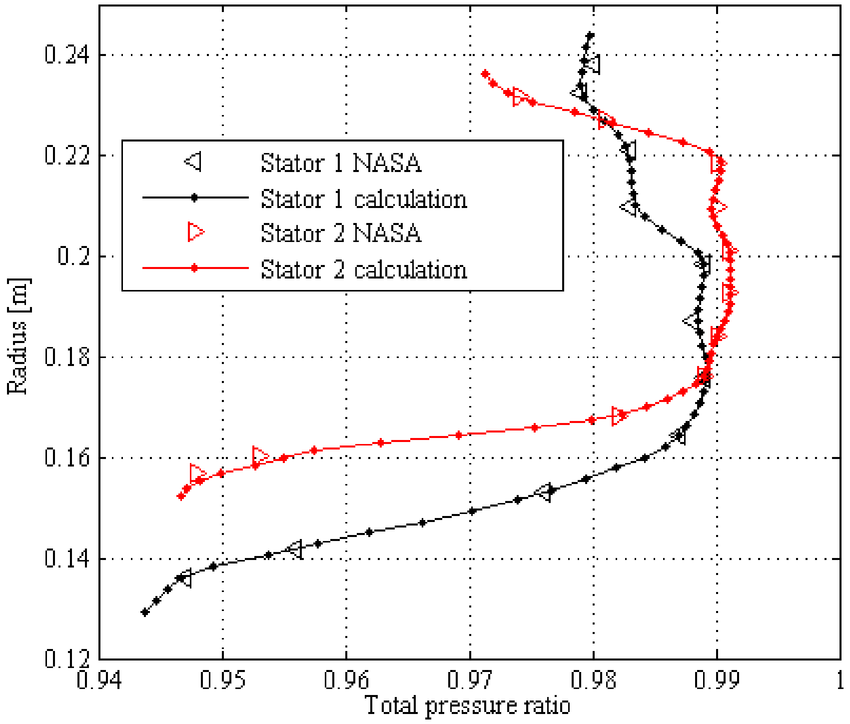

Figure 59. Total pressure profiles of stator 1 and stator 2

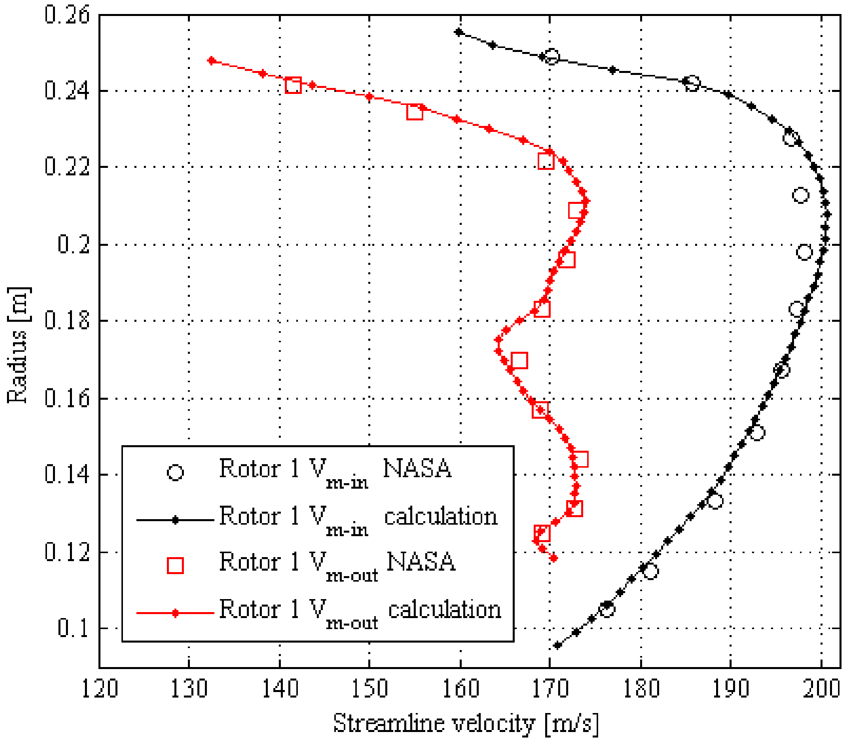

Figure 60. Rotor 1 inlet and outlet streamline velocity distributions

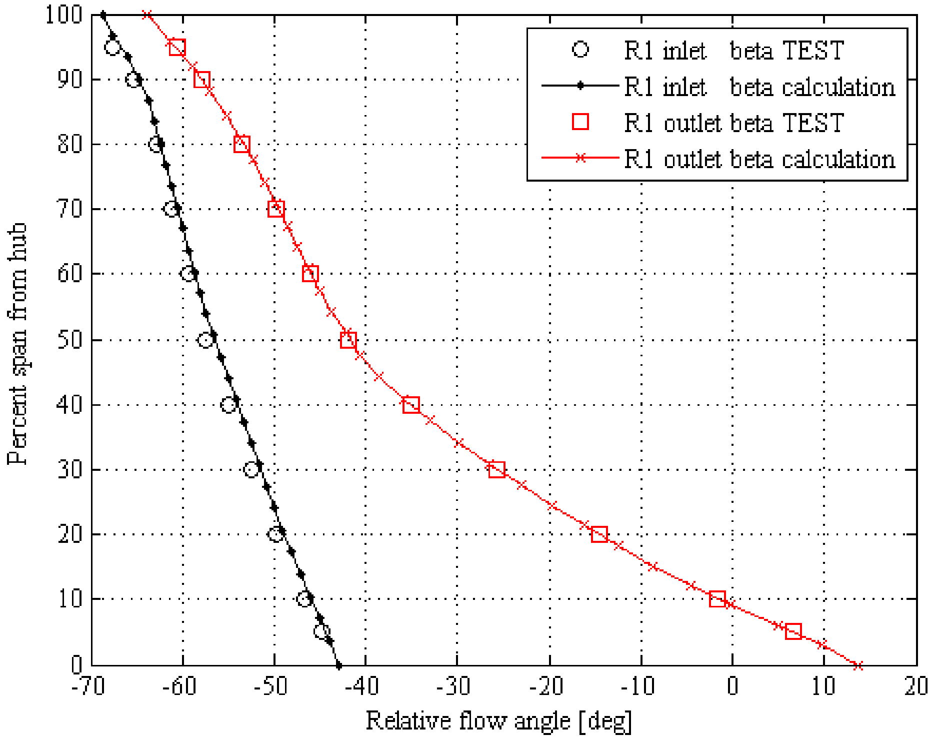

Figure 61. Rotor 1 inlet and outlet relative flow angle distributions

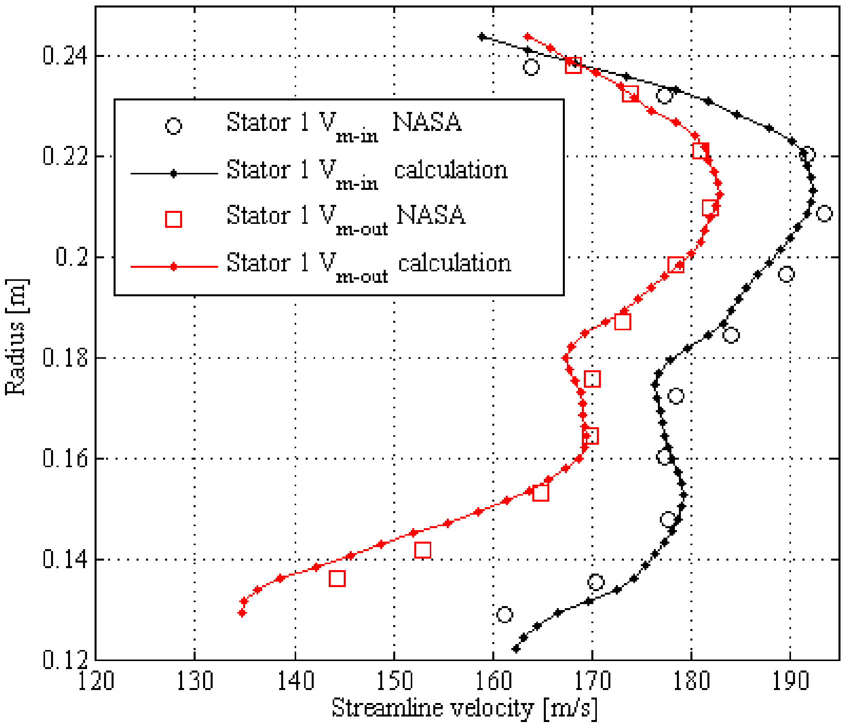

Figure 62. Stator 1 inlet and outlet streamline velocity distributions

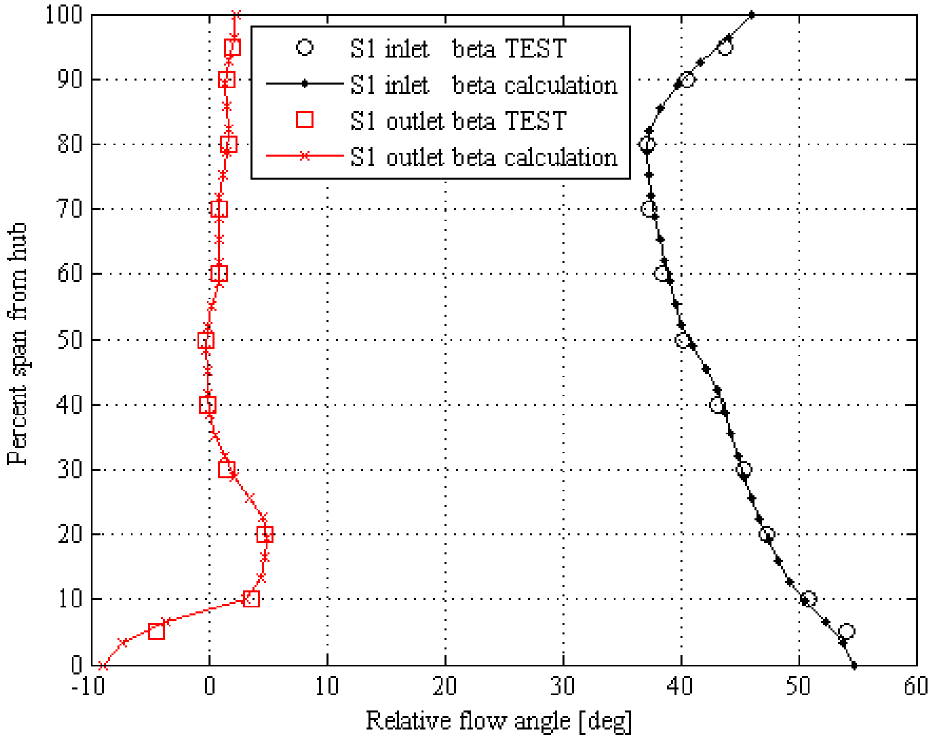

Figure 63. Stator 1 inlet and outlet relative flow angle distributions

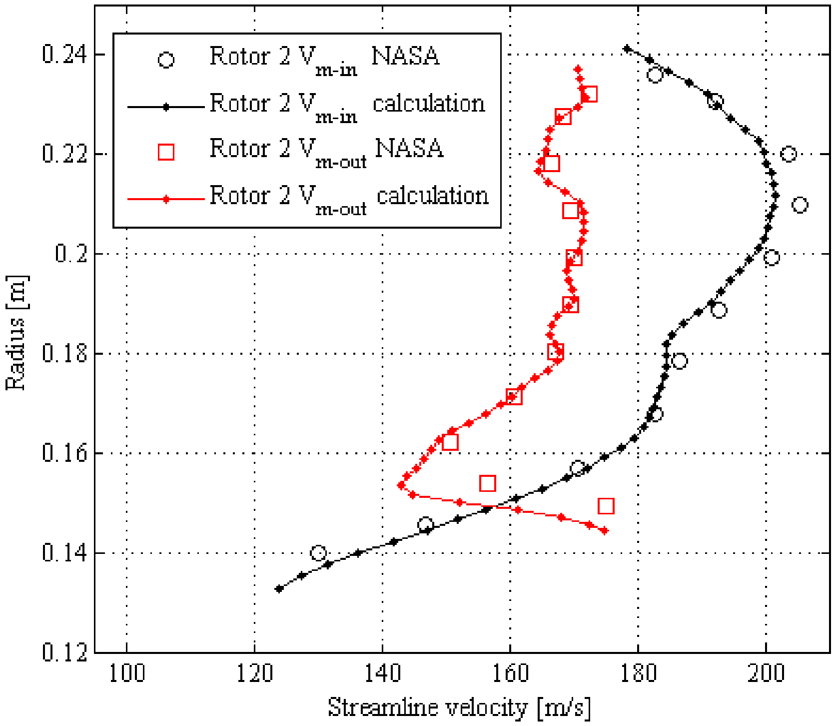

Figure 64. Rotor 2 inlet and outlet streamline velocity distributions

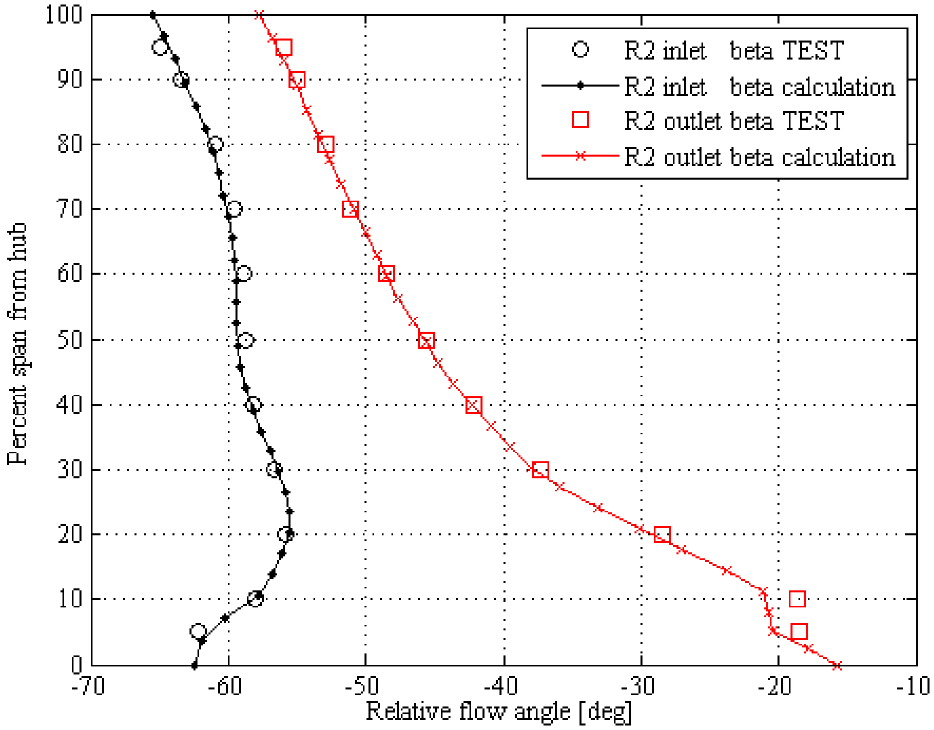

Figure 65. Rotor 2 inlet and outlet relative flow angle distributions

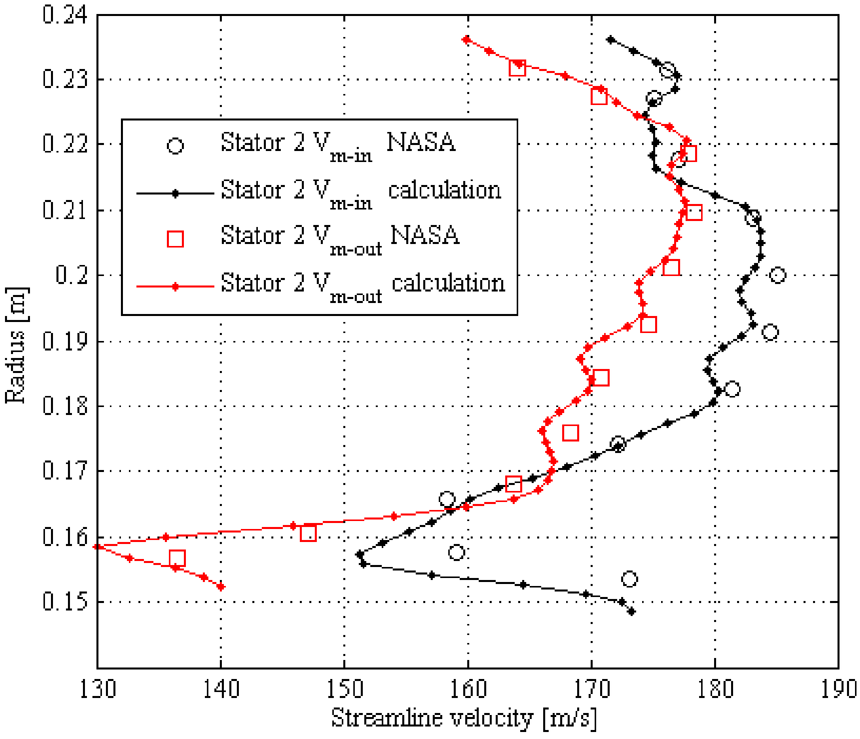

Figure 66. Stator 2 inlet and outlet streamline velocity distributions

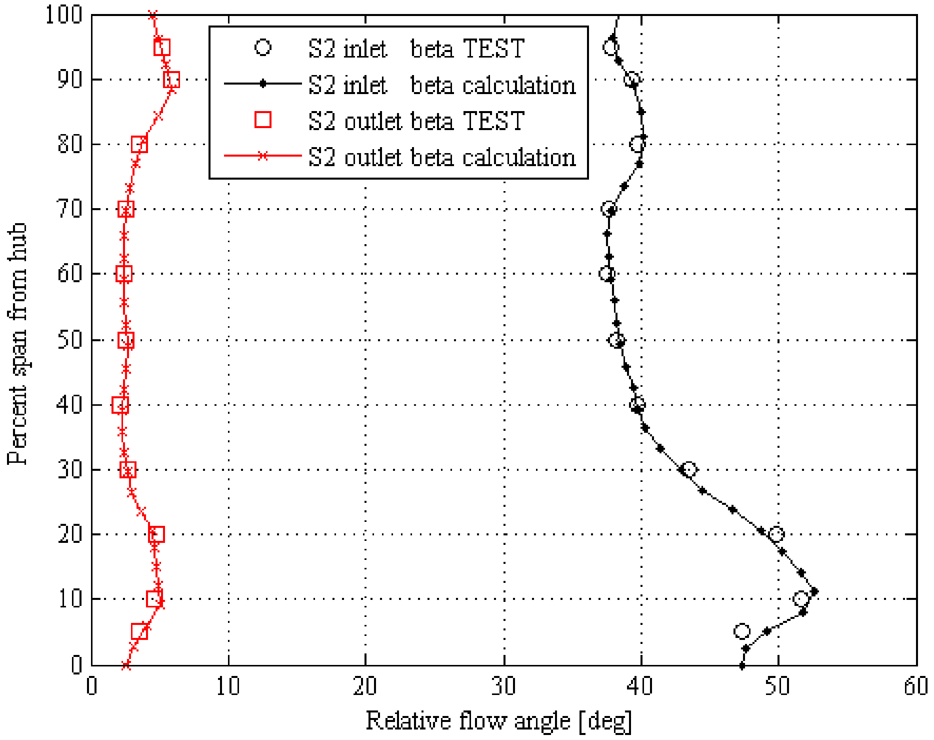

Figure 67. Stator 2 inlet and outlet relative flow angle distributions

5.2.2. Results with the Empirical Models

In this section, the empirical models of section 3.4.1 are activated to obtain the loss coefficients and minimum loss incidence and deviation angles. Off-design models are also used to correct the loss coefficients. Advanced geometry information, i.e. the maximum camber locations of the first rotor (other blade rows have *a/c*=0.5), are also extracted from the test report [87], presented in Table 6, are taken into account in the models.

Comparisons of the overall results between SLC prediction and experiments are presented in Table 7, where good agreement is observed. Table 8 presents the errors in the predicted spanwise profiles. In this table, the mean error is calculated as the average of $100x((X_{SLC}\text{-}X_{test})^2)^{1/2}/\ X_{test}$, where "X" represents either of meridional velocity, exit relative flow angle or rotor pressure ratio. Therefore different signs do not eliminate each other. The standard deviations of the errors already consider the absolute values and different signs do not eliminate each other. Inner and outer 5% spans, where viscous effects are dominating and test data is not available, are excluded in these comparisons. A decent agreement is observed, considering the challenging nature of the test case due to higher-than-intended experimental mass flow rate and extreme stator loadings, where excessive turning is applied for the stators such that around 15 degree overturning is required to make flow axial at stator exits due to high deviation levels. This is expected to be rarely encountered in modern designs, because it causes strong secondary flow effects and stall margin to be around only 2 percent [87]. Hence, it is quite challenging for the empirical models to predict the losses in this compressor, especially in the rear stages, considering an error in an upstream blade row is directly translated to the downstream rows and the downstream rows have the biggest errors. In this regard, the observed errors are assessed as acceptable. Moreover, the flow angle distributions, which are the most important parameters in profile design, are not affected much by the errors in the meridional velocity distributions.

In addition to the above averaged errors, details of the spanwise profiles are presented in Figure 68 through Figure 77. Compared to the previous section, where loss coefficients are specified from the test data, as expected, the agreement is not as perfect. This shows the importance of loss models in prediction of compressor flow fields. Nevertheless, the predictions still seem highly satisfactory considering the approximate nature of the through flow modeling. Moreover, the estimation quality is on par with the ones obtained in the open literature [53]. The rather higher discrepancies near the end walls are expected since the flow is highly 3D in those regions.

Table 6. Maximum camber location data of the first rotor [87]

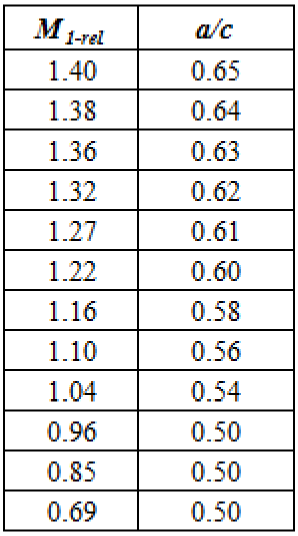

$M_{1\text{-}rel}$	a/c
1.40	0.65
1.38	0.64
1.36	0.63
1.32	0.62
1.27	0.61
1.22	0.60
1.16	0.58
1.10	0.56
1.04	0.54
0.96	0.50
0.85	0.50
0.69	0.50

Table 7. Comparisons of overall performances

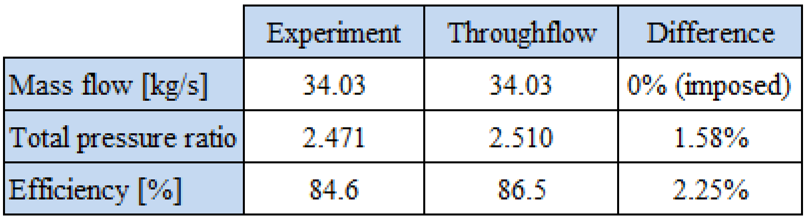

	Experiment	Throughflow	Difference
Mass flow [kg/s]	34.03	34.03	0% (imposed)
Total pressure ratio	2.471	2.510	1.58%
Efficiency [%]	84.6	86.5	2.25%

Table 8. Errors in spanwise profiles

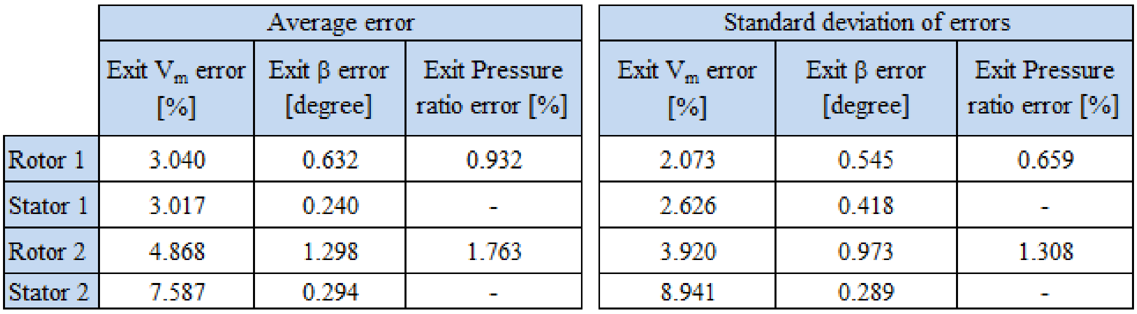

	Average error			Standard deviation of errors		
	Exit V_m error [%]	Exit β error [degree]	Exit Pressure ratio error [%]	Exit V_m error [%]	Exit β error [degree]	Exit Pressure ratio error [%]
Rotor 1	3.040	0.632	0.932	2.073	0.545	0.659
Stator 1	3.017	0.240	-	2.626	0.418	-
Rotor 2	4.868	1.298	1.763	3.920	0.973	1.308
Stator 2	7.587	0.294	-	8.941	0.289	-

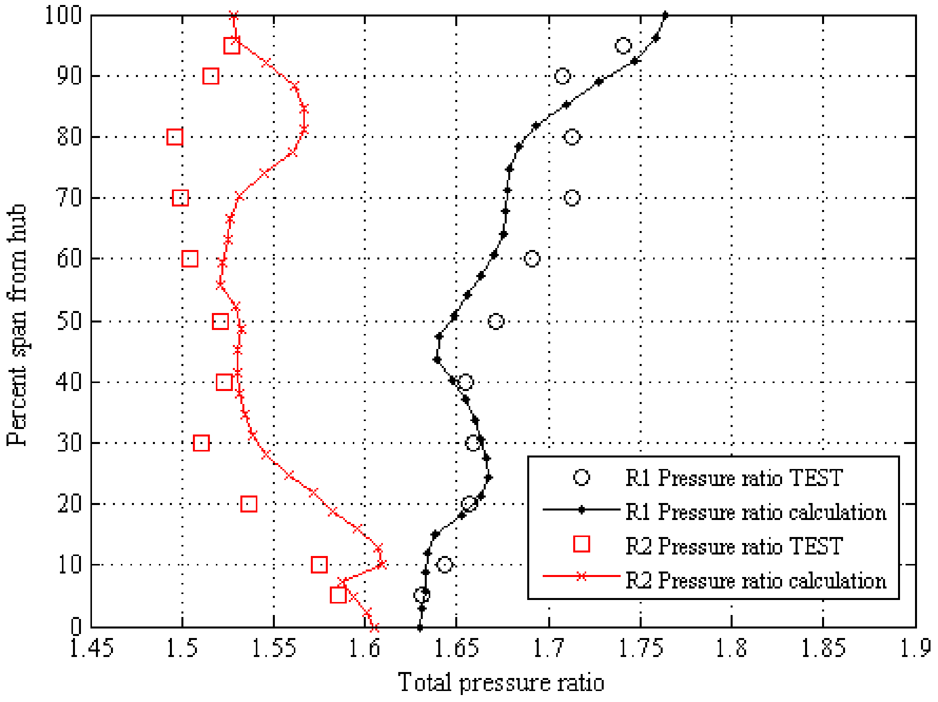

Figure 68. Rotor 1 and rotor 2 total pressure ratio distributions

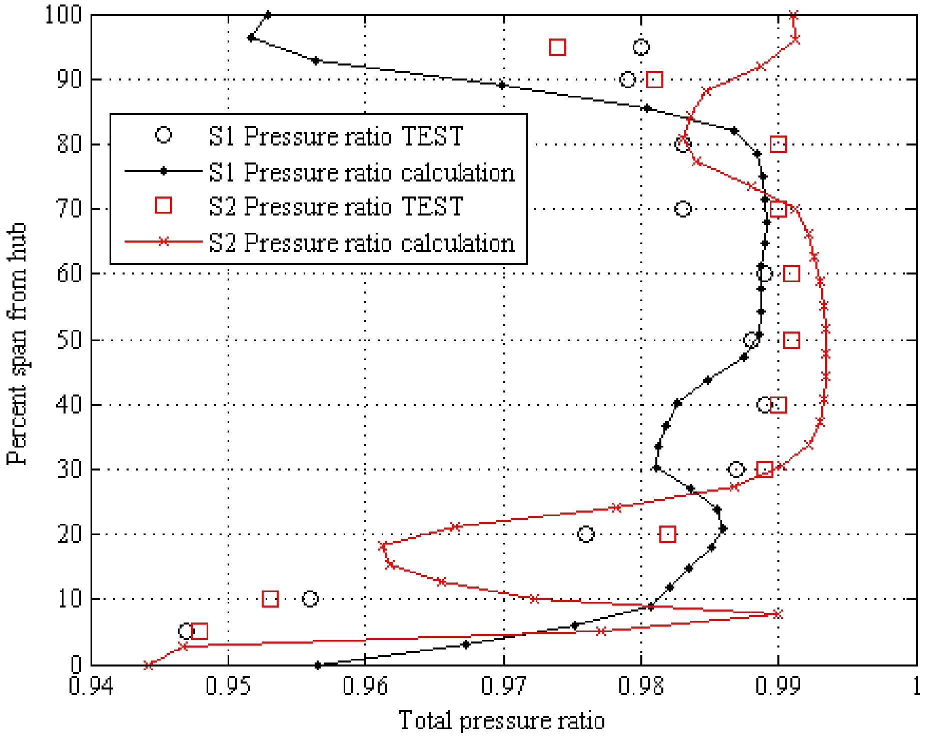

Figure 69. Stator 1 and stator 2 total pressure ratio distributions

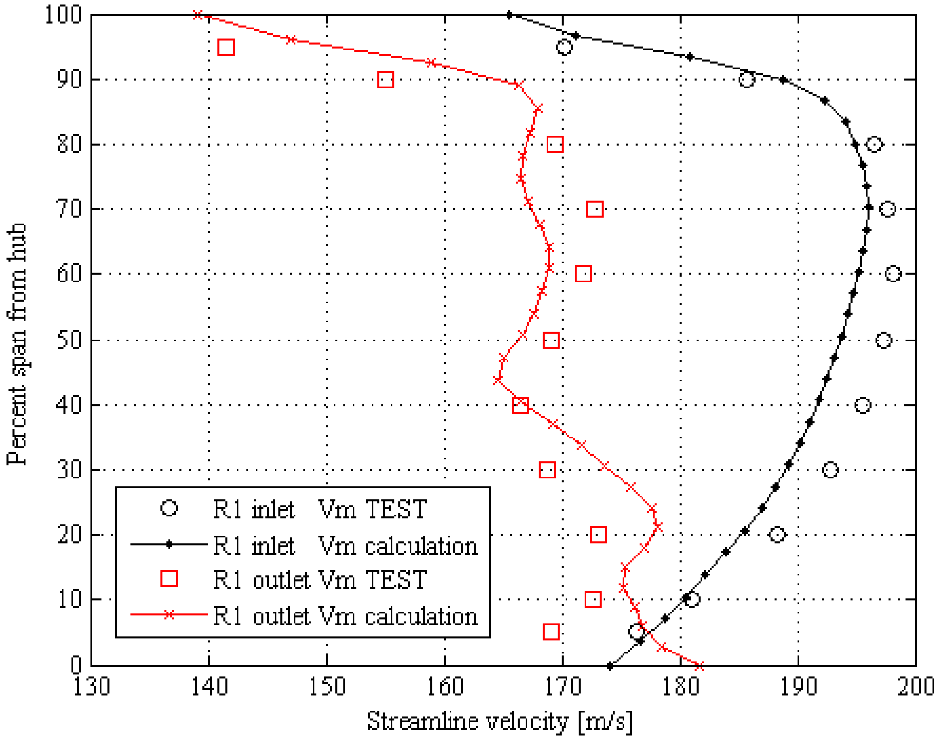

Figure 70. Rotor 1 inlet and outlet streamline velocity distributions

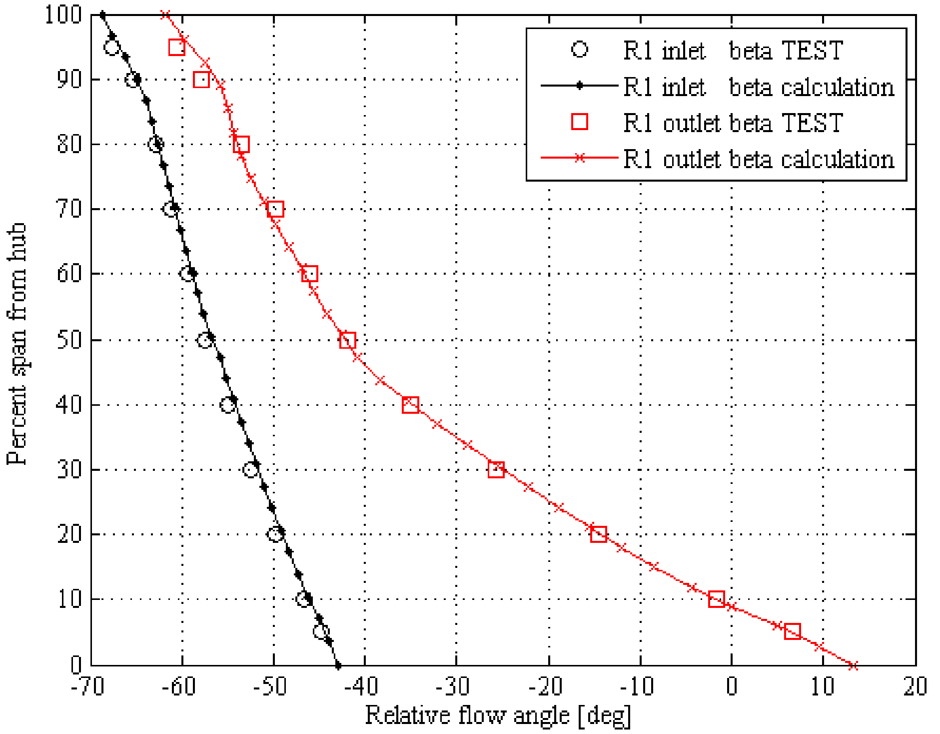

Figure 71. Rotor 1 inlet and outlet relative flow angle distributions

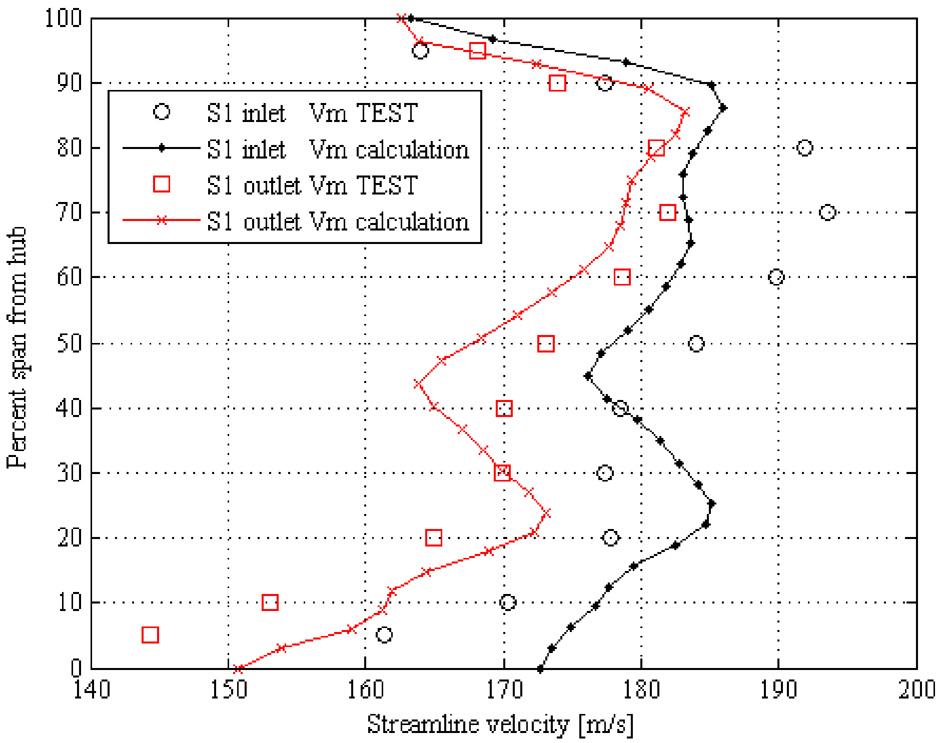

Figure 72. Stator 1 inlet and outlet streamline velocity distributions

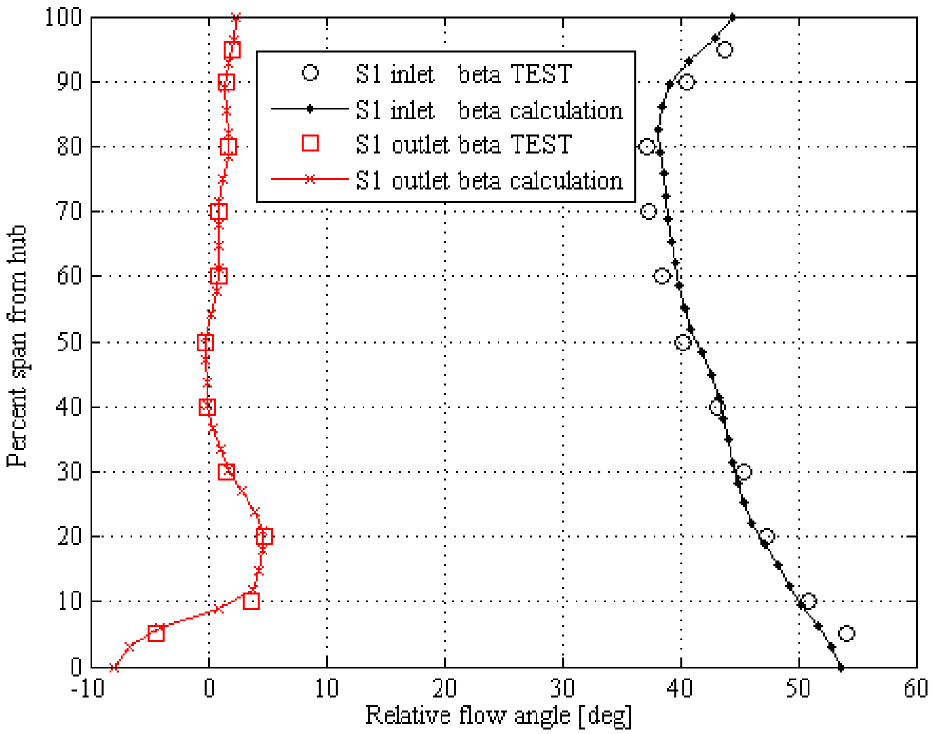

Figure 73. Stator 1 inlet and outlet relative flow angle distributions

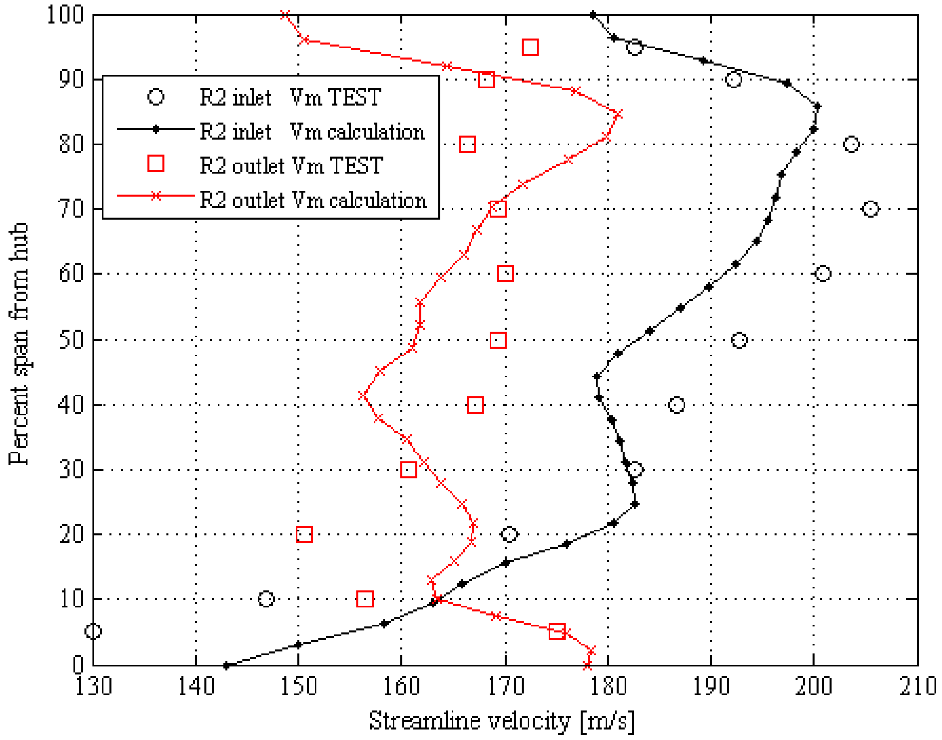

Figure 74. Rotor 2 inlet and outlet streamline velocity distributions

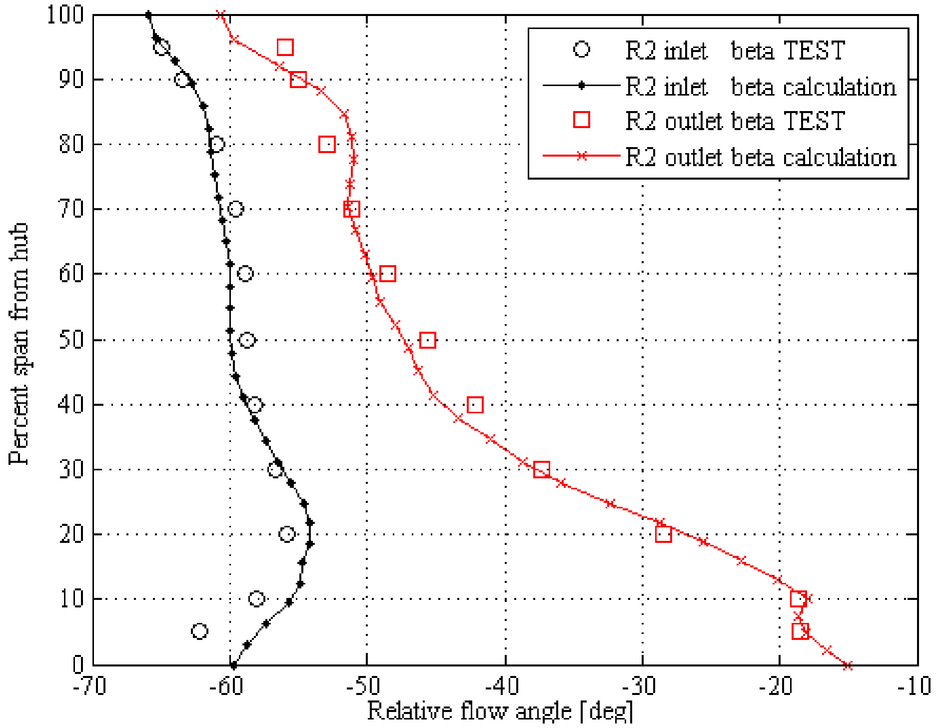

Figure 75. Rotor 2 inlet and outlet relative flow angle distributions

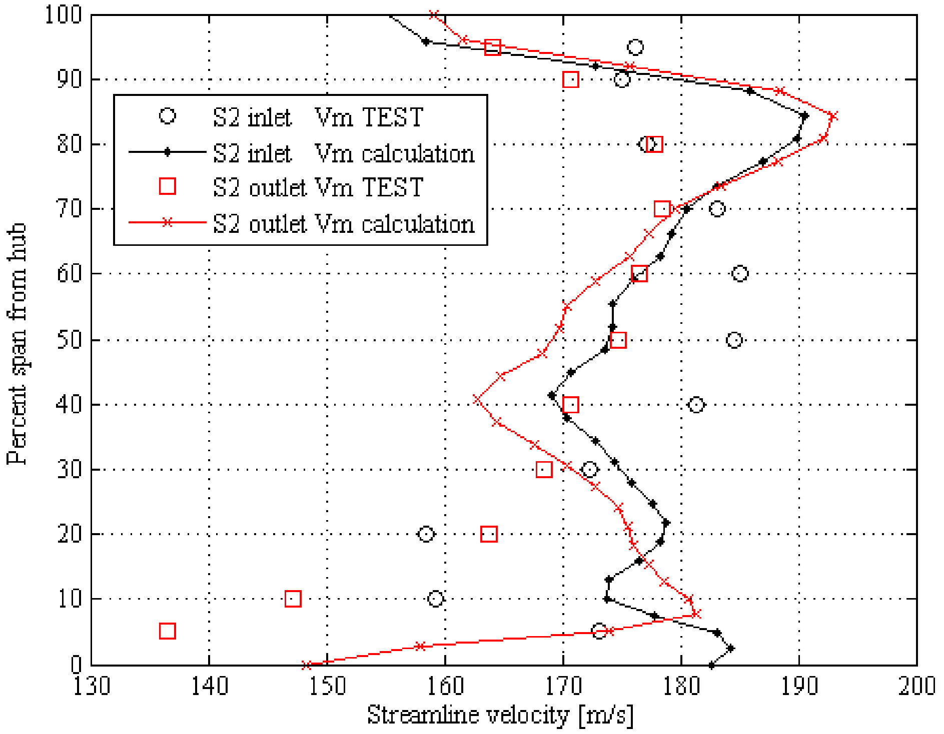

Figure 76. Stator 2 inlet and outlet streamline velocity distributions

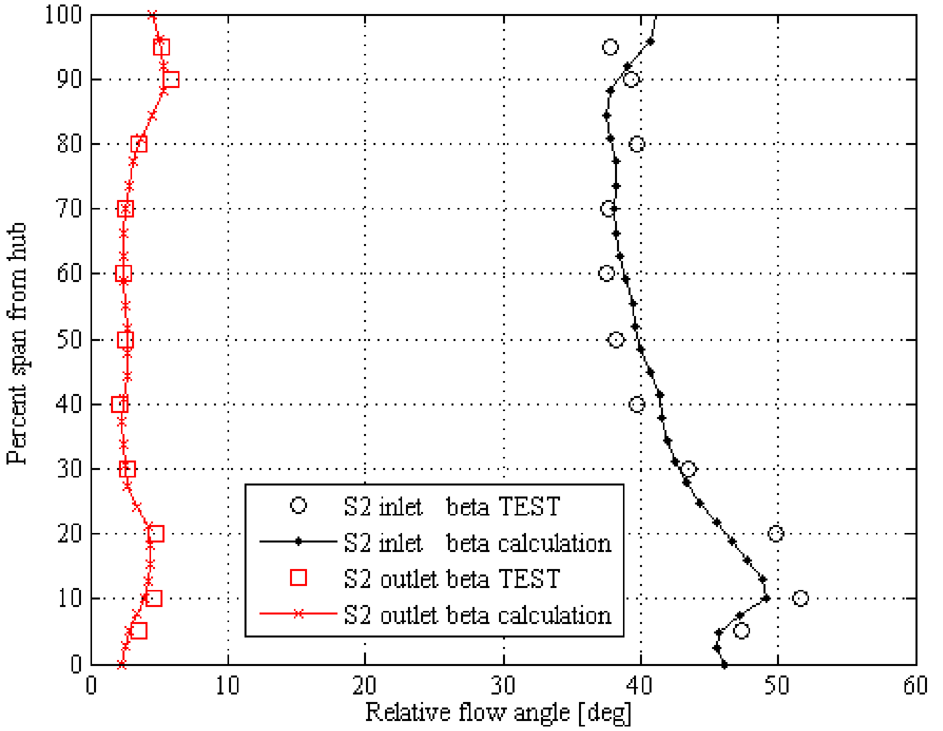

Figure 77. Stator 2 inlet and outlet relative flow angle distributions

5.3. CFD-Based 3D Validation on a Custom-Designed Fan Stage

In this section, in addition to the NASA 2-stage fan, a new single-stage transonic compressor test case, which is designed by the author of this study by the methods developed in this study, is investigated. The fan is representative of typical high-speed fans and generates a challenge for the through-flow solver. The empirical models are calibrated such that the both 3D single-stream test cases (NASA 2-stage fan and the current case) have satisfactory results. Therefore the correlations and extensions of section 3.4.1 are a product of cumulative results of these test cases. The third 3D test case, GE-NASA by-pass fan (section 5.4), directly uses the already calibrated models in SLC-experiment comparisons.

Meridional view and SLC grid of the compressor is presented in Figure 78. The design values are presented in Table 9. It is a high speed and high pressure-ratio compressor with 0.93 hub and 1.41 tip inlet relative Mach numbers and 1.72 total pressure ratio. Empirical-correlation-estimated efficiency is 0.874. The high speed indicates that this is at the edge of transonic definition; therefore it can be classified as a supersonic compressor, except the small portion at the rotor hub. This is specially selected to create a challenge for the empirical models.

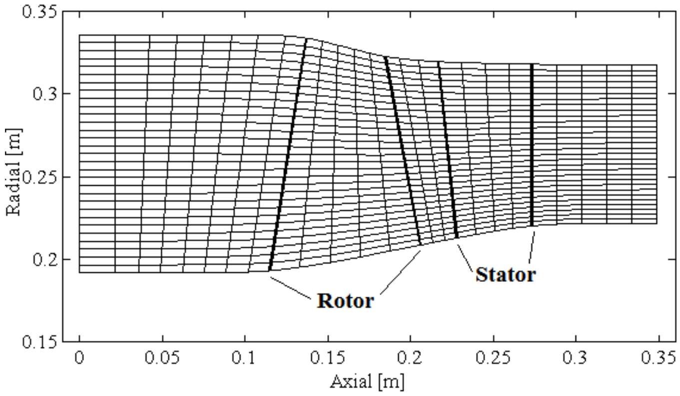

Figure 78. Meridional view and SLC grid of the transonic stage

The rotor is made of custom-designed profiles by a modifying the camberline with a second-order Bezier curve. Turning is shifted rearwards as inlet relative Mach number increases. The stator is made of DCA profiles. The 3D view of the machine is shown in Figure 79. The detailed design features, as spanwise profiles, are presented in this section in Figure 80 through Figure 100. The endwall boundary layer blockage results are also presented in Figure 82.

Table 9. Custom compressor main design parameters

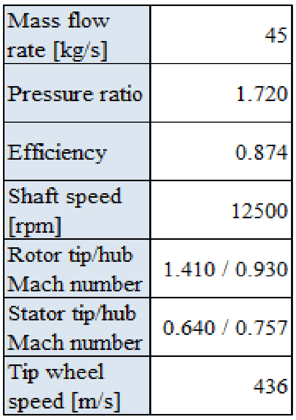

Mass flow rate [kg/s]	45
Pressure ratio	1.720
Efficiency	0.874
Shaft speed [rpm]	12500
Rotor tip/hub Mach number	1.410 / 0.930
Stator tip/hub Mach number	0.640 / 0.757
Tip wheel speed [m/s]	436

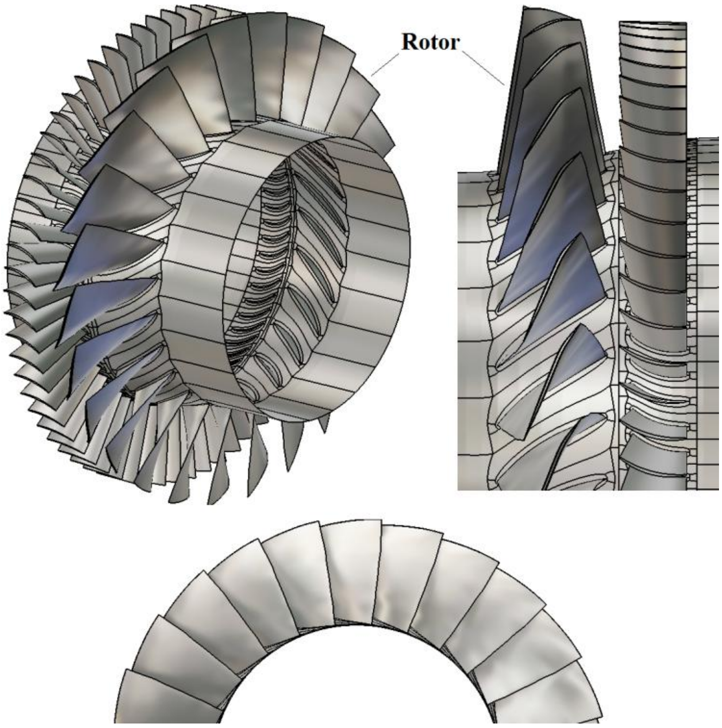

Figure 79. 3D view of the stage

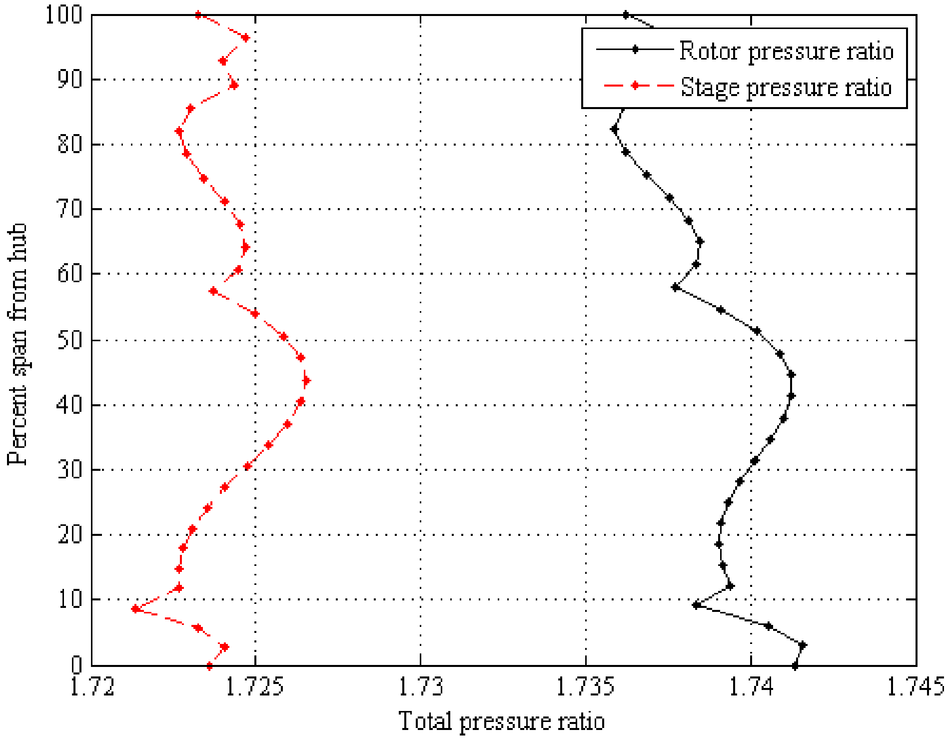

Figure 80. Rotor and stage total pressure ratio distributions

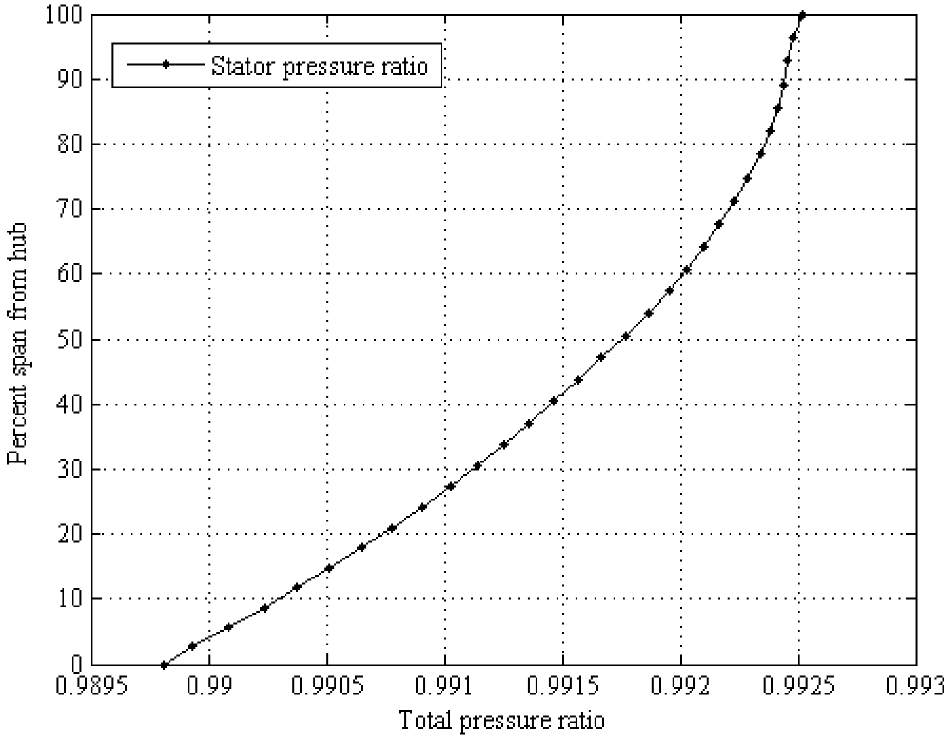

Figure 81. Stator total pressure ratio (loss) distribution

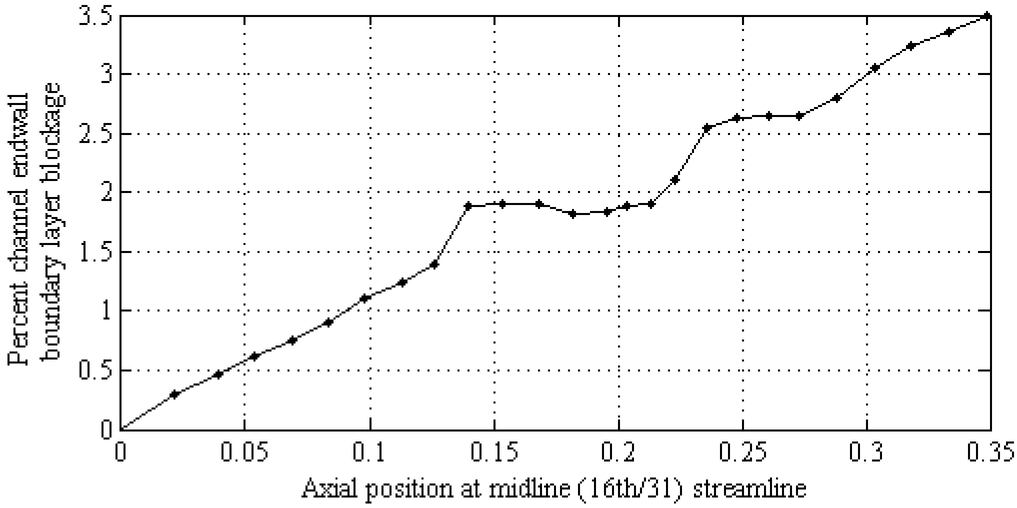

Figure 82. Estimated percent passage blockage distribution

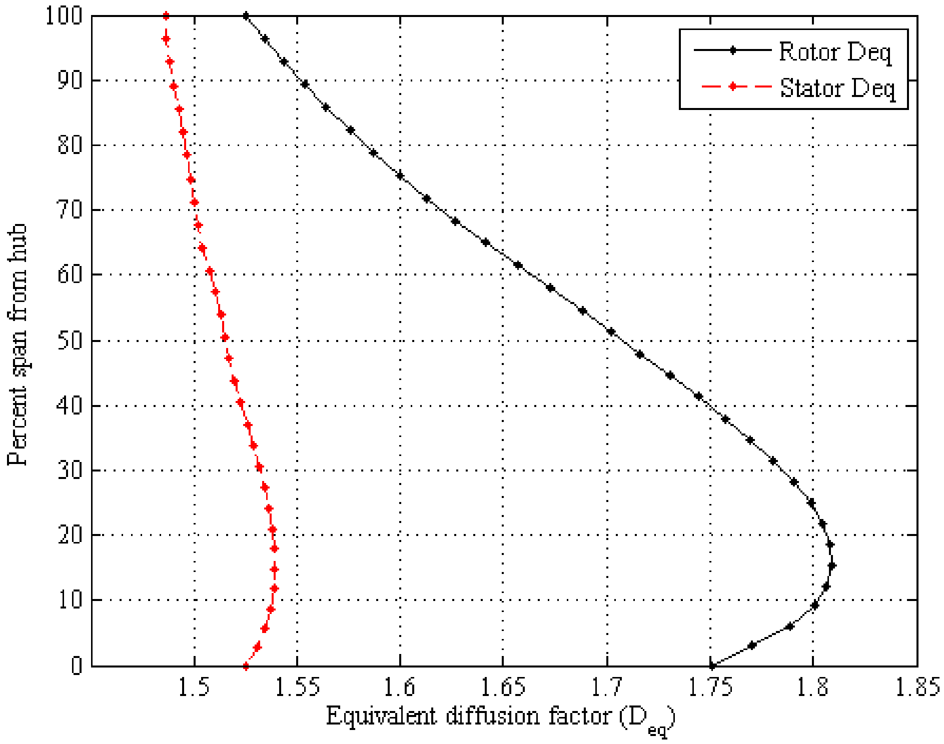

Figure 83. Rotor and stator equivalent diffusion factor distributions

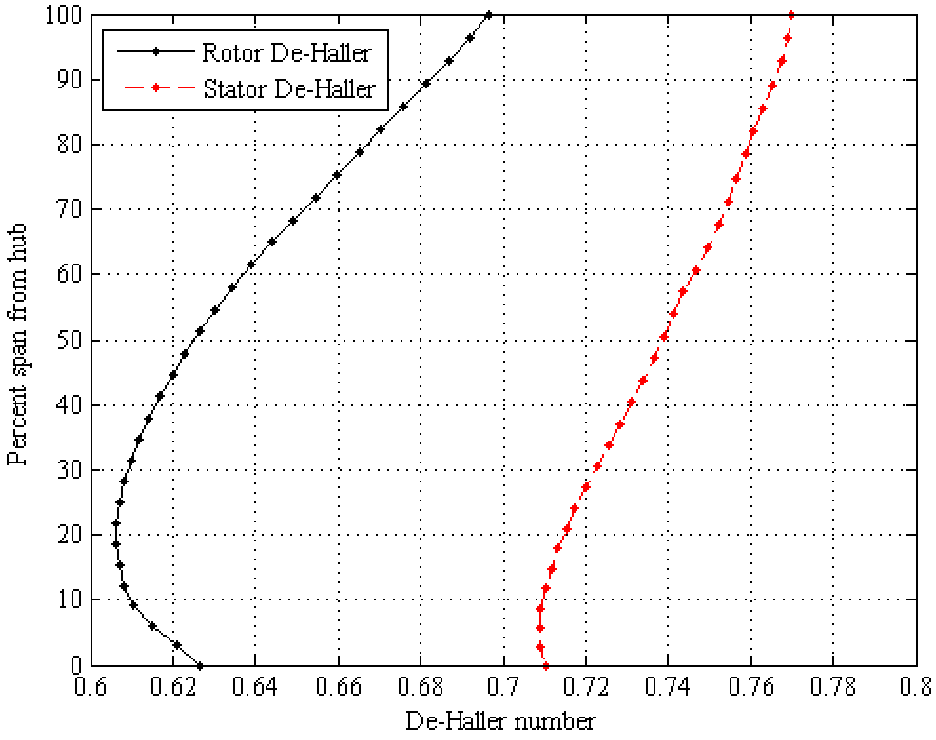

Figure 84. Rotor and stator De-Haller number distributions

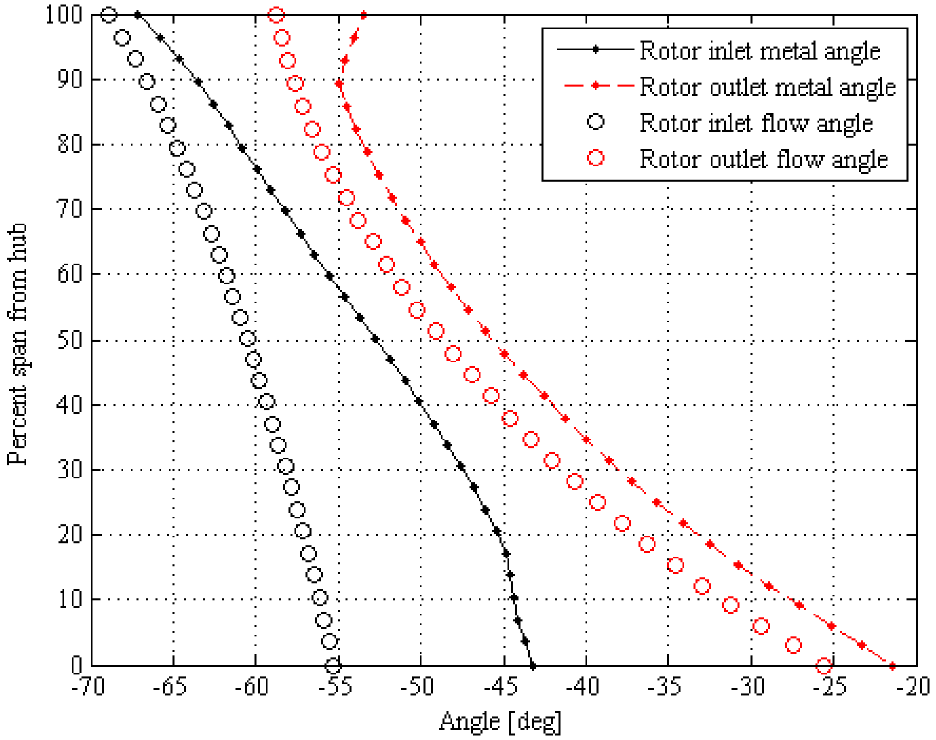

Figure 85. Rotor inlet and outlet metal and flow angles distributions

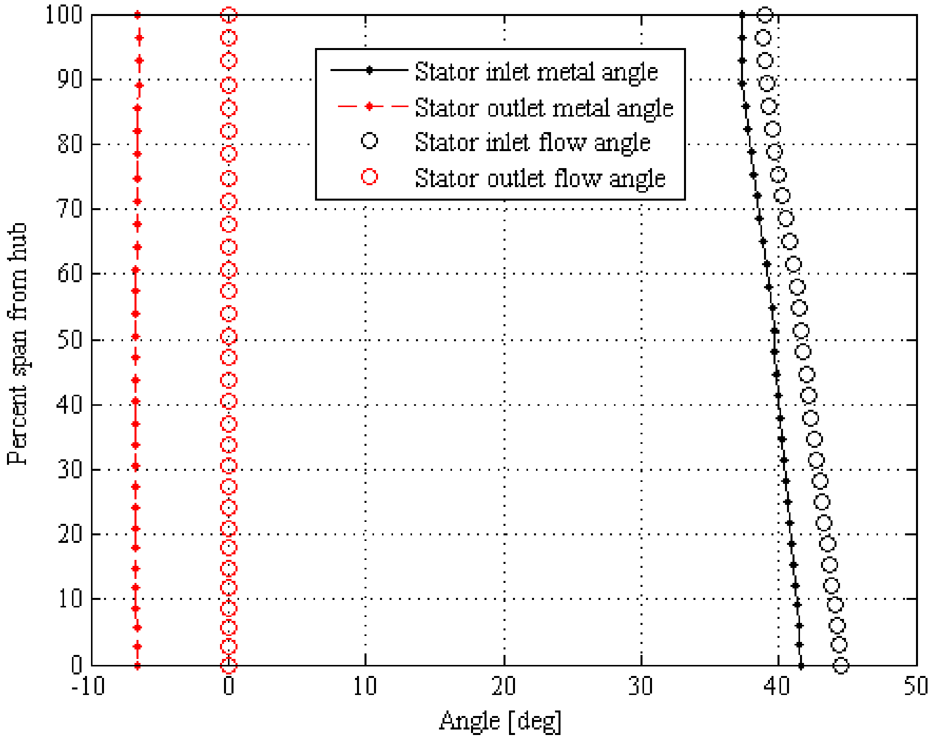

Figure 86. Rotor inlet and outlet metal and relative flow angles distributions

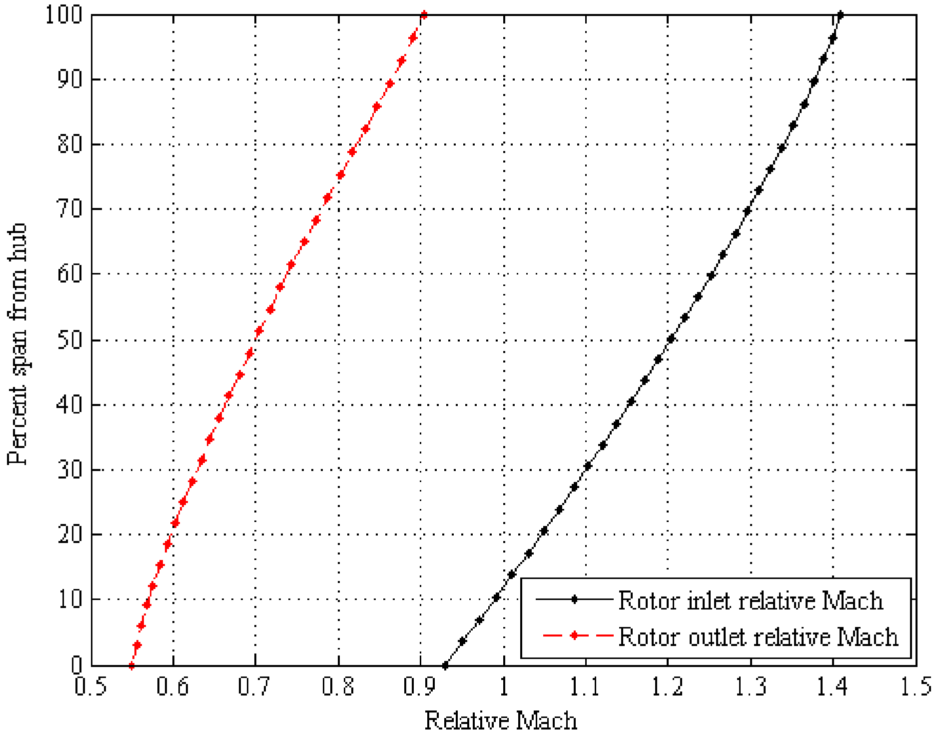

Figure 87. Rotor inlet and outlet relative Mach number distributions

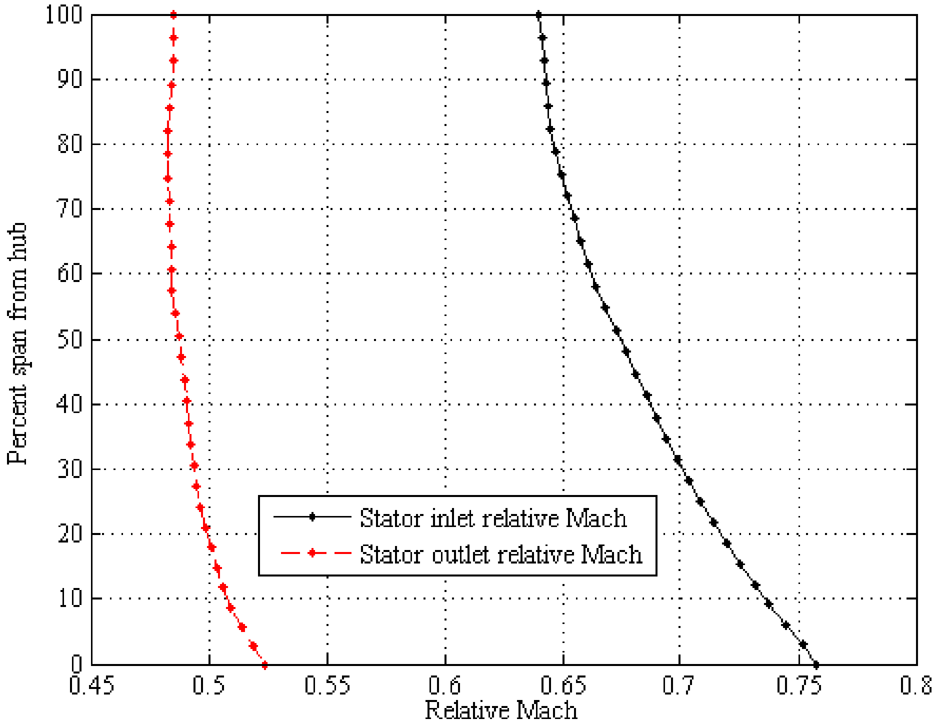

Figure 88. Stator inlet and outlet relative Mach number distributions

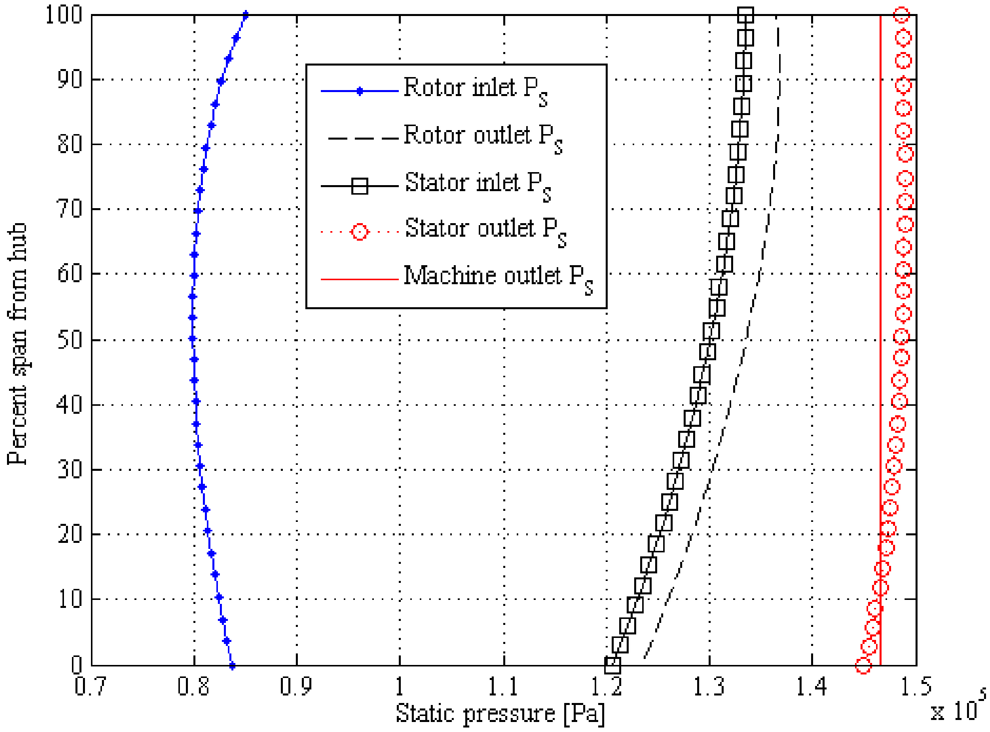

Figure 89. Distributions of static pressure along the fan

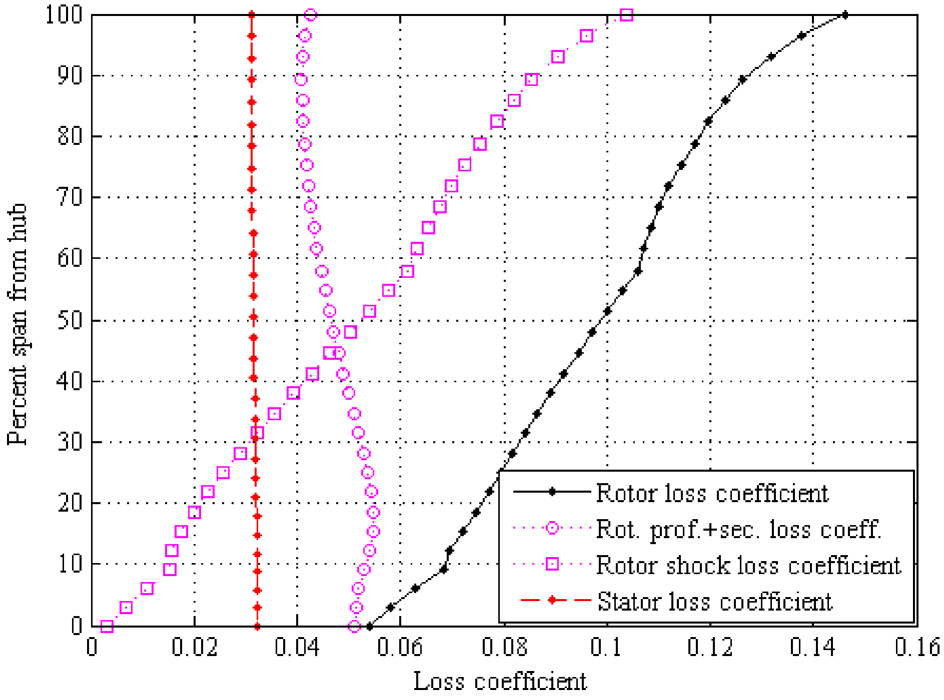

Figure 90. Rotor and stator total pressure loss coefficient distributions

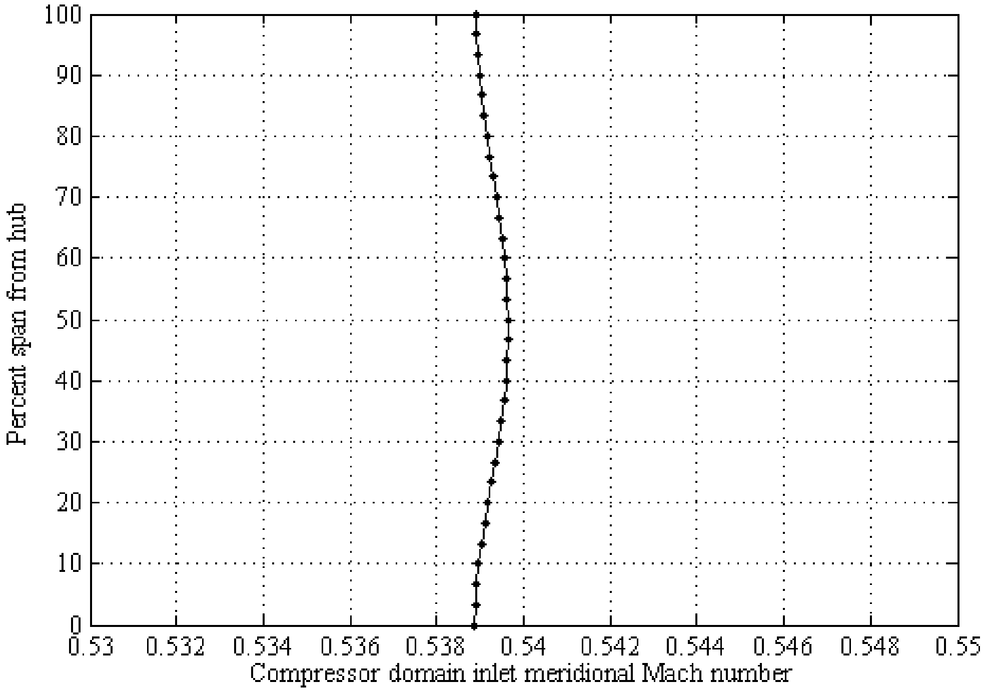

Figure 91. Compressor inlet Mach number distribution

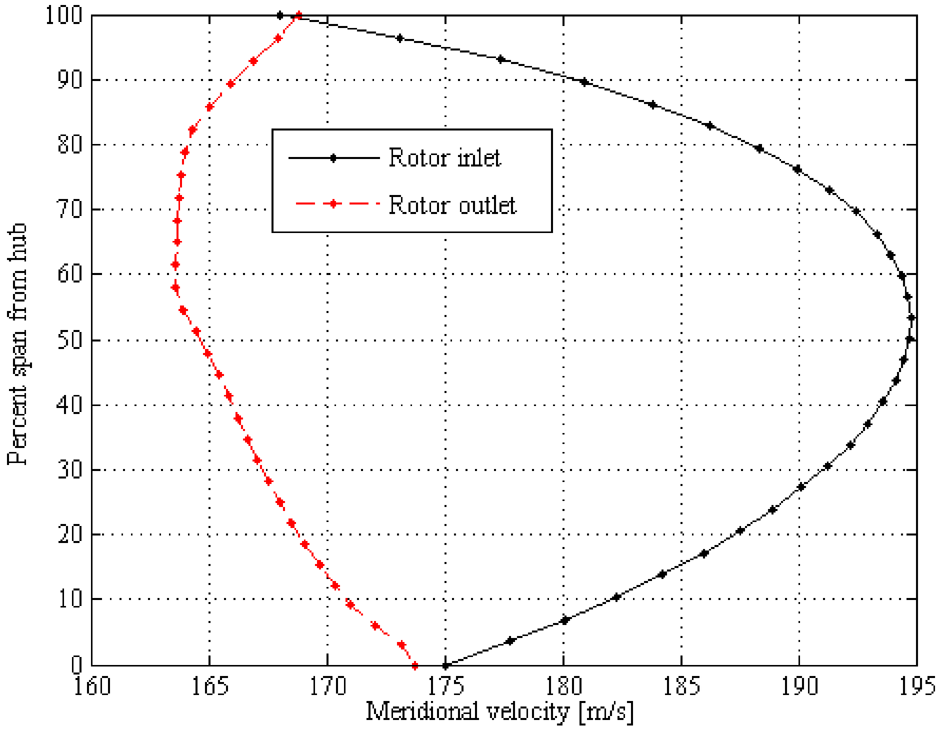

Figure 92. Rotor inlet and outlet streamline velocity distributions

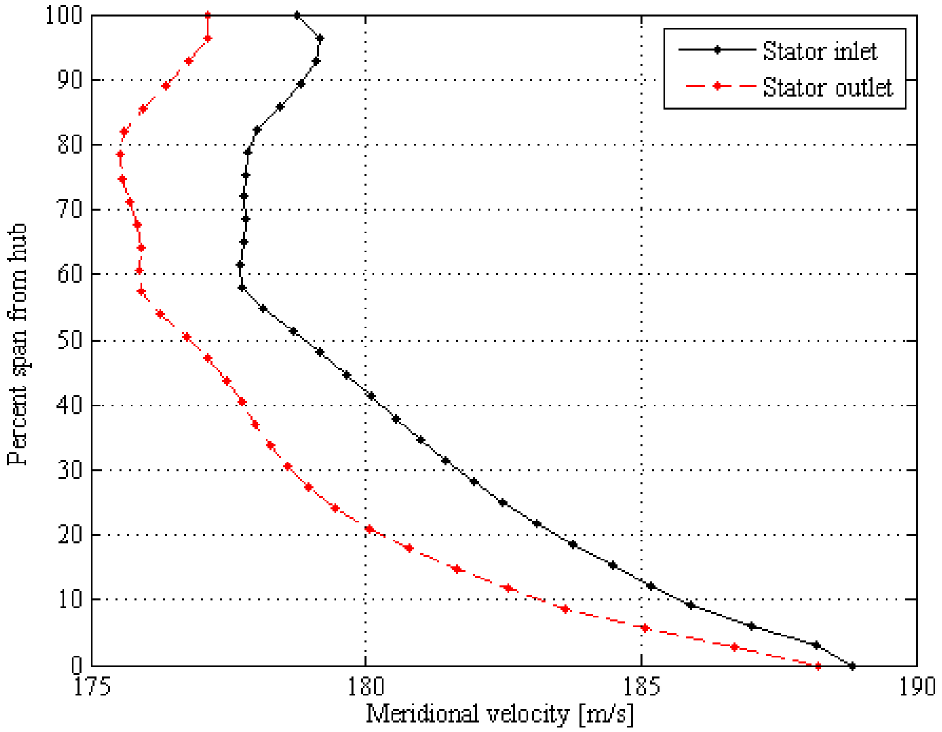

Figure 93. Stator inlet and outlet streamline velocity distributions

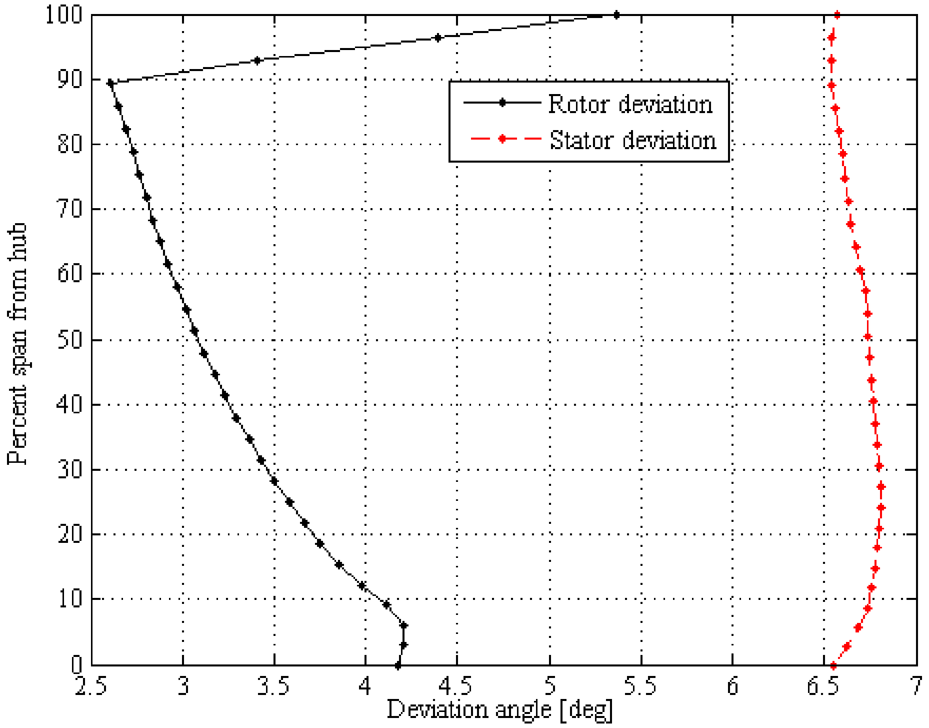

Figure 94. Rotor and stator deviation angle distributions

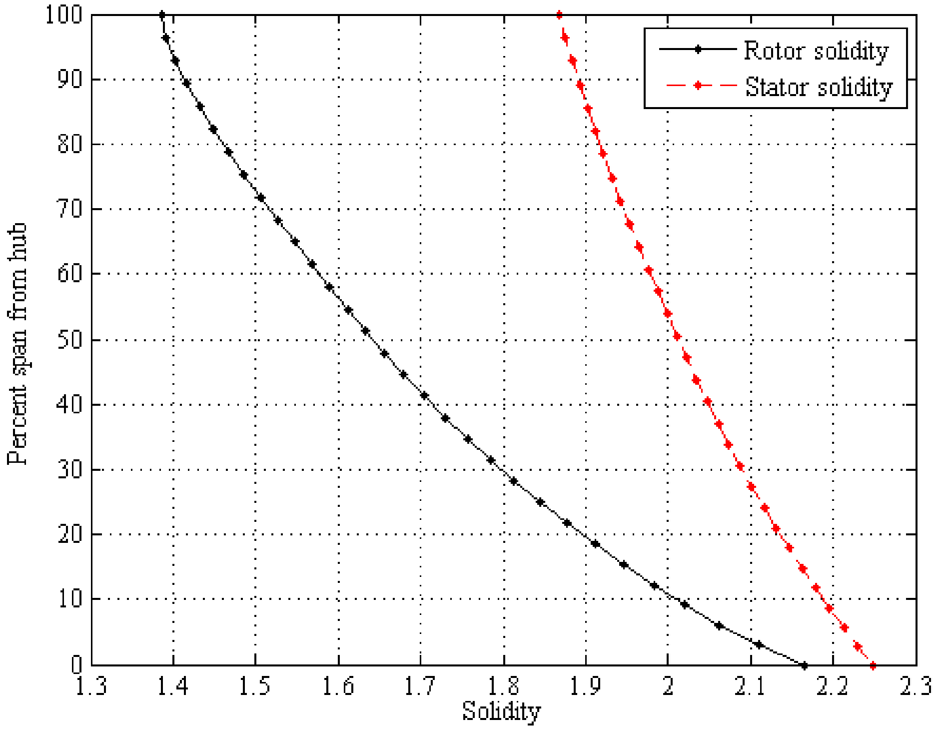

Figure 95. Rotor and stator solidity distributions

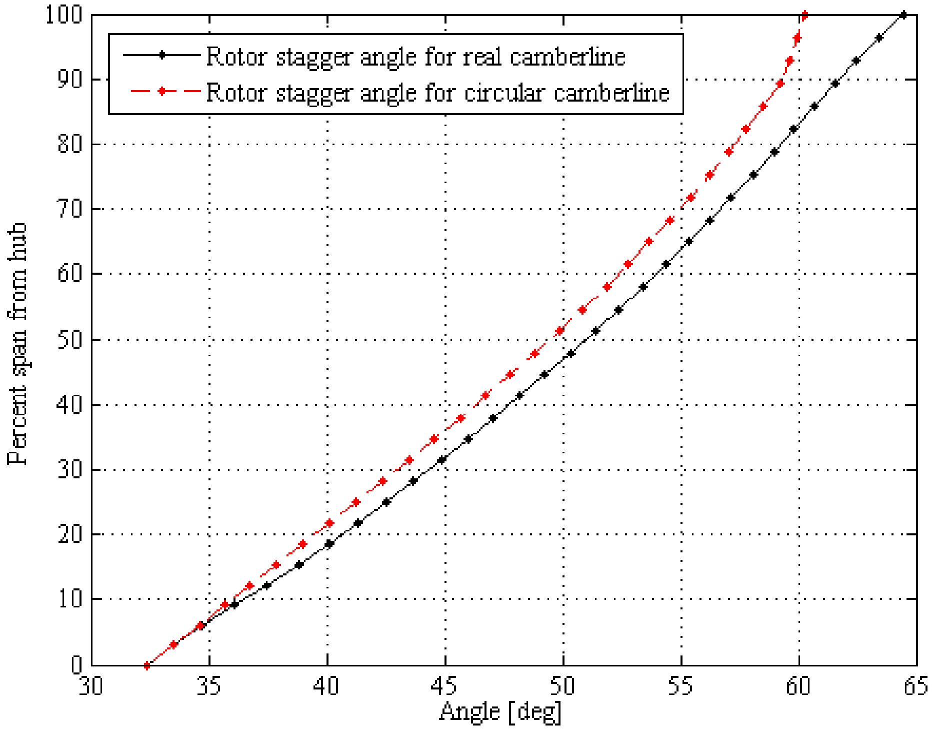

Figure 96. Rotor and stator stagger angle distributions

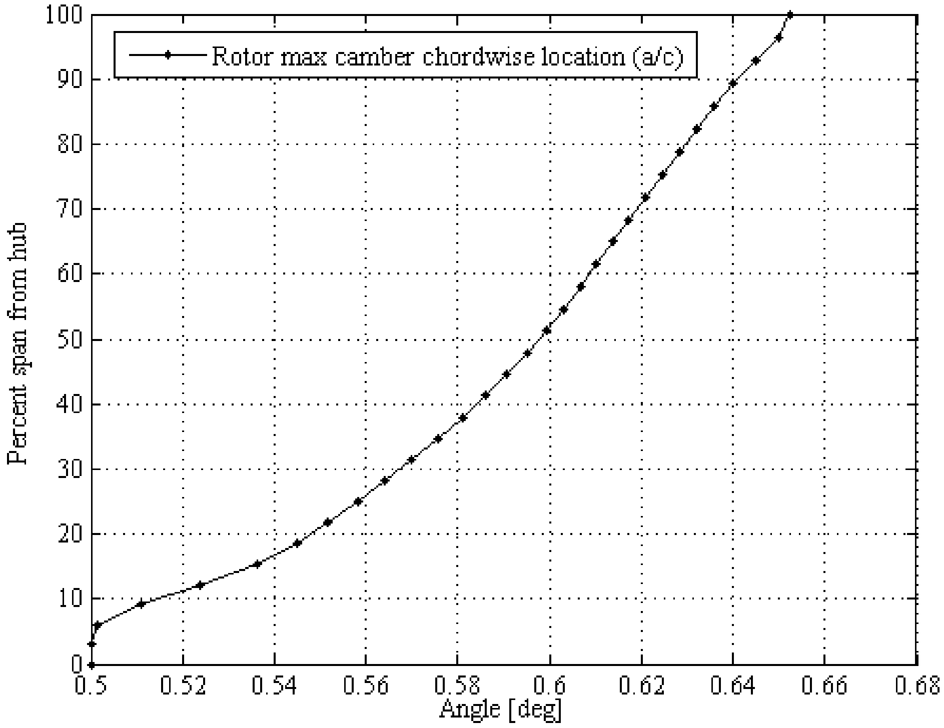

Figure 97. Rotor maximum camber location distribution

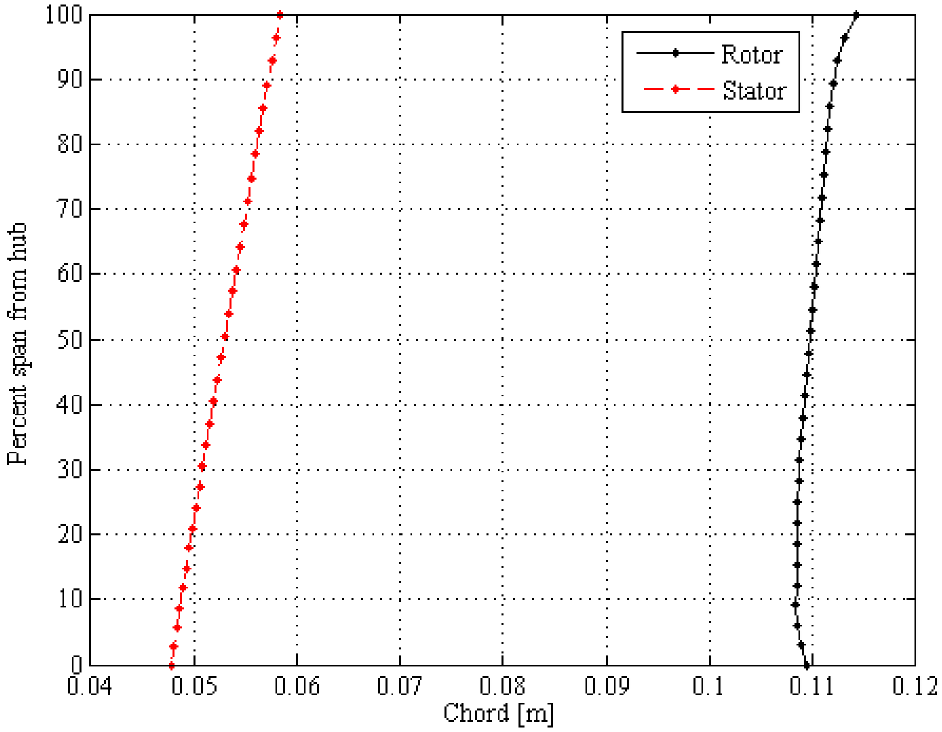

Figure 98. Rotor and stator chord length spanwise distribution

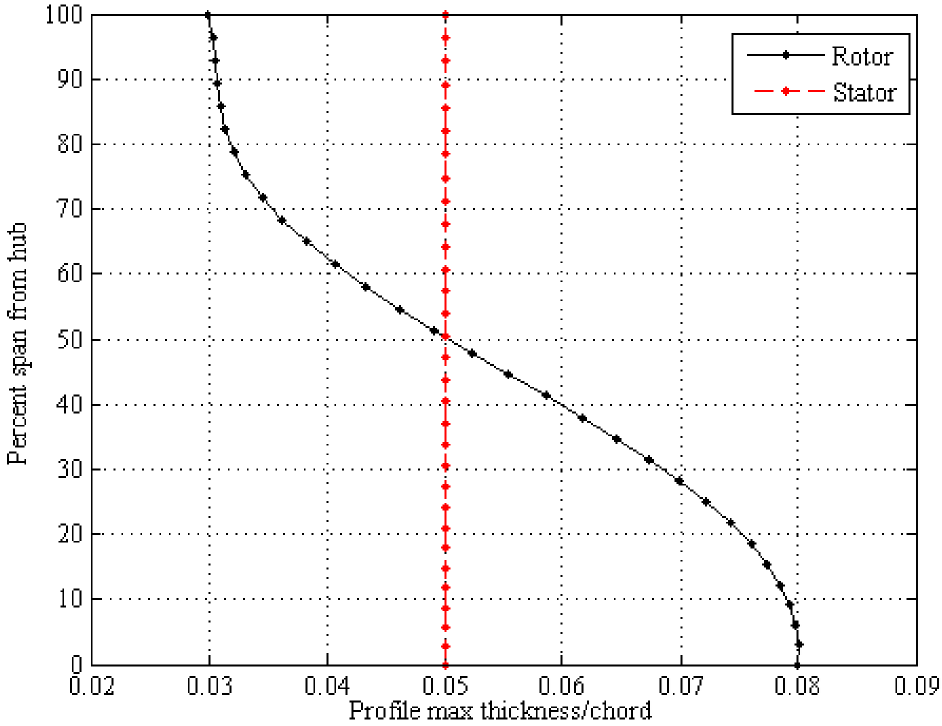

Figure 99. Rotor and stator maximum thickness-to-chord ratio distribution

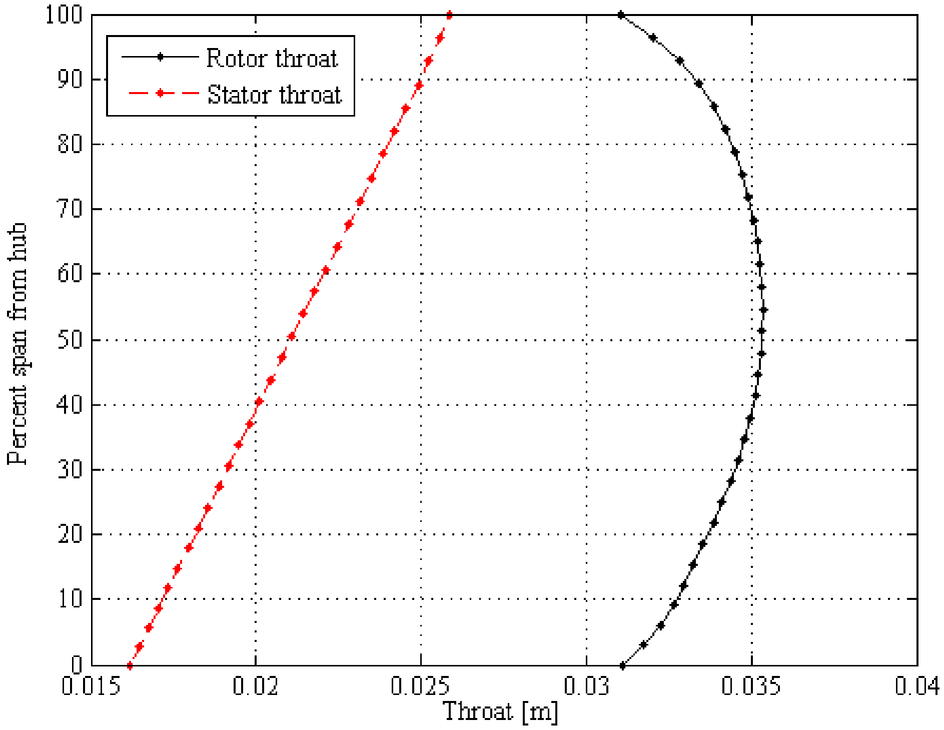

Figure 100. Estimated throat opening distributions for rotor and stators

5.3.1. Description and Validation of Benchmark 3D CFD Software

A commercial software, NUMECA FINE/TURBO, which is specially dedicated to turbomachinery modeling, is used for structured meshing and obtaining 3D viscous CFD solutions. During both the CFD-SLC comparisons and the CFD validation of the current sub-section, around 125 cells streamwise, 100 cells in tangential direction (between two blades) and 150 elements in spanwise direction are used. 25 of the spanwise cells are concentrated in the shroud region for the rotor clearance. y^+ values are below unity to resolve boundary layers. In total, there are almost 2M volumes per stage. Spalart-Allmaras turbulence model is employed and all physical properties are modeled as temperature dependent.

The baseline version of the current benchmark CFD methodology was already validated against Rotor 37 test case in an AGARD report related to validation of various CFD codes [89]. Additional validation for the latest version of the software is also performed in scope of this thesis on the same test case (NASA Rotor 37), whose test data is presented by another test campaign performed by Suder [90]. The data is extracted at 100% of NASA rotor 37 design speed and 20.31kg/s mass flow rate (slightly higher than the design value) at the survey denoted in Figure 101. Data uncertainty is reported to be 0.3kg/s for mass flow, 100Pa for total pressure and 0.6K in total temperature. The CFD-test comparison is presented in Figure 102, where a generally decent agreement is observed. The discrepancy on total pressure at the hub, being consistent with the comparison in the AGARD report [89], is expected to arise due to rotational effects, which cannot be modeled accurately by a one-equation eddy viscosity model. Difference between the ideal and the deformed manufactured models may also have been contributed to this deviation. Also, the NASA rotor 37 is a very high pressure ratio rotor with a pressure ratio larger than 2. The custom-designed fan of this chapter is a stage with a pressure ratio of 1.75. Therefore even better agreement may be obtained with the custom-designed fan due to less harsh conditions. In conclusion, the CFD is capable of producing generally acceptable, if not perfect, solutions even for a more highly-loaded fan and the following SLC-CFD comparisons are valid.

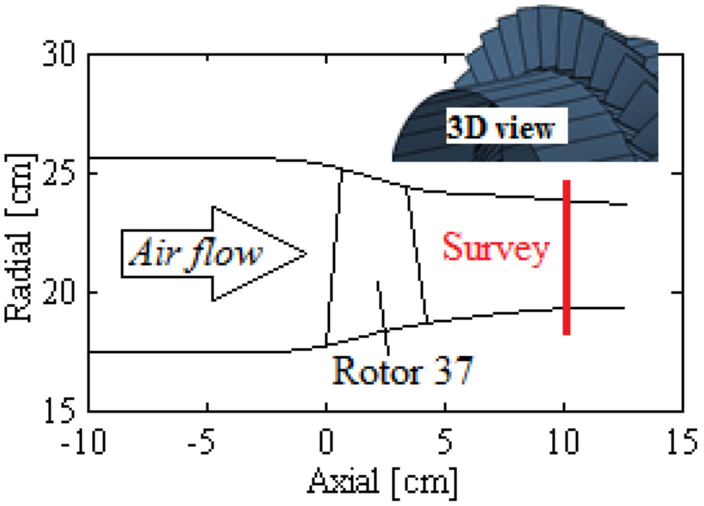

Figure 101. View of NASA Rotor 37 and measurement survey location

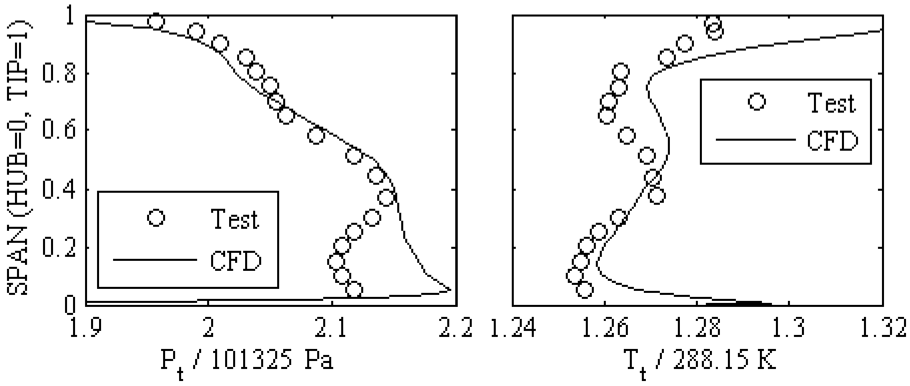

Figure 102. CFD-Test comparisons

5.3.2. Comparison with 3D CFD Results

Comparison of overall performances is presented in Table 10. Very good agreement between the SLC solver and 3D CFD, around or less than 1% difference, is observed. Table 11 presents the errors in the predicted spanwise profiles. In this table, the mean error is calculated as the average of $100x((X_{SLC}-X_{CFD})^2)^{1/2}/\ X_{CFD}$, where "X" represents either of meridional velocity, exit relative flow angle or rotor pressure ratio. Therefore different signs do not eliminate each other. The standard deviations of the errors already consider the absolute values and different signs do not eliminate each other. Inner and outer 5% spans, where viscous effects are dominating, are excluded in these comparisons. The table indicates less than 3% difference for the meridional velocity profiles, less than 1^o difference in the relative flow angle profiles and less than 0.5% difference in the rotor pressure ratio profile. Closer looks at those profiles are presented in Figure 103 through Figure 107. In all those figures, as expected from the above average discrepancies, very good trend-wise agreement is observed between the CFD output and the SLC prediction. Those results are more encouraging than the SLC-test comparisons of NASA 2-stage fan due to lack of experimental uncertainties such as inlet flow profiles, geometric deformations, measurement uncertainties, uncertainties due to data processing, etc. The empirical models are shown to be valid in simulating the flowfield.

Table 10. Comparisons of overall performances

	Throughflow design	3D CFD	Difference
Mass flow [kg/s]	45.0	44.5	-1.1%
Total pressure ratio	1.720	1.705	-0.9%
Efficiency [%]	87.43	86.74	-0.8%

Table 11. Errors in spanwise profiles

	Average error			Standard deviation of errors		
	Exit V_m error [%]	Exit β error [degree]	Exit Pressure ratio error [%]	Exit V_m error [%]	Exit β error [degree]	Exit Pressure ratio error [%]
Rotor 1	1.090	0.232	0.403	0.792	0.158	0.267
Stator 1	2.836	0.836	-	1.090	0.402	-

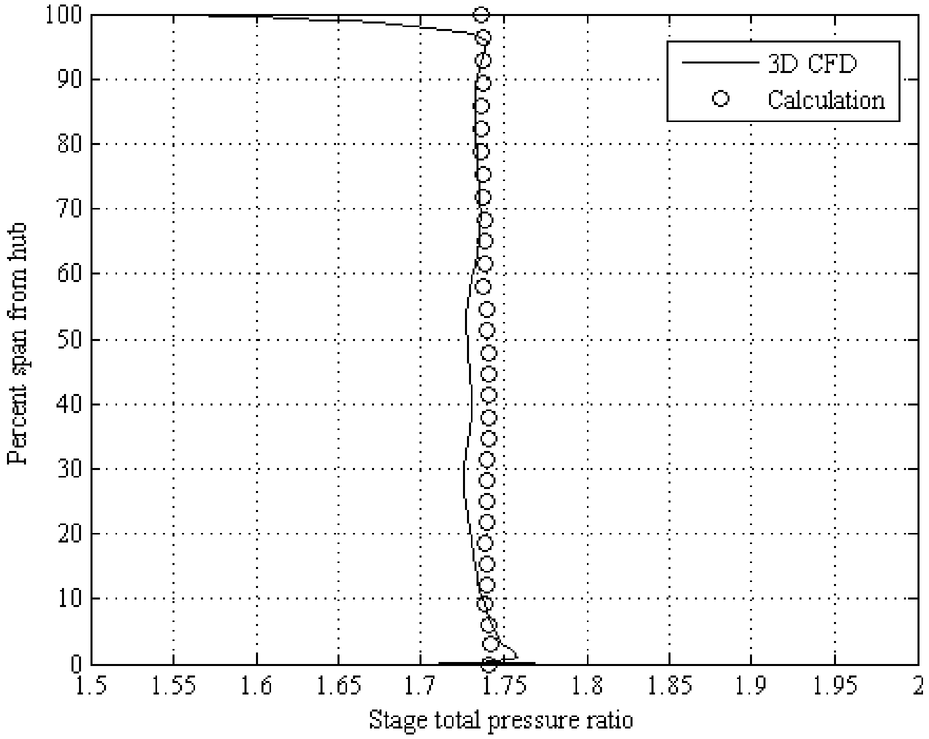

Figure 103. Stage total pressure spanwise distribution

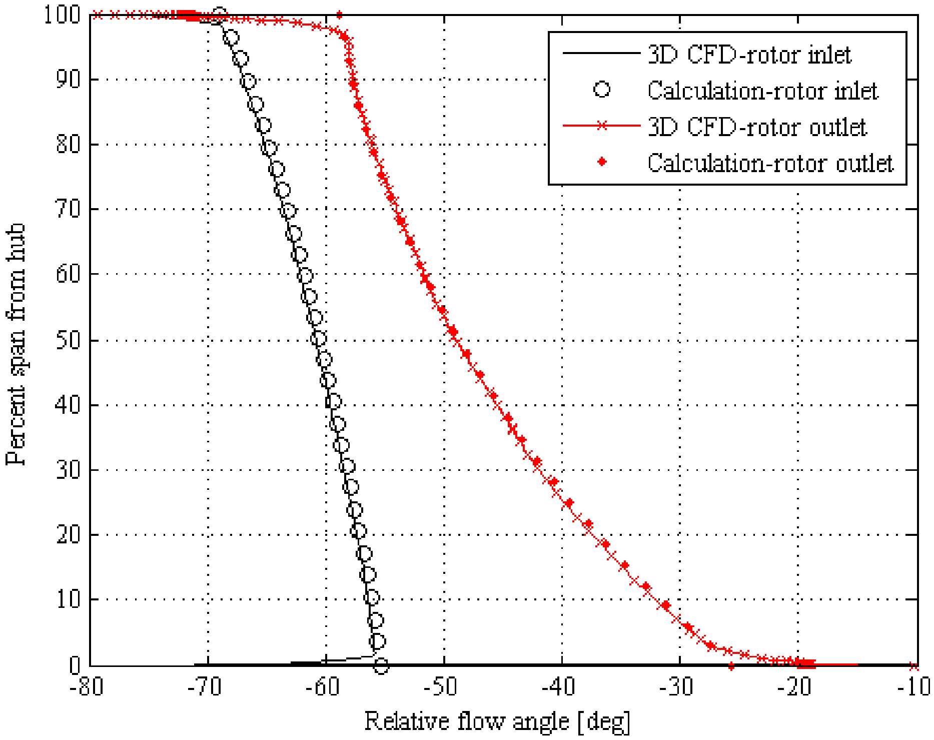

Figure 104. Relative flow angle spanwise distributions of the rotor

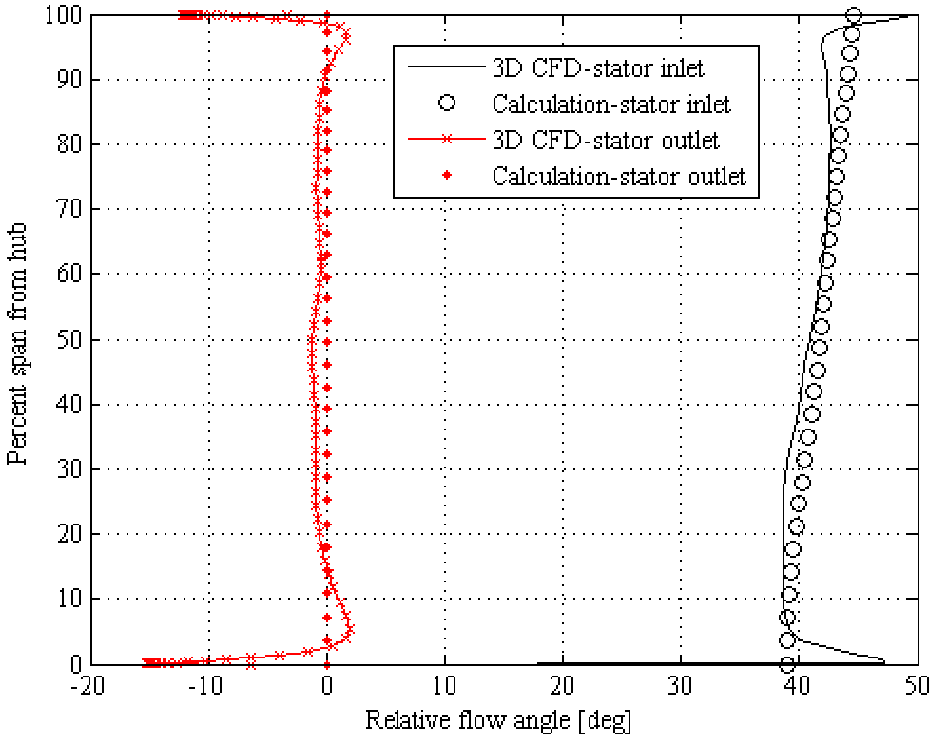

Figure 105. Relative flow angle spanwise distributions of the stator

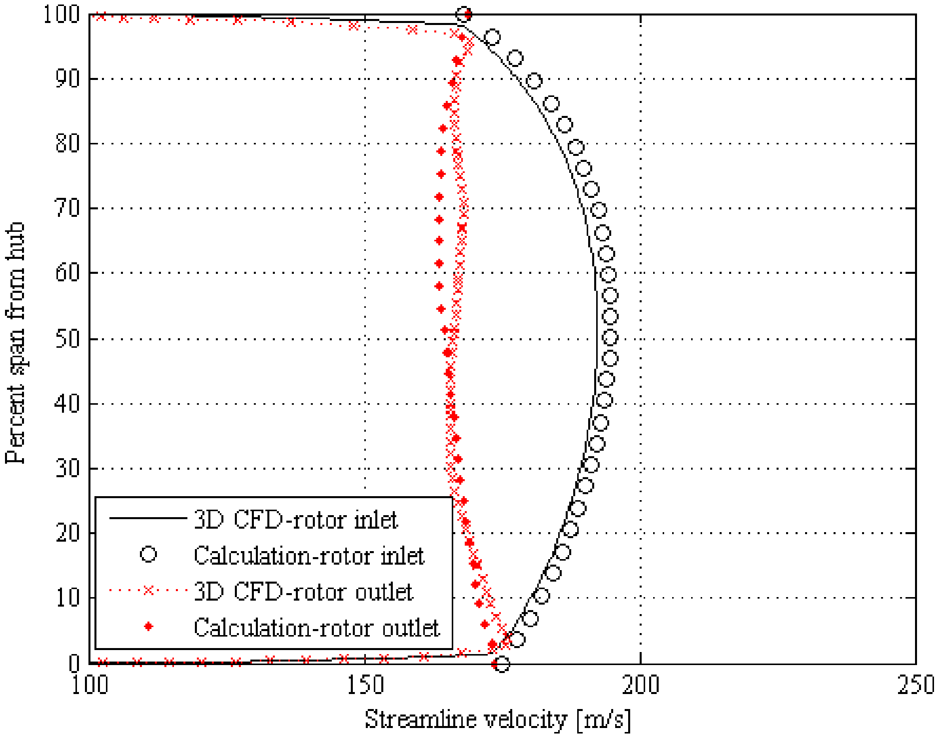

Figure 106. Streamline velocity spanwise distributions of the rotor

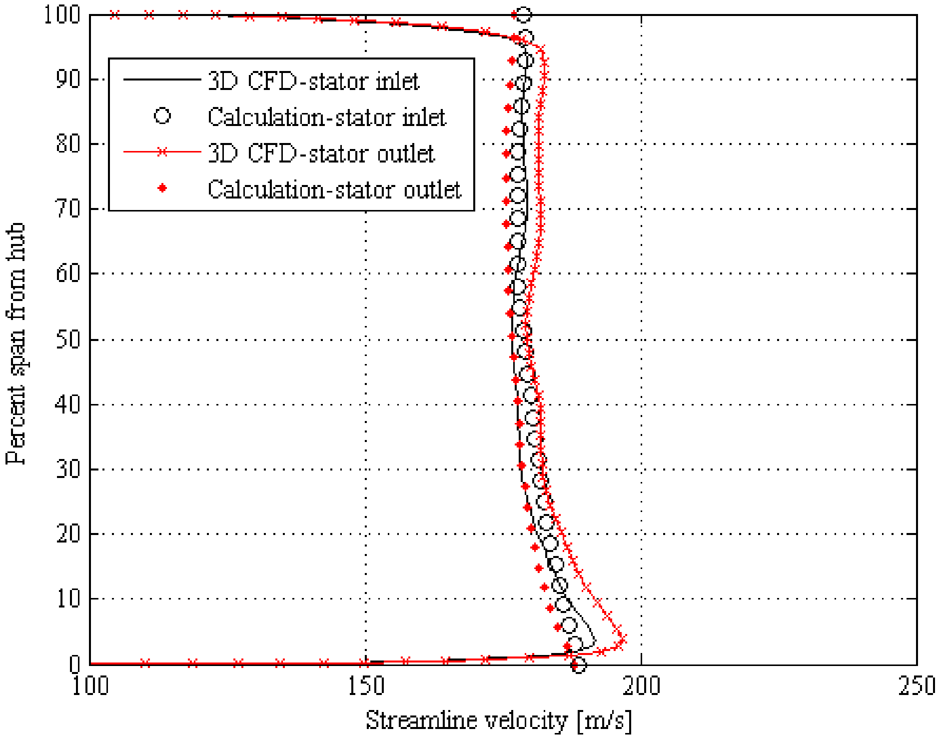

Figure 107. Streamline velocity spanwise distributions of the stator

5.4. GE-NASA By-Pass Fan System

The validation of the complete models developed, including the developed solver, the split-flow methodology and the calibrated correlations are validated against General Electric and NASA advanced technology fan. The tested geometry consists of a fan rotor, a downstream splitter that divides flow path into by-pass and core engine ducts, a by-pass outlet guide vane (OGV) and a core engine inlet guide vane (IGV), although untested original design also consists two-stage booster. The aerodynamic design documentation is presented by Sullivan et al. [70]. Major design parameters as targets are tabulated in Table 12. The design is a highly challenging because of high tip Mach number (more than 1.6) and very high fan-face “axial” Mach number (~0.8 instead of typical value of 0.55). The post-processed aerodynamic test data is documented by the same authors in another volume of the report [91]. Tests with many different advanced inlets and exhaust ducts are performed. In the current comparisons, only the data with standard short bellmouth inlet is used. Magnitudes of the measurement uncertainties are similar with NASA 2-stage fan (Section 5.2). Two photographs from the test rig are presented in Figure 108 and Figure 109. Meridional view and SLC grid is presented in Figure 110.

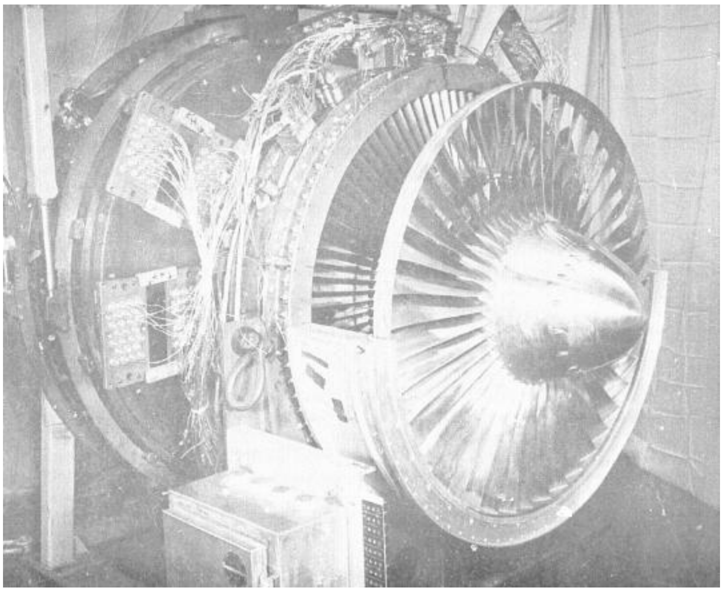

Figure 108. View of the fan and by-pass vanes [91]

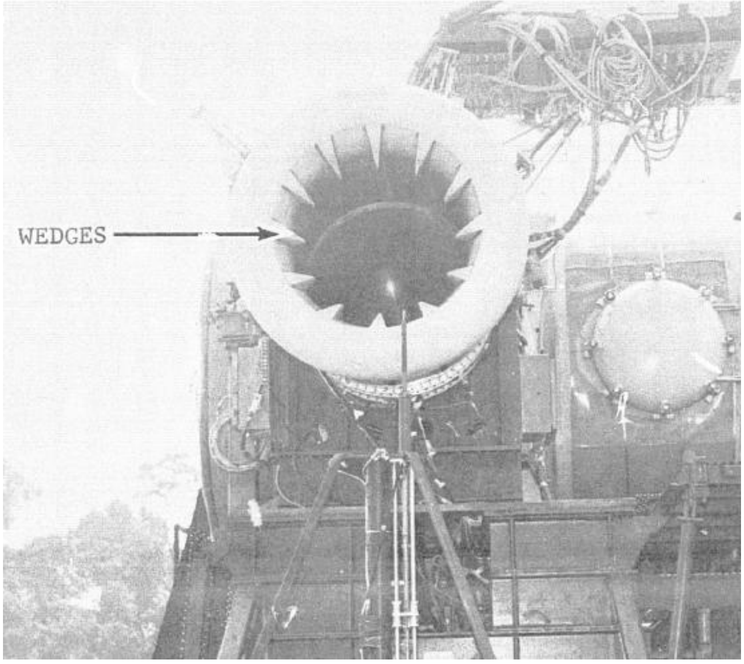

Figure 109. View of the fan in the test bed [91]

Table 12. Design goals of the fan [70]

Corrected mass flow rate [kg/s]	117.9
Fan tip Mach number	1.638
Fan pressure ratio (by-pass side)	1.83
Fan pressure ratio (core side)	1.73
Objective adiabatic efficiency	84
Fan inlet hub/tip ratio	0.38
Fan tip diameter [m]	0.9037
Corrected shaft speed [rmm]	10628
Corrected tip wheel speed [m/s]	503
By-pass ratio	6

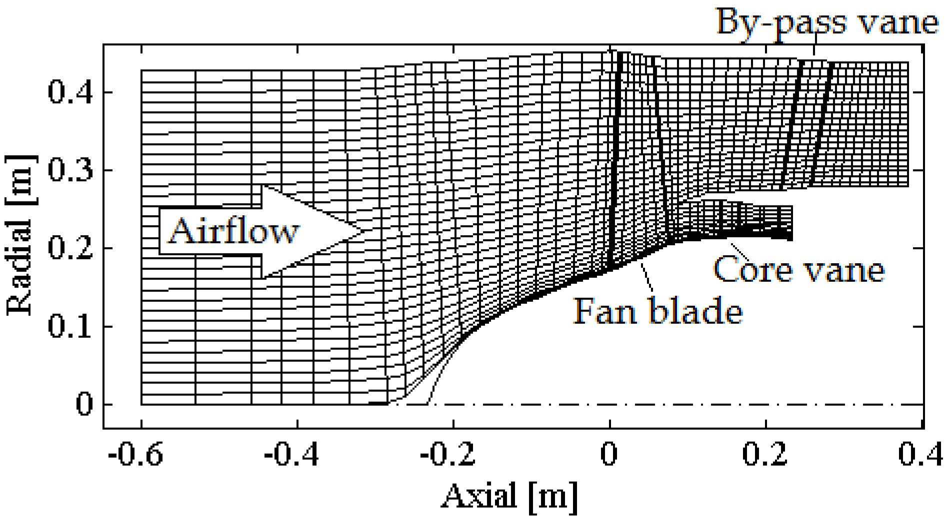

Figure 110.SLC grid of GE-NASA by-pass fan

Comparisons of SLC calculations and the measured data for overall performances are given in Table 13. Very good agreement is observed in the average fan pressure ratio and decent agreement is observed for the corresponding efficiency. Discrepancies, however, are slightly bigger for the spanwise distributions, as presented in Table 14, but still assessed as decent for a through-flow approximation. In this table, similar to the previous cases, the mean error is calculated as the average of 100x((X_{SLC}-

$X_{test})^{2})^{1/2}/ X_{test}$, where “X” represents either of meridional velocity, exit relative flow angle or rotor pressure ratio. Therefore different signs do not eliminate each other. The standard deviations of the errors already consider the absolute values and different signs do not eliminate each other. Inner and outer 5% spans, where viscous effects are dominating and test data is not available, are excluded in these comparisons.

Table 13. Comparisons of overall performances

	Experiment	Throughflow	Difference
Mass flow [kg/s]	114.55	114.55	0% (imposed)
Total presure ratio	1.770	1.771	0.06%
Efficiency [%]	85.7	83.97	-2.02%

In addition to the averaged discrepancies, the details of the spanwise distributions are depicted in Figure 111 through Figure 117. Figure 111 presents comparison of fan total pressure ratio, where trends are also well captured by the developed SLC methodology. Similarly, Figure 112 and Figure 113 present fan rotor inlet and outlet meridional velocities and relative flow angles. Again, good agreement is observed.

Table 14. Errors in spanwise profiles

	Average error			Standard deviation of errors		
	Exit V_m error [%]	Exit β error [degree]	Exit Pressure ratio error [%]	Exit V_m error [%]	Exit β error [degree]	Exit Pressure ratio error [%]
Fan rotor	5.087	1.795	1.923	4.822	1.185	1.111
By-pass OGV	6.616	1.559	-	7.370	0.330	-
Core IGV	4.138	1.188	-	2.795	1.059	-

By-pass OGV spanwise profile predictions are presented in Figure 114 for meridional velocity and Figure 115 for the corresponding relative flow angle distributions. The discrepancies seem to be larger than that of the fan rotor, especially near the tip region. The main reason of this is believed to be the higher-than-test tip fan rotor pressure ratio (and lower-than-test entropy) in the SLC solution (see Figure 111), which results in a slightly higher fan tip meridional velocity (see Figure 112). Hence, this higher-than-test tip momentum propagates to the by-pass OGV and causes higher-than-test velocities there also. Moreover, the system does not operate at the intended design point due to long bellmouth, extensive probes and unexpected deformation of the fan blade, which results in lower-than-intended mass flow rate in the tests (114.5 kg/s [91] instead of the intended 117.9kg/s of Table 12). Therefore, considering the extra uncertainties due to off-design effects, the results seem acceptable. It is expected that the agreement with tests would be higher if the fan was working in its design point.

Lastly, the core IGV results are presented in Figure 116 for meridional velocity distributions and Figure 117 for relative flow angle distributions. Very similar error sources with the ones of the by-pass OGV predictions are also valid for the core IGV SLC predictions. An additional error source is the highly 3D nature of the fan root flow, due to the existence of more than 60 degree hub turning (excessive for a typical compressor [8]). The mixing effects may not be well captured in a 2D through-flow model. In conclusion, the agreement is very satisfactory for a through-flow solution.

Considering the slight off-design operation, deflection of fan blades in high rotational speeds and the empirical models are calibrated for tip relative Mach numbers up to 1.4 in the prior test cases but the current case has a tip relative Mach number more than 1.6, the performance of the SLC solver becomes even more evident. In summary, the developed methodology is capable of simulating the current case within engineering level of accuracy.

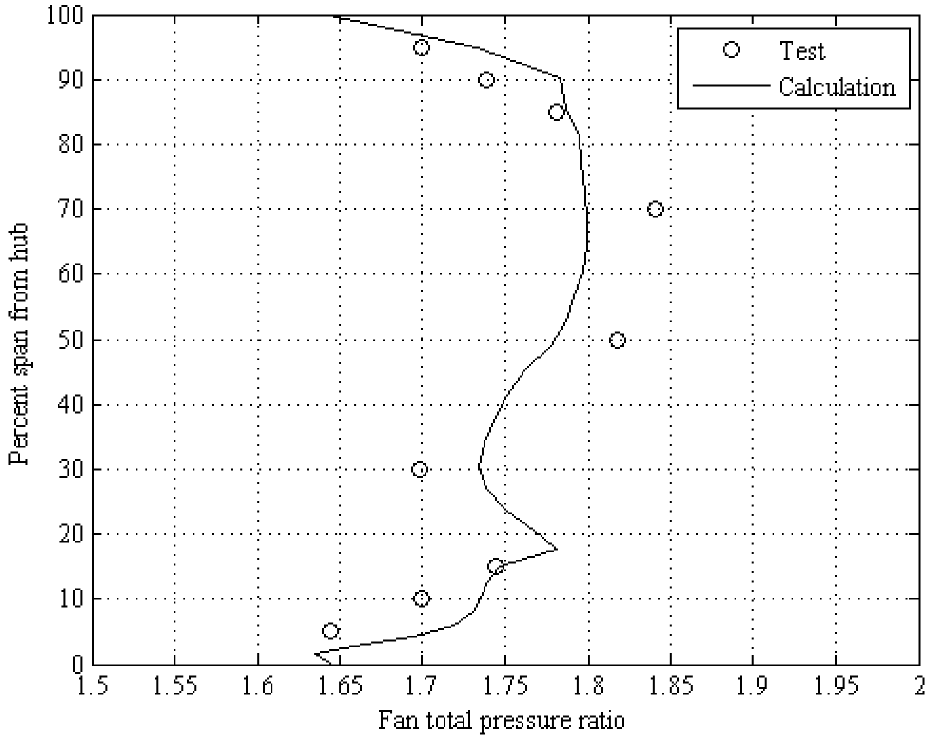

Figure 111. Fan rotor pressure ratio

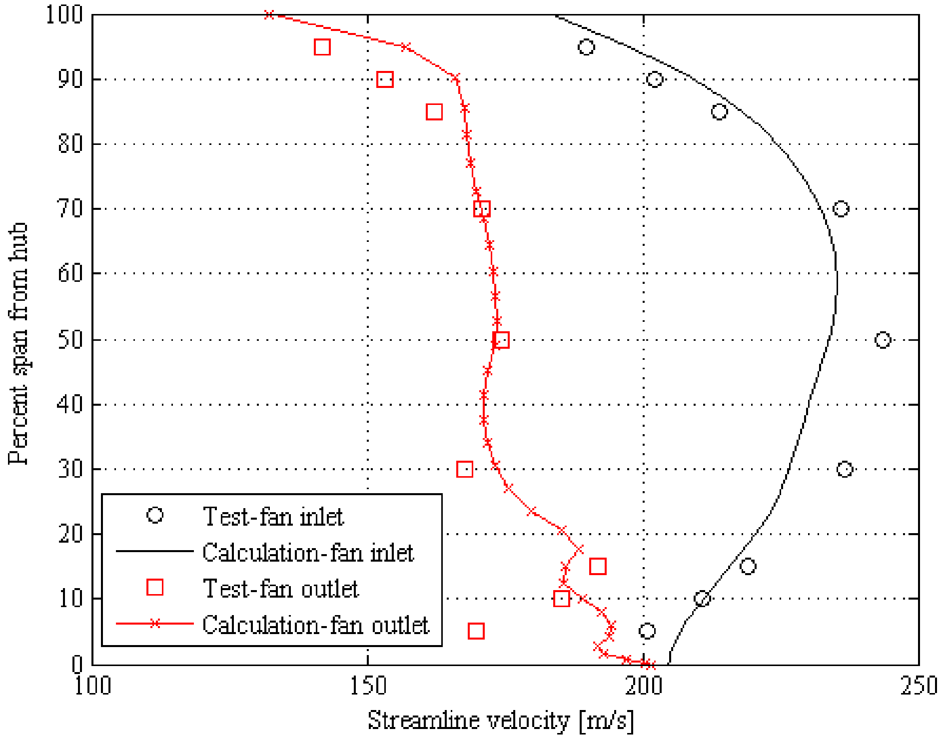

Figure 112. Fan rotor inlet and outlet streamline velocity distributions

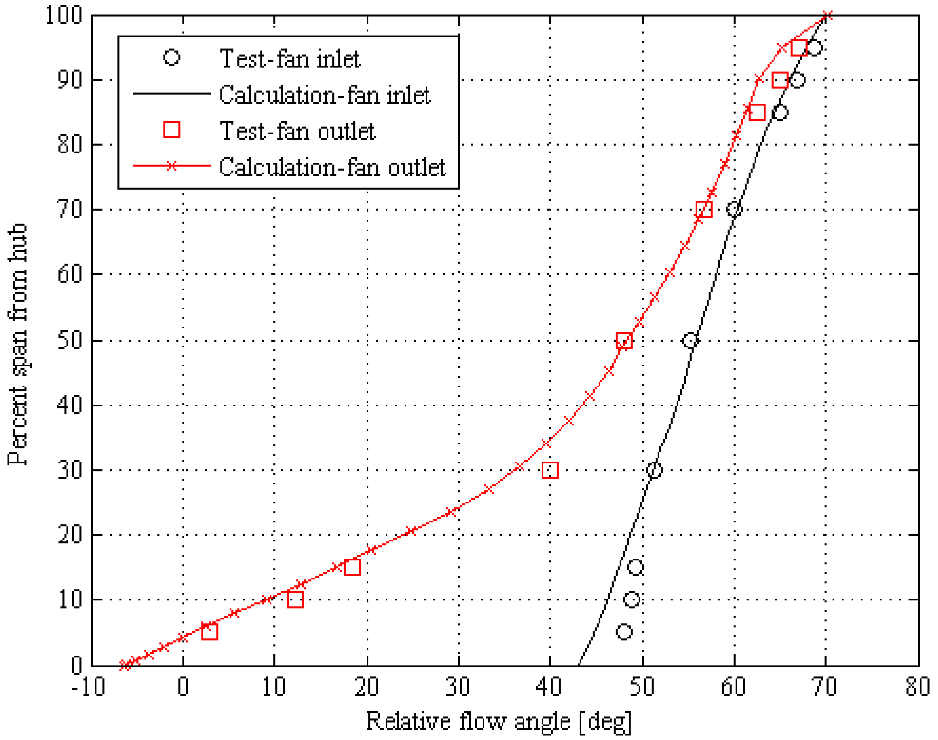

Figure 113. Fan rotor inlet and outlet relative flow angle distributions

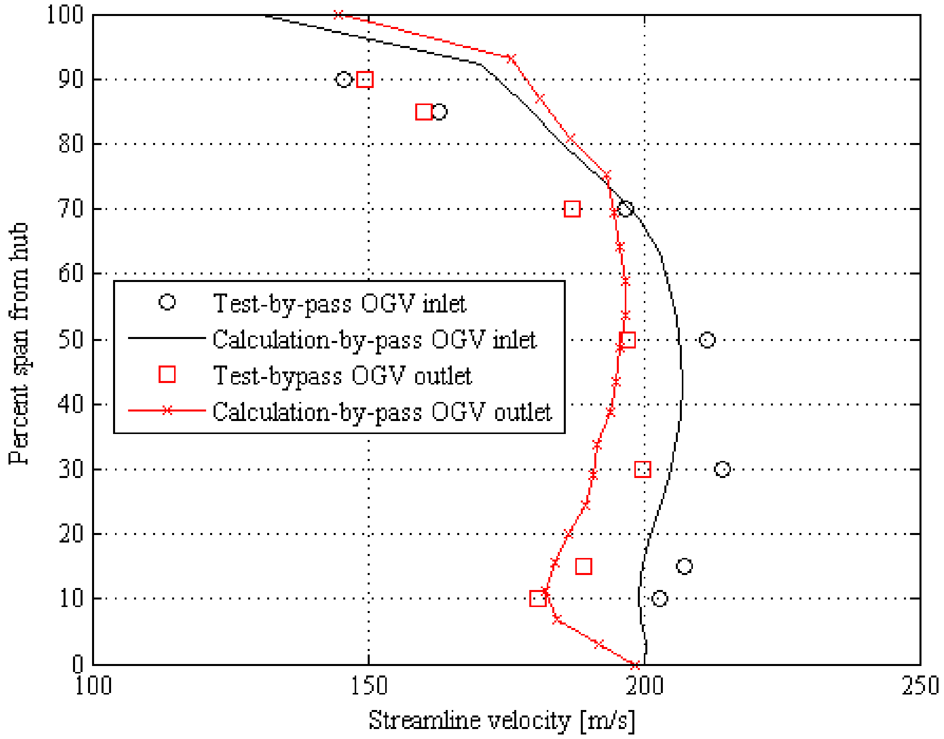

Figure 114. By-pass OGV inlet and outlet streamline velocity distributions

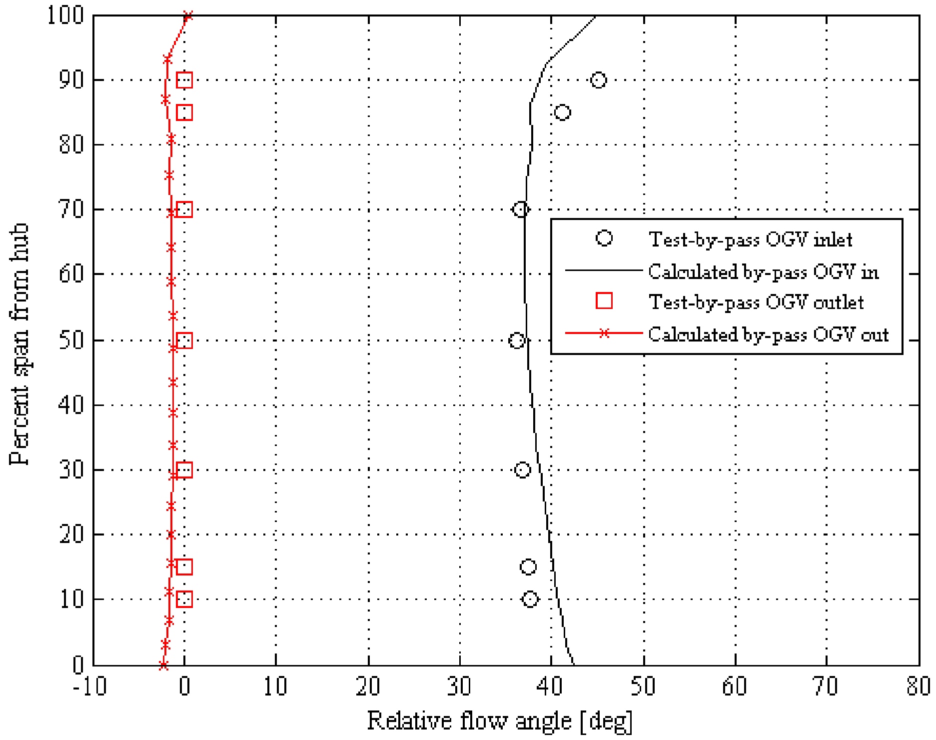

Figure 115. By-pass OGV inlet and outlet relative flow angle distributions

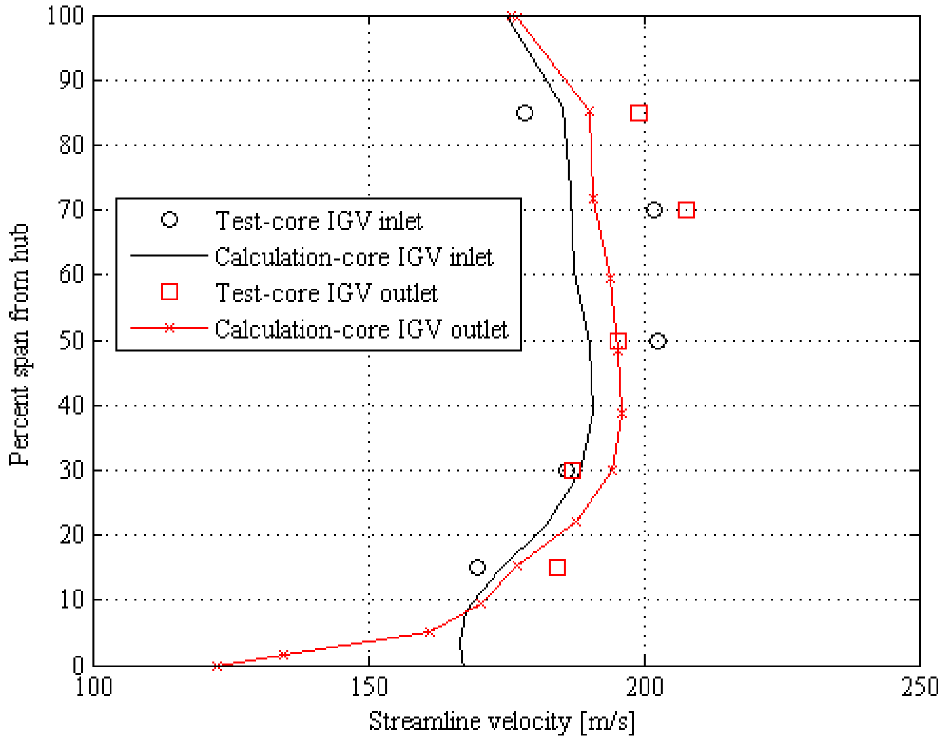

Figure 116. Core IGV inlet and outlet streamline velocity distributions

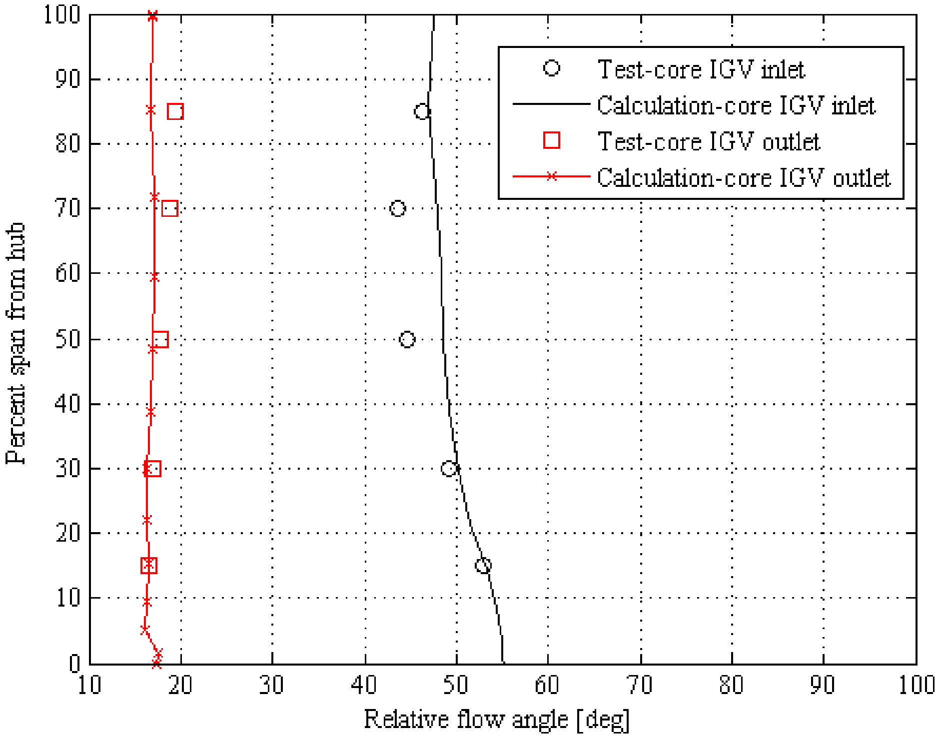

Figure 117. Core IGV inlet and outlet relative flow angle distributions

CHAPTER 6

CONCLUSIONS

Streamline curvature axisymmetric swirling compressible flow solver is developed, which has a newly developed general and practical split-flow capability for turbofan engine modeling capability with a computational time that is at least 1/100 of three dimensional Navier-Stokes analysis methods. The methodology includes turbomachinery blade models, which converts the solver absolute quantities into relative blade inlet and outlet quantities and calculates pressure and enthalpy rise through each blade row, from hub to tip. The turbomachinery module also includes detailed empirical correlations for relative total pressure loss coefficient (friction, secondary flow and shock), optimum incidence, deviation and boundary layer blockage.

The methodology is validated on a total of six test cases. Three of these are two-dimensional split-flow ducts that do not include blades, and aimed at validating the solver and its split-flow capability. Other two of those test cases are high-pressure-ratio single-stage and two-stage fan systems with transonic blades. The single-stage fan is designed in scope of this thesis and a three-dimensional CFD-based validation is carried out. The two-stage fan is the publicly available NASA fan and its performance is obtained from published experimental data. Those two fans do not have flow splitters but are used to calibrate the empirical models and validate single-stream solutions of the flow solver. Finally, the remaining test case is NASA-sponsored General Electric by-pass fan, which both have a split-flow geometry and high-performance turbomachinery. Its performance is obtained from published experimental data. This test case is used to validate complete methodology.

The agreement between the developed through-flow methodology and all of those validation cases is shown to be very good, maximum observed errors are within 1.6% in pressure ratio, 2.3% in efficiency, 8% in velocity and 1.8^{o} in flow angle. For future work, validation with more test cases should be performed to increase generality of the empirical models.

As a future work, it is also highly recommended that brand-new empirical models may be developed for a selected type of airfoil designs using computational fluid dynamics. This could even be done on 3D basis to include secondary flow effects, even if it would be computationally very expensive. Any advanced regression method or artificial neural networks may be used to obtain a relation between blade design parameters (inputs) and the corresponding performances (outputs). Moreover, such empirical correlations should also be developed for centrifugal compressors. In such a case, it would be possible to model centrifugal stage(s), which are usually employed in small engines. Another area of improvement is to include capability to model curved quasi-orthogonals, as for curved leading and trailing edges, which are specified before the solution, as done for flow paths. Finally, the blockage model may be improved significantly to better take into account the effects of blade rows. Even if the current simplified model provides acceptable outputs for one or two stage turbomachinery systems, the results may become unacceptable when many stages are considered.

REFERENCES

[1] E. A. Baskharone, Principles of Turbomachinery in Air-Breathing Engines, Cambridge University Press, 2006.

[2] "www.cfmaeroengines.com," CFM Aero Engines, 2015. [Online].

[3] C.-H. Wu, "A General Theory of Three-Dimensional Flow in Subsonic and Supersonic Turbomachines of Axial, Radial and Mixed-Flow Types," NACA TN-2604, 1952.

[4] R. I. Lewis, Turbomachinery Performance Analysis, Elsevier Science&Technology Books, 1996.

[5] T. Dickens and I. Day, "The Design of Highly Loaded Axial Compressors," *Journal of Turbomachinery*, vol. 133, p. 031007, 2011.

[6] J. D. J. Anderson, Modern Compressible Flow With Historical Perspective, 3rd Edition, McGraw Hill, 2004.

[7] R. J. Dunker, "A Shock Loss Model For Supercritical Subsonic Flows in Transonic Axial Flow Compressors," AGARD CP-401, 1987.

[8] N. A. Cumpsty, Compressor Aerodynamics, 5th ed., Krieger Publishing Company, 2004.

[9] O. Domercq, "Aero Engine Design: From State of the Art Turbofans Towards Innovative Architectures - HP Compressor Aerodynamics: 3D Design and Stage Matching," in *VKI Lecture Series 2008-03*, 2008.

[10] N. Smith, "Aero Engine Design: From State of the Art Turbofans Towards Innovative Architectures - The Aerodynamic Design of the LP System," in *VKI Lecture Series 2008-03*, 2008.

[11] J. Lepine, "Aero Engine Design: A State of the Art - Fan Aerodynamic Design," in *VKI Lecture Series 2003-6*, 2003.

[12] S. Shahpar, "Optimisation Strategies Used in Turbomachinery Design From an Industrial Perspective," in *Introduction to Optimization and Multidisciplinary Design in Aeronautics and Turbomachinery*, 2010.

[13] G. Karadimas, "Design of High Performance Fans Using Advanced Aerodynamic Codes," *Journal of Turbomachinery,* vol. 110, pp. 419-425, 1988.

[14] J. F. Escuret, D. Nicoud and P. Veysseyre, "Recent Advances in Compressor Aerodynamic Design and Analysis," NATO RTO EN-1, 1998.

[15] A. J. Wennerstrom, Design of Highly Loaded Axial-Flow Fans or Compressors, Concepts Eti, 2001.

[16] N. Cumpsty, "Some Lessons Learned," *Journal of Turbomachinery,* vol. 132, 2010.

[17] S. Damle, T. Dang, J. Stringham and E. Razinsky, "Practical Use of Three-Dimensional Inverse Method for Compressor Blade Design," *Journal of Turbomachinery,* vol. 121, pp. 321-325, 1999.

[18] L. M. Larosiliere, J. R. Wood, M. D. Hathaway, A. J. Medd and T. Q. Dang, "Aerodynamic Design Study of Advanced Multistage Axial Compressor," NASA TP-2002-211568 and ARL-TR-2859, 2002.

[19] N. Gauger, "Adjoint Approaches in Aerodynamic Shape Optimization and MDO Context, Parts I-III," in *von Karman Institute for Fluid Dynamics Lecture Series*, 2012.

[20] R. Braembussche, "Numerical Optimization for Advanced Turbomachinery Design," in *Optimization and Computational Fluid Dynamics*, Springer Berlin Heidelberg, 2008.

[21] P. Tiwari, A. Stein and Y. Lin, "Dual-Solution and Choked Flow Treatment in a Streamline Curvature Throughflow Solver," in *Proceedings of ASME Turbo Expo 2011*, Vancouver, Canada, 2011.

[22] J. D. Denton and W. N. Dawes, "Computational Fluid Dynamics for Turbomachinery Design," *Proc Instn Mech Engrs,* vol. 213, pp. 107-124,

1999.

[23] P. Calzada, "Aero Engine Design: From State of the Art Turbofans Towards Innovative Architectures - Aerothermodynamic Design of Low Pressure Turbines," in *VKI Lecture Series 2008-03,* 2008.

[24] M. Joly, T. Verstraete and G. Paniagua, "Full Design of a Highly Loaded Fan by Multi-Objective Optimization of Through-Flow and High-Fidelity Aero-Mechanical Performances," in *Proceedings of ASME Turbo Expo 2012,* Copenhagen, Denmark, 2012.

[25] N. Lecerf, D. Jeannel and A. Laude, "A Robust Design Methodology For High Pressure Compressor Throughflow Optimization," in *Proceedings of ASME Turbo 2003,* Georgia, USA, 2003.

[26] K. Park, M. Turner, K. Siddappaji, S. Dey and A. Merchant, "Optimization of a 3-Stage Booster Part 1: The Axiymmetric Multi-Disciplinary Optimization Approach to Compressor Design," in *Proceedings of ASME Turbo Expo 2011,* Vancouver, Canada, 2011.

[27] J. H. Harlock and J. D. Denton, "A Review of Some Early Design Practice Using Computational Fluid Dynamics and a Current Perspective," *Journal of Turbomachinery,* vol. 127, pp. 5-13, 2005.

[28] N. Falck, "Axial Compressor Mean Line Design," MSc Thesis, Lund University, 2008.

[29] J. Chauvin, Meridional Flow in Axial Turbomachines (Course Note 99), von Karman Institute for Fluid Dynamics, 1977.

[30] L. H. J. Smith, "Axial Compressor Aerodesign Evolution at General Electric," *Journal of Turbomachinery,* vol. 124, pp. 321-330, 2002.

[31] L. H. Smith, "The Radial-Equilibrium Equations of Turbomachinery," *Journal of Engineering for Power,* vol. 88, pp. 1-12, 1966.

[32] R. A. Novak, "Streamline Curvature Computing Procedures for Fluid Flow Problems," *Trans ASME Journal of Engineering for Power,* vol. 89, pp. 478-90, 1967.

[33] H. Marsh, "A Digital Computer Program for the Through-Flow Fluid Mechanics in an Arbitrary Turbomachine Using a Matrix Method," British Aeronautical Research Council Reports and Memoranda R. & M. No.3509, 1968.

[34] C. Hirsch and Warzee G., "An Integrated Quasi-3D Finite Element Calculation Program for Turbomachinery Flows," *Journal of Engineering for Power,* vol. 101, no. 1, pp. 141-148, 1979.

[35] A. Spurr, "The Prediction of 3D Transonic Flow in Turbomachinery Using a Combined Throughflow and Blade-to-Blade Time Marching Method," *The International Journal of Heat and Fluid Flow,* vol. 2, 1980.

[36] A. Sturmayr, "Evolution of a 3D Structured Navier-Stokes Solver Towards Advanced Turbomachinery Applications," PhD Thesis, University of Vrije, 2004.

[37] S. R. Taddei, F. Larocca and F. Bertini, "Euler Inverse Axisymmetric Solution for Design of Axial Flow Multistage Turbomachinery," in *Proceedings of ASME Turbo Expo 2010*, Glasgow, UK, 2010.

[38] F. Gu and M. Anderson, "CFD-Based Throughflow Solver in a Turbomachinery Design System," in *ASME Turbo Expo 2007*, Montreal, Canada, 2007.

[39] J. Simon, "Contribution to Throughflow Modeling for Axial-Flow Turbomachines," PhD Thesis, University of Liege, 2007.

[40] S. Lieblein, "Incidence and Deviation-Angle Correlations for Compressor Cascades," *Trans ASME Journal of Basic Engineering,* vol. 82, pp. 575-87, 1960.

[41] S. Lieblein and W. H. Roudebush, "Theoretical Loss Relations for Low-Speed Two Dimensional Cascade Flow," NACA TN 3662, 1956.

[42] R. H. Aungier, Axial Flow Compressors: A Strategy for Aerodynamic Design and Analysis, ASME Press, 2003.

[43] R. A. Braembussche, Blade to Blade Flow in Turbomachines (Course note 172), von Karman Institute for Fluid Dynamics, 2005.

[44] "Aerodynamic Design of Axial Flow Compressors," NASA SP-36, 1965.

[45] C. Koch and L. Smith, "Loss Sources and Magnitudes in Axial-Flow Compressors," *Journal of Engineering for Power,* vol. 98, no. 3, pp. 411-424, 1976.

[46] F. Sieverding, B. Ribi, M. Casey and M. Meyer, "Design of Industrial Axial Compressor Blade Sections for Optimal Range and Performance," *Journal of Turbomachinery,* vol. 126, pp. 323-331, 2004.

[47] C. D. Harris, "NASA Supercritical Airfoils: A Matrix of Family-Related Airfoils," NASA Technical Paper 2969, 1990.

[48] O. Leonard and R. A. Braembussche, "Design Method for Subsonic and Transonic Cascade with Prescribed Mach Number Distribution," *Journal of Turbomachinery,* vol. 114, 1992.

[49] H. Lichtfuss, "Customized Profiles - The Beginning of an Era," in *Proceedings of ASME Turbo Expo 2004,* Vienna, Austria, 2004.

[50] R. B. Ginder, A. J. Britton, W. J. Calvert, I. McKenzie and J. M. Parker, "Design of Advanced Blading for a High-Speed HP Compressor Using an S1-S2 Flow Calculation System," Royal Aerospace Establishment Technical Memorandum P 1196, 1990.

[51] M. B. Giles, "Some Thoughts on Eploiting CFD for Turbomachinery Design," in *IMeche Symposium on Exploiting CFD for Turbomachinery Design*, 1998.

[52] C. Hirsch and J. D. Denton, "Throughflow Calculations in Axial Turbomachinery," AGARD AR 175, 1981.

[53] M. Çetin, A. Ş. Üçer, C. Hirsch and G. K. Serovy, "Application of Modified Loss and Deviation Correlations to Transonic Axial Compressors," AGARD R 745, 1987.

[54] A. Schmitz, M. Aulich and E. Nicke, "Novel Approach for Loss and Flow-Turning Prediction Using Optimized Surrogate Models in Two-Dimensional Compressor Design," in *Proceedings of ASME Turbo Expo 2011,* Vancouver, Canada, 2011.

[55] K. M. Boyer, "An Improved Streamline Curvature Approach for Off-Design Analysis of Transonic Compression Systems," PhD Thesis. Virginia Polytechhnic Institute and State University, 2001.

[56] V. Pachidis, P. Pilidis, I. Templalexis and L. Marinai, "An Iterative Method for Blade Profile Loss Model Adaptation Using Streamline Curvature," *Journal of Engineering for Gas Turbines and Power,* vol. 130, 2008.

[57] J. Dunham, "A New Endwall Model for Axial Compressor Throughflow Calculations," *Journal of Turbomachinery,* vol. 117, 1995.

[58] J. H. Horlock, "The Determination of End-Wall Blockage in Axial Compressors: A Comparison Between Various Approaches," *Journal of Turbomachinery,* vol. 122, pp. 218-224, 2000.

[59] G. Adkins and L. Smith, "Spanwise Mixing in Axiai-Flow Turbomachines," *Journal of Engineering for Power,* vol. 104, 1982.

[60] S. Gallimore and N. Cumpsty, "Spanwise Mixing in Multistage Axial Flow Compressors: Part I - Experimental Investigation," *Journal of Turbomachinery,* vol. 108, 1986.

[61] S. Gallimore, "Spanwise Mixing in Multistage Axial Flow Compressors: Part II - Throughflow Calculations Including Mixing," *Journal of Turbomachinery,* vol. 108, 1986.

[62] D. Wisler, R. Bauer and T. Okiishi, "Secondary Flow, Turbulent Diffusion, and Mixing in Axial-Flow Compressors," *Journal of Turbomachinery,* vol. 109, 1987.

[63] J. Dunham, "Modelling of Spanwise Mixing in Compressor Through-Flow Computations," *Proc Instn Mech Engrs,* vol. 211, 1997.

[64] R. Mönig, F. Mildner and R. Röper, "Viscous-Flow Two-Dimensional Analysis Including Secondary Flow Effects," *Journal of Turbomachinery,* vol. 123, 2001.

[65] M. Casey and C. Robinson, "A New Streamline Curvature Throughflow Method For Radial Turbomachinery," in *Proceedings of ASME Turbo Expo 2008*, Berlin, Germany, 2008.

[66] V. Pachidis, p. Pilidis, I. Templalexis, T. Korakianitis and P. Kotsiopoulos, "Prediction of Engine Performance Under Compressor Inlet Flow Distortion Using Streamline Curvature," *Journal of Engineering for Gas Turbines and Power,* vol. 129, 2007.

[67] P. Shan, "A Mass Addition Approach to the Bypass Turbomachine Through Flow Inverse Design Problem," *Journal of Mechanical Science and Technology,* vol. 22, 2008.

[68] W. J. Calvert and A. W. Stapleton, "Detailed Flow Measurements and Predictions for a Three-Stage Transonic Fan," *Journal of Turbomachinery,* vol. 116, pp. 298-305, 1994.

[69] T. Sullivan and D. Parker, "Design Study and Performance Analysis of a High-Speed Multistage Variable-Geometry Fan for a Variable Cycle Engine," NASA CR-159545, 1979.

[70] T. J. Sullivan, J. L. Younghans and D. R. Little, "Single Stage, Low Noise Advanced Technology Fan. Volume 1: Aerodynamic Design," NASA-CR-134801, 1976.

[71] T. J. Sullivan , G. W. Luebering and R. D. Gravitt, "Energy Efficient Engine Fan Test Hardware Detailed Design Report," NASA-CR-165148, 1980.

[72] D. C. Wisler, L. Koops, A. McDaniel, J. Juenger and J. Cornell, "Chapter 3: Fan and Compressor Systems," in *Jet Engines and Propulsion systems For Engineers*, T. W. Fowler, Ed., GE Aircraft Engines, 1989.

[73] M. Shaw and R. W. Murdoch, "Computer Modeling of Fan-Exit-Splitter Spacing Effecs on Flow Response to Distortion," NASA CR-167879, 1982.

[74] M. S. Li, "2D Low ByPass-Ratio Turbofan Modelling," PhD Thesis, Cranfield University, 2004.

[75] D. Wilkinson, "Stability, Convergence, and Accuracy of Two-Dimensional Streamline Curvature Methods Using Quasi-Orthogonals," in *Proceedings of the Institution of Mechanical Engineers*, 1969.

[76] M. Gunton, "Performance Prediction for Turbomachines," PhD Thesis, Durham University, 1981.

[77] M. Shaalan and H. Daneshyar, "A Critical Assessment of Methods of Calculating Slope and Curvature of Streamlines in Fluid Flow Problems," *Proc. Inst. Mech. Eng.*, vol. 186, no. 70, pp. 891-896, 1972.

[78] J. Kleppler, "Technique to Predict Stage-by-Stage, Pre-Stall Compressor Performance Characteristics Using a Streamline Curvature Code with Loss and Deviation Correlations," MSc Thesis, University of Tennessee, 1998.

[79] G. Miller, G. Lewis and M. Hartmann, "Shock Losses in Transonic Compressor Blade Rows," *Journal of Engineering for Power,* vol. 83, no. 3, pp. 235-241, 1961.

[80] A. Wennerstrom and S. Puterbaugh, "A Three-Dimensional Model for the Prediction of Shock Losses in Compressor Blade Rows," *Journal of Engineering for Gas Turbines and Power,* vol. 106, no. 2, pp. 295-299, 1984.

[81] R. W. Fox, P. J. Pritchard and A. T. McDonald, Introduction to Fluid Mechanics, 7 ed., John Wiley & Sons, 2010.

[82] H. Creveling, "Axial-Flow Compressor Computer Program for Calculating Off-Design Performance," NASA CR-72472, 1968.

[83] V. Pachidis, "Gas Turbine Advanced Performance Simulation," PhD Thesis, Cranfield University, 2006.

[84] M. Petrovic, A. Wiedermann and M. Banjac, "Development and Validation of a New Universal Through Flow Method for Axial Compressors," in *Proceedings of ASME Turbo Expo 2009,* Orlando, USA, 2009.

[85] J. D. Anderson, Computational Fluid Dynamics: The Basics with Applications, McGraw-Hill, 1995.

[86] "ANSYS Fluid Dynamics Verification Manual Release 14.0," ANSYS INC., 2011.

[87] D. Urasek, W. Gorrell and W. Cunnan, "Performance of Two-Stage Fan Having Low-Aspect-Ratio First Stage Rotor Blading," NASA TP-1493, 1979.

[88] W. Cunnan, W. Stevans and D. Urasek, "Design and Performance of a 427-Meter-Per-Second-Tip-Speed Two Stage Fan Having a 2.40 Pressure Ratio," NASA TP-1314, 1978.

[89] J. Dunham, "CFD Validation for Propulsion System Components," AGARD AR-355, 1994.

[90] K. Suder, "Experimental Investigation of the Flow Field in a Transonic, Axial Flow Compressor With Respect to the Development of Blockage and Loss," PhD Thesis, Case Western Reserve University, 1996.

[91] T. Sullivan, I. Silverman and D. Little, "Single Stage, Low Noise Advanced Technology Fan. Volume 4: Fan Aerodynamics," NASA-CR-134892, 1977.

[92] R. Denos, Turbomachinery Cycles and Components, von Karman Institute for Fluid Dynamics, Course Note 163, 2005.

[93] E. A. Baskharone, Principles of Turbomachinery in Air-Breathing Engines, Cambridge University Press, 2006.

APPENDIX A

DIMENSIONAL ANALYSIS OF TURBOMACHINERY

Nondimensionalization has great importance in fluid dynamics to simulate a flow in terms of nondimensional (similarity) parameters rather than actual physical parameters. If a flowfield is described by n physical parameters (i.e. pressure drop as a function of geometry, density, viscosity, etc.) and they contain m fundamental units (distance, mass, time, etc.) then n-m nondimensional parameters (pressure coefficient as a function of Reynolds number, etc.) are sufficient to describe the same flowfield. This allows engineers to simulate a flow in an environment and model lengthscale which is different than the actual environment and scale, as long as the independent nondimensional parameters are equal. This is valid for turbomachinery applications as well. As tests will be performed at sea level, design inputs are corrected for standard sea level conditions (101325Pa and 288.15K) using the similarity parameters. Then the resulting flowfield and nondimensional performance parameters will be the same. It has been shown in [92] that functional relationship for a fan (or in general any turbomachinery) is:

$$\Pi, \eta = f\left(\frac{\dot{m}\sqrt{R_g T_{01}}}{P_{01} D^2}, \frac{\omega D}{\sqrt{\gamma R_g T_{01}}}, \gamma, \frac{\rho \omega D^2}{\mu} \right) \tag{A.1}$$

Where the two dependent nondimensional parameters are total-to-total pressure ratio and efficiency (η), respectively; while the independent nondimensional parameters are mass flow coefficient, nondimensional speed (or thermodynamic speed), specific heat ratio (γ) and rotor Reynolds number, respectively. R_g is the gas constant for a specific gas, μ is the dynamic viscosity and D is the outer diameter. 01 and 03 are the inlet and outlet stations, respectively.

For a fan operating with air, gas constants can be eliminated from the non-dimensional parameters:

$$\Pi, \eta = f\left(\frac{\dot{m}\sqrt{T_{01}}}{P_{01}D^2}, \frac{\omega D}{\sqrt{T_{01}}}, \frac{\rho\omega D^2}{\mu}\right) \tag{A.2}$$

It is usually impossible to match both the second (nondimensional speed) and the third (rotor Reynolds number) dependent parameters simultaneously; therefore the exact dynamic similarity usually cannot be achieved. However considering relatively weak Reynolds number dependency especially at high Reynolds numbers (Re_c> 5x10^5 where Re_c is the Reynolds number defined by chord length rather than fan diameter), the rotor Reynolds number can be omitted from the relation [93]. This is the case for most of the fans.

On the other hand, around 1/3 scaling in sea level leads to perfect dynamic similarity with 10668mm altitude designed engines (when γ is assumed constant and mass flow coefficient and nondimensional speed is also matched), without neglecting Reynolds number effect. A case-specific perfect matching can be calculated for specific design. However this is true only for a single point (at the given altitude). Therefore Reynolds number effect is generally completely neglected as long as Re_c>5x10^5. In conclusion the final functional relationship, neglecting Reynolds number effect, is:

$$\Pi, \eta = f\left(\frac{\dot{m}\sqrt{T_{01}}}{P_{01}D^2}, \frac{\omega D}{\sqrt{T_{01}}}\right) \tag{A.3}$$

Dynamic similarity between the standard sea level condition (denoted by subscript “*std*”) and any arbitrary condition (i.e. cruise design point) can be obtained as:

$$\left.\frac{\dot{m}\sqrt{T_{01}}}{P_{01}D^2}\right|_{sea\,level\,(std)} = \frac{\dot{m}\sqrt{T_{01}}}{P_{01}D^2} \Rightarrow \dot{m}_{std} = \frac{\dot{m}\sqrt{\theta}}{P_{01}/P_{01,std}} \tag{A.4}$$

$$\left.\frac{ND}{\sqrt{T_{01}}}\right|_{sea\,level\,(std)} = \frac{ND}{\sqrt{T_{01}}} \Rightarrow N_{std} = \frac{N}{\sqrt{T_{01}/T_{01,std}}} \tag{A.5}$$

Those similarity parameters (Eq.A.3) may also be used to scale-down the design to cut down test costs. Figure A.1 and Figure A.2 show variation of (equivalent) percent mass flow rate, power and rotational speed requirement as a function of scaling down. In those figures 100% represents the value at 1/1 scaling (either in altitude or sea level equivalent).

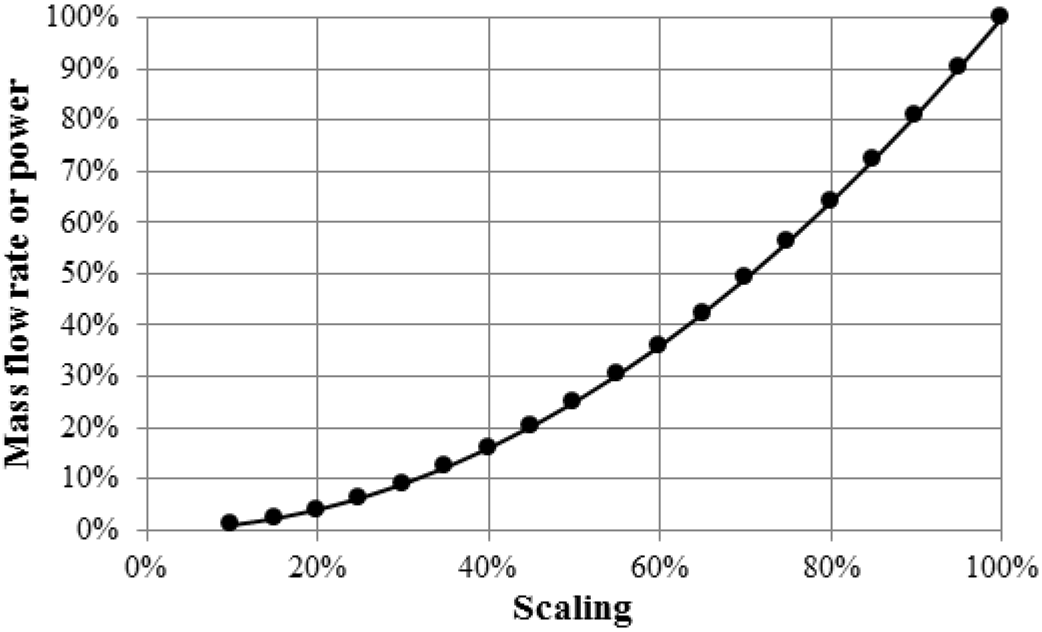

Figure A.1. Effect of scaling down on equivalent mass flow rate or power

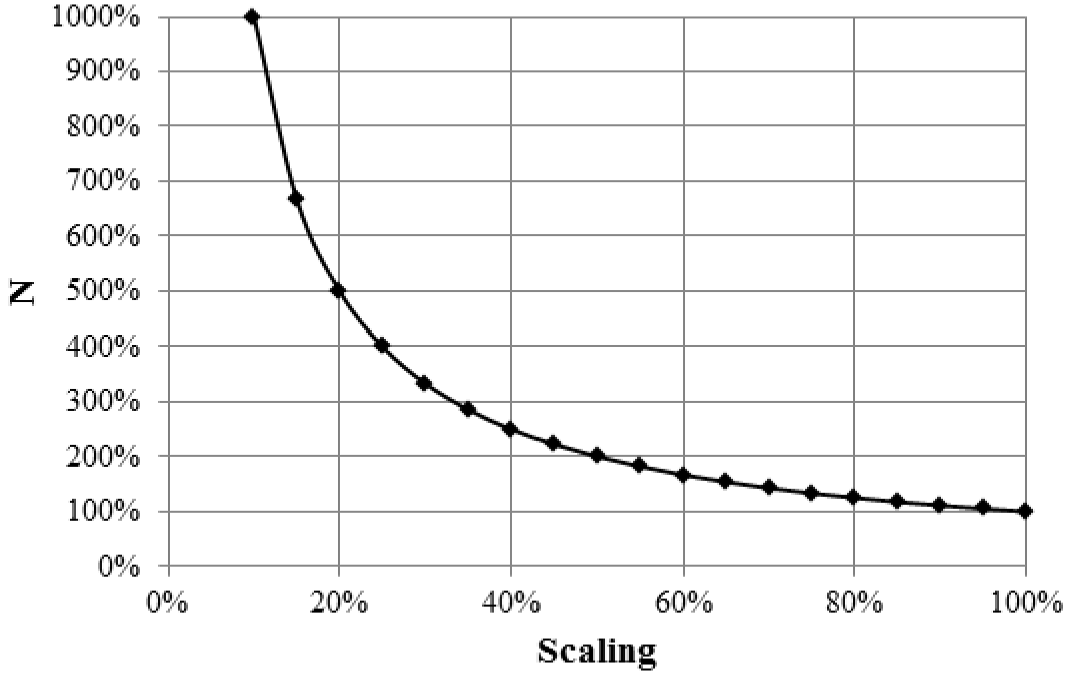

Figure A.2. Effect of scaling down on equivalent rotational speed

APPENDIX B

SIMPLE RADIAL EQUILIBRIUM

A simplified form of the streamline curvature method (full normal equilibrium) is the simple radial equilibrium, which assumes purely axial flow ($V_r=0$) with no streamline curvature effects at the calculation points, along with assumptions of steady inviscid axisymmetric flow but supported by a body of empirical database, as discussed in the literature review section. Calculations are done numerically along stations placed radially at various axial locations that are generally at bladeless (duct) regions of the passage such as at the leading and trailing edges of blades. The given number of nodal points on those stations defines the number of streamlines (Figure 10), which floats on radial direction depending on streamtube continuity. The same linking procedures with the full normal equilibrium exist for information passing in the streamwise direction.

This kind of modeling is still usable for machines, either incompressible or compressible, where streamline curvature effects and radial velocity can be neglected [8]. Equations along the radial calculation stations represent the force balance acting on a fluid particle with the only forces being pressure force and centrifugal force due to swirl:

$$\frac{1}{\rho}\frac{dP}{dr}=\frac{V_\theta^2}{r} \tag{B.1}$$

Defining total (stagnation) enthalpy as:

$$H=h+\frac{V_\theta^2}{2}+\frac{V_z^2}{2} \tag{B.2}$$

Substituting Eq.B.2 and second law of thermodynamics into Eq.B.1 gives the final equation valid for compressible flow:

$$\frac{dH}{dr} = T\frac{ds}{dr} + V_\theta \frac{dV_\theta}{dr} + \frac{V_\theta^2}{r} + V_z \frac{dV_z}{dr} \tag{B.3}$$

This is the so-called "non-isentropic simple radial equilibrium equation (NISRE)". The solution of the integrated version of this equation requires the radial distributions swirl (V_θ) to be imposed behind each blade row. Total enthalpy, pressure and axial velocity distributions, therefore flow angle distributions, at each axial station are obtained as a result of iterative calculations of NISRE, continuity and state equations. The radial entropy distribution is the term that takes into account all kind of viscous or 3D losses, where boundary layer or wake blockages are taken into account in continuity equation [29]. All those data is dependent on the flowfield, therefore an iterative procedure is required (see streamline curvature method or literature review section for details).

APPENDIX C

DUMMY DOMAIN EXTENSIONS

This appendix is prepared to obtain computational domain dummy inlet and outlet extension length requirements for CFD-SLC comparisons of Section 5.1. Basically, streamline curvature and slope terms in a SLC solver must be handled accurately in order to get a meaningful result. As it is difficult to accurately calculate streamline curvature at the ends of streamlines, there is a benefit in extending the domain such that the solution is not affected by the end-effects, even if inlet velocity direction and outlet static pressure distribution is inherently a result of SLC solution, unlike finite volume solvers. Finite volume solvers need such domain extensions; because of the aforementioned fact that inlet and outlet conditions are known over average values, but node-by-node inlet flow direction and exit static pressure distribution, required as boundary condition, may not be known. Specifying those approximate boundary conditions at those extensions, namely dummy inlet and outlet, allow more realistic conditions to occur at the real domain inlet and outlet. As the finite volume solvers are expected to be more sensitive to those extensions due to above reasons, the following study is carried out with finite volume computations, assuming the results are on the conservative side for SLC solutions.

The minimum required dummy extension lengths at inlet and outlet are tested for fan rotor flowpath portion of the test-case geometry of 5.1.1. The cropped geometry is shown in Figure C.1 and the real domain (without extensions) is distinguished as the domain bounded by ‘*real domain inlet*’ and ‘*real domain outlet*’. Boundary conditions are the same as the ones used in Section 5.1.1. As the hub endwall facing the upcoming air is highly ramped (around 45 degrees), the potential effect of this flowpath on the upstream flow is rather very high among typical engines. Therefore findings of this section may be used for other geometries as well. On the outlet side, the required extension is obtained for the cropped geometry (no downstream flow splitter and duct branches). Nevertheless, this may also be on the conservative side as the hub to shroud radius ratio of ‘*real domain outlet*’ is a small value (0.45) and curvature is large, so that hub-to-shroud static pressure variations are expected to be large, leading to conservative (longer) required dummy extension, applicable as a general guideline.

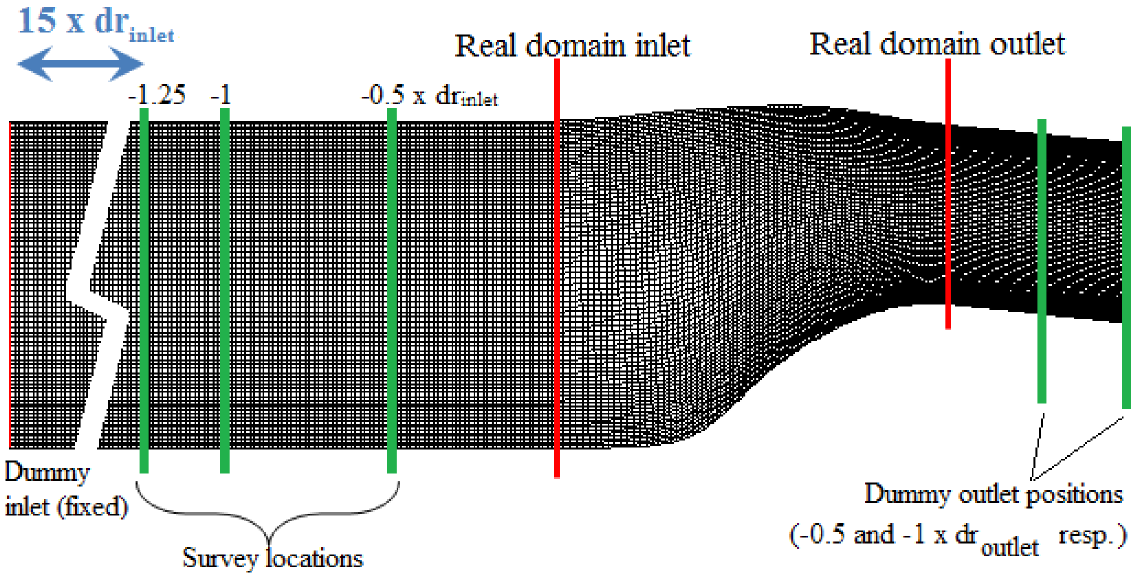

Figure C.1. The tested dummy extension lengths

Minimum required dummy inlet length is the length at which the velocity component normal to the mainstream (axial) is almost zero. Therefore, a velocity vector normal to inlet boundary (or parallel to inlet walls) can be specified in finite volume solvers. A computational model with sufficiently long inlet and outlet extensions is generated based on the aforementioned geometry (Figure C.1; 15 times the inlet shroud to hub radius difference at inlet and 2 times the radius difference at the outlet) and analysis at inlet Mach numbers 0.25 and 0.4 are performed. Rather small Mach numbers are selected, because the lower the Mach number, the stronger the downstream potential effect, and the bigger the required dummy inlet length. Data is acquired at axial locations 0.5, 1 and 1.25 radius differences (dr) upstream of real inlet, as shown in Figure C.1. It is clear from the results shown in Figure C.2 that an inlet extension of 1.25dr is sufficiently a safe value, resulting a radial velocity less than 0.1% of the axial velocity (or mainstream, for generality), even for the lower Mach number case.

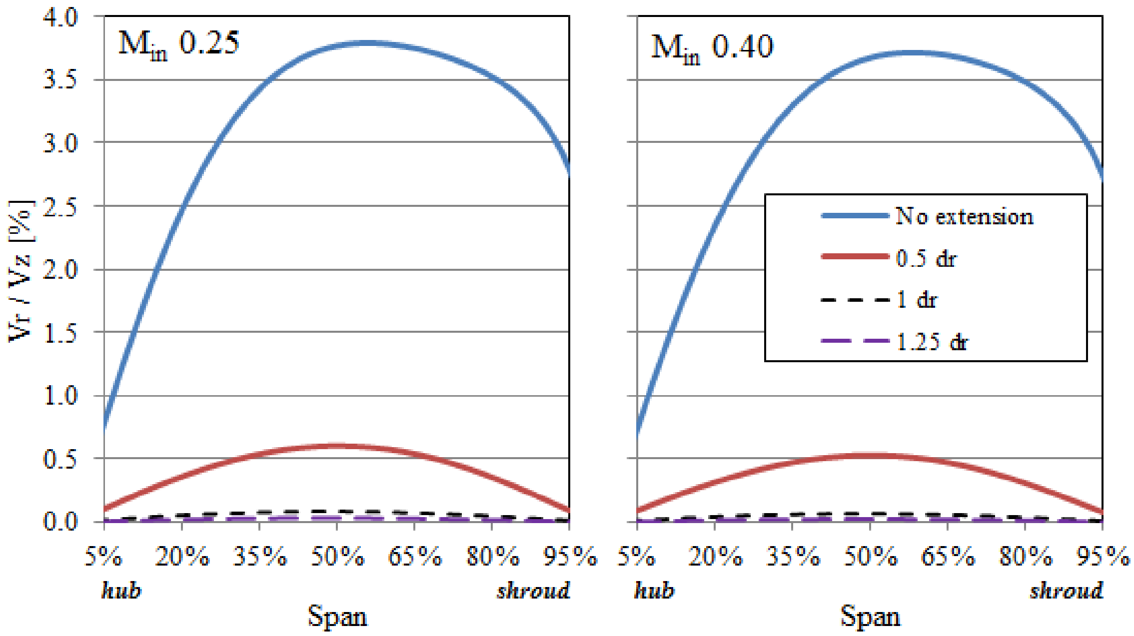

Figure C.2. Results of the inlet dummy extension study

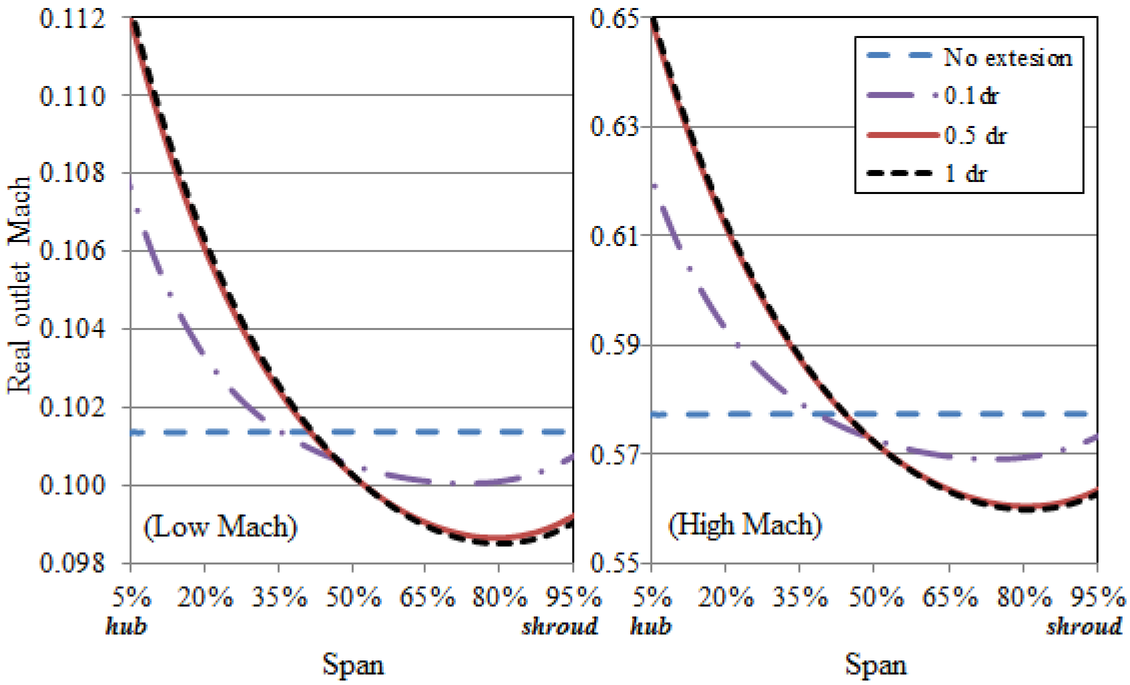

Figure C.3. Outlet dummy extension effects

A similar analysis is also performed for the determination of dummy outlet length requirement (Figure C.1). The criteria for the outlet extension, being a straight extension that is tangent to the real exit, is simply obtaining realistic conditions at the real domain outlet by avoiding undesirable effects of needing to specify average static pressure at the computational domain outlet. Contrary to the inlet counterpart, where a single model is used, different models with different dummy outlets are used. Dummy inlet is kept constant at the optimum value (1.25dr) of above inlet analysis. Constant static pressure is specified at the exit and Mach number distribution at the real outlet is monitored until this distribution is not changed with increased dummy outlet length. Two different average Mach numbers, 0.1 and 0.6, at the real outlet are tested. The wider Mach range, compared to the inlet study, is due to wider possible operating conditions at the discharge of any compressor. Figure C.3 shows the result of the analysis. As expected, like the inlet one, the lower Mach number results in longer outlet extension requirement due to higher back propagation. It is evident that there is virtually little difference between the extensions of 0.5 and 1dr for both cases. This means that 0.5dr is a sufficient extension length. The differences between the two are maximum 0.3% and 0.2% for the lower and higher Mach number cases, respectively. Average differences are roughly half of these maximum values. It is obvious that specifying constant static pressure at the real outlet for the case considered simply causes unacceptably wrong results for the present case. These analyses conclude that it is better to use at least 1dr outlet extension, or more for conservativeness, considering area variations may exist when the exit is not purely axial.

APPENDIX D

STREAMLINE CURVATURE MESH DEPENDENCY

This appendix presents mesh dependency study to be used in Section 5.1. Only the first case, the high by-pass ratio case, is investigated but the remaining low and medium by-pass ratio cases use similar mesh sizes. Both quasi-orthogonal spacing and streamline number is considered for optimization. As discussed in Section 3.3, quasi-orthogonal spacing effect is studied in literature and the double-spline fit method employed in this study is shown to be accurate down to 5 points per smallest wavelength obtained from Fourier decomposition of any streamline. Nevertheless, error in smallest wavelength component may not reflect overall error, which may be smaller than estimated. Therefore a direct mesh dependency study is carried out in the specific case investigated in two steps: the first one is to determine quasi-orthogonal spacing with initially assumed 33 total streamlines and the second one is to determine optimum number of streamlines. The initial mesh with 33 streamlines, denoted as '*coarse*', consists of 16, 21 and 23 quasi-orthogonals in fan, by-pass and core domains, respectively. The refined mesh, denoted as '*medium*', is twice as dense and consists of 31, 41 and 45 quasi-orthogonals, in the same domain order as the coarse mesh. The further refined mesh, denoted as '*fine*', is roughly 1.5 times denser than the medium mesh, and consists of 51, 69 and 75 quasi-orthogonals, in the same domain order as the other two. The three meshes are shown in FiguD.1. While dummy outlets have same mesh densities as the bulk domain, dummy inlet mesh is kept coarse in all meshes for stability reasons. Moreover, this is believed to have no influence on the overall result due to zero streamline curvature and slope.

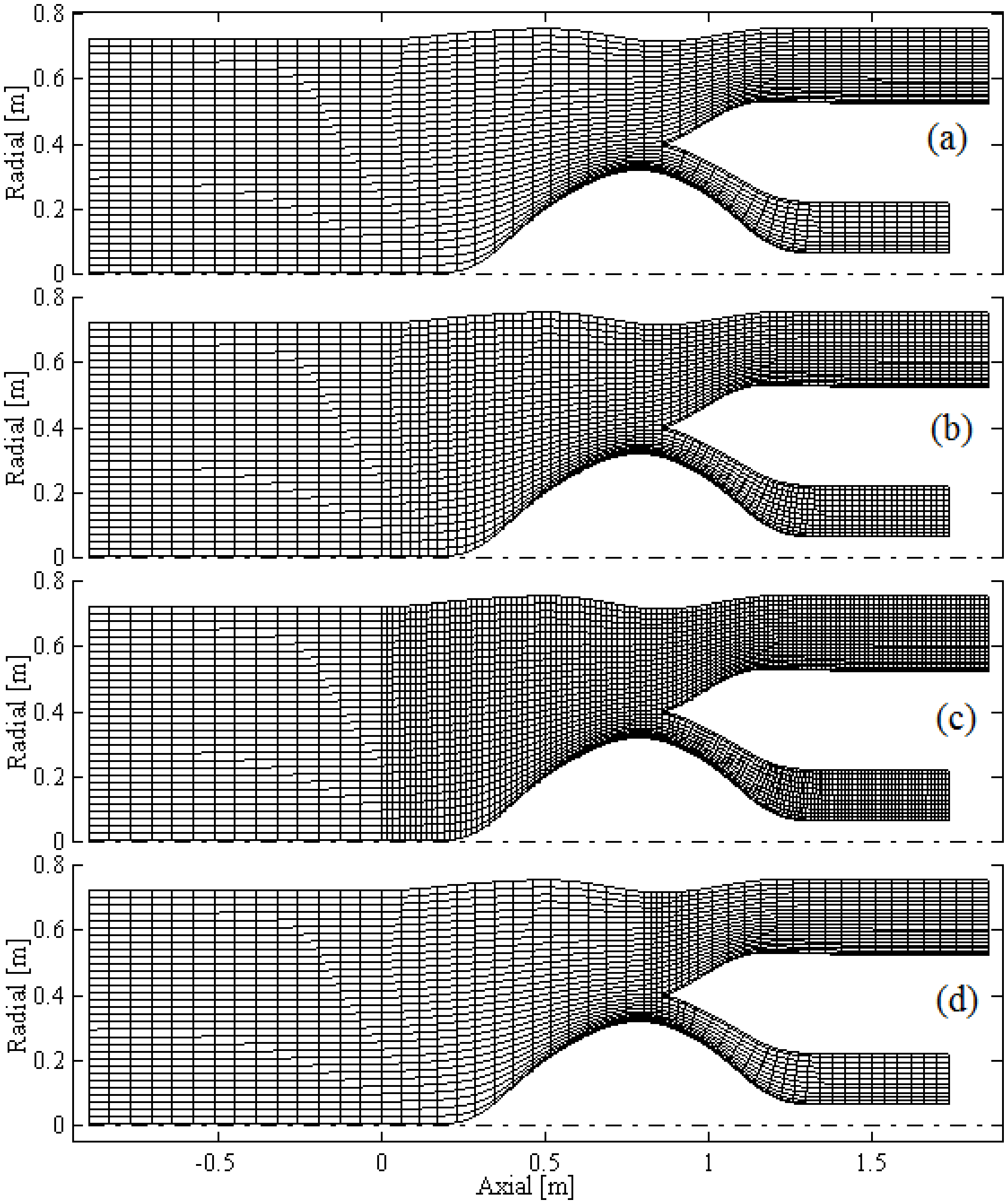

Figure D.1. Coarse (a), medium (b), fine (c) and hybrid (d) grids

Results on core/by-pass mass flow distribution are given in Table D.1, where all the mesh densities show good results, although the coarse mesh yields 0.27% difference in core mass flow and 0.31% difference in by-pass ratio. Wall velocity distributions are compared in more detail in Figure D.2, Figure D.3 and Figure D.4 for fan, by-pass and core ducts wall velocity distributions, respectively. Although trends are the same and values are very similar for all meshes, maximum difference between coarse and fine meshes is around 5% in wall velocity near splitter leading edge. But, difference is generally much less than 1% in remaining sections. Likewise but better, difference between medium and fine mesh is maximum around 1.5% at the same point. Again, differences are much less than 1% in remaining sections.

Table D.1. Effect of quasi-orthogonal spacing on mass flow distribution

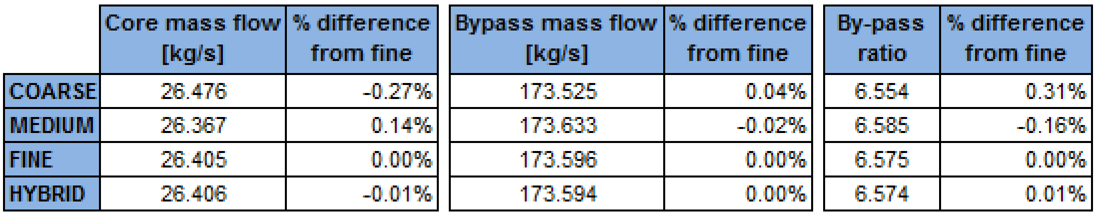

	Core mass flow [kg/s]	% difference from fine	Bypass mass flow [kg/s]	% difference from fine	By-pass ratio	% difference from fine
COARSE	26.476	-0.27%	173.525	0.04%	6.554	0.31%
MEDIUM	26.367	0.14%	173.633	-0.02%	6.585	-0.16%
FINE	26.405	0.00%	173.596	0.00%	6.575	0.00%
HYBRID	26.406	-0.01%	173.594	0.00%	6.574	0.01%

Based on above results, the fine mesh can be assumed as mesh-independent in terms of quasi-orthogonal spacing, because further refinement is not expected to yield meaningful improvement. On the other hand, fine mesh is computationally expensive and its density should only be preserved in critical regions. Therefore, optimum mesh is selected as a combination of coarse and fine meshes. The regions where streamline curvature is largest must have denser quasi-orthogonals. This is detected to be the proximity of split interface, where curvature is largest (due to both aggressive endwalls and presence of high-wedge-angle splitter). The resulting mesh is denoted as hybrid mesh, which is also shown in Figure D.1, together with the three meshes. It is shown in Table D.1 that difference in mass flow distribution to both ducts is virtually the same as the fine mesh. Wall velocity distributions shown in Figure D.2, Figure D.3 and Figure D.4 also indicate that results of the hybridized mesh are almost the same as the fine mesh results. Therefore the quasi-orthogonal spacing of the hybridized mesh is used for the rest of this section, although mesh independency of streamline number will be determined below.

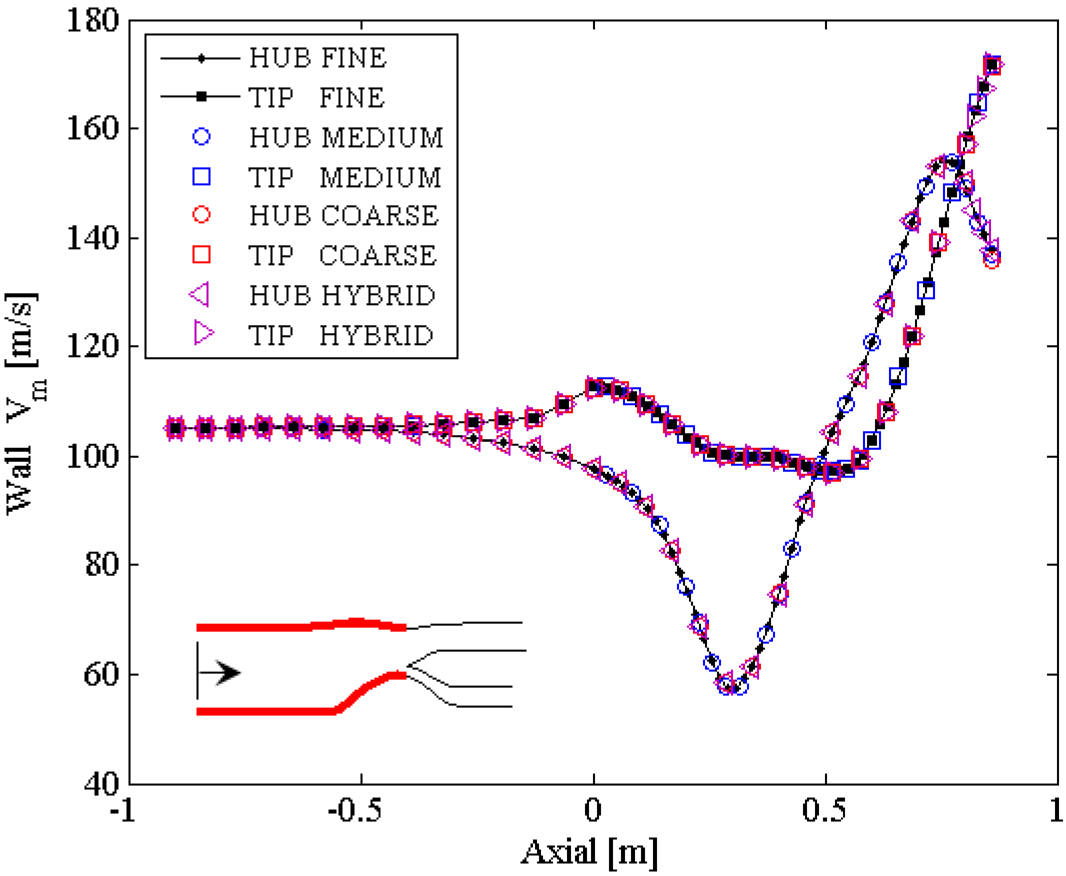

Figure D.2. Fan duct wall velocity distributions for different meshes

Before determining the required number of streamlines, it is beneficial to setup a criterion for quasi-orthogonal spacing near the splitter region. It can be assumed that grid aspect ratio near the splitter (spacing/height) is mainly a function of height to maximum local streamline radius of curvature ratio. Using the values of the optimized hybrid mesh, below criterion is obtained in this section:

$$\frac{\text{spacing}}{\text{height}} = 0.03\,\text{height}\left(K_m\right)_{\max} \qquad \text{(D.1)}$$

The formula is valid for meridional Mach numbers at around 0.4 and further increase of Mach number may demand denser mesh due to increased sensitivity of solution to streamline curvature at higher Mach numbers. Nevertheless, it can be used as a guideline or first guess rather than an exact criterion.

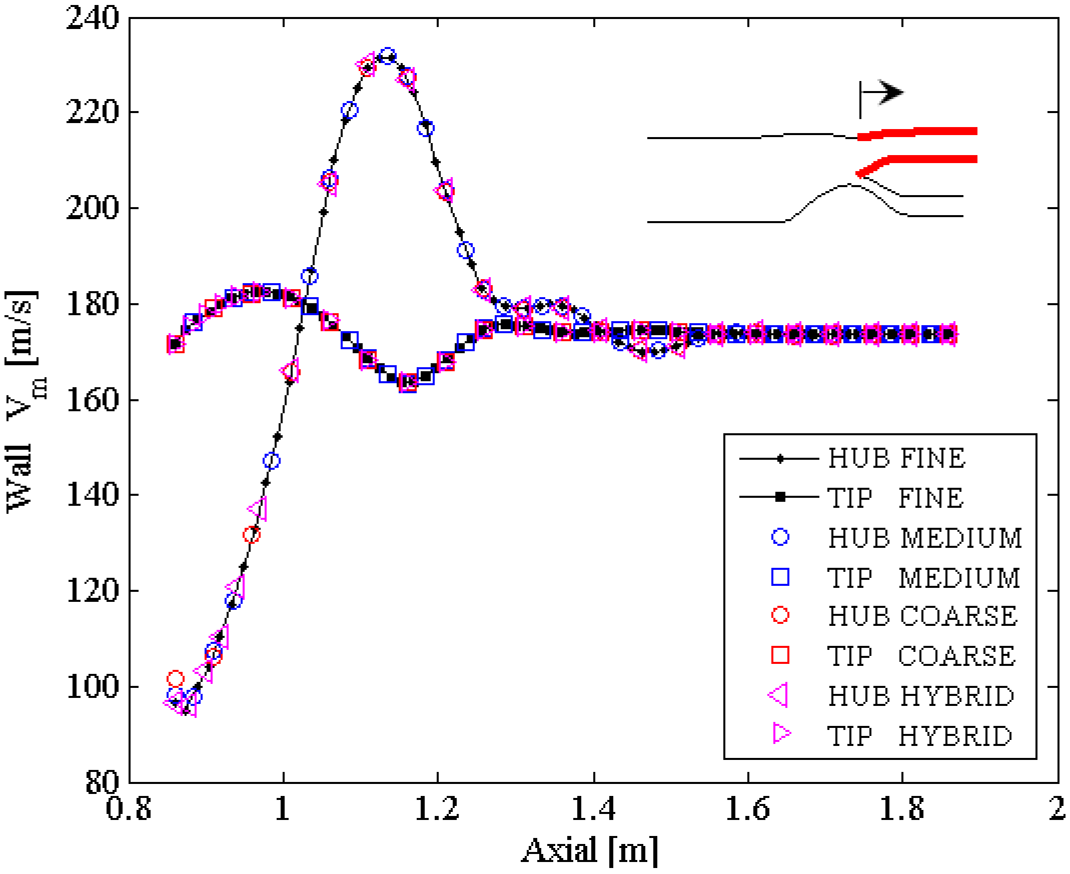

Figure D.3. By-pass duct wall velocity distributions for different meshes

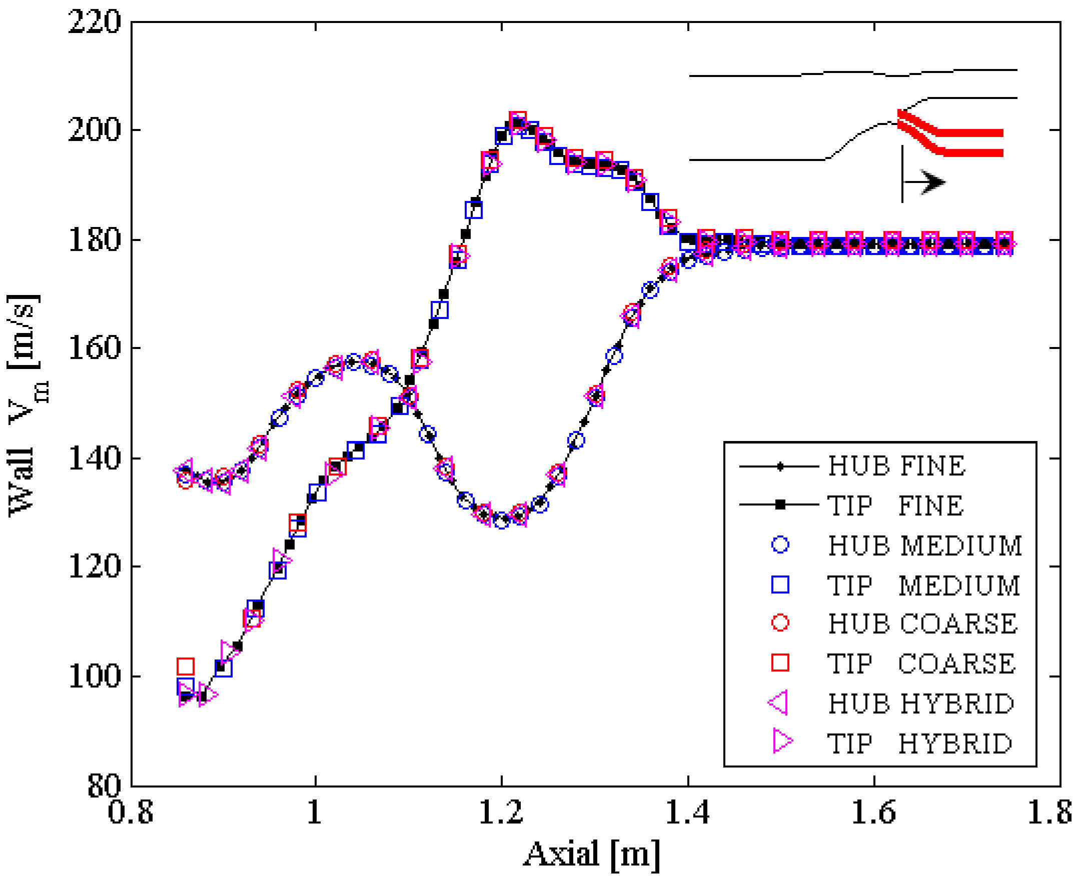

Figure D.4. Core duct wall velocity distributions for different meshes

Finally, the effect of streamline number is checked by performing the solution with 60 streamlines, as compared to the original solution with 33 streamlines. The result is shown at the most critical region, splitter interface, as radial profile of meridional velocity at constant axial position in Figure D.5, where it is evident that increase of streamlines from 33 to 60 has little effect, less than 1%, on the velocity profile. This is also outlined in Table D.2, which presents overall results on mass flow rate distribution. It can then be assumed that further increase in streamline number will yield a change even less than this error. Therefore, both 33 and 60 streamlines are acceptable based on accuracy requirement and analysis type. For more accuracy, 60 streamlines are selected for the rest of this section. The final mesh for the aforementioned high by-pass ratio case of Section 5.1.1 is shown in Figure D.6, which the same as the hybrid mesh but with more streamlines. As an output of this study, the low and medium by-pass ratio cases of Section 5.1.2 use a very similar mesh density.

Table D.2. Effect of streamline number on mass flow distribution for hybrid mesh

	Core mass flow [kg/s]	% difference	Bypass mass flow [kg/s]	% difference	By-pass ratio	% difference
33 streamlines	26.4057	-0.86%	173.5943	0.13%	6.5741	1.00%
60 streamlines	26.6342		173.3658		6.5091	

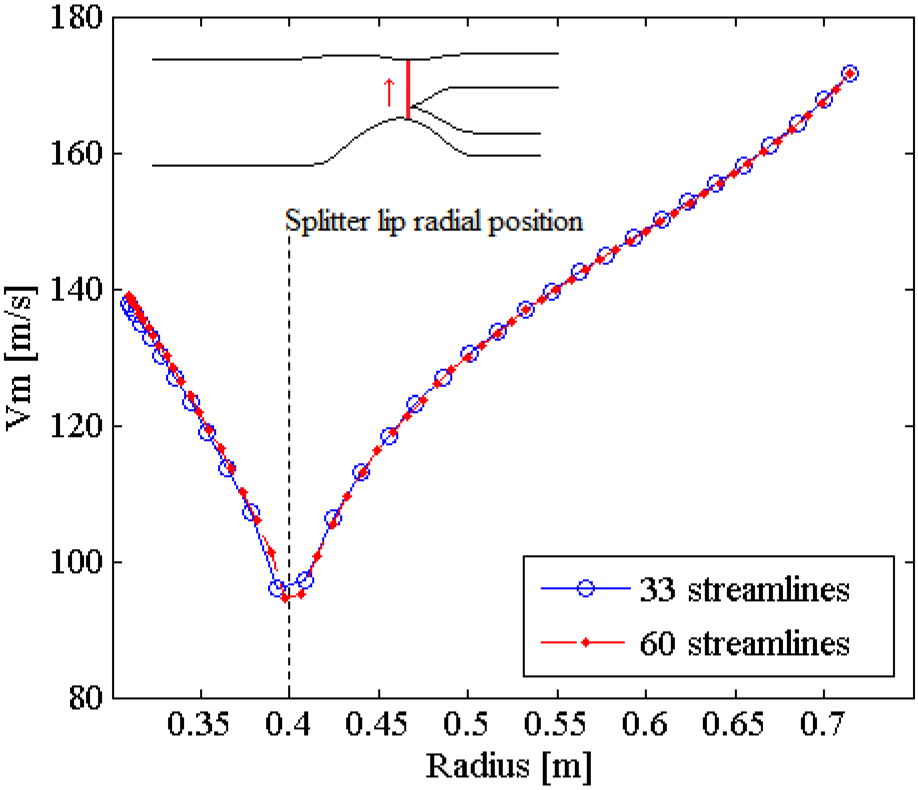

Figure D.5. Effect of streamline number

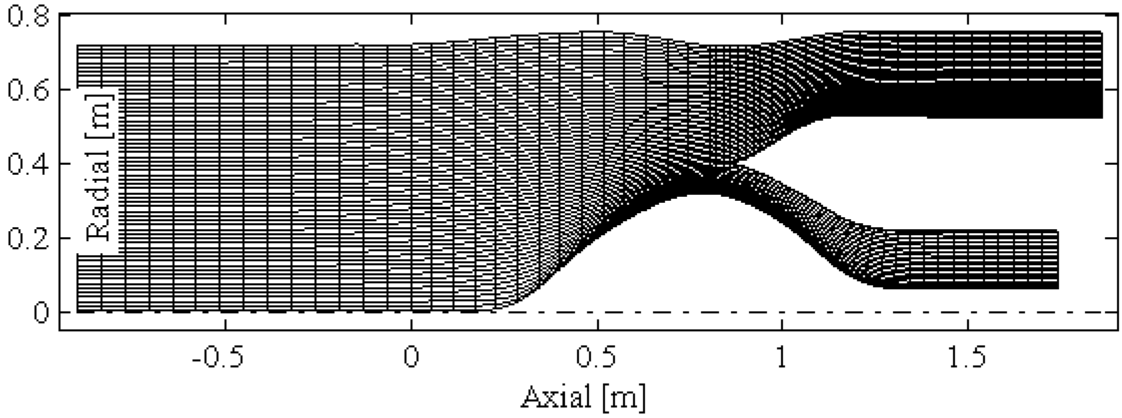

Figure D.6. The final mesh

APPENDIX E

ARTIFICIAL VISCOSITY FOR 2D CFD COMPARISONS

This appendix presents effects of artificial viscosity that is observed in finite volume solutions. Only the high by-pass ratio case of Section 5.1.1 is investigated but the outputs are valid for the low and medium by-pass ratio cases of Section 5.1.2.

Unlike streamline curvature solvers, which do not allow entropy to change along any streamline unless they are directly specified by external models (existence of turbomachinery and endwall boundary layers), unrealistic entropy increase and total pressure drop due to numerical errors can occur in inviscid finite volume solvers (artificial viscosity or numerical dissipation [85]).

The finite volume mesh described above minimizes artificial viscosity effects, but it is beneficial to estimate local error magnitude in the final finite volume output. To do this, a simple one dimensional analysis is carried out at all nodes. Compressible flow relation relating static-to-total pressure ratio to Mach number is [81]:

$$\frac{P}{P_0}=\left(1+\frac{\gamma-1}{2}M^2\right)^{-\gamma/(\gamma-1)} \quad\Rightarrow\quad M=\left\{\frac{2}{\gamma-1}\left[\left(\frac{P}{P_0}\right)^{(\gamma-1)/-\gamma}-1\right]\right\}^{1/2} \tag{E.1}$$

Ideally, total pressure along a streamline must be constant (in this case uniform as at inlet boundary condition value of 101325 Pa). Nevertheless, artificial viscosity reduces this value locally near walls. Finite volume calculated '*erroneous*' Mach number can be estimated from above formula using local values of total and static pressures extracted from the solution file (Mach number is not extracted directly to be consistent in all steps of this simplified analysis):

$$M_{\text{Finite volume}} = \left\{ \frac{2}{\gamma - 1} \left[\left(\frac{P_{\text{Finite volume}}}{P_{0-\text{Finite volume}}} \right)^{(\gamma-1)/-\gamma} - 1 \right] \right\}^{1/2} \tag{E.2}$$

Ideal local Mach number can be estimated assuming that static pressure is not affected from artificial viscosity, and in non-ideal case, only dynamic component is assumed to reduce (because static pressure is mostly imposed from surrounding fluid). Therefore total pressure is kept at its true value (101325 Pa) at all nodes and finite volume-calculated static pressure is assumed as artificial viscosity-free. Then local ideal Mach number is calculated from:

$$M_{ideal} = \left\{ \frac{2}{\gamma - 1} \left[\left(\frac{P_{\text{Finite volume}}}{101325} \right)^{(\gamma-1)/-\gamma} - 1 \right] \right\}^{1/2} \tag{E.3}$$

The difference between Mach numbers calculated from above formulas gives rough estimate of local error in Mach number:

$$Error_{Mach} = M_{\text{Finite volume}} - M_{ideal} \tag{E.4}$$

As an alternative, similar error levels are obtained if one uses the ratio of calculated-to-ideal total pressure ratio, eliminating static pressure, to directly estimate Mach number error:

$$Error_{Mach} = \left\{ \frac{2}{\gamma - 1} \left[\left(\frac{P_{0-\text{Finite volume}}}{101325} \right)^{(\gamma-1)/-\gamma} - 1 \right] \right\}^{1/2} \tag{E.5}$$

Defined SLC-finite volume comparison survey locations for the high by-pass ratio case of Section 5.1.1 are presented in Figure 39. Estimated errors in Mach number are presented in Figure E.1. It is shown that maximum 0.01-0.02 error in Mach number magnitude can be expected locally. On the other hand, error in bulk of flow is well below 0.005. The comparisons at the surveys are made in light of these error distributions at corresponding surveys.

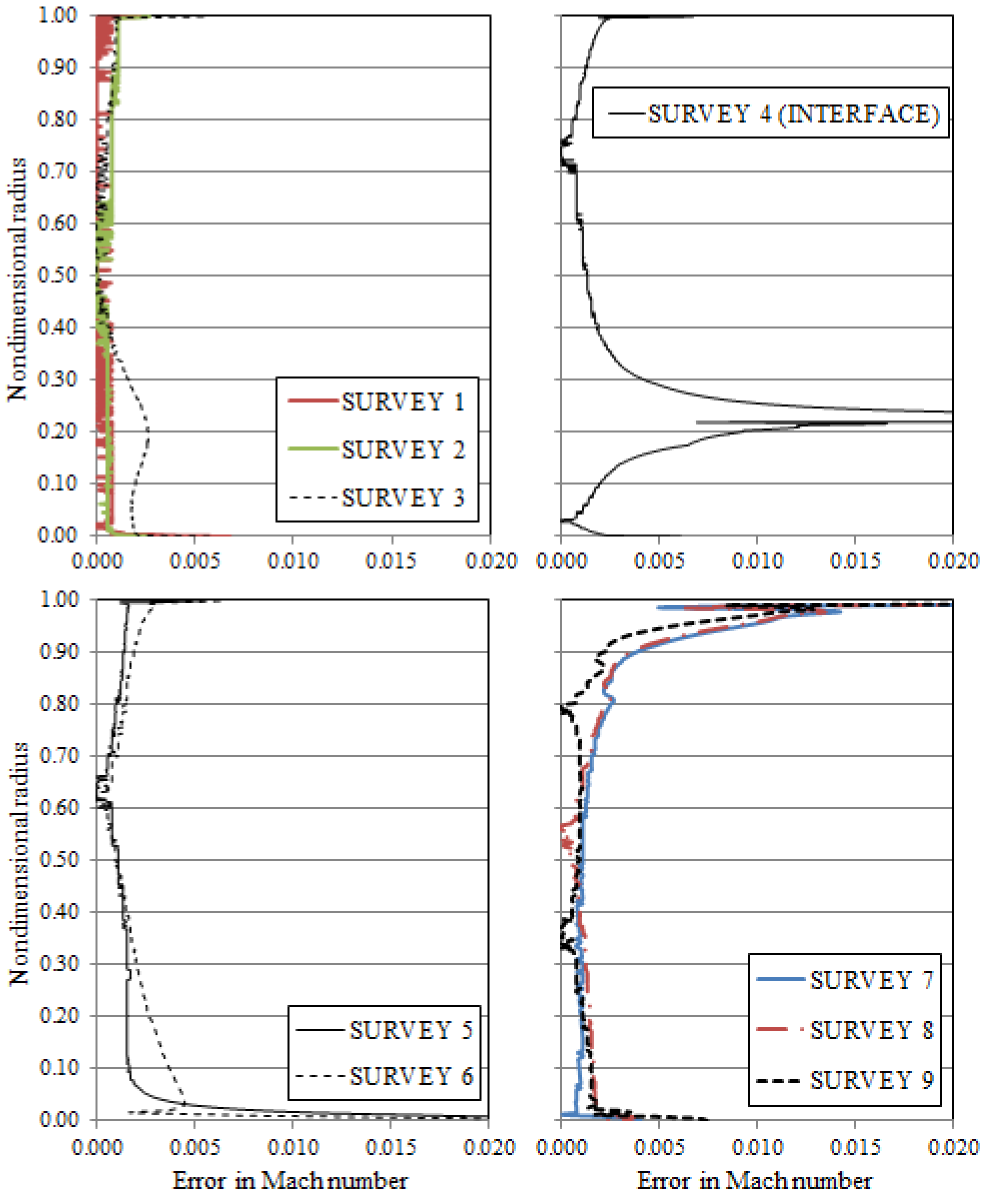

Figure E.1. Estimated finite volume Mach number errors in the surveys

VITA

Sercan ACARER was born in Izmir/TURKEY in December 13, 1985. He graduated from Dokuz Eylul University, Mechanical Eng. Dept. in 2008 and then from M.Sc. in the same dept. in 2010. He then became research assistant and PhD Student in Izmir Institute of Technology. He graduated with honor degree from 1-year master-after-master program of von Karman Institute for Fluid Dynamics in 2011. There, he mainly studied compressor aerodynamics and experimental techniques. In parallel with the educational program, he involved in a project related to high by-pass ratio fan measurements with advanced aerodynamic probes. He started to work in Tusaş Engine Industries (TEI) in 01.2012, his position is lead aerodynamics engineer. He completed his PhD studies in Mechanical Engineering Department of Izmir Institute of Technology.

Publications

- **Acarer, S.**, Özkol, Ü. (2015), "A New Through-Flow Method for Inverse Design of Turbofan Engine Split-Flow Fan Systems," (ongoing for a journal publication).
- Cukurel, B., **Acarer, S.**, Arts, T. (2012), "A Novel Perspective to High Speed Cross-Hot-Wire Calibration Methodology," Experiments in Fluids, Vol. 53, pp. 1073-1085.
- **Acarer, S.**, Özkol, Ü. (2015), "Development of a New Universal Inverse Through-Flow Program and Method for Fully Coupled Split-Flow Turbomachinery Systems," Proceedings of ASME Turbo Expo Turbine Technical Conference and Exposition 2015, Montreal, Canada.
- **Acarer, S.**, Tatar, V. and Türk, S. (2015), "A Numerical and Experimental Study on Heat Transfer at the Gas Turbine Exhaust Cone," 7th Baltic Heat Transfer Conference, Tallinn, Estonia (Accepted).
- Tatar, V., **Acarer, S.** and Türk, S. (2015), "Thermal Analysis of a Gas Turbine Exhaust Cone and Comparison with Experimental Data," 8th Ankara International Aerospace Conference, Ankara, Turkey (Accepted).
- Topal, E., **Acarer, S.** and Kırgız, T (2013), "The Design and Performance Evaluation of a Novel Air/oil Separator for Use in a Miniature Jet Engine," Proceedings of 49th AIAA Joint Propulsion Conference, California, U.S.A.
- **Acarer, S.**, Yasa, T. and Enser, Ç. (2012), "Atmospheric Jet Design for Probe Calibrations (originally written in Turkish)," National Aerospace Conference (UHUK).
- Çanakçı, C. and **Acarer, S.** (2009), "Design Principles of Geothermal Energy Greenhouse Heating Systems" (originally written in Turkish), 9th Turkish National Congress of HVAC & Sanitary Engineering (TESKON).